

Dissertation

submitted to the
Combined Faculty of Natural Sciences and Mathematics
of Heidelberg University, Germany
for the degree of
Doctor of Natural Sciences

Put forward by
Steffen Therre, M. Sc.
born in Wadern
Oral examination: July 28, 2020

Radiocarbon in Stalagmites:

Indicator of Climate Variability

and

Key to Atmospheric Radiocarbon Reconstruction

Referees:

Prof. Dr. Norbert Frank

Prof. Dr. André Butz

Abstract

Due to their ability to record climate change over large periods of time, stalagmites remain a primary focus of paleoclimatology. Utilizing high-precision age determination methods such as U-series dating, it is possible to measure climate-induced variations of the geochemical composition of speleothems over the time of their growth periods. This dissertation focuses on the investigation of radiocarbon (^{14}C) concentration in several stalagmites. To this end, a new setup for the chemical preparation of carbonate samples for ^{14}C measurements was planned and successfully put into operation. The incorporation of ^{14}C into stalagmites is dependent on various climate-related processes in the soil and in the karst host rock above the cave. Using stable isotope ratios and trace element concentrations, this was investigated in two case studies with high-resolution ^{14}C measurements. Reduced ^{14}C concentration was observed in a stalagmite originating from Moomi Cave on Socotra Island which is indicative of aged soil organic matter influencing the stalagmite formation. It was demonstrated that a combination of higher soil humidity and denser vegetation towards the end of the last glacial period caused higher stalagmite ^{14}C concentration. In a second study on a stalagmite from Sofular Cave in Turkey, the ^{14}C signature allowed for the observation of various aspects of soil carbon dynamics from the last glacial period through into the Holocene. Moreover, the record suggests an increase of atmospheric ^{14}C concentration coincident with the geomagnetic minimum approximately 41000 years ago. This may contribute to the ongoing effort to improve radiocarbon calibration datasets, on which the ^{14}C dating method is based. Lastly, a summary of various stalagmite studies conducted at the Institute of Environmental Physics and a review of the relevant processes of stalagmite ^{14}C incorporation is presented.

Zusammenfassung

Stalagmiten stehen aufgrund ihrer Eigenschaft, Klimaveränderungen über lange Zeiträume aufzeichnen zu können, im Fokus der Paläoklimaforschung. Hochpräzise Datierungen mit der Uran-Zerfallsreihen-Methode ermöglichen es, mit hoher zeitlicher Auflösung zu bestimmen, wie die geochemische Zusammensetzung von Höhlenmineralen während ihres Wachstums klimabedingt variierte. In dieser Dissertation steht die Untersuchung von Radiokohlenstoff (^{14}C) in Stalagmiten im Vordergrund. Hierzu wurde eine neue Anlage zur chemischen Aufbereitung von Karbonatproben für die ^{14}C -Messung entwickelt und erfolgreich in Betrieb genommen. Der Einbau von ^{14}C in Stalagmiten hängt von klimabedingten Prozessen im Boden sowie im Karstgestein über der Höhle ab. Mithilfe von stabilen Isotopenverhältnissen und Spurenelementkonzentrationen wurde dies in zwei Fallstudien mit hochaufgelösten ^{14}C -Messungen untersucht. In einem Stalagmit aus der Moomi-Höhle auf Sokotra wurde eine stark reduzierte ^{14}C -Konzentration gemessen, die auf den Einfluss von gealterter organischer Bodensubstanz zurückzuführen ist. Es wurde gezeigt, dass höhere Bodenfeuchtigkeit und Vegetationsdichte zum Ende der letzten Eiszeit einen höheren ^{14}C -Gehalt im Stalagmit zur Folge hatten. In einer zweiten Studie an einem Stalagmit aus der Sofular-Höhle in der Türkei konnten anhand der ^{14}C -Signatur verschiedene Aspekte der Kohlenstoffdynamik im Boden von der letzten Eiszeit bis ins Holozän beschrieben werden. Darüber hinaus wurden Hinweise auf eine erhöhte ^{14}C -Konzentration der Atmosphäre während der Abschwächung des Erdmagnetfeldes vor etwa 41 000 Jahren gefunden. Dies kann zur Verbesserung des Kalibrierungsdatensatzes beitragen, auf dem die ^{14}C -Datierung basiert. Zuletzt wird eine Zusammenfassung von mehreren am Institut für Umweltphysik durchgeführten Studien und der relevanten Prozesse für ^{14}C in Stalagmiten präsentiert.

Contents

1	Introduction	11
I	Theoretical Background and Methods	13
2	Fundamentals	15
2.1	Speleothems as archives of the paleoclimate	15
2.1.1	Formation of stalagmites	15
2.1.2	Composition of stalagmites	16
2.2	Uranium-series dating	18
2.3	Radiocarbon dating	20
2.3.1	Natural formation and distribution of radiocarbon	20
2.3.2	Radiocarbon dating	22
2.4	Atmospheric radiocarbon and calibration	24
2.5	Stalagmite tracers & proxies of paleoclimatology	27
2.5.1	Stable isotopes	27
2.5.2	Radiocarbon in stalagmites	29
2.5.3	Trace elements Mg and Sr in stalagmites	32
2.6	Climate change during the last 50 kyr	34
3	Methods	37
3.1	Uranium-series dating	37
3.1.1	MC-ICP-MS measurement	37
3.1.2	Data analysis and correction	39
3.1.3	Age vs. depth modeling	39
3.2	Radiocarbon dating	40
3.2.1	Sampling	40
3.2.2	Carbon dioxide extraction and graphitization	40
3.2.3	AMS measurement	41
3.2.4	Reservoir age and DCF modeling	43
3.3	Trace elements	44

II	Establishing a new Carbon Dioxide Extraction Line	45
4	Establishing a new Extraction Line for ^{14}C Analysis of Carbonates	47
4.1	Developing a new extraction line	47
4.1.1	Configuration	48
4.1.2	Calibration volume	48
4.2	Sample treatment and measurement	51
4.2.1	Extraction	52
4.2.2	Graphitization	52
4.2.3	AMS measurement	52
4.3	Results and analysis	53
4.3.1	Blanks	53
4.3.2	International standards	55
4.3.3	Efficiency of carbonate sample extraction	56
4.3.4	Radiocarbon dating of paleoclimate archives	57
4.4	Conclusion	59
III	Radiocarbon in Stalagmites: Indicator of Climate Variability and Key to Atmospheric ^{14}C Reconstruction	61
5	Climate-induced Speleothem ^{14}C Variability on Socotra Island	63
5.1	Introduction	63
5.2	Sample and methods	64
5.2.1	Socotra Island and stalagmite M1-5	64
5.2.2	Measurement techniques	65
5.3	Results	66
5.3.1	U-series dating	66
5.3.2	Radiocarbon dating	67
5.3.3	Mg/Ca ratio	68
5.4	Discussion	69
5.4.1	U-series dating and age–depth model	69
5.4.2	DCF and implications for radiocarbon calibration	69
5.4.3	Climatic controls of DCF at Moomi Cave	70
5.4.4	Glacial termination climate dynamics on Socotra Island	72
5.5	Conclusions	73
6	Soil Carbon Dynamics and Atmospheric Signals in Stalagmite ^{14}C at Sofular Cave	75
6.1	Introduction	75
6.2	Sample location and methods	76
6.2.1	Sofular Cave and stalagmite So-1	76
6.2.2	Past climate on the southern Black Sea	77
6.2.3	Methods of dating and elemental measurements	78

6.3	Results	79
6.3.1	Age modeling of stalagmite So-1	79
6.3.2	^{14}C data reporting and Dead Carbon Fraction	80
6.3.3	DCF of stalagmite So-1	82
6.3.4	Elemental ratios	84
6.4	Discussion	85
6.4.1	^{14}C and U-series: A combined So-1 age model	86
6.4.2	DCF of a temperate climate stalagmite during Termination I	88
6.4.3	Multi-proxy analysis of DCF controls in the glacial period	91
6.4.4	Atmospheric ^{14}C during the Laschamp geomagnetic event	98
6.5	Conclusion	101
7	Reviewing Stalagmite DCF Drivers in Various Climate Settings	103
7.1	Introduction	103
7.2	Compiled stalagmite DCF studies and sites	105
7.3	Discussion	108
7.3.1	Carbon cycling influence on DCF	108
7.3.2	Limestone dissolution processes and climate dependence	111
7.3.3	Climate controls on stalagmite carbon mechanisms	113
7.4	Conclusion	115
8	Conclusions and Outlook	117
9	List of Publications of the Author	121
	Appendix	I
A	Supplementary Data	III
A.1	Stalagmite So-1, Sofular Cave	III
A.2	Stalagmite M1-5, Moomi Cave	XIII
A.3	Compiled stalagmite ^{14}C records from various studies	XV
B	List of Figures	XVII
C	List of Tables	XIX
D	List of Abbreviations	XXI
	Bibliography	XXIII
	Acknowledgements	XLI

1 Introduction

The goal of paleoclimate research is to reconstruct past changes of the Earth's climate from environmental archives, such as ice cores, sea and lake sediments, corals, tree-rings or speleothems. In these climate archives, the information on the climate conditions at the time of formation is stored in their geochemical composition in form of proxy data like trace element concentrations, isotopic ratios or other physical characteristics. Paleoclimate research aims to establish new proxies and to find new applications of existing ones, and thus, to broaden the understanding of the Earth's climate system, its feedbacks, and changes. This enables the projection of regional and global consequences of the ongoing, accelerating anthropogenic climate warming (IPCC 2013).

In recent years, an increasing number of paleoclimate studies have focused on speleothems, and stalagmites in particular. This is primarily due to their many favorable features compared to other climate archives. Speleothems can grow over long and continuous time spans and are protected from natural erosion processes. Moreover, they can generally be dated with high precision utilizing the radiometric U-series method. Therefore, studies on stalagmites were able to contribute significant records of past climate conditions like the transitions from glacial to interglacial periods (Wang et al. 2001, Cheng et al. 2016). Amongst the commonly used climate proxies in speleothem research are the stable isotope ratios of carbon and oxygen, or trace element concentrations in the calcite of stalagmites. These are used to gain information on past precipitation amounts, temperature or ecosystem variability. Additionally, the incorporation of radioactive isotopes, such as radiocarbon, into stalagmites is increasingly investigated.

Radiocarbon (^{14}C) dating was initially introduced by Willard F. Libby, and is still successfully utilized until today, as a radiometric method to determine the age of samples which contain carbon of organic origin (Libby et al. 1949). However, large difficulties arose after the initial applications of ^{14}C dating from the poorly understood past variability of atmospheric ^{14}C concentration. Since then, inter-calibration records like IntCal13 (Reimer et al. 2013) have been compiled from highly-resolved overlapping tree-ring ^{14}C data for the last 14 kyr, as well as from marine carbonates, lake sediments, and stalagmites that reflect the changing atmospheric ^{14}C levels throughout the last 50 000 kyr. With this calibration data, ^{14}C dating results can be converted into calendaric dates.

Stalagmites contain traces of ^{14}C , because a main carbon source in speleothem formation is soil CO_2 originating from plant respiration and organic matter decomposition, which is at near-atmospheric ^{14}C concentrations. However, the incorporation of very old carbon from dissolved limestone into stalagmite calcite leads to a systematic but not precisely quantifiable bias in speleothem ^{14}C towards older ages (Hendy and Wilson 1968). This bias is referred to as *dead carbon fraction* (DCF) which describes the proportion of carbon in the stalagmite not containing ^{14}C .

It was shown that the DCF in speleothems can vary vastly due to changes in the limestone dissolution process (Hendy 1971). Additionally, an influence of local climatic conditions and interactions in the soil-rock zone was determined (Genty et al. 1999, 2001). It was also demonstrated how rainfall and soil infiltration can be connected to DCF variability in tropical climates (Griffiths et al. 2012, Noronha et al. 2014). Moreover, the influence of aging soil organic matter (SOM) on soil gas CO₂ and subsequently stalagmite DCF were discussed (Fohlmeister et al. 2011a, Noronha et al. 2015). In recent studies, cases of extremely high DCF in combination with unusual stable carbon isotope ratios were attributed to excess limestone dissolution by sulfuric acids (Spötl et al. 2016, Bajo et al. 2017). However, the mechanisms which determine the ¹⁴C incorporation into stalagmites throughout different climate zones are far from being entirely understood.

Nonetheless, the recently published high-resolution stalagmite record by Cheng et al. (2018) from Hulu Cave, China, was able to present atmospheric ¹⁴C reconstruction back to more than 53 kyr before today, although some significant discrepancies from IntCal13 arose. While the Hulu Cave record still needs to be consolidated with the existing data, it still seems clear that stalagmites can be a crucial and perhaps the most promising contribution to ¹⁴C calibration efforts. It is therefore imperative to conduct further research on stalagmites with respect to reconstructing atmospheric ¹⁴C variability and, consequently, to focus on the driving climate factors of speleothem DCF.

Through comprehensive ¹⁴C studies on stalagmites from arid and temperate climate zones in combination with stable isotope data and trace element analysis, so far unexplored climate-dependent processes can be characterized. This enables the interpretation of stalagmite ¹⁴C as an indicator of climate change and helps to understand soil and limestone processes, which may facilitate the contribution to atmospheric ¹⁴C reconstruction. These are the main goal of this dissertation.

To that end, high-precision ¹⁴C measurements of carbonate samples were conducted, which require sample preparation procedures that minimize contamination. To achieve this, a newly established extraction line for carbonate samples is presented in chapter 4 together with a characterization after the first time of successful operation. In chapter 5 a case study on stalagmite M1-5 from Moomi Cave, Socotra Island, is presented revealing a very high level of DCF in which long-term trends linked to a transitioning glacial climate, as well as vast short-term ¹⁴C variability are observed. The high contribution of aged SOM at peak glacial conditions and the impact of denser vegetation on DCF are unprecedented and demonstrate that DCF can be used in arid climates to trace vegetation dynamics. A potential contribution to ¹⁴C calibration is discussed in chapter 6, in which stalagmite So-1 from Sofular Cave in a temperate climate in Northern Turkey is presented. Previous ¹⁴C studies revealed soil carbon cycling impact on the DCF during the last glacial termination (Rudzka et al. 2011). The new multi-proxy analysis reaching back 42 kyr shows that atmospheric ¹⁴C variability can likely be reconstructed from stalagmite ¹⁴C, even if DCF is not constant over time.

At the end of the thesis, chapter 7 provides a summary of published stalagmite records and unpublished data from the Institute of Environmental Physics to give a review on the determining mechanisms on stalagmite radiocarbon.

Part I

Theoretical Background and Methods

2 Fundamentals

2.1 Speleothems as archives of the paleoclimate

The research discipline of paleoclimatology relies on the reconstruction of past climate conditions through the investigation of suitable climate archives. According to their origin, those are divided into different categories, including marine, terrestrial, lacustrine and cryospheric archives. Speleothems belong to the category of terrestrial climate archives. In general, speleothems are secondary mineral deposits of calcareous material (calcite or aragonite) that grow in naturally formed caves. The term *speleothem* is a composite word of the Ancient Greek terms σπήλαιον, *spélaion* (cave) and θήμα, *théma* (deposit). They mostly grow in caves which are situated in carbonate rocks, such as limestone (CaCO_3) or dolomite ($\text{CaMg}[\text{CO}_3]_2$) and can occur in different forms such as stalagmites, stalactites or flowstones (Fairchild and Baker 2012).

As a climate archive, their perhaps most important feature is the relatively continuous storage of paleoclimate information in form of tracers and proxies during their growth periods. That information is transported into the cave through the percolating water entering the cave and is subsequently deposited at the drip site over long periods of time. Stalagmites provide many favorable features as a speleothem climate archive: Their growth is in general very regular along a distinct growth axis with chronological stratification. They are therefore preferred as climate archives over stalactites. The last decades saw significant developments in investigation methods and technologies in paleoclimate research, such as accelerator mass spectrometry, multi-collector mass spectrometry, laser ablation techniques and many others. Those technologies allowed for an increase in measurement quality, and subsequently data precision, while the required sample material continuously decreased. Concerning stalagmites, this paved the way for high-resolution and high-precision paleoclimate data analysis.

In the following sections, an overview is given on the formation of speleothems and their relevant features as paleoclimate archives.

2.1.1 Formation of stalagmites

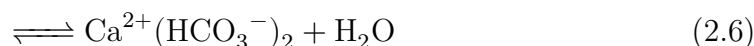
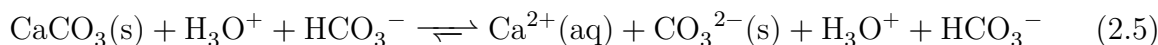
Stalagmites, like all speleothems, form as a result of carbonate precipitation inside caves. Important prerequisites for this process to occur are a continuous inflow of percolating water from the surface area above the cave as well as high CO_2 concentrations in the soil zone.

Due to root respiration of active vegetation and microbial activity (decomposition of organic material), the soil zone CO_2 concentration is significantly higher than that of the

surrounding atmospheric air. The partial pressure of CO_2 ($p\text{CO}_2$) in the soil air can rise to levels as high as 10 % (Fairchild and Baker 2012). Once the seepage water is in contact to the soil gas phase the under-saturation of the water is equilibrated by the dissolution of gaseous CO_2 , resulting in the formation of carbonic acid (H_2CO_3). This acid progressively dissociates at higher pH into bicarbonate (HCO_3^-) and carbonate (CO_3^{2-}) ions:



The resulting acidic solution percolates from the soil zone further down into the vadose zone of the epikarst, where it dissolves the carbonate host rock. In case of limestone, which consists of calcium carbonate, the resulting equilibrium is:



The path of the solution down into the cave is determined by the cracks and fissures in the epikarst and host rock. Upon entering the cave atmosphere, the solution is in contact with the cave air, and equilibrates with the present conditions. Cave air in general has lower partial CO_2 pressures than the soil or karst zone. In the case of well-ventilated caves, it can be as low as the local atmospheric air (Fairchild and Baker 2012). The discrepancy in partial CO_2 pressures of the soil/epikarst and cave air imposes a constraint on the chemical equilibrium that shifts it towards enhanced degassing of CO_2 from the supersaturated solution. As described by equation Eq. 2.7, this degassing involves the precipitation of CaCO_3 .



Stalagmite growth depends on many parameters in this chemical equilibrium such as drip rate, cave temperature, partial pressure of CO_2 in the soil zone, the epikarst or the cave and cave ventilation. These aspect, that directly or indirectly depend on climate, play an important role for the development of speleothems and their morphology (Dreybrodt 1999, Kaufmann and Dreybrodt 2004).

The processes contributing to stalagmite formation are illustrated in Fig. 2.1 by a transect from atmosphere down to the karst environment around the cave (adapted from Fairchild and Baker 2012).

2.1.2 Composition of stalagmites

As a consequence of steady carbonate precipitation from degassing drip water as described by eq. (2.7), the carbonate aggregates as crystals and grows to form speleothems. The most common form of carbonate crystals in speleothems is the calcite configuration, but

rarer forms such as aragonite also occur (Fairchild and Baker 2012). The geochemical composition of stalagmites (e.g. oxygen and carbon isotopes of the calcite, trace elements in the crystal matrix) depends on several factors.

In a comprehensive review study on environmental signals in speleothems (Fairchild et al. 2006), five sources are highlighted which determine the geochemical composition of the drip-water, and ultimately of the speleothem carbonate: atmospheric input above the cave, vegetation and soil zone composition, the karstic aquifer, primary speleothem crystal growth and secondary alteration.

For instance, the incorporation of uranium from the carbonate bedrock as a trace metal into the stalagmite matrix enables the precise age determination and thus forms the chronological basis for paleoclimate investigations of stalagmites (see section 2.2). Other trace elements have been moved into the focus of paleoclimate research, such as the ratio of Mg^{2+} and Ca^{2+} ions in the drip water and their elemental ratio in stalagmite carbonate.

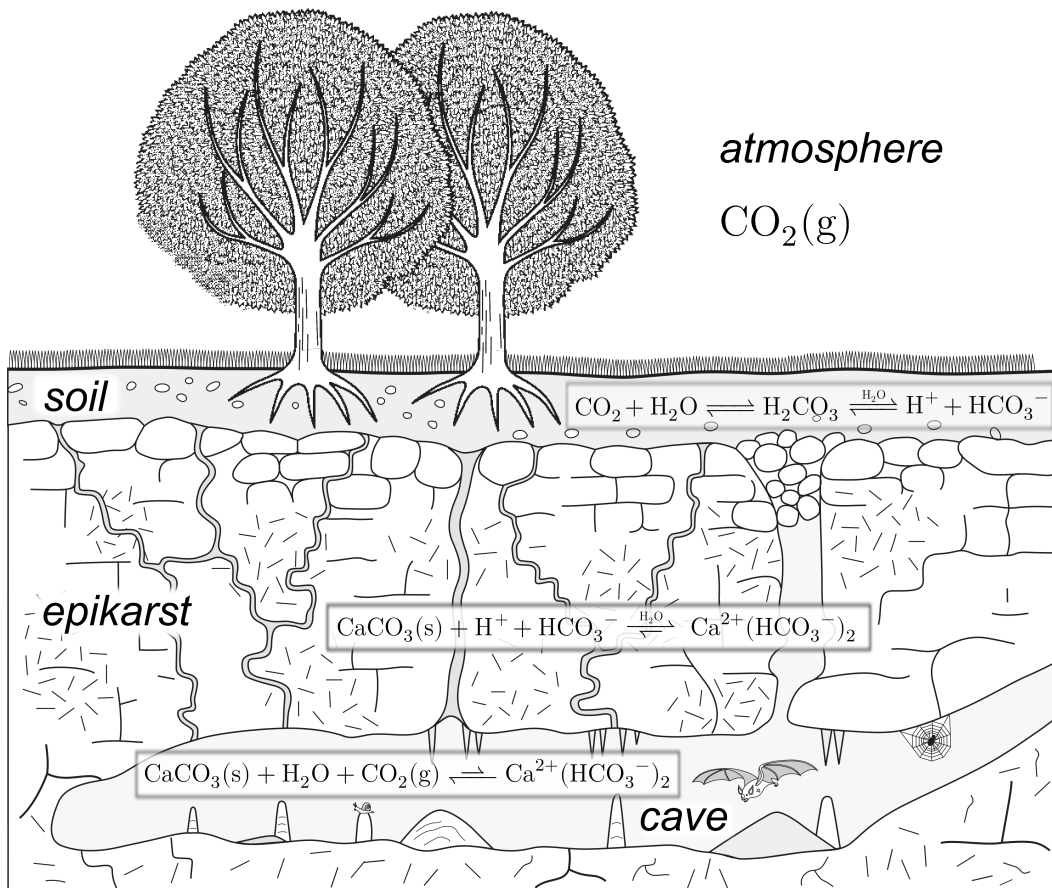


Figure 2.1: This illustration shows the processes relevant for speleothem formation. CO_2 from the atmosphere is introduced into the soil zone by root respiration and microbial organisms where it is dissolved to an acidic solution by water infiltrating the soil. The dissolved carbonate from the epikarst is re-precipitated in the cave environment and forms speleothems. Illustration adapted and modified from Fairchild and Baker (2012).

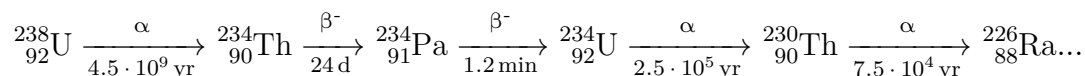
This ratio is influenced by many climate-dependent factors like the hydrological conditions in the karst bedrock above the cave (Fairchild et al. 2000, 2001, Griffiths et al. 2012) or calcite precipitation processes (Treble et al. 2015) and is generally considered as a precipitation proxy. Other trace elements that are often in the focus of paleoclimate studies include strontium, phosphorus, titanium, and aluminum (Wassenburg et al. 2012, Warken et al. 2018).

In addition to trace elements, the calcium carbonate as the main composite of the speleothem can also provide crucial paleoclimate information. The isotopic ratio signatures of the stable carbon and oxygen isotopes have been used to reconstruct past climate changes through stalagmite records from monsoonal regions and temperate settings (Wang et al. 2001, Spötl and Mangini 2002, Burns et al. 2003, Fleitmann et al. 2003, Spötl et al. 2006, Fleitmann et al. 2009, Dykoski et al. 2005).

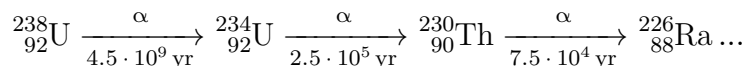
2.2 Uranium-series dating

The chronology of stalagmites can be determined by various dating methods. One of the most reliable and accurate methods is U-series radiometric dating, which enables precise age determination for the last 500 000 years (Richards 2003, Scholz and Hoffmann 2008).

U-series dating is based on the radioactive decay of the most abundant ^{238}U isotope and the build-up of its daughter nuclides until, eventually, secular equilibrium is reached. ^{238}U decays via short-lived isotope states to its daughter isotopes ^{234}U and ^{230}Th (respective half-lives are indicated below the arrows):



Due to the large discrepancies of the half-lives, the decay chain can be reduced to the long-lived isotopes, neglecting the intermediate, short-lived nuclides.



If the process described by this reduced decay chain is not in or very near to secular equilibrium, it is possible to assess the starting point of the disequilibrium by quantifying how close it has approached secular equilibrium (Ivanovich 1994).

The accurate age determination itself is based on two fundamental assumptions: The first assumption is that the highly soluble uranium is transported from the karst layers above the cave to the stalagmite through drip water, and subsequently incorporated into the crystal structure without any additional, less soluble thorium being built into the speleothem matrix. Secondly, it is assumed that after the calcite precipitation, the initial substances are no longer subject to exchange processes that alter the concentration of the involved isotopes. This is often referred to as the “closed system” assumption (Ivanovich and Harmon 1992, Scholz and Hoffmann 2008). If these idealized conditions hold, the time of calcite deposition on the speleothem starts the clock on the decay chain, assuming no initial thorium. The U-series age itself (referred to as t in this section) can then

be numerically determined by two equations following the derivation of Ivanovich and Harmon (1992), which describe the activity ratios of the daughter nuclides of ^{238}U and their temporal development during the decay.

$$\left(\frac{^{234}\text{U}}{^{238}\text{U}}\right)(t) = \left(\left(\frac{^{234}\text{U}}{^{238}\text{U}}\right)_{\text{init}} - 1\right) \cdot e^{-\lambda_{234}t} + 1 \quad (2.8)$$

$$\left(\frac{^{230}\text{Th}}{^{238}\text{U}}\right)(t) = (1 - e^{-\lambda_{230}t}) + \left(\left(\frac{^{234}\text{U}}{^{238}\text{U}}\right)(t) - 1\right) \cdot \frac{\lambda_{230}}{\lambda_{230} - \lambda_{234}} \cdot (1 - e^{-(\lambda_{230} - \lambda_{234})t}) \quad (2.9)$$

where $(^{234}\text{U}/^{238}\text{U})_{\text{init}}$ is the initial activity ratio and λ are the decay constants of the respective isotopes ($\lambda = \ln 2 / T_{1/2}$). Two variables in the equations from above are unknown, namely $(^{234}\text{U}/^{238}\text{U})_{\text{init}}$ and t . The other ratios can be measured by mass spectrometry, and thus, t can be numerically determined. A graphical solution to these equations is illustrated in Figure 2.2.

However, these equations are only valid if the assumptions of no initial ^{230}Th and a closed system hold. In realistic circumstances, the initial thorium concentration is always greater than zero. Detrital material that is incorporated into the stalagmite matrix can contain significant amounts of thorium and other elements. Nonetheless, if the initial thorium content can be subtracted from the accumulated decay product, accurate dating

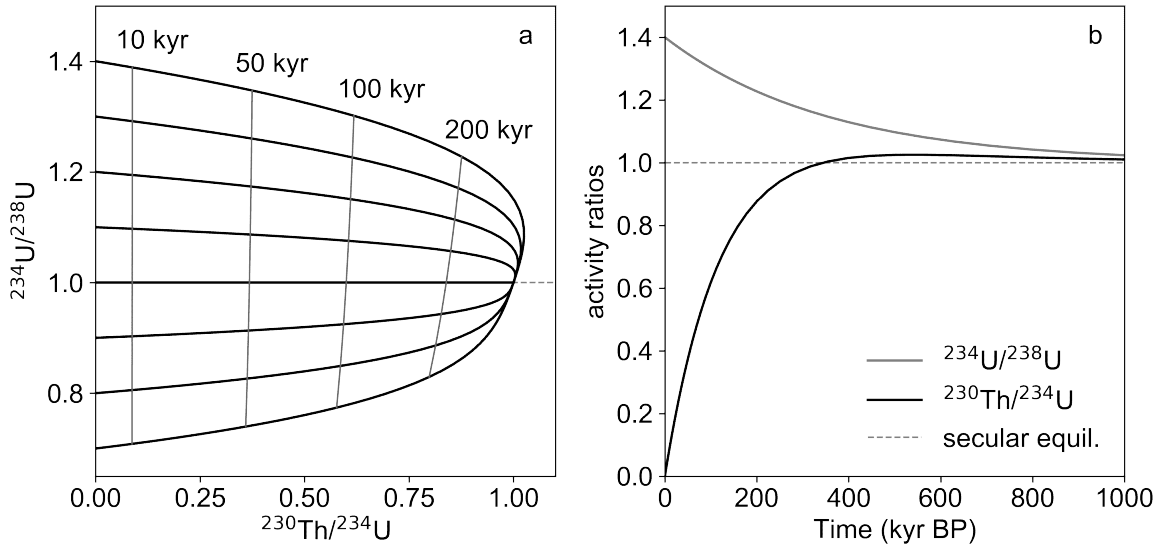


Figure 2.2: Graphical solution to the U-series dating equations. The temporal evolution of isotope ratios ($^{230}\text{Th}/^{234}\text{U}$) and ($^{234}\text{U}/^{238}\text{U}$) for different initial ($^{234}\text{U}/^{238}\text{U}$) ratios is shown (a). The isotope ratios are connected across different initial ($^{234}\text{U}/^{238}\text{U}$) for four exemplary times to show the concept of *isochrones*, which are lines of constant time. With time going towards 1000 kyr, the isotope ratios approach secular equilibrium (b).

is still feasible. For this purpose, the ^{232}Th content is measured, which is not part of the decay chain of ^{238}U and is also considered stable on the timescales of U-series dating. A bulk activity ratio of $(^{232}\text{Th}/^{230}\text{Th}) = 0.90 \pm 0.45$ is used, which is based on a mean mass ratio of $(^{232}\text{Th}/^{238}\text{U}) = 3.8$ in the Earth's continental crust and on the assumption that decay products of detrital material are in secular equilibrium (Ivanovich and Harmon 1992, Wedepohl 1995, Hellstrom 2006). While these ratios are a good overall approximation of the continental elemental ratio, spatial variations are possible depending on the host rock conditions. For clean samples without significant contamination, however, the bulk approximation yields sufficiently accurate results in most cases.

2.3 Radiocarbon dating

The following segments aim to describe the fundamental background of the radiometric dating method based on the instable natural carbon isotope ^{14}C which was first described by Willard F. Libby (Libby 1946, Libby et al. 1949). A focus lies on the formation and distribution of ^{14}C in the natural carbon cycle and the decay which is the basis for the application as a radiometric dating method for organic and carbonous samples.

2.3.1 Natural formation and distribution of radiocarbon

Carbon occurs on Earth as three different isotopes, of which the stable isotopes ^{12}C and ^{13}C make up virtually the entire amount of carbon atoms with abundances of 98.9 % and 1.1 %, respectively (Mook 2000). Radiocarbon (^{14}C) is the naturally occurring radioactive isotope of carbon with an abundance of roughly 10^{-12} , reflecting the steady state between ^{14}C production and decay.

^{14}C is continuously produced in the upper troposphere and in the stratosphere by nuclear reactions with the highly abundant ^{14}N atom (Anderson 1947). In detail, cosmic radiation enters the upper atmosphere and creates by-products such as thermal neutrons during the transformation processes. These thermal neutrons are captured by nitrogen atoms and cause the following nuclear reaction:



Since the Earth's geomagnetic shielding is less efficient at higher geomagnetic latitudes, radiocarbon production is higher there than at low latitudes (Masarik and Beer 1999, 2009). The carbon atoms from the nuclear reaction above are highly reactive and are oxidized by the surrounding oxygen in the air to ^{14}CO and subsequently to $^{14}\text{CO}_2$. As carbon dioxide, ^{14}C is then homogeneously mixed into and distributed throughout the troposphere (Nydal 1968), although slight offsets between the hemispheres are observed in the modern atmosphere (Reimer et al. 2013). Since the atmospheric carbon pool is a part of the natural carbon cycle, ^{14}C is subsequently distributed across all segments including the biosphere and the hydrosphere. By photosynthesis it is incorporated into flora and then the biosphere. The short turnover times and fast metabolisms cause the

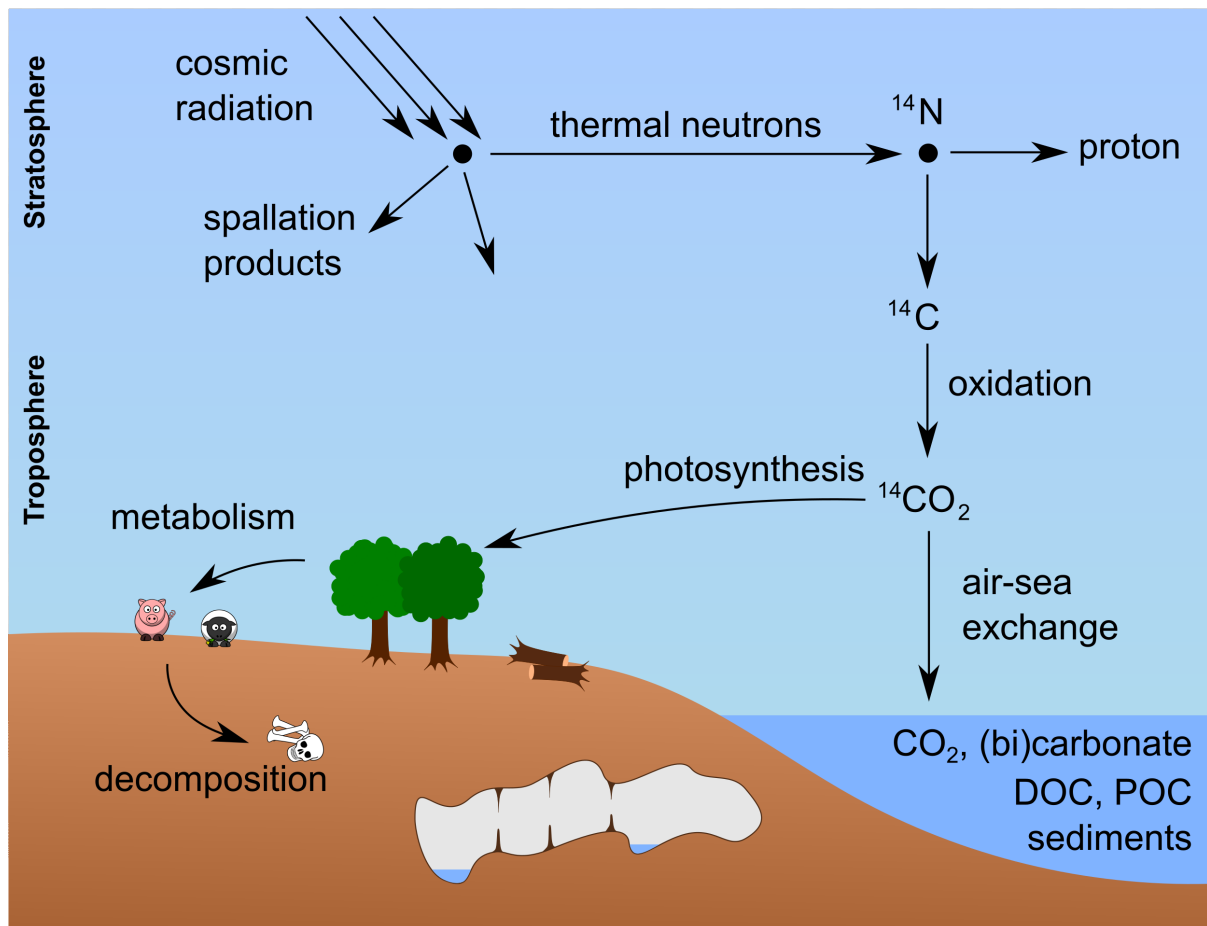


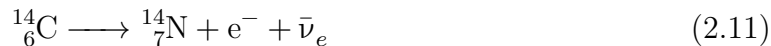
Figure 2.3: Illustration of the natural production and distribution of ^{14}C from the atmosphere into the biosphere and the ocean. Thermal neutrons trigger nuclear reactions with nitrogen atoms in the upper atmosphere creating ^{14}C which is oxidized to $^{14}\text{CO}_2$ and distributed in the troposphere. Photosynthesis transports ^{14}C into the biosphere, air-sea-exchange causes the solution of ^{14}C in ocean water. There, carbon is present as dissolved CO_2 , (bi)carbonate ions and dissolved or particulate organic carbon (DOC and POC, respectively).

biosphere to have approximately the same ^{14}C concentration as the contemporaneous atmosphere. In the hydrosphere, the largest reservoir is the upper ocean water layer, into which $^{14}\text{CO}_2$ is mixed by air-seawater-exchange. Here, the concentration of ^{14}C is always slightly diluted compared to the atmosphere. This effect is called *reservoir effect*.

2.3.2 Radiocarbon dating

Radioactive decay and principles of ^{14}C dating

The radioactive isotope ^{14}C decays in a β^- -decay into ^{14}N with a physical half-life of (5730 ± 40) years (Godwin 1962).



Since radiocarbon is an immanent part of the natural carbon cycle, it is constantly integrated into living organisms by metabolism processes such as photosynthesis and ingestion. If this exchange is halted – for instance by the death of an organism – uptake ceases and the radiocarbon activity decreases over time with the decay constant λ according to the radioactive decay law.

$$\frac{dN}{dt} = -\lambda \cdot N \quad (2.12)$$

If the initial activity, number of atoms or concentration is known, this enables the determination of the starting time of the radioactive decay clock by measuring the remaining atoms N or activity A . Solving the differential eq. (2.12) for the time t since the beginning of the decay results in the fundamental equation of radiocarbon dating:

$$t = \frac{1}{\lambda} \cdot \ln \left(\frac{N_0}{N(t)} \right) \quad (2.13)$$

In this equation, N_0 is the initial number of ^{14}C atoms in a sample, $N(t)$ refers to the remaining number of atoms at the time of measurement. If $N(t)$ or the equivalent activity $A(t)$ of the sample is determined by methods like accelerator mass spectrometry (AMS) or decay counting, the radiocarbon age t can be determined using the conventional radiocarbon half-life of 5568 yr, assuming a constant initial radiocarbon concentration in the atmosphere. All radiocarbon ages are based on this conventional half-life (often referred to as “Libby half-life”), in contrast to the physical half-life of (5730 ± 40) yr which was only determined after the method had already been established. The result of Equation (2.13) does not represent the actual calendar age, but is only referred to as “conventional radiocarbon age”. That is because the initial assumption made by the pioneers of the dating method (Arnold and Libby 1951) of a constant atmospheric ^{14}C concentration was shown to be incorrect. It was proven that the atmospheric ^{14}C was very variable during the last 50 000 years. To obtain the actual calendar age of a sample, the past evolution of the atmospheric ^{14}C concentration needs to be known to a sufficient precision, and conventional radiocarbon ages need to be converted into calendar ages. This process is called “calibration” (see section 2.4).

Apart from the convention of using the Libby half-life, several guidelines were agreed on concerning the reporting of ^{14}C dating results. These include corrections for isotopic mass fractionation, the formal notation of results, and their units and references. A short overview is given on these aspects in the following paragraph. Further, more detailed descriptions were given by Stuiver and Polach (1977) and Stenström et al. (2011).

Isotope fractionation, correction and normalization

During the exchange processes in the carbon cycle, isotopic mass fractionation takes place. For instance, plants incorporate ^{12}C to a higher extent than ^{13}C and ^{14}C during photosynthesis. This causes a systematic shift in the isotope ratios compared to the atmospheric CO_2 . Consequently, not correcting for this effect would lead to inconsistent ^{14}C ages depending on the amount of fractionation. To quantify the isotopic signature of stable isotopes, the δ -notation is used which puts the isotopic ratio of a sample in context to a defined standard material isotope ratio. For ^{13}C , the standard is the Vienna Pee Dee Belemnite (VPDB), which refers to a fossil specimen.

$$\delta^{13}\text{C} = \left(\frac{\frac{^{13}\text{C}}{^{12}\text{C}}_{\text{sample}}}{\frac{^{13}\text{C}}{^{12}\text{C}}_{\text{VPDB}}} - 1 \right) \cdot 1000 \text{‰} \quad (2.14)$$

Radiocarbon is also affected by mass fractionation and therefore needs to be corrected as well. Since the results from various samples materials need to be comparable, all reported results are normalized to the mean isotopic signature of a generic wood sample ($\delta^{13}\text{C} = -25 \text{‰}$). The normalization factor of every sample with respect to its $\delta^{13}\text{C}$ is extrapolated to its ^{14}C signature by assuming that the $^{14}\text{C}/^{12}\text{C}$ normalization is given as the squared value of the $^{13}\text{C}/^{12}\text{C}$ normalization factor (Stuiver and Robinson 1974).

To maintain comparability between samples that were measured at different times, all radiocarbon dates are reported with respect to a defined activity and isotopic signature of a designated standard material. Historically, this standard was the oxalic acid standard OxI, which was gained from a crop of sugar beets in 1955. Its radiocarbon activity was defined relative to the ^{14}C concentration of the pre-industrial atmosphere. Since OxI is no longer available, a second standard was produced, which is still in use. This standard is the oxalic acid standard OxII (Stuiver 1983).

By convention, all ^{14}C measurements are reported as if they had been measured in the year 1950 CE, i.e. their measured activity is decay-corrected. Hence, conventional radiocarbon ages are reported in the unit “yr BP” (years before present), where “present” is the year 1950 CE. With these conventions, it is possible to report ages from different laboratories throughout the world with the same reference, independent of the time of ^{14}C determination, thus guaranteeing international comparability.

Reporting of ^{14}C dating results

Radiocarbon provides a variety of equivalent units and quantities to express the results from ^{14}C dating. The best-known unit is the conventional radiocarbon age $t_{14\text{C}}$ as defined in Equation (2.13). This *age* can be transformed into the conventional radiocarbon activity $a^{14}\text{C}$ with the decay constant ($\lambda_{\text{Lib}}^{-1} = 8033 \text{ yr}$).

$$a^{14}\text{C} = \exp(-\lambda_{\text{Lib}} \cdot t_{14\text{C}}) \cdot 100 \text{‰} \quad (2.15)$$

This quantity is expressed in the unit percent, in particular *percent modern carbon* or

pmC (Stenström et al. 2011). Following the aforementioned conventions, a ^{14}C age of $t_{14\text{C}} = 0$ yields an activity of 100 pmC, which emphasizes the reference to the ^{14}C activity of the atmosphere in 1950 CE. It is important to note that ^{14}C ages can be negative if activities are higher than 100 pmC, which occurs for modern samples.

Another related unit is the per mil notation of a measured activity with respect to the 1950 CE standard atmospheric activity. The definition is then analogous to that of any δ -notation, as seen in Equation (2.14).

$$\Delta^{14}\text{C} = \left(\frac{A_{\text{SN}}}{A_{\text{ON}}} - 1 \right) \cdot 1000 \text{‰} \quad (2.16)$$

In the fraction, A_{SN} denotes the specific sample activity, normalized for mass fractionation to $\delta^{13}\text{C} = -25 \text{‰}$. A_{ON} is the sample activity of the 1950 CE standard atmosphere, as defined through the international standard OxI, normalized to $\delta^{13}\text{C} = -25 \text{‰}$ (Stenström et al. 2011). Following this definition, the per mil notation relates to $a^{14}\text{C}$:

$$\Delta^{14}\text{C} = (a^{14}\text{C} - 1) \cdot 1000 \text{‰} \quad (2.17)$$

This last quantity is often used when results are put into the context of the atmospheric radiocarbon signature, like in paleoceanography or dendrochronology.

2.4 Atmospheric radiocarbon and calibration

A large focus of this dissertation is on the variation of atmospheric radiocarbon in the last 50 000 years. In the presented studies in Part III, radiocarbon dating is mostly used as an environmental tracer and climate proxy, rather than to perform actual calendaric dating. It is therefore worthwhile to give further information on the reasons and the extent of ^{14}C concentration fluctuations in the atmosphere during the last 50 000 years.

In contrast to the early assumptions by Libby (1946), the initial ($^{14}\text{C}/^{12}\text{C}$) ratio in the troposphere is not constant. Combined inter-calibration records like IntCal13 (Reimer et al. 2013) prove that the natural variation of ^{14}C concentration in the atmosphere was more than 50 % in the past, compared to modern levels. In IntCal13, several radiocarbon records from paleoclimate archives were combined, that were deemed suitable to precisely and accurately reflect the changing atmospheric ^{14}C levels throughout the last 50 kyr. In this way, radiocarbon dating results can be converted into calendaric dates (calibration of ^{14}C results). Tree-ring records are the preferred environmental archive for that purpose, because they directly reflect the atmospheric ^{14}C content without a significant offset and because their layering allows to determine the accurate calendar dates. Due to these aspects, dendrochronological records of overlapping tree-rings form the basis for the youngest part of IntCal13, where the atmospheric $\Delta^{14}\text{C}$ is therefore known best (Schaub et al. 2008, Hua et al. 2009, Reimer et al. 2013). Together with floating tree-ring records, that lack an absolute anchorage in the continuous dendrochronological records, this combined robust data reaches back to roughly 14 kyr BP. Before this period, the uncertainty is significantly higher and other climate archives need to be considered for

^{14}C reconstruction. These archives include stalagmite records (Beck et al. 2001, Hoffmann et al. 2010, Southon et al. 2012), lacustrine sediment cores (Bronk Ramsey et al. 2012) and marine archives like corals (Hughen et al. 2006, Bard et al. 2013, Durand et al. 2013, Heaton et al. 2013). Additionally, tree-ring records from older areas can be used as floating archives, even though there is no direct connection to younger records. For instance, this was achieved by the investigation of a Kauri tree record spanning 1300 yr (Turney et al. 2010) near the Laschamp geomagnetic reversal event (Laj et al. 2013, Lascu et al. 2016) at roughly 41 kyr BP, in a cross-combination effort with radiogenic ^{10}Be nuclide signatures in ice-core archives (Muscheler et al. 2014, Staff et al. 2019). These findings revealed the possibility of an area of systematically higher radiocarbon concentration in the atmosphere at the Laschamp reversal, which is not reflected in the IntCal13 data. Recent studies have corroborated this by providing high-precision ^{14}C data that indicates atmospheric $\Delta^{14}\text{C}$ deviations from IntCal13 consensus data and also proves vast variations of more than 400 ‰ atmospheric ^{14}C concentration on time-scales of roughly 1000 years (Cheng et al. 2018).

The long-term trends in atmospheric $\Delta^{14}\text{C}$ are illustrated in Figure 2.4. They reflect shifts in the equilibrium of radiocarbon input into and output from the atmosphere. Natural input of radiocarbon into the Earth's system is almost exclusively controlled by cosmic radiation neutron flux in the upper atmosphere. The ^{14}C production rate is thus subject to fluctuations of the cosmic ray flux incident on the heliosphere and to geomagnetic field variations which can alter the atmospheric shielding from cosmic irradiation and solar activity (Damon and Linick 1986, Bard et al. 1990, Muscheler et al. 2004, 2005, Köhler et al. 2006, Bronk Ramsey 2008). It has been proven that the ^{14}C production is linked to the solar cycle (Burchuladze et al. 1980) and is susceptible to singular cosmic radiation events (Scifo et al. 2019). The natural ^{14}C production rate in the atmosphere is closely linked to geomagnetic field modulation, where lower field activity is directly associated to higher ^{14}C production on millennial timescales and vice versa (Muscheler et al. 2005). Geomagnetic reversal events have been associated with increased production of ^{14}C (Muscheler et al. 2014, Cheng et al. 2018). Prominent examples of those events are the Mono Lake and Laschamp excursions (Lund et al. 2017) during the last glacial period at roughly 34 and 41 kyr BP, respectively. The implications of the aforementioned events can be observed in many records of radiogenic atmospheric nuclides, such as ^{10}Be , ^{14}C and ^{36}Cl in drilling cores from the Greenland ice shield (Wagner et al. 2000, Muscheler et al. 2004). The events have been confirmed by the Hulu Cave stalagmite records (Cheng et al. 2018).

Apart from these external forcings on the atmospheric radionuclide production, past changes of carbon cycling and of the carbon reservoirs had a large impact on the ^{14}C budget of the atmosphere. During the last glacial termination a dilution trend in $\Delta^{14}\text{C}$ started that resulted in a drop of roughly 190 ‰ between 17 and 14.6 kyr BP (Lal and Charles 2007, Burke and Robinson 2012). Upwelling of very old carbon dioxide stocks from deep ocean layers and subsequent mixing into upper ocean layers caused the degassing of large amounts of old CO_2 into the atmosphere in the southern ocean. An anti-correlation of CO_2 concentration and $\Delta^{14}\text{C}$ in the atmosphere after the Last Glacial Maximum (LGM)

across the Termination I was also demonstrated (Burke and Robinson 2012).

The influences of production rate variability and changes in the equilibrium of the carbon cycle are prominently depicted in the atmospheric inter-calibration records and are responsible for short-term sub-decadal peaks as well as long-term, millennial trends (see Figure 2.4).

Apart from natural variations, significant anthropogenic changes in $\Delta^{14}\text{C}$ are present in the recent three centuries. Those were initiated by the industrial revolution in the 18th century, when increasing fossil fuel combustion caused a large input of CO_2 into the atmosphere not containing any ^{14}C . The result was a decrease in $\Delta^{14}\text{C}$ of 15 to 25 ‰ until 1950 CE (Tans et al. 1979). Due to the high levels of fossil fuel combustion in

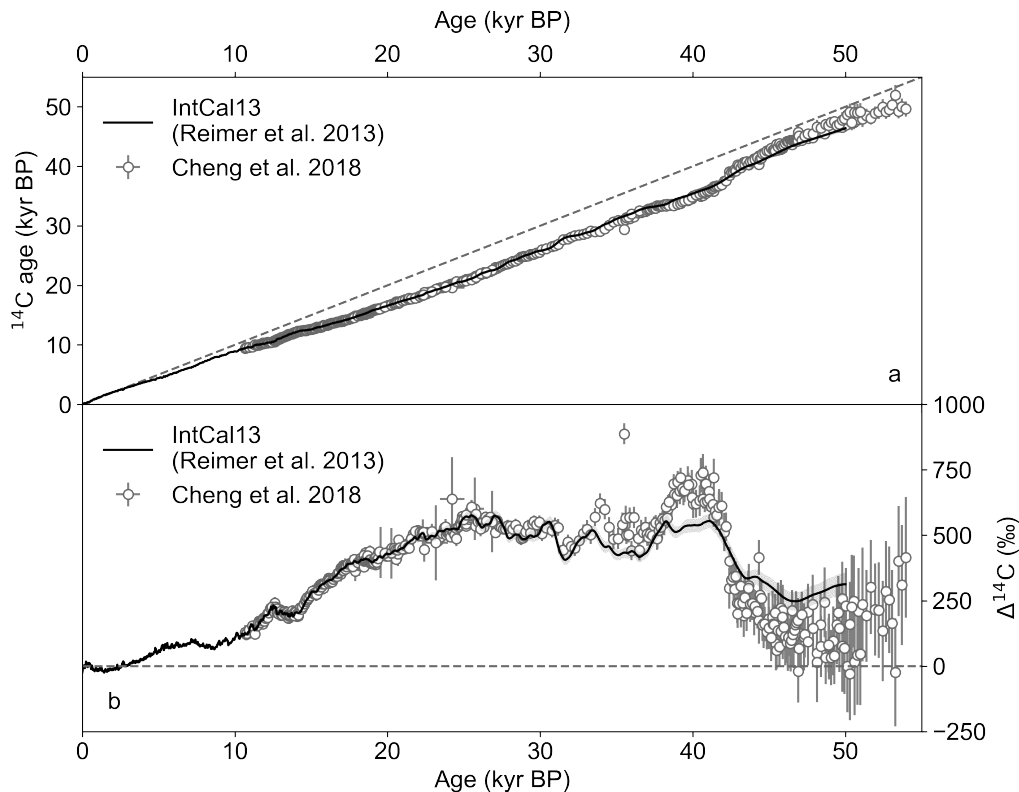


Figure 2.4: Atmospheric calibration records and ^{14}C concentration over the last 53 kyr BP. The upper graph (a) shows the calibration data from IntCal13 (Reimer et al. 2013) and the DCF-corrected stalagmite ^{14}C record from Hulu Cave (Cheng et al. 2018). Both records are plotted as ages in units of calendar yr and conventional ^{14}C yr before present. In the lower plot (b), the ^{14}C concentration derived from IntCal13 and Hulu Cave is shown as $\Delta^{14}\text{C}$ over calendar age. Both records prove significant variations over time, even higher than 400 ‰ between 42 and 40 kyr BP (Cheng et al. 2018). The highest temporal resolution and precision of ^{14}C concentration is available from 0 to 14 kyr BP, due to continuous dendrochronological records.

modern times, an even stronger depletion could theoretically be observed today. However, this effect is overprinted by the additional radiocarbon that was released in the era of atmospheric nuclear testing. In the 1950s and 1960s, above-ground detonations of atomic bombs created additional thermal neutron flux in the upper atmosphere, that resulted in a short-term doubling of the atmospheric ^{14}C concentration (Levin et al. 2010). After the atmospheric nuclear test ban treaty in 1963, the observed fast decrease of $\Delta^{14}\text{C}$ in the atmosphere and its distribution among the carbon reservoirs allowed for numerous investigations into the exchange mechanisms of the carbon cycle, which were also performed on stalagmites (e.g. Genty and Massault 1999, Fohlmeister et al. 2011a, Ruzicka-Phillips et al. 2013). Additionally, this strong increase of ^{14}C activity enabled new approaches for radiocarbon dating of modern samples, with much higher age precision of 1 to 2 calendar years (Wild et al. 2000, Cook et al. 2020).

2.5 Stalagmite tracers & proxies of paleoclimatology

The tools to investigate the paleoclimate on environmental archives are environmental tracers and climate proxies. While the selection of those tools has grown drastically over the last years, proxies such as stable isotopes have contributed to massive advances in paleoclimate research over the last decades. The following sections will aim to explain the two categories of environmental tracers and proxies that are used extensively in this project, focusing on stable isotopes, trace elements, and radiocarbon, with a particular focus on their application in stalagmite studies.

2.5.1 Stable isotopes

Fractionation processes like chemical reactions and phase transitions are dependent on the isotopic mass and change the stable isotope ratios of the involved elements. The most important ones in paleoclimatology are the stable isotopes of oxygen (^{18}O) and carbon (^{13}C) which are expressed in the δ -notation, as previously introduced in Equation (2.14). Since stalagmites consist of carbonates, both isotopes are investigated in stalagmite studies for various purposes. The variety of processes that contribute to fractionation in the dripwater and the dissolved carbonate during stalagmite formation exacerbates the interpretation of the stable isotopes. Whereas stable oxygen is influenced by both atmospheric processes during the evaporation and transport of moisture and the calcite precipitation in the cave, the carbon signature reflects soil and karst processes that are limited to the cave site and the regional processes. However, depending on the regional conditions and climatological considerations, both proxies can provide crucial insight into climate-relevant factors like precipitation variation and soil activity. Comparing both isotopic records can provide important insights into kinetic fractionation processes occurring during stalagmite formation in the cave (Hendy 1971, Scholz et al. 2009).

Stable oxygen isotopes as atmospheric and karst proxy

Although karst and cave processes during stalagmite formation have to be considered for $\delta^{18}\text{O}$, stable oxygen in stalagmites is generally interpreted with respect to the water that reaches the cave vicinity as precipitation. From the evaporation of the water at the source until the eventual condensation and precipitation on the respective site, the isotopes of water are subject to phase transition fractionation processes during the ongoing condensation on the pathway of the water vapor. The continuous depletion is described as a Rayleigh process, implying that the longer a water vapor parcel travels and precipitates, the lower the $\delta^{18}\text{O}$ values of the rain (Craig 1961, Hendy 1971). This is described as the *continental effect* (Dansgaard 1964, Rozanski et al. 2013). Increased rainout due to orographic uplift of the water vapor is called *altitude effect*. On larger timescales, the significantly increased amount of fresh-water that is stored on continental shelves during glacial periods needs to be considered. Due to the increased removal of light stable isotopes during evaporation, the ocean water signature was significantly increased in glacial isotopes (*ice volume effect*, Lea et al. 2002). Dansgaard (1964) first described the so-called *amount effect* as an observed negative correlation of $\delta^{18}\text{O}$ and the intensity of precipitation. Many studies have used this relationship to study the variability of precipitation in low latitudes over times of polar temperature swings such as the Dansgaard-Oeschger cycles during the last glacial period and throughout Termination I (Wang et al. 2001, Burns et al. 2003, Shakun et al. 2007).

For many low-latitude locations, the $\delta^{18}\text{O}$ can be used to investigate precipitation strength by interpreting the signal as influenced by the amount effect if the source reservoir of the precipitation that reaches the respective site can be assumed constant. However, for some temperate locations, global climate shifts result in a general change of wind patterns that affect the source of precipitation reaching the site (Cole et al. 1999). This effect can superpose the signal from the amount and the ice-volume effect and require site-specific investigations into the dynamics of the isotopic signals. Stalagmite So-1 from Sofular cave in Northern Turkey, which is further investigated in Chapter 6 of this dissertation, is an example of this superposition of source changes and the amount effect in $\delta^{18}\text{O}$ (Fleitmann et al. 2009).

Stable carbon isotopes as soil and vegetation proxy

While the oxygen signature in stalagmites provides access to the origins and amount of the precipitation, $\delta^{13}\text{C}$ in the stalagmite carbonate is influenced by processes from the soil zone through the karst limestone dissolution until the calcite precipitation in the cave (Genty et al. 2001). Among the determining factors are the soil microbial activity and the vegetation above the cave which determines the signature of the CO_2 from root respiration in the soil gas (Baker et al. 1997, Genty et al. 2003). C3 plants are generally characterized by lower values of roughly -25 to -30 ‰ in the respired CO_2 , whereas C4 plants show higher signatures around -10 to -15 ‰. Climatic changes that force the vegetation to adapt from one to another plant type might be observable in stalagmite $\delta^{13}\text{C}$ (Dorale 1998, Fleitmann et al. 2009).

Limestone dissolution adds carbon from the karst which is at much higher $\delta^{13}\text{C} \approx 0\text{‰}$ and shifts the stable carbon isotope signature from the initially low soil gas $\delta^{13}\text{C}$ towards higher values. A major factor that determines the dissolved inorganic carbon (DIC) levels in the drip water is the difference between an open or closed limestone dissolution system (Hendy 1971, Genty et al. 2001). Closed system conditions are usually linked to a waterlogged karst that inhibits the exchange of DIC with soil CO_2 . This leads to a high concentration of bicarbonate that originates from limestone carbonate in the drip water. The eventual $\delta^{13}\text{C}$ in the stalagmite can therefore be higher than in the case of an open system, where the dissolved limestone bicarbonate is substituted by CO_2 from the soil zone with a much lower $\delta^{13}\text{C}$ (Genty et al. 2001, Clark and Fritz 2013).

Calcite precipitation and fractionation

Calcite precipitation from the drip water in the cave is the last process during the formation of a stalagmite that determines the eventual stable isotopic signature of the calcite. The fractionation in this step is mainly dependent on factors such as cave temperature, pCO_2 in the cave air and drip-rate on the stalagmite top. Seasonal environmental changes like cave ventilation and variations of relative humidity in the cave air can have direct effects on the equilibration of the solution from which the calcite precipitates. These effects have been modeled and described by experimental approaches (Scholz et al. 2009, Deininger et al. 2012, Hansen et al. 2019). Prior calcite precipitation (PCP) before the percolation water reaches the drip site, as well as rapid degassing in the cave are generally connected with kinetic fractionation effects, which cause significantly increased isotopic signatures as compared to equilibrium fractionation (Scholz et al. 2009, Dreybrodt and Scholz 2011, Deininger et al. 2012). Since this affects carbon isotopes in the solution as well as oxygen isotopes, the $\delta^{13}\text{C}$ and $\delta^{18}\text{O}$ of the stalagmite calcite are often highly correlated in these cases (Spötl et al. 2005, Frisia et al. 2011, Scholz et al. 2012a).

2.5.2 Radiocarbon in stalagmites

The formation of stalagmites involves two major carbon sources, as described in Section 2.1.1. These are the soil gas CO_2 at near-atmospheric or at atmospheric ^{14}C concentrations and the carbonate in the karstic limestone above the cave, which does not contain ^{14}C and is therefore referred to as *dead carbon*. Those reservoirs and their interactions determine the final radiocarbon content of the drip water and consequently of the stalagmite. Figure 2.5 gives an overview of the carbon reservoirs and their influence on stalagmite radiocarbon.

Dead and aged carbon contribution to the formation of speleothems causes a shift of radiocarbon ages to much older ages than the respective atmospheric levels would suggest. This discrepancy is the reason why radiocarbon dating cannot be used to obtain stalagmite chronologies without making assumptions on the extent and temporal variability of the offset between stalagmite and atmospheric ^{14}C . Throughout the literature, this offset is referred to as dead carbon fraction (DCF) or dead carbon proportion. The DCF is also sometimes expressed as *reservoir age* in terms of radiocarbon years, i.e. the difference

between the ^{14}C age of the stalagmite and of the atmosphere at the time of calcite precipitation.

The soil CO_2 originates directly or indirectly from atmospheric CO_2 , which is transported into the porous soil through ventilation or is emitted through respiration by living organisms like plants, microorganisms and microbial bacteria. While the CO_2 from respiration processes of living plants is at atmospheric ^{14}C concentration, it was shown that, depending on the turnover times of the soil organic matter (SOM), the final ^{14}C signature of soil gas can be biased towards lower activities (Trumbore 2000, 2009, Fohlmeister et al. 2011a). Turnover times for soil carbon can be below 1 yr for labile and short-lived soil fractions, while stable stocks can age for thousand years, depending on the soil characteristics and configuration (Trumbore 2000, 2009). Especially in deeper soil layers, the formation of stable and very old carbon becomes more likely (Mathieu et al. 2015, Balesdent et al. 2018).

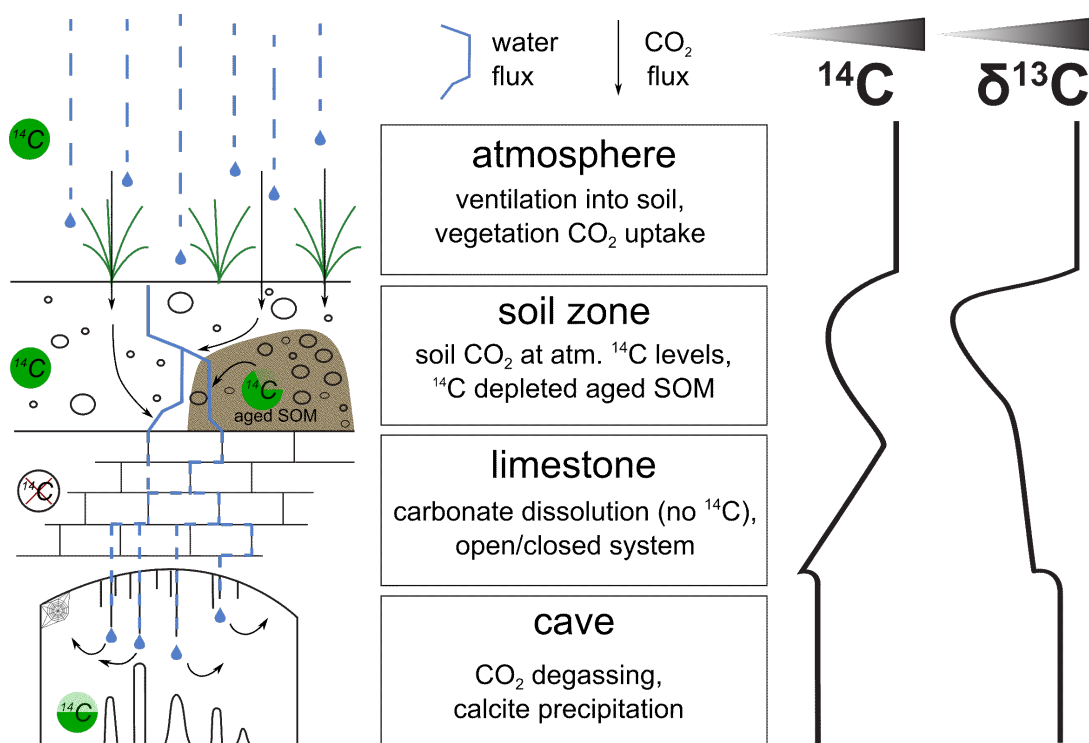


Figure 2.5: Sources of carbon and radiocarbon during stalagmite formation. Atmospheric CO_2 enters the soil zone by root respiration and ventilation. The soil CO_2 is at extremely high levels due to organic input from plants and microorganisms. Aged SOM can lower the ^{14}C concentration. The dissolved CO_2 in the percolation water dissolves limestone carbonate, which does not contain ^{14}C . The solution enters the cave and degases, due to the pCO_2 difference, leading to carbonate precipitation and speleothem formation. Blue lines represent water, black lines CO_2 fluxes. The lines on the right represent exemplary ^{14}C and $\delta^{13}\text{C}$ signatures of the CO_2 and the drip water, respectively. Graphic adapted and changed from Lechleitner et al. (2016a).

In a theoretical concept that considers a closed system carbon dissolution (see section 2.5.1), each mole of bicarbonate ions from soil CO_2 creates one mole of dissolved carbonate ions from the dead limestone. With the assumption of a quasi-atmospheric $\Delta^{14}\text{C}$ soil CO_2 , this results in a maximum DCF of 50 % (Hendy 1971). Under open system conditions, an additional exchange across the soil air-water phase occurs in the epikarst, where carbonate ions in the solution that originate from dissolved limestone calcite are partially replaced by bicarbonate from the soil gas. The resulting stalagmite DCF is significantly lower and can reach a theoretical minimum of 0. Case studies report typical values as low as 10 to 5 % for near-open conditions (Rudzka et al. 2011, Southon et al. 2012, Noronha et al. 2014). Both configurations of limestone dissolution represent theoretical extremes that do not occur in reality. Rather, limestone dissolution happens at intermediate states that approach either of the theoretical configurations. DCF values below 0 % indicate sample contamination, systematic errors of the determined calendar age, or biased atmospheric reference data. However, DCF values higher than 50 % have been observed in stalagmites, which grew in near-closed system dissolution configurations with additional input of limestone carbonate due to excess limestone dissolution by sulfuric acid in the soil (Spötl et al. 2016, Bajo et al. 2017) or due to the influence of aged SOM (Therre et al. 2020).

Together with stable carbon isotope data, stalagmite ^{14}C can allow for conclusions concerning the limestone dissolution. Modeling studies found that closed system conditions and excess limestone dissolution shift the DCF to higher values. In contrast, an open system is linked to lower DCF values (Hendy 1971, Genty et al. 2001, Fohlmeister et al. 2011b). A correlation of DCF and $\delta^{13}\text{C}$ might indicate that excess limestone dissolution systematics is the main reason for the observed effects (Spötl et al. 2016, Bajo et al. 2017). The major carbon sources of stalagmite formation are summarized in Table 2.1.

Climate influence on stalagmite DCF has been shown by many studies and is based on the changes in calcite dissolution and contribution from SOM. A closed system is generally attributed to a waterlogged karst, where the ratio of soil gas to water is smaller than in an open system. These conditions are observed for increased infiltration and precipitation. Several studies in tropical, humid climate zones that investigated independent precipitation proxies have shown this positive correlation of stalagmite DCF and infiltration of the soil zone (Griffiths et al. 2012, Noronha et al. 2014, Lechleitner et al. 2016a). Conversely, lower infiltration is generally attributed to more open system calcite dissolution, and therefore lower DCF. The age distribution of SOM, which affects the ^{14}C signature in the soil gas, is also subject to climate change. Carbon cycling variability in the soil due to changing precipitation amounts or temperatures in a time of climatic change has been shown to exert major control on stalagmite radiocarbon. For instance, the decomposition of older carbon pools in the SOM can cause the DCF in stalagmites to cross the theoretical 50 % threshold, as will be presented in Chapter 5.

The assessment of DCF variability and its climate susceptibility is of major importance for efforts to contribute to radiocarbon calibration using stalagmite data (Fohlmeister et al. 2011a). All stalagmites that have been used in these efforts so far, have relied on the assumption of a climate-independent DCF that is sufficiently constant and near an

Table 2.1: For the major carbon sources in stalagmite formation, the characteristic $\delta^{13}\text{C}$ and ^{14}C activity are given. The data are taken from (Hendy 1971, Genty et al. 2001, McDermott 2004, Trumbore 2009, Fohlmeister et al. 2011b, Bajo et al. 2017). The additional column in $\delta^{13}\text{C}$ indicates the influence of the endmember on the stalagmite calcite $\delta^{13}\text{C}$.

carbon source	$\delta^{13}\text{C}$	$a^{14}\text{C}$
atmospheric CO_2	-8‰	$\approx a^{14}\text{C}_{\text{atm}}$
soil CO_2 (C3 vegetation)	-25 to -30‰	$\approx a^{14}\text{C}_{\text{atm}}$
soil CO_2 (C4 vegetation)	-10 to -15‰	$\approx a^{14}\text{C}_{\text{atm}}$
aged SOM (1 yr to 10^3 yr)	\approx soil CO_2	$\approx a^{14}\text{C}_{\text{atm}}$ to $0.6 a^{14}\text{C}_{\text{atm}}$
limestone	-2 to 2‰	0

open system that the ^{14}C signature can be assumed to reflect atmospheric ^{14}C variability. The stalagmites included in the last inter-calibration record IntCal13 (Reimer et al. 2013) originate either from subtropical settings on the Bahamas (Beck et al. 2001, Hoffmann et al. 2010) or from Hulu Cave in a continental temperate climate in China (Southon et al. 2012, Cheng et al. 2018). The Hulu Cave stalagmites showed an a low and relatively constant DCF of $(5.6 \pm 0.8)\%$ in the period of highest precision of atmospheric ^{14}C data and climate-induced DCF variations during the last glacial termination are not observed. In the Bahamas stalagmites, the DCF is much higher at $(23.0 \pm 2.8)\%$ and significant and systematic DCF variability is seen during throughout the glacial termination. Nonetheless, the potential of stalagmites to contribute to the inter-calibration datasets is demonstrated by these studies.

2.5.3 Trace elements Mg and Sr in stalagmites

The incorporation of trace element ions other than Ca^{2+} into the stalagmite carbonate matrix enables the establishment of environmental proxies linked climate-dependent processes in the soil or karst zone above the cave. These elements include magnesium, titanium, barium, strontium, phosphorus and numerous other trace metals. The mechanism of trace metal incorporation and its utilization for environmental and climatic interpretation is explained in this section, with a special focus on the ratios of Mg/Ca and Sr/Ca in stalagmite calcite. Together with radiocarbon, a high-precision age model, and stable isotopes, elemental ratio analysis of stalagmite carbonate can be used to gain insight into the hydrological conditions during speleothem growth, that are directly linked to climatic conditions at the time of stalagmite growth.

In paleoclimatology, Mg and Sr in stalagmites are used as proxies for the hydrological conditions in the karst. Their measurements in stalagmites can provide insight into variability of infiltration and precipitation and have been applied in several speleothem studies (Verheyden et al. 2000, Fairchild et al. 2001, Fairchild and Treble 2009, Cruz et al.

2007, Griffiths et al. 2010, 2012, Sinclair et al. 2012, Treble et al. 2015, Warken et al. 2018, 2019). Several processes contribute to the Sr and Mg signature of a stalagmite, among them hydroclimatic processes via water–rock interaction such as the dissolution of aragonite or dolomite, changes in water/rock residence time or karst hydrology, cave atmosphere, prior calcite precipitation (PCP), drip rate variability or soil processes. The stalagmite mass ratio of Sr or Mg with Ca does not necessarily reflect the ratio of the drip water that enters the cave or of the bedrock above the cave (Fairchild et al. 2000). Since Ca is transported from calcite into an aqueous solution much faster than Mg and Sr, longer residence time of waters in the karst zone will be reflected in the drip water and in the stalagmite by higher Mg/Ca and Sr/Ca ratios than for short contact time of the percolation water phase and the host rock (Fairchild et al. 2000). This relationship is the key argument for the interpretation of Mg/Ca ratios as infiltration proxy. It has been argued that higher residence time is equivalent to a lower input of water from above, i.e. low infiltration and precipitation on the cave site. Therefore, increased Mg/Ca ratios are generally interpreted as an indicator for dryer conditions, and *vice versa*. Several studies have used these relationships to infer precipitation variations in paleoclimate records, together with other proxies (Verheyden et al. 2000, Cruz et al. 2007, Fairchild et al. 2000). A periodical or persistent correlation of Mg/Ca ratios with stalagmite DCF was shown, which demonstrates the influence of precipitation and infiltration rate on the limestone dissolution systematics (Griffiths et al. 2012, Noronha et al. 2014, Lechleitner et al. 2016a). Quantitative precipitation reconstructions from elemental ratios could recently be achieved on a late Holocene, seasonally resolved stalagmite record from Romania (Warken et al. 2018).

Together with Sr, the Mg signature can provide a tool to assess the influence of PCP during the formation of the stalagmite. Once the bicarbonate enriched solution is transferred from the regime of high $p\text{CO}_2$ (in the soil zone and the epikarst) into areas with reduced CO_2 concentration, the chemical equilibrium is shifted, forcing the precipitation of carbonate from the solution. If this occurs before the percolation water reaches the drip site, e.g. due to an air phase in the epikarst, this process is referred to as *prior calcite precipitation*. Since larger air phases in the karst are commonly related to drier conditions, enhanced prior calcite precipitation is expected in more arid climatic conditions (Fairchild et al. 2000, Johnson et al. 2006). In the transition from a solution to carbonate, Ca is preferably removed from the solution, compared to Sr and Mg. PCP can therefore cause significantly higher Mg/Ca and Sr/Ca ratios in the stalagmite, which can be much higher than in the host rock above the cave (Fairchild and Treble 2009, Treble et al. 2015). Since this process is equivalent for Sr, prior calcite precipitation can cause higher and covariant Mg/Ca and Sr/Ca ratios (Fairchild et al. 2000, 2006, Sinclair et al. 2012).

2.6 Climate change during the last 50 kyr

Based on its physical half-life (5730 yr), radiocarbon can be used as a dating tool and as an environmental proxy on time scales reaching back to roughly 50 kyr BP. In this period, the climate of the Earth transitioned from glacial conditions at the end of the Pleistocene into the current warm period (Holocene). This transition is commonly referred to as Termination I.

During the last glacial period, the global ice volume reached its maximum expansion between 26.5 and 19 kyr BP, which is called Last Glacial Maximum (LGM) (Clark et al. 2009). The following deglaciation during Termination I accelerated quickly during the Bølling/Allerød (B/A) interstadial after 14.7 kyr BP, but was interrupted by the Younger Dryas (YD) cold-reversal, a pronounced cooling episode after 12.9 kyr BP (Dansgaard et al. 1993, Steffensen et al. 2008). Approximately at 11.7 kyr BP, an abrupt warming occurred at the end of Termination I, which defines the starting point of the Holocene, the most recent warm period of Earth's climate which persists until today Walker et al. (2009). The aforementioned features are distinctly imprinted into the $\delta^{18}\text{O}$ signature of Greenland ice cores, such as the NGRIP data (Rasmussen et al. 2006), where higher values indicate periods of climate warming (see lower panel of Figure 2.6).

Apart from the long-term climate change and the stadial/interstadial episode of B/A and YD, the ice-core data also clearly shows very pronounced peaks to warmer climates throughout the last glacial, which represent the Dansgaard/Oeschger cycles (D/O 1–13 in the considered time scale, see Figure 2.6). These cycles correspond to fast warming episodes on decadal time scales followed by gradual or rapid cooling in high latitudes of the Northern Hemisphere (Johnsen et al. 1992, Dansgaard et al. 1993, Rahmstorf 2003). Extreme cooling events in the Northern Hemisphere can also be deduced as periods of low $\delta^{18}\text{O}$ in the NGRIP data throughout the glacial. These are the so-called Heinrich Stadials (HS1 to HS5 in the considered time scale, see Figure 2.6), which were caused by massive iceberg discharges from the Laurentide ice sheet into the North Atlantic, leading to reduced oceanic heat transport to higher latitudes (Heinrich 1988, Broecker 1994, Hemming 2004).

The effect of cooling and warming events which were observed in Greenland ice-core records on lower and mid-latitudinal climate has been a crucial subject of paleoclimate research. Stalagmite records show patterns in their stable isotope data which coincide with the rapid cooling/warming events in the glacial and with the YD and B/A during Termination I (Wang et al. 2001, Burns et al. 2003, Shakun et al. 2007, Fleitmann et al. 2009). In Figure 2.6, two stalagmite records from two sites are shown which clearly exhibit signals of high-latitude climate influence in their stable isotope signature. At Hulu Cave, a combined record of three stalagmites identifies a link between Greenland temperature changes and variations of meridional heat and moisture transport in the Western Pacific region, which affects the East Asian Monsoon, thus supporting the idea that the Greenland events are not confined to higher latitudes, but have a strong teleconnection to at least the entire hemispheric climate (Wang et al. 2001). Low and mid-latitude precipitation was influenced by North Atlantic temperature changes, in the form of increased tropical rainfall for periods of warmer high-latitude temperatures, as deduced from a stalagmite from

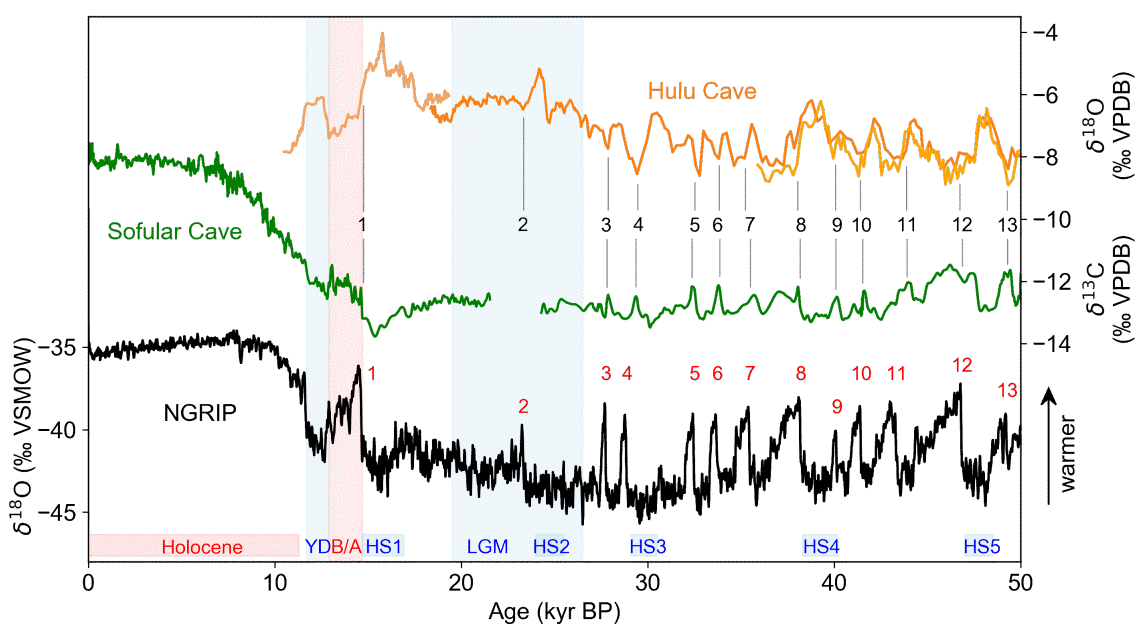


Figure 2.6: Climate variability of the last 50 kyr BP recorded by the Greenland NGRIP ice core $\delta^{18}\text{O}$ data (black) (Rasmussen et al. 2006). Also shown are the stalagmite records from Sofular Cave (Fleitmann et al. 2009), which shows the ecosystem response in $\delta^{13}\text{C}$ (green) and Hulu Cave $\delta^{18}\text{O}$ of three stalagmites indicating monsoon precipitation increase during warmer Greenland temperatures (Wang et al. 2001). The $\delta^{18}\text{O}$ peaks are towards more negative values due to the isotopic precipitation amount effect. The NGRIP data clearly shows the transition from peak glacial conditions in the Last Glacial Maximum (LGM, blue area) through the Bølling/Allerød warming (B/A, red) and and Younger Dryas cold reversal (YD, blue). Heinrich Stadials (HS1–5) and Dansgaard/Oeschger interstadials (D/O 1–13) can be seen in the NGRIP plot (Clark et al. 2009, Johnsen et al. 1992, Dansgaard et al. 1993, Hemming 2004) Both stalagmite records show distinct isotopic responses to Northern Hemispheric climate change.

Moomi Cave, Socotra Island (Burns et al. 2003). At a temperate cave site in Northern Turkey, the D/O cycles were linked to rapid and sensitive climate and ecosystem responses, seen in fast $\delta^{13}\text{C}$ fluctuations at Sofular Cave stalagmites (Fleitmann et al. 2009).

3 Methods

The vast majority of analyses on environmental archives which are performed for paleoclimatology rely on mass spectrometry or mass spectroscopy. Arguably the most crucial aspect of investigating a climate archive is its chronology, i.e. the age determination and reliable allocation of a likely age for every subsample. In the following sections, the methods utilized in the course of this project will be explained, with a focus on the development of a reliable age-depth relationship. Additionally, the ^{14}C dating methods for stalagmite samples are described with respect to sampling, chemical preparation and AMS measurement.

3.1 Uranium-series dating

The age determination of carbonate archives which incorporate uranium during their formation can be successfully achieved if the assumption of a closed system holds and if no significant amounts of decay products or parent nuclides of the U-decay chain are present (see section 2.2). The U-series age determination relies on the precise measurements of isotope abundance of several U and Th isotopes. For this study, these measurements were carried out on a multi-collector inductively coupled plasma mass spectrometer (MC-ICP-MS) after chemical isotope purification by wet column-chromatography. The resulting isotope ratios are used for data analysis and age correction during the age calculation.

3.1.1 MC-ICP-MS measurement

The technology used for U-series dating in this study is MC-ICP-MS. The measurements are carried out on a Thermo-Fisher Neptune Plus at the Institute of Environmental Physics (IUP) which was described in detail by Arps (2017). Before the measurements, carbonate samples are chemically pretreated following the procedures described in Douville et al. (2010) and Shen et al. (2012). Depending on the ^{238}U concentration, approximately 50 to 200 mg calcite material is sampled for a measurement (by drilling, sawing or cutting). The specific application of the chemistry for sample preparation at the IUP is elaborated by Wefing et al. (2017). The samples are dissolved before being spiked with ^{229}Th , ^{233}U and ^{236}U . Wet column chromatography achieves purification of U and Th and effectively separates the elements from the calcite sample matrix. This provides high sample concentrations and thus stability in the mass spectrometer during the measurements.

For the measurement, the liquid sample solution is converted into a dry aerosol in argon mixed with nitrogen by a Cetac Aridus II desolvating nebulizer device. Subsequently, it is injected into the plasma source of the mass spectrometer. The setup of the Thermo Fisher

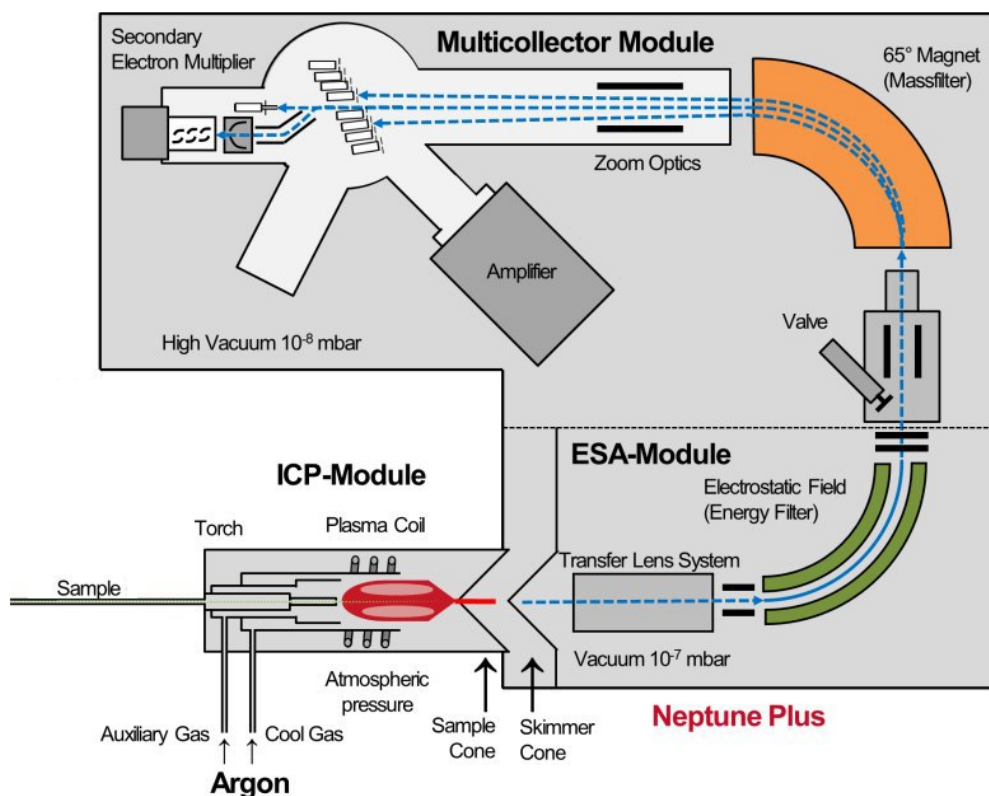


Figure 3.1: Schematic illustration of the essential components of the Thermo Fisher Neptune Plus MC-ICP-MS, that was used for U-series dating measurements in this study. The three main components are: The ion source (ICP module), the electrostatic analyzer (ESA) and the multi-collector module. The illustration correctly describes the measurement setup, while in reality the Thermo Fisher Neptune is effectively mirror-inverted (Förstel 2017).

Neptune Plus is illustrated in Figure 3.1. In the following list, the essential components are presented and briefly explained.

- In the **ion source** (inductively coupled plasma module), an argon plasma is maintained at temperatures > 8000 K, into which the nebulized aerosol from the liquid sample dissolution is injected and subsequently ionized.
- The ions are then extracted into the **electrostatic analyzer (ESA)** across two pressure gradients via the sample cone and the skimmer cone. They enter through the ion extraction lens into the transfer optics lens stack, which is used to focus the ions onto the entrance slit of the mass analyzer. The electrostatic field of the analyzer achieves shaping and focusing of the ion beam according to their energy. Positively charged ions leave the ESA at an angle of 90° respective to the initial injection and are accelerated by 10 kV to their final energy.

- In the **multi-collector module**, the ion the ion species are separated to different tracks according to their masses by a magnetic sector field and then focused by the zoom optics on the focal plane of the detector module. For detection, eight movable Faraday cups and a fixed center cup are installed, as well as an off-axis secondary electron multiplier. The sensitivity of the cups can be adapted by a range of resistors from 10^{10} to $10^{13} \Omega$. In the multi-collector module, operation vacuum levels are at approximately 10^{-8} mbar (Arps 2017, Förstel 2017).

3.1.2 Data analysis and correction

The intensities measured in the multi-collector module of the mass spectrometer undergo several steps of data correction taking into account effects such as mass tailing of the most abundant isotopes, hydrate ion correction and detector characteristics.

To account for the occurring drift during a longer measurement run, every sample is bracketed by the HU1-standard, a sample with assumed activity ratios of ($^{234}\text{U}/^{238}\text{U}$) and ($^{230}\text{Th}/^{238}\text{U}$) in secular equilibrium. For the measurements in this study, this standard was reproduced at a value of $1.000\,02 \pm 0.000\,82$ for ($^{234}\text{U}/^{238}\text{U}$) and $1.000\,04 \pm 0.000\,82$ for ($^{230}\text{Th}/^{238}\text{U}$). The uncertainty is the 1σ standard deviation from 517 samples over 22 months. This translates to a reproducibility of 0.82 ‰ for both ratios. Full process blanks yield values lower than 0.04 fg and 0.4 fg for ^{230}Th and ^{234}U , respectively. Radiometric ages were calculated from the isotope ratios with the half-lives from Cheng et al. (2000). Whenever more recently published values of those half-lives were used for the calculation, however, the results did not change significantly. To account for the detrital correction of the ^{230}Th isotope, a weight ratio $^{232}\text{Th}/^{238}\text{U}$ of 3.8 (Wedepohl 1995) and secular radioactive equilibrium within the uranium decay chain was assumed. All determined and ^{230}Th corrected ages are given in reference to the year 1950 CE for reasons of consistency and to simplify the comparison to radiocarbon ages.

3.1.3 Age vs. depth modeling

In paleoclimatology, the most crucial aspect for the analysis of climate proxies and tracers is the allocation of an accurate time for the considered data by an adequate age determination procedure. In stratified climate archives such as stalagmites, ice cores, lake sediments or coral mounds, a method that has proven to be successful is the modeling of a continuous age-depth relation by interpolation between age data points determined by methods such as U-series dating.

For stalagmites in particular, software and models have been developed to determine the growth patterns of continuously deposited calcite, whilst taking into account potential growth discontinuities. This modeling software is based on stepwise linear interpolation, higher-order polynomial models, or Poisson deposition processes. A comparative study with exemplary performance analysis on an artificial dataset was carried out by Scholz et al. (2012b). For this study, the initial age-depth relation was mostly achieved by using the StalAge algorithm Scholz and Hoffmann (2011) which uses a linear interpolation approach. Since large data sets tend to put a high burden on the modeling software,

it may be worthwhile to perform area-wise modeling for multiple segments of the data. Additionally, weaknesses of models often show when data points imply a reversal of stratigraphic order or when hiatuses occur. These points and data segments were therefore revisited after the use of software and modeling and, if necessary, manually corrected.

3.2 Radiocarbon dating

In fields like archeology, radiocarbon dating is used for the direct determination of the age of a sample, that was in continuous exchange with the atmosphere. Climate archives in paleoclimatology are amenable to this method of age determination only under certain prerequisites. Nonetheless, the mass-spectrometric measurement of the radiocarbon concentration in a carbonous sample by AMS can provide insights into the environmental processes that contributed to its formation. The following sections describe the methods that were used for sampling, preparation and ^{14}C measurement of carbonate samples, stalagmites in particular. An elaborate description of this process is given in Chapter 4, where a newly established carbonate extraction line is presented.

3.2.1 Sampling

The sampling of calcite samples, such as speleothems, corals, or foraminifera, for AMS ^{14}C dating requires sufficient sample material to gain approximately 1 mg of carbon. Since the considered climate archives predominantly consist of calcium carbonate (CaCO_3 , molar mass: 100.09 g mol^{-1}), the ratio to the molar mass of carbon (12.01 g mol^{-1}) suggests a minimum calcite mass of roughly 8.33 mg to achieve a sufficient ion current during the AMS measurement.

For this study, carbonate climate archives were sampled¹ by either drilling or by cutting with a diamond-wire saw. Due to the stratigraphy and morphology of stalagmites, it is crucial to follow growth patterns (layers) during the sampling procedure to avoid interference from other layers. Drilled samples have a high potential to exchange with ambient air due to their vastly increased surface area, which can be avoided by evacuating the sample containers and by fast sample processing. Solid samples pieces can be leached in a weak acid shortly before chemical preparation to remove contaminated material from the sample surface.

3.2.2 Carbon dioxide extraction and graphitization

The detailed description of CO_2 extraction and graphitization is given in Chapter 4. Here, a summary of the two chemical preparation steps to convert CaCO_3 into graphite is given.

¹The terms *sample* and *subsample* are often used synonymously in literature. Yet, distinctions are occasionally made where a stalagmite as a whole is referred to as a *sample*, whereas the calcite material taken from one particular stalagmite for further analysis is called *subsample*. In this section, the terms *sample/sampling* always mean the calcite quantity taken from one particular stalagmite.

The extraction of CO_2 is achieved by hydrolysis with hydrochloric acid in an evacuated glass-tube setup. In a dry-ice/acetone freezing trap, the H_2O in the emerging gas mixture is removed and the purified CO_2 is subsequently captured in gas containers by liquid nitrogen cooling.



Numerous pressure gauges and a calibrated confined volume provide several control mechanisms for the procedure.

After the extraction, the CO_2 is transformed into graphite in a graphitization setup (Unkel 2006). Hydrogen gas is added in a small reactor chamber in the empirically determined ratio for the best reaction efficiency, together with a previously chemically cleaned iron catalyst. At a temperature of 575°C , the carbon dioxide is reduced in a two step reaction and precipitates as graphite on the surface of the iron powder.



Freezing traps remove the emerging H_2O during the reaction. After three to four hours, the reaction is complete and the iron-graphite compound is stored in glass tubes until the measurement.

3.2.3 AMS measurement

For this dissertation, the ^{14}C measurements were carried out by accelerator mass spectrometry (AMS) on a compact AMS setup especially designed for radiocarbon dating, named Mini Carbon Dating System (MICADAS) (Synal et al. 2007, Wacker et al. 2010a, Suter et al. 2010). Its technology allows for high-precision measurements of the $^{12}\text{C}/^{14}\text{C}$ ratio with low interference from molecular compounds, using the 1^+ charge state for carbon ions. Additionally, the ($^{13}\text{C}/^{12}\text{C}$) ratio is determined during the ^{14}C analysis for a precise mass fractionation correction. The general setup consists of an ion source with a sample magazine, the low energy magnet, the 200 kV acceleration unit with the gas stripper, high-energy magnet, electrostatic analyzer (ESA) and detection modules (gas ionization chamber for ^{14}C atoms). The facility at the Curt-Engelhorn-Center Archaeometry (CEZA) in Mannheim, Germany, which conducted the reported measurements, was characterized by Kromer et al. (2013). In this section, the most relevant modules of the instrument are listed (Synal et al. 2007).

- The ions are created in the **Cs^+ beam sputter ion source** with a spherical ionizer at voltages from 5 to 12 keV. After the negative ionization of the graphite sample, the ion beam is extracted from the ion source at energies up to 40 keV with currents of 30-50 μA .
- The following **low energy mass spectrometer** consists of a dipole magnet with a bending radius of 25 cm. An offset Faraday cup in the magnet image plane records the ^{12}C current before injection into the accelerator (used for transmission

determination). For the injection of the different isotope species into the accelerator unit, a fast beam pulsing system is included, with very short sequenced pulse times of 50 μs (^{12}C), 40 ms (^{14}C), 500 μs (^{13}C) and again 50 μs (^{14}C). This enables the measurement of the different carbon isotopes in the detection unit in very fast succession.

- Once the masses are separated, the ions are accelerated by a high voltage platform in a **200 kV tandem accelerator** configuration. The stripper gas is inserted into the evacuated acceleration unit by a continuous gas flow through a high-pressure gas transfer line outside the unit.
- The emerging ions enter the achromatic second **high energy mass spectrometer**. In a 90° magnet with a bending radius of 35 cm, the masses are p/q -separated. Apart from two Faraday cups to measure the ^{12}C and ^{13}C currents, another cup is installed between the other two to analyze the currents of ^{13}C from $^{13}\text{CH}^-$ molecule fragments that were broken by the stripper gas and entered the high-energy mass spectrometer with the ^{14}C current. This Faraday cup is particularly important for background corrections.
- After the mass separation, a **spherical electrostatic analyzer (ESA)** provides

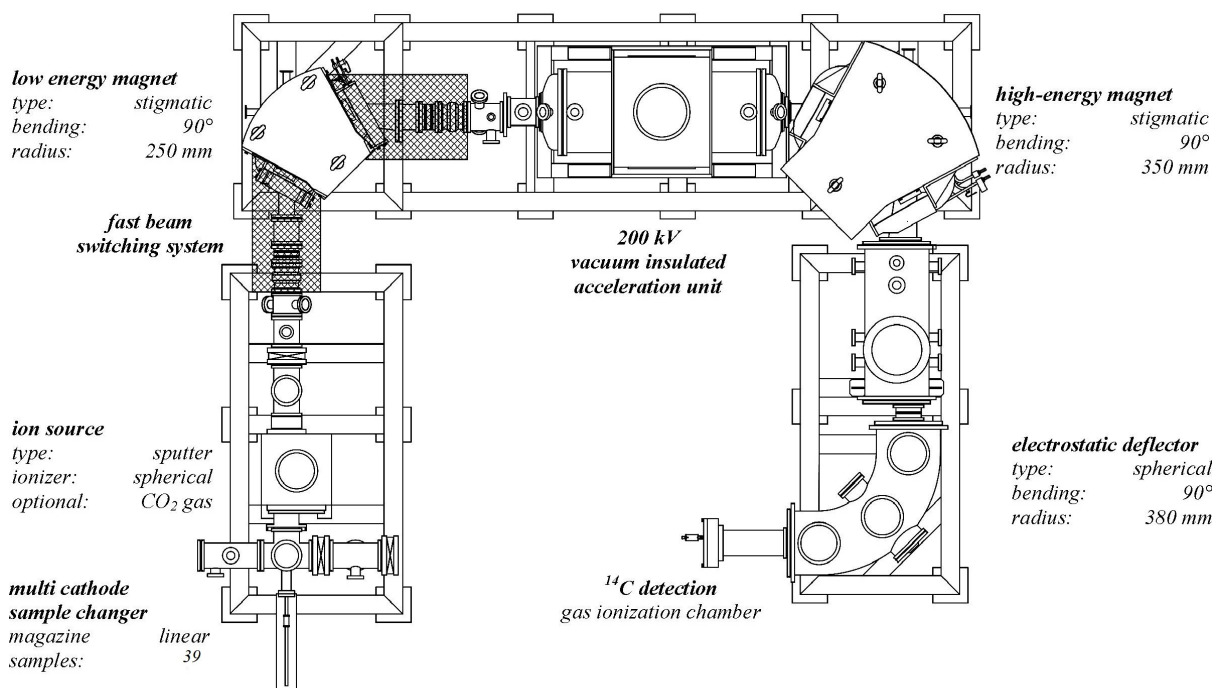


Figure 3.2: Schematic illustration of the essential components of the MICADAS AMS at Curt-Engelhorn-Centre Archaeometry, which was used for ^{14}C dating measurements in the scope of this dissertation, adapted and modified from Synal et al. (2007).

non-energy dispersive beam deflection and energy selection.

- The ^{14}C ions pass the two high-energy modules and enter a **gas ionization detection chamber** filled with 20 mbar of isobutane through a 50 nm Si_3N_3 foil, where they dissipate their total energy of 428 keV.

At the MICADAS instrument in Mannheim, the setup is operated at a beam transmission of roughly 40 %, under normal conditions. During a measurement cycle, a linear sample magazine contains 39 targets, typically holding 5 oxalic acid II-standards, 5 blanks, and 29 samples. Total measurement time per target is roughly 50 min. The blank measurements show an apparent ^{14}C age exceeding 50 000 yr, allowing for stable and precise ^{14}C dating measurements (Kromer et al. 2013). For data analysis, the BATS tool is used (Wacker et al. 2010b). The mean $^{14}\text{C}/^{12}\text{C}$ ratio of the oxalic acid II-standard samples is assigned to the literature value of 134.07 pmC (following Stuiver 1983). Blank correction is achieved by subtracting the mean blank $^{14}\text{C}/^{12}\text{C}$ ratio from the sample measurements. All reported results are corrected for isotopic mass fractionation and normalized to $\delta^{13}\text{C} = -25 \text{‰}$.

3.2.4 Reservoir age and DCF modeling

If a ^{14}C dating result is used for the determination of a reservoir age or stalagmite DCF rather than for direct dating purposes, the initial radiocarbon activity ($a^{14}\text{C}_{\text{init}}$) can be reconstructed. This requires an otherwise determined age (eg. U-series dating, layer counting etc.) or a modeled sample age (t_{mod}). Invoking Equation (2.15) and the physical decay constant of the radioactive decay of the ^{14}C isotope ($\lambda_{\text{decay}}^{-1} = 8267 \text{ yr}$) yields the following term for a so-called *initial* activity ($a^{14}\text{C}_{\text{init}}$):

$$a^{14}\text{C}_{\text{init}} = a^{14}\text{C}_{\text{meas}} \cdot \exp(\lambda_{\text{decay}} \cdot t_{\text{mod}}) \quad (3.4)$$

$$= \exp(\lambda_{\text{decay}} \cdot t_{\text{mod}} - \lambda_{\text{Lib}} \cdot t^{14}\text{C}) \quad (3.5)$$

A focus in ^{14}C studies on speleothems lies on the comparison of the initial ^{14}C activity in the speleothem layer and the atmospheric ^{14}C concentration ($a^{14}\text{C}_{\text{atmo}}$) at the time of deposition. The atmospheric activity is retrieved from atmospheric reconstruction data sets, the most important ones being the inter-calibration set IntCal13 (Reimer et al. 2013) and the recently published stalagmite radiocarbon record from Hulu Cave (Cheng et al. 2018). To obtain the respective atmospheric activities as well as their uncertainties, a Monte Carlo approach is performed by generating a Gaussian data set of $N = 10^6$ ages around the modeled age (t_{mod}). Subsequently, the corresponding atmospheric activity for every age was determined from the interpolated atmospheric radiocarbon data set. The value and uncertainty of $a^{14}\text{C}_{\text{atmo}}$ can then be analyzed by the data that was generated through projection of the Gaussian on the atmospheric calibration set.

The immanent offset between the initial radiocarbon activity in the speleothem and the atmospheric radiocarbon activity is often reported as *reservoir age*. This is a quantity with the unit of conventional ^{14}C years defined as the difference between measured radiocarbon

age in the stalagmite and the corresponding atmospheric radiocarbon age obtained from calibration data.

$$t_{^{14}\text{C}, \text{res}} = t_{^{14}\text{C}, \text{meas}} - t_{^{14}\text{C}, \text{atmo}} \quad (3.6)$$

With the equations above, the dead carbon fraction (DCF) is given as:

$$\text{DCF} = \left(1 - \frac{a_{^{14}\text{C}_{\text{init}}}}{a_{^{14}\text{C}_{\text{atmo}}}} \right). \quad (3.7)$$

This quantity is usually expressed in the unit percent (%). Following the definition given by eq. (3.7), a DCF of 0 means that the investigated stalagmite had exactly the same activity as the atmospheric data set suggest at the time of deposition.

3.3 Trace elements

Two different techniques are used in the scope of this dissertation to determine the element ratios of the stalagmite samples. Approximately 1 to 2 mg of calcite were drilled for each sample measurement. The sample material was then dissolved in 0.5 M HNO₃ and diluted to a Ca²⁺ concentration of 10 ppm.

At the IUP, a Thermo Fisher iCAP Q inductively coupled plasma quadrupole mass spectrometer (ICPQMS) was used. To provide data comparability and reproducibility, some samples were analyzed by different measurement methods at the Institute of Earth Sciences at Heidelberg University using an ICP optical emission spectrometer (ICP-OES) 720. Mg/Ca ratios of two measured standards have a 1 σ reproducibility < 1% for the ICPQMS. For the OES setup, the internal standard deviation is < 1% (1 σ) for Ca²⁺, Mg²⁺ and Sr²⁺. The SPS SW2 is used as a standard, and the long-term 1 σ reproducibility is 2.0% for Ca²⁺, 3.3% for Mg²⁺ and 3.4% for Sr²⁺ (Warken et al. 2018). Several internal standard measurements of the investigated ratios were performed on the two different setups and the respective ratios were normalized to exclude data bias and ensure reproducibility. The results are reported as dimensionless mass ratios.

Part II

Heidelberg Radiocarbon Lab - Establishing a new Carbon Dioxide Extraction Line

4 Establishing a new Extraction Line for ^{14}C Analysis of Carbonates

In this chapter, the development of a new extraction line for the chemical preparation of carbonate samples for ^{14}C measurements by accelerator mass spectrometry (AMS) is described. Planning and construction of the new extraction setup was the subject of Lukas Proß's Bachelor Thesis (Proß 2018), which was supervised in the frame of this PhD project. The chemical extraction process is generally divided into two steps. Firstly, carbon dioxide is extracted from carbonate by hydrolysis of the sample. Secondly, the carbon dioxide gas is reduced to graphite before the latter is inserted into the ion source of the AMS setup. During the chemical preparation, the sample is prone to contamination by, for instance, ambient air at modern or close-to-modern radiocarbon signature. Therefore, a large focus of extraction and graphitization is on controlling the respective processes by consistent pressure monitoring, achieving sufficient evacuation levels and avoiding leakage. The newly established extraction line at the Radiocarbon Laboratory of the Institute of Environmental Physics (IUP) in Heidelberg, achieves all this and also significantly increases sample throughput by allowing for successive preparation of six samples in one day. Additionally, the setup is designed to allow for an automated operation in near future, which was not finalized yet as of the end of this project. The following sections explain the layout, operation and characterization. Performance assessment was achieved by multiple standard and blank testing with successful outcome. As a case study, a summary of ^{14}C dating results of several speleothem studies performed on the new setup is given.

4.1 Developing a new extraction line

Radiocarbon dating has provided the environmental sciences with an indispensable tool to investigate a wide range of processes involving the exchange, storage or transformation of carbon. At the IUP at Heidelberg University, radiocarbon dating has historically belonged to one of the central disciplines (see studies Munnich 1957, Kromer and Münnich 1992). Advances in carbon cycle research, paleoclimatology, paleoceanography, physics of the atmosphere and physics of aquatic systems have often based on ^{14}C as tracer or as a climate proxy (Levin et al. 2008, Kromer et al. 2010, Fohlmeister et al. 2011a, Therre et al. 2020). Radiocarbon studies at the IUP have profited from the establishment of an AMS facility, which has increased measurement precision and has reduced required sample material (Synal et al. 2007, Kromer et al. 2013). In paleoclimatology and paleoceanography a special focus lies on carbonate climate archives, such as speleothems, fossil cold water

corals and foraminifera.

To perform high-precision ^{14}C measurements of carbonate samples, a new carbon dioxide extraction line was established at the IUP. The new setup is presented in this study together with a performance characterization and results from the first years of operation.

Previous studies have shown that the extraction of carbon dioxide from carbonate samples is reliably performed in evacuated glass setups with gas transport by temperature forcing induced by liquid nitrogen (Tisnérat-Laborde et al. 2001). Operation pressure values in the setups during sample processing should be below 10^{-4} mbar to avoid contamination by ambient air and to avoid memory effects. Moreover, it is desirable to process more than one sample at a time for the sake of process optimization. These aspects were taken into account during the configuration of the new extraction line. Its general characteristics are outlined in the following sections.

4.1.1 Configuration

For the sake of an evenly distributed vacuum, the setup was designed in a circular configuration with the central evacuation pump located in the middle of the setup. Six carbonate samples can be connected to the evacuation line and can then be prepared consecutively with one cooling trap (dry ice and acetone) for all samples. A calibration volume is included in the setup to assess the efficiency of the extraction process allowing for the identification of potentially incomplete reactions.

The setup is schematically depicted in Figure 4.1. Borosilicate glass was used to form the gas transport tubes of the setup. The valves integrated in the setup are semiautomatic and allow for both pressure regulated and manual operation. The turbomolecular/membrane pump combination is connected to the center tube of the glass setup and provides pressures as low as 10^{-6} mbar at the center of the extraction line (sensor S1).

Five pressure sensors are used to monitor the vacuum and extraction progress: One Pirani gauge is included for each the sample (S2), cooling trap (S3), and gas phase part (S4) of the setup, respectively. A combined Pirani/capacitance gauge for accurate measurements of the CO_2 pressure is connected to the calibration volume (S4) and one combined Pirani/cold cathode gauge at the center tube (S1) is used for vacuum performance surveillance.

4.1.2 Calibration volume

Incomplete hydrolysis of the carbonate samples may result in isotopic mass discrimination which could affect the results of ^{14}C measurement. To control the efficiency of the extraction reaction, an additional volume confined by two valves was added to the circular setup between the freezing trap and the gas containers. Since Pirani gauges only have a limited area of linearity for CO_2 (up to 1 mbar), a capacitance sensor was installed in this volume to provide accurate values for the CO_2 pressure. In theory, the calculation of the substance amount, i.e. the mass of the resulting carbon dioxide, can be calculated by invoking the ideal gas law with the pressure p , Volume V , mass m , temperature T and

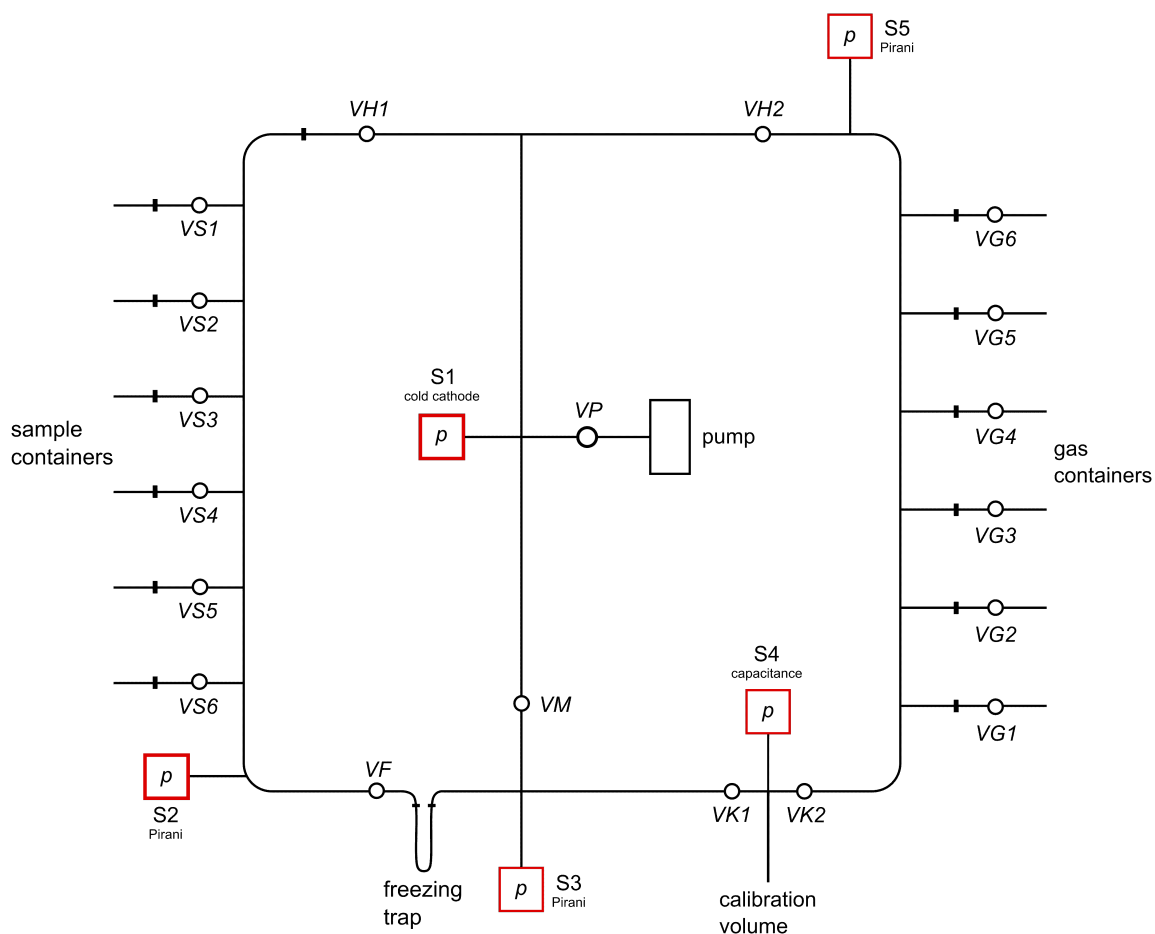


Figure 4.1: Schematic plan of the extraction line setup. The carbonate samples are connected to the line (see left side of the graphic). Each sample (number 1 through 6) is transferred from its sample container connection (VS) through the freezing trap into the calibration volume and afterwards into the respective gas container (VG). Valves (circles), module glass joints (bars) and pressure gauges (red squares) are depicted in the graphic.

molar mass M and the specific (R_S) or universal gas constant (R).

$$pV = m R_S T \quad (4.1)$$

$$m = \frac{pVM}{RT} \quad (4.2)$$

However, systematic errors of the capacitance gauge or of the volumetric measurement of the calibration volume have to be taken into consideration. To avoid these effects, an additional experimental calibration of the pressure-volume relationship was conducted by measuring the CO_2 pressure in the calibration volume for pieces of carbonate with precisely determined masses spread across the range of the expected sample masses (from 6 to 14 mg). The results of this experiment showed the expected linear relationship between carbonate mass and measured pressure in the calibration volume ($R^2 = 0.9977$, $N = 9$, $p < 0.01$).

Figure 4.2 depicts the relation of pressure and sample mass that is approximated by fitting the linear function $f(x) = a \cdot x + y_0$ to the data. The resulting calibration function is given by Equation (4.3).

$$p(m) = (16.03 \pm 0.23) \text{ mbar mg}^{-1} \cdot m + (1.76 \pm 2.12) \text{ mbar} \quad (4.3)$$

The observed offset between the experimental linear relationship and the ideal gas law can be attributed mainly to systematic errors of the used capacitance gauge that scale with pressure. The y-intercept of the linear fit is not significantly different from zero which shows that the measured pressure in the gauge is proportional to the input mass of carbonate sample.

From the aforementioned relation expressed by Equation (4.3), an inverse function $m(p_{\text{meas}})$ can be inferred allowing the calculation of processed carbon mass from the CO_2 pressure measured in the calibration volume. Here, the sample is assumed to be pure CaCO_3 which allows for a simple calculation of the processed carbon mass by invoking the molar masses of calcium carbonate ($M_{\text{CaCO}_3} = 100.09 \text{ g mol}^{-1}$) and carbon ($M_{\text{C}} = 12.01 \text{ g mol}^{-1}$). The explicit mathematical expression for the extracted carbon mass depending on the measured value in the calibration volume yields:

$$m_{\text{C}}(p_{\text{meas}}) = \frac{M_{\text{C}}}{M_{\text{CaCO}_3}} \cdot m_{\text{CaCO}_3}(p_{\text{meas}}) \quad (4.4)$$

$$= \frac{M_{\text{C}}}{M_{\text{CaCO}_3}} \cdot (61.72 \pm 1.28) \cdot 10^{-3} \text{ mg mbar}^{-1} \cdot p_{\text{meas}} + (0.00 \pm 0.22) \text{ mg} \quad (4.5)$$

In addition to the absolute value of the carbon mass, the efficiency of the extraction reaction can also be assessed. Therefore, the measured pressure is compared to the expected pressure, which depends on the initial carbonate mass as described by Equation (4.3). The resulting ratio is interpreted as reaction efficiency η_{extr} .

$$\eta_{\text{extr}} = \frac{p_{\text{meas}}}{p(m)} \quad (4.6)$$

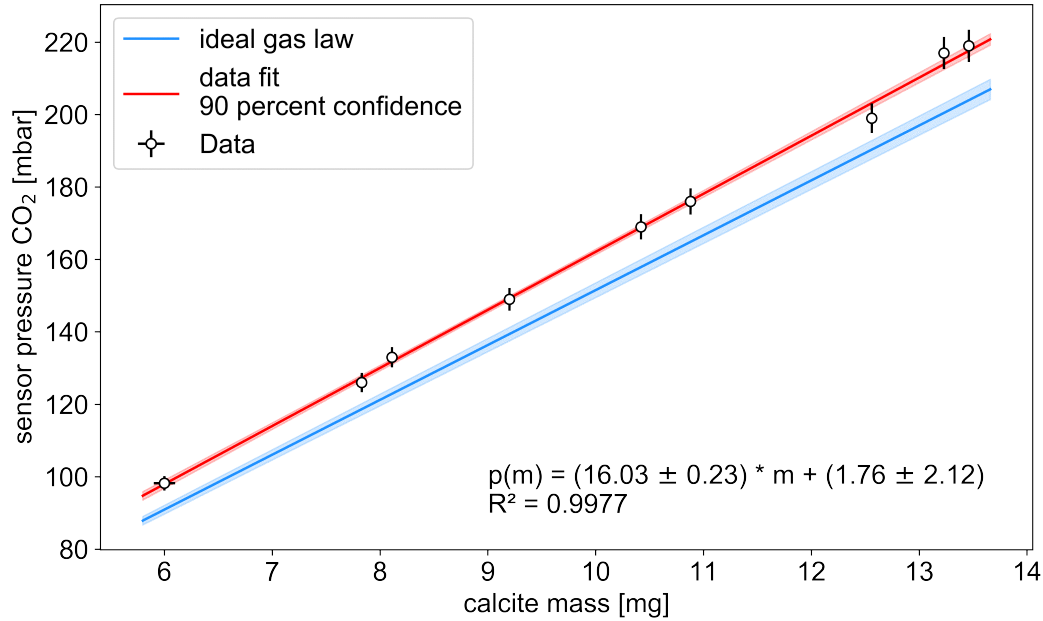


Figure 4.2: Characterization of the calibration volume. A linear relation between sample mass and measured sensor pressure is observed. The data reflect systematically higher pressure in the calibration volume than expected from the ideal gas law. The fitted linear function in its inverse form is used for the efficiency assessment of the extraction.

With η_{extr} , the characteristics of different sampling methods can be distinguished and the overall performance of the extraction setup can be characterized and monitored.

4.2 Sample treatment and measurement

The new setup is designed for the CO₂ extraction from carbonate samples for AMS radiocarbon measurements. For this purpose, approximately 1 mg of graphite is required in the ion source (Synal et al. 2007, Kromer et al. 2013) after completed extraction and graphitization. An initial bulk mass of 10 mg carbonate from the sample is sufficient, assuming CaCO₃ and the respective molar masses.

To avoid sample contamination before the chemical preparation, pretreatment is required depending on the nature of the sample (powder, pieces, granulate, ...). Carbonate pieces are leached in hydrochloric acid (4% HCl) for approximately one minute, then dried at 60 °C for one hour. If samples have to be drilled as a powder, the resulting material is not leached and should therefore be processed shortly after sampling to avoid contamination. Process blanks from carbonate older than the detection limit of radiocarbon (marble, IAEA C1 or mid-Pleistocene stalagmites) are prepared alongside samples and undergo the same sample treatment to account for possible contamination during extraction or

graphitization. The following sections shortly highlight the individual steps during sample preparation for radiocarbon measurement.

4.2.1 Extraction

After pretreatment, the samples are inserted into the cleaned containers. As a hydrolyzing agent, 0.5 ml of hydrochloric acid are injected into the acid compartments. The loaded container is then connected to the extraction line and evacuated for approximately 15 minutes ($p < 10^{-4}$ mbar). After checking for leakage, the acid is poured on the carbonate by manually turning the containers. When the carbonate sample is completely hydrolyzed (seconds for powdered samples, ca. 1 minute for piece samples), the resulting gaseous mixture of CO_2 and H_2O is expanded into the freezing trap where the emerging water vapor is removed. The purified CO_2 is collected in the calibration volume by a cooling trap filled with liquid nitrogen, where it is expanded to obtain the pressure at lab conditions in the calibrated volume (see section 4.1.2). Lastly, the CO_2 is transported to and confined in the gas containers.

4.2.2 Graphitization

The extracted CO_2 in the gas containers is transferred to a graphitization setup that is described and characterized by Unkel (2006). To reduce the CO_2 to C, the gas is transferred into a reaction container and hydrogen gas is added in a stoichiometrically determined ratio. As a catalyst for the endothermic reaction, 3 to 4 mg of iron powder are located in the tubes. The catalyst is chemically cleaned before the graphitization by oxidizing with ambient air and subsequent two-fold reduction with hydrogen gas at 400°C . Once the reactors are loaded, the reactors are heated to 575°C over 3 to 4 hours until the pressure in the reactor no longer decreases. During the reaction, the CO_2 is converted to CO and subsequently precipitates as graphite (C) on the surface of the iron powder catalyst. After the reaction is finished, the compound of graphite and iron powder is stored in glass tubes until the eventual measurement on the AMS.

4.2.3 AMS measurement

The AMS measurements for this study are carried out on the MICADAS AMS at Curt-Engelhorn-Center Archaeometry (CEZA) in Mannheim, Germany. The measurement procedure and AMS facility is described in detail in section 3.2.3. For the measurements the iron-graphite compound is pressed mechanically into metal targets and inserted into the Cs^+ ion source of the mass spectrometer.

To calibrate the measured $^{14}\text{C}/^{12}\text{C}$ ratios and thus to obtain reliable radiocarbon dates, standards and blanks are measured in an alternating pattern with actual samples during a measurement schedule. Oxalic-acid II standards are used for calibration and the measured ratios are corrected for background and contamination obtained from blanks in the sample magazine.

4.3 Results and analysis

This section focuses on the characterization with multiple blank and carbonate standard measurements. Also, an overview of the radiocarbon dates of stalagmite paleoclimate archives is given, that were measured on the new extraction line.

4.3.1 Blanks

The limiting factor for radiocarbon measurements towards higher ages is the detection limit of the utilized measurement method. For MICADAS AMS, this limit is typically in the area of 49 000 to 51 000 yr, determined by the lowest $^{14}\text{C}/^{12}\text{C}$ ratio which can still be significantly distinguished from the machine background (Kromer et al. 2013). In addition to machine background, external contamination of the samples can limit the maximum age range where radiocarbon is still reliably detectable.

The quantification of both machine background and sample contamination is achieved by processing and measuring blanks along with the other samples. For radiocarbon measurements, these blanks generally consist of carbonous materials that do not contain measurable ^{14}C amounts, due to their age. It is preferable to choose the blank material as similar as possible to the sample material of interest, i.e. calcite (stalagmites, corals etc.) or organic material. This ensures that samples, as well as blanks, are treated the same in the course of chemical preparation and measurement. Systematic errors in the background correction can thereby be minimized. Potential sources of contamination during sample preparation include ambient air, (organic) residuals on the samples due to insufficient cleaning and memory effects from previous samples.

For the new extraction setup, numerous blanks were measured after the installation to characterize its performance and to exclude memory effects and contamination in the

Table 4.1: Measured AMS pseudo radiocarbon activity for different blank materials. For WM2 piece samples, the uncertainty does not represent the standard deviation of a whole data-set, but only of the individual measurement.

blank	form	N	^{14}C activity pmC	^{14}C age yr
IAEA C1	piece	9	0.167 ± 0.042	$51\,379 \pm 2018$
marble	piece	35	0.213 ± 0.077	$49\,536 \pm 5029$
WM2	piece	1	$0.146 \pm 0.010^*$	$52\,469 \pm 543^*$
all	piece	45	0.203 ± 0.074	$50\,364 \pm 2974$
marble	powder	28	0.209 ± 0.059	$49\,552 \pm 2275$
WM2	powder	7	0.190 ± 0.044	$50\,321 \pm 1853$
all	powder	35	0.206 ± 0.057	$50\,050 \pm 2450$

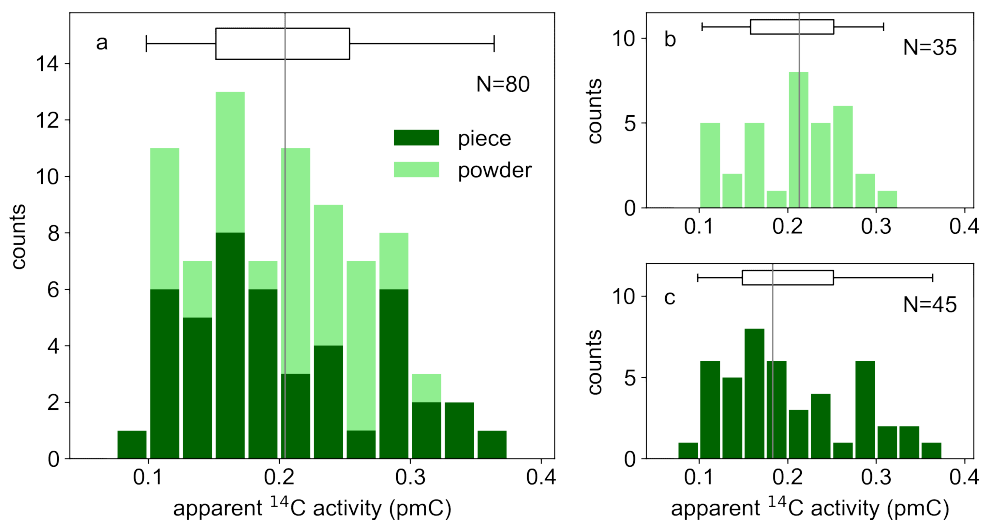


Figure 4.3: Histogram of blank samples measured since the installation of the new extraction line. A total of 80 blanks were processed, the distribution of all measured ^{14}C activities is shown (a), additionally the histograms for powdered (b) and piece (c) samples. The boxplots on top of the histograms depict the statistical distribution with the median highlighted by the line.

new line. Since most samples processed in the setup are calcite, the most commonly utilized blank material is taken from a marble block (age $\gg 50\,000$ yr) or a stalagmite with known U-series ages older than the detection limit of radiocarbon dating. Other blanks were taken from the IAEA C1 international standard which was produced from crushed Carrara marble. The blank measurements are quantified by their pseudo radiocarbon age or activity (without background correction). Eighty blank samples were prepared since the installation of the new extraction line, approximately half of them as powdered samples which were taken with a hand drill, the other half as cut solid pieces. The distribution is seen in Figure 4.3.

The overall distribution shows that in terms of apparent ^{14}C activity, the blanks range between 0.099 pmC and 0.364 pmC, with a mean of (0.204 ± 0.067) pmC and a median activity of 0.204 pmC. Considering the distinction between powdered samples and cut pieces of blank material, the powdered samples seem rather uniformly distributed around their mean value (0.206 ± 0.057) pmC. While the mean of cut samples is quite similar at (0.203 ± 0.074) pmC, the distribution less uniform with a median at 0.183 pmC. Disregarding the single WM2 piece sample, the most reliable blank material with both lowest apparent activity and smallest statistical variation is the international IAEA C1 standard. Although this type of blank produces the lowest amount of ^{14}C counts in the AMS, it is recommended that the blank be selected with respect to the investigated samples to account for possible contamination during sample preparation. However, the IAEA C1 blank is best to be used as a means to quantify the background performance of the preparation setup. An itemized list of the various blanks is given in Table 4.1.

4.3.2 International standards

The calibration of the AMS measurement is achieved by assigning the literature value of the oxalic acid II standard (134.07 pmC, Stenström et al. 2011) to the weighted mean of the measured $^{14}\text{C}/^{12}\text{C}$ ratio. By subtracting the average ratio of the blank samples, the background is determined and subtracted from all samples (Wacker et al. 2010b). In theory, by assigning isotope ratios to these two fixed points a comprehensive evaluation of radiocarbon ages to all samples is possible. To recognize and avoid systematic errors in the calibration of the ultimate radiocarbon age calculation, radiocarbon standards are measured together with the other samples. The international carbonate standard IAEA C2 provided by the International Atomic Energy Agency has a consensus radiocarbon activity of (41.14 ± 0.03) pmC and (-8.25 ± 0.31) ‰ VPDB for $\delta^{13}\text{C}$. Significant deviations of the measured data would point out systematic errors in the measurement or extraction procedure.

A total of 55 measured C2 samples is considered for this study, of which 33 were prepared on the new carbonate extraction line whereas the other 22 are the most recent ones from previous preparation routines in the Heidelberg ^{14}C lab. A graphic evaluation of the IAEA C2 measurements is given in Figure 4.4. The mean value and standard deviation of C2 samples measured on the new setup is at (41.058 ± 0.225) pmC ($N = 33$), compared to previous measurements at (40.704 ± 0.502) pmC ($N = 22$). Thus, after the implementation of the new carbonate preparation setup, the mean measured activity is closer to the literature value of (41.14 ± 0.03) pmC and reproducibility has improved from 1.23 to 0.547 %.

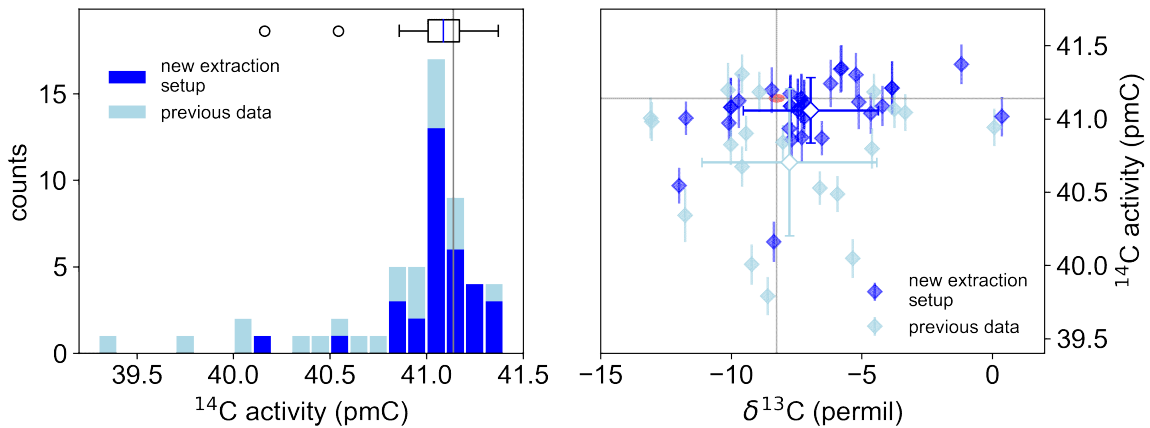


Figure 4.4: Histogram of measured IAEA C2 samples (left) and distribution of AMS measured ^{14}C vs. $\delta^{13}\text{C}$ (right). Light blue denotes measurements carried out on the old setup. Dark blue are samples measured on the new extraction line. The vertical line represents the respective consensus values as given by the IAEA. Statistical evaluation of the new data is given by the boxplot on top of the histogram with the median at 41.09 pmC.

Even though the results from the old setup were already in agreement with the assigned values, the new extraction line has significantly improved the data reproducibility for IAEA C2. The ^{14}C activity distribution is now far more symmetrical and low extrema do not occur as frequently.

There are several causes for high deviations from the consensus value. For instance, if the subtracted blanks of the measurement run were significantly higher in activity than normal, this would point to a contamination source at some point of the chemical preparation. However, if that contamination did not affect the C2 samples in the same manner, the background correction would cause systematically lower activities across the entire scale. Thus, a narrower distribution points to both higher C2 reproducibility and a lower level of contamination on the new setup.

4.3.3 Efficiency of carbonate sample extraction

In section 4.1.2 the reaction efficiency η_{extr} was introduced as the ratio of measured pressure in the calibration volume over the expected pressure, depending on the input mass, as described by eq. (4.6).

Reasons for the reaction efficiency to be < 1 include the loss of CO_2 gas due to leakage in the extraction setup. The main cause of a low efficiency is incomplete reaction of the initial carbonate sample with the added hydrochloric acid. This effect is especially prominent in powdered carbonate samples as opposed to piece samples. In Figure 4.5 the data set of this study is shown depicting efficiency over sample mass.

The discrepancy between powdered and piece samples becomes clear when the histograms are considered. For powdered samples, the mean efficiency is at $(88.28 \pm 10.03)\%$, with the median at 91.47% . Here, the distribution is relatively unsymmetrical with a distinct tailing towards low efficiencies and a minimum value of $\eta_{\text{extr, min}} = (63.45 \pm 2.93)\%$. For samples in solid form, the mean efficiency is $(99.58 \pm 4.96)\%$. The distribution is far more symmetrical and the median at 99.65% is virtually the same as the mean value.

The effect of a reduced average extraction efficiency is caused by the increased reaction speed of HCl with powdered material as opposed to solid pieces. Once the hydrolysis agent is poured on the calcite powder in the evacuated sample container the complete reaction takes place almost instantaneously and the material is catapulted upwards by the emerging gases. There, it partially adheres to the inner walls where the acid can no longer reach it and it remains in carbonate form.

Since adhesive forces in the glass tubes are not as strong for larger pieces as they are for small powder particles, this effect generally does not occur for piece samples. Therefore, solid pieces of carbonate are preferred for the extraction process, although for some samples it is not possible to cut or saw pieces, for example if a very precise sampling along a growth layer is required. Cut pieces are also less prone to contamination by CO_2 in the ambient air due to their reduced surface area. Moreover, the sampling of powdered material always involves a high probability of contamination by the used drilling bits due to the high temperatures occurring during the drilling.

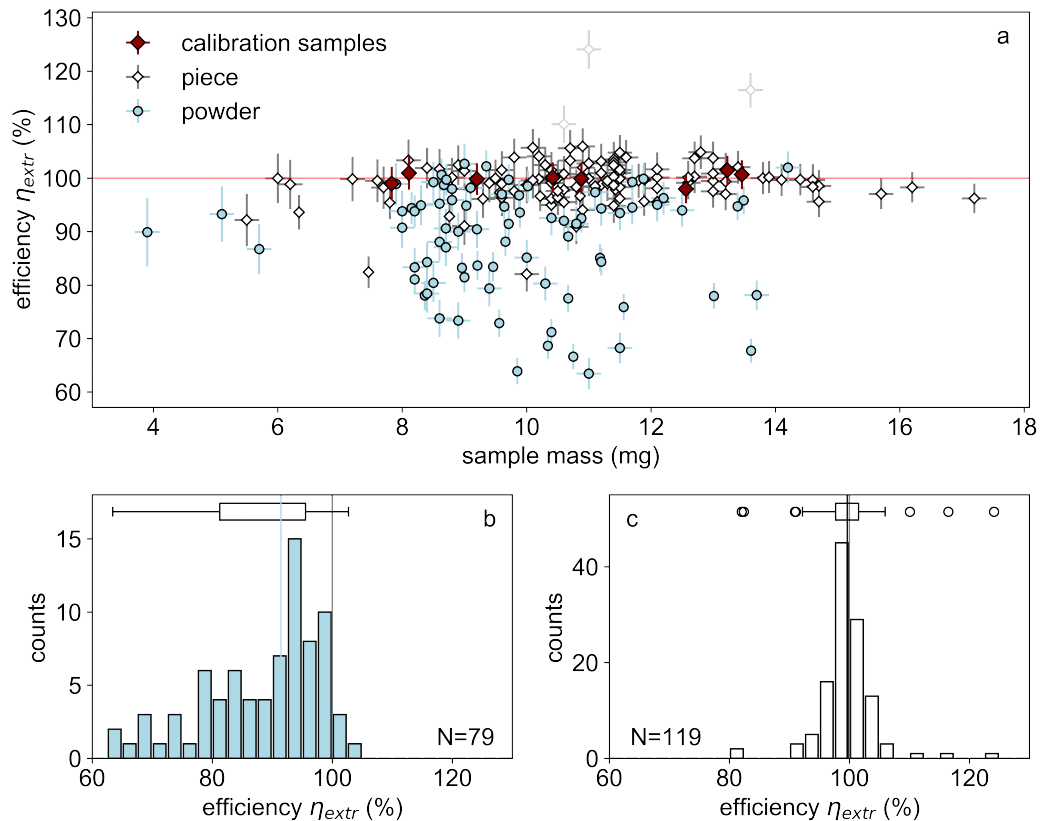


Figure 4.5: Efficiency assessment of the new carbonate extraction line. The efficiency is calculated by comparing the measured pressure in the calibration volume to the expected pressure calculated by Equation (4.3). The upper plot (a) shows the set of carbonate samples prepared since its installation. The clear difference between powdered and piece samples is clarified by the histograms below (b, c).

4.3.4 Radiocarbon dating of paleoclimate archives

The purpose of the construction of the new extraction line was to create the best possible prerequisites for high-precision radiocarbon measurements of carbonate samples. A special focus here lies on environmental archives of past and present climates. Radiocarbon has a half-life of $T_{1/2} = 5730$ yr and thus provides a powerful tool for climate reconstruction of the last 50 000 yr.

Especially for periods going back further than 30 000 yr, towards the detection limit of radiocarbon dating, high precision and data reproducibility are required for the sample preparation and measurement process. With the new extraction setup and the previously outlined characterizations, the sample preparation lines together with a MICADAS AMS are a powerful combination for high-precision and reproducible ^{14}C measurements of paleoclimate archives.

On the newly established setup, several studies were conducted on terrestrial climate

archives, especially on speleothem samples from various climatic origins. The research interest here lies on the effects of climate change on the incorporation of radiocarbon in the stalagmite carbonate. Due to the interplay of atmospheric CO_2 and limestone carbonate during the formation of stalagmites, the discrepancy of atmospheric and stalagmite radiocarbon age at the time of formation (radiocarbon reservoir age) is considered for investigations of the carbon cycle or of climatic change.

More than 260 speleothem subsamples from six different stalagmites were prepared and measured according to the procedure laid out in Section 4.2. In addition to the radiocarbon measurements, U-series dating or relative age determination by layer counting was performed to obtain an adequate age model. The six samples investigated over the past years cover an age range from modern times to more than 40 000 yr before present (see Table 4.2).

In Figure 4.6, all speleothem ^{14}C results are combined in one graph in terms of initial $\Delta^{14}\text{C}$, i.e. corrected for the physical decay of ^{14}C since the time of initial carbonate precipitation in the respective cave. Thus, the results can directly be put in context to the atmospheric radiocarbon level at that time to assess the radiocarbon reservoir and its potential climatic controls.

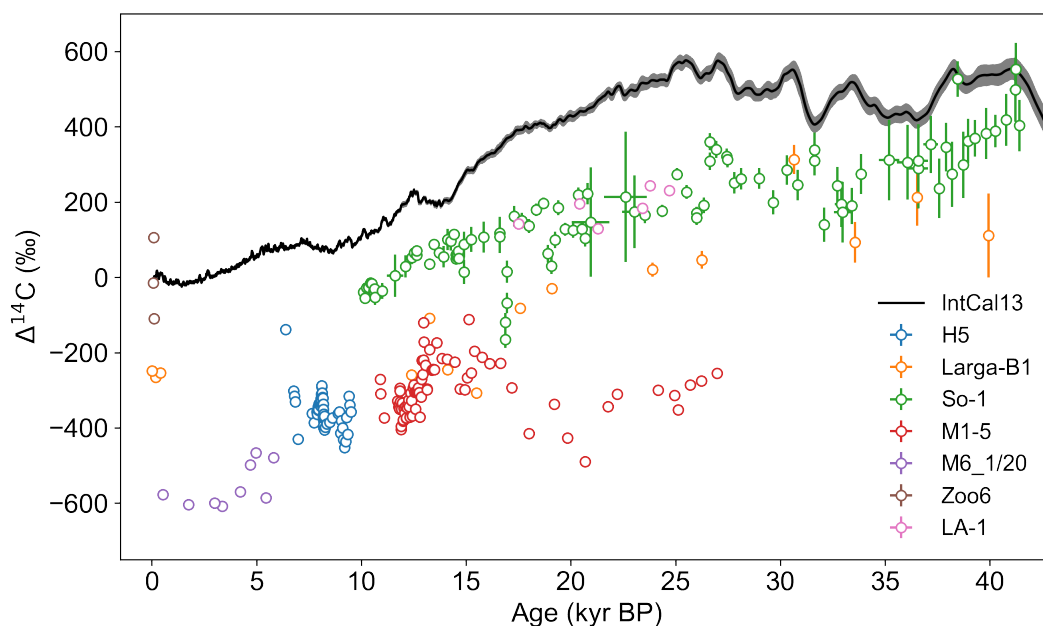


Figure 4.6: Combined plot of all radiocarbon analyses performed on various speleothem samples. All data that was produced with the extraction setup in the Heidelberg lab is shown in terms of $\Delta^{14}\text{C}$ vs. the U-series date that was obtained by direct measurements at the same depth or age vs. depth modeling. The atmospheric reference refers to IntCal13 (Reimer et al. 2013).

Table 4.2: List of stalagmite samples of which radiocarbon measurements were performed in the Heidelberg ^{14}C lab with the newly established extraction line. Given are sample name and origin, the number of obtained radiocarbon dates (N) the range of measured initial $\Delta^{14}\text{C}$ (i.e. at time of stalagmite deposition).

Sample	Location	N	age yr BP	$\Delta^{14}\text{C}_{\text{init}}$	
				min	max
H5	Hoti Cave, Oman	57	6380–9500	-452	-138
So-1	Sofular Cave, Turkey	111	10160–41490	-166	510
Larga-B1	Cueva Larga, Puerto Rico	15	180–39940	-307	313
M1-5	Moomi Cave, Socotra	78	10900–27000	-489	-112
M6_1/20	Schratten Cave, Switzerland	9	525–5805	-608	-466
Zoo6	Zoolithen Cave, Germany	3	60–100	-109	106
LA-1	Cueva Larga, Puerto Rico	6	17510–24710	130	243

The data of stalagmite So-1 show a relatively small reservoir age (i.e. shift between atmospheric and stalagmite radiocarbon) between 10 000 and 41 500 yr BP, whereas the data from M6_1/20, H5 and M1-5 indicate a rather large reservoir age. The So-1 data from stalagmite So-1 (Sofular Cave, Northern Turkey) will be discussed in great detail in Chapter 6. In case of the M1-5 record, the discrepancy between atmosphere and stalagmite ^{14}C is explained by high input of aged soil organic matter and an increased share of dead carbon from limestone dissolution at the site on Socotra Island (Therre et al. 2020). Similar effects might explain the low $\Delta^{14}\text{C}$ of H5 from Oman. In case of the sample M6_1/20 from Schratten Cave, an additional input of dissolved limestone by sulfuric acid is suggested, which causes systematically low $\Delta^{14}\text{C}$ values. The modern Zoo6 sample has grown amidst the anthropogenic increase of atmospheric radiocarbon following the extensive nuclear bomb testing until 1963.

The combined record of stalagmite samples shows that the newly established radiocarbon preparation line can be reliably used for paleoclimatological investigations of carbonate samples. The combination of sample preparation in Heidelberg and measurement at the MICADAS AMS in Mannheim has proven to be successful.

4.4 Conclusion

A new radiocarbon extraction line for carbonate samples was established at the Heidelberg Radiocarbon Lab at the Institute of Environmental Physics. The characterizations by multiple blank and international standard measurements have proven that contamination levels are sufficiently low to perform measurements approaching the detection limit of radiocarbon dating.

Moreover, the reproducibility of IAEA C2 measurement has significantly increased. In the first years, several samples were investigated, in particular from seven stalagmites originating from different climate zones. The measurements have demonstrated that the

combination of new extraction setup and AMS analysis provide perfect prerequisites for the advancement of climate research by using radiocarbon dating in many future studies.

Part III

Radiocarbon in Stalagmites: Indicator of Climate Variability and Key to Atmospheric ^{14}C Reconstruction

5 Climate-induced Speleothem ^{14}C Variability on Socotra Island

The following chapter is a case study of radiocarbon as a climate-tracer in speleothems. The dead carbon fraction (DCF) of stalagmite M1-5 from Moomi Cave on Socotra Island in the western Arabian Sea was assessed through a new set of high-precision U-series and ^{14}C dates. The data for this study were collected in the course of a Master's thesis which included a preliminary qualitative paleoclimate interpretation (Therre 2016). In the course of this dissertation, that first approach was further developed and substantiated through quantitative analysis. The record was subsequently put into a paleoclimate context and the significant novel aspects of its interpretation were investigated and elaborated. This allowed the subsequent peer-reviewed publication of the study (Therre et al. 2020). The analysis reveals an extreme case of very high and also climate-dependent DCF. This indicates a high influence of aged soil organic matter (SOM) and nearly completely closed-system carbonate dissolution conditions. The study highlights the influence of a changing climate on stalagmite ^{14}C by pointing out how changing humidity and infiltration affects vegetation density and, thus, carbon cycling. Very high DCF values proved a high input of aged soil organic matter during the LGM, whereas dynamic soil processes dominated in the Younger Dryas with vast sub-centennial DCF variations. This is of particular relevance for speleothem studies that aim to reconstruct past atmospheric ^{14}C (e.g., for the purposes of ^{14}C calibration), as these would rely on largely climate-independent soil carbon cycling above the cave.

The following chapter is a shortened summary of the article “Climate-induced speleothem radiocarbon variability on Socotra Island from the Last Glacial Maximum to the Younger Dryas” (Therre et al. 2020), published in the peer-reviewed journal *Climate of the Past*. Unless otherwise indicated, the figures are not changed from those in the original publication.

5.1 Introduction

The published article (Therre et al. 2020) focuses on the climate-induced variability of speleothem radiocarbon, which was investigated on stalagmite M1-5 from Moomi Cave on Socotra Island.

The expansion of radiocarbon calibration to older ages laid high focus on stalagmites as potential contributors to help constrain the reconstruction of atmospheric $\Delta^{14}\text{C}$. Several studies have successfully proven that stalagmites can provide precise, high-resolution data for these purposes (Beck et al. 2001, Hoffmann et al. 2010, Southon et al. 2012, Cheng

et al. 2018) and were included into inter-calibration data-sets like Reimer et al. (2013). A key to perform atmospheric reconstruction is the understanding of carbon cycling above the cave. So far, only speleothems with reasonable constant and low DCF could be used in this effort. However, such a situation is unusual, as significant impacts on DCF can arise from carbonate dissolution or climate and carbon cycle changes. By combining ^{14}C dating and elemental Mg/Ca analysis, a connection between precipitation (net infiltration) and stalagmite DCF was observed. Several studies attributed this relation to changes in open- vs. closed-system conditions of limestone dissolution, which controls the contribution of very old host rock carbonate to drip water dissolved inorganic carbon (DIC) (Griffiths et al. 2012, Noronha et al. 2014). In other studies, the influence of aging soil organic matter (SOM) on stalagmite DCF was assessed, and a connection between depleted soil gas $^{14}\text{CO}_2$ and higher DCF was found (Fohlmeister et al. 2011a, Rudzka et al. 2011). In cases of extremely high DCF above 50 %, the influence of sulfuric acid on enhanced limestone dissolution could be shown (Bajo et al. 2017).

This study presents a fast-grown stalagmite which documents the climate transition from the Last Glacial Maximum into the emerging Holocene in a geographical setting influenced by the East African–Indian monsoon (Shakun et al. 2007, Fleitmann et al. 2007). Stable-isotope data from this speleothem were adapted from a previous study (Shakun et al. 2007). Together with a new set of U-series dates and a detailed age-depth-model, as well as high-precision ^{14}C dates and elemental Mg/Ca ratios, a comprehensive climate record was established. This study documents how increasing moisture on Socotra Island through the ending glacial is associated with decreasing DCF. It proves that the input of $^{14}\text{CO}_2$ into the soil zone through denser vegetation above the cave is the determining factor for soil carbon cycling above Moomi Cave.

5.2 Sample and methods

5.2.1 Socotra Island and stalagmite M1-5

Socotra Island is located in the western Arabian Sea, roughly 250 km east of the Horn of Africa (Somalia) and 380 km south of the Arabian Peninsula. It is approximately 130 km long and 30 km wide. Its topography varies from coastal plains in the north and south of the island to elevated plateaus several hundred meters above sea level (m a.s.l.). The innermost part of the island consists of a mountainous area with elevations of up to 1500 m a.s.l. (Figure 5.1 c). The archipelago is mainly made up of Precambrian basement rocks that are in part overlain by Cretaceous or Tertiary plateau limestone (Schlüter 2008). The maritime climate of Socotra Island is influenced by the East African–Indian monsoon system. The Intertropical Convergence Zone (ITCZ) migrates across the Island biannually between its Northern Hemisphere winter and its summer position (see Figure 5.1 a,b), causing the bimodal distribution of precipitation with high levels in April/May and October to December (Shakun et al. 2007). The total amount of modern climate precipitation ranges from 67 mm/yr near the coastal plains, to more than 500 mm in the inner highlands (Scholte and De Geest 2010).

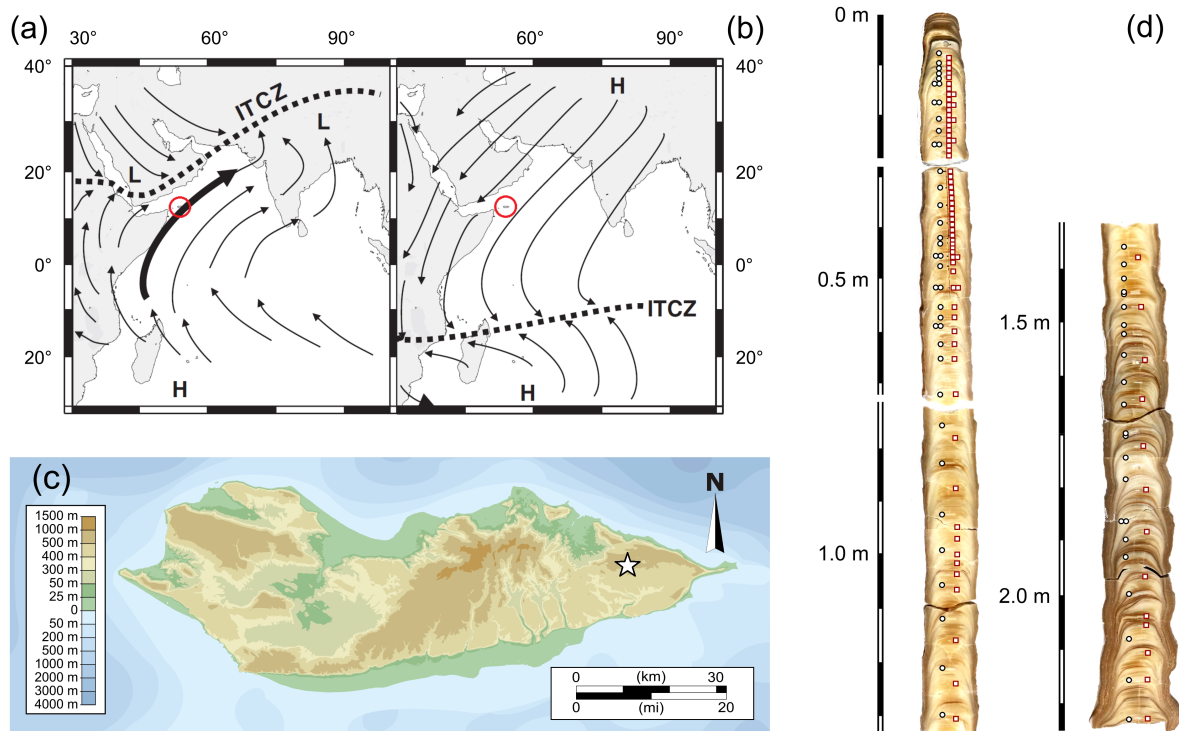


Figure 5.1: Fig. (a) and (b) show the geographic position of Socotra Island (red circle) with the prevailing monsoonal surface wind patterns in boreal summer (a) and winter (b) relative to the Intertropical Convergence Zone (ITCZ) (graphic adapted from Fleitmann et al. 2007). In a topographic map (c), the position of Moomi Cave in the east of the island is indicated by a white star. A composite photograph of stalagmite M1-5 (d) indicates where U-series dating samples (black circles) and ^{14}C dating samples (red squares) were taken. Combined figure, adapted from (Therre et al. 2020).

Stalagmite M1-5 was collected from Moomi Cave in 2002, which lies on a limestone plateau (Moomi Plateau, ca. 500 m a.s.l.) in the eastern part of the island ($12^{\circ}32'4''\text{N}$, $54^{\circ}19'0''$; Figure 5.1 c). Moomi Cave is approximately 1 km long, largely horizontal, and overlain by 20 m of bedrock (Burns et al. 2003). Stalagmite M1-5 (Figure 5.1 d) is approximately 2.2 m long and 10 to 15 cm wide and grew roughly 1 km from the cave entrance. The lower part of the stalagmite from its base to approximately 1.5 m distance from the top shows distinct changes in layer coloring and is wider than the upper part.

5.2.2 Measurement techniques

The measurement techniques used for this study are described in detail in Chapter 3. For further information on the particular methods, the reader is referred to the respective sections in that chapter.

Forty U-series dating samples were analyzed at the Heidelberg Institute of Environmental Physics on a Thermo Fisher Neptune Plus MC-ICP-MS, following the procedures described

in Douville et al. (2010), Arps (2017), Wefing et al. (2017). M1-5 was previously U-series dated at the Isotope Geology Laboratory, University of Bern. In total, 62 age data points are presently available, in addition to the previous age determination efforts by Shakun et al. (2007).

A total of 78 stalagmite ^{14}C measurements were performed on stalagmite M1-5, including 6 duplicates for which all steps including the subsampling, preparation, and measurement were repeated. Sampling and chemical preparation (CO_2 extraction, graphitization) was performed at the Heidelberg Institute of Environmental Physics, the AMS measurements were conducted at the 200 kV tandem MICADAS (mini carbon dating system) at the Curt-Engelhorn-Centre Archaeometry gGmbH in Mannheim, Germany (Synal et al. 2007, Kromer et al. 2013). Process blanks were prepared yielding apparent blank activities consistently lower than 0.25 pmC (apparent blank ^{14}C ages of 48 to 56 kyr). Oxalic Acid II standards were used for calibration and IAEA C2 international ^{14}C standards were measured to exclude systematic errors.

The Mg/Ca ratio measurements were performed at the Institute of Environmental Physics at Heidelberg University using a Thermo Fisher iCAP Q inductively coupled plasma quadrupole MS (ICPQMS), while data were also collected at the Institute of Earth Sciences at Heidelberg University using an ICP optical emission spectrometer (ICP-OES) 720. Further information on the measurement can be found in (Warken et al. 2018). Comparability of the results from both setups was ensured by normalizing the Mg/Ca ratios with respect to a series of internal standard measurements that were carried out in both laboratories.

5.3 Results

5.3.1 U-series dating

U-series dating revealed ^{238}U concentrations ranging from roughly 700 to 2900 ppb and ^{232}Th concentrations between ca. 15 ppt and 21 000 ppt. The determined ^{230}Th corrected ages reveal a stalagmite growth from (27.11 ± 0.20) kyr BP to 10.890 ± 0.034 kyr BP and the relative uncertainty of the age data range from 0.2 to 1.0 %. The resulting chronology shows no major outliers and is characterized by a high data resolution. It therefore significantly refines the previously published chronology by Shakun et al. (2007). Age–depth modeling was performed using a stepwise implementation of StalAge (Scholz and Hoffmann 2011) between the resolved growth discontinuities. The growth rate of stalagmite M1-5 is fairly constant during the last glacial termination as well as during the interstadials from approximately 17.2 to 11.7 kyr BP at an average growth rate of roughly 0.23 mm/yr. A distinct 800-year hiatus was identified at 110 mm (from top) from 11.7 to 10.9 kyr BP (henceforth referred to as discontinuity “D1”). Above this hiatus, the stalagmite growth continued at a high rate of approximately 0.30 mm/yr for a short period at the beginning of the Holocene. For the older part of the stalagmite, a lower growth rate is observed: from 27.2 to 17 kyr BP, the average rate is 0.086 mm/yr with another 1200-year-long hiatus after 23.5 kyr BP (discontinuity “D2”). The overall rate of approximately 0.130 mm/yr

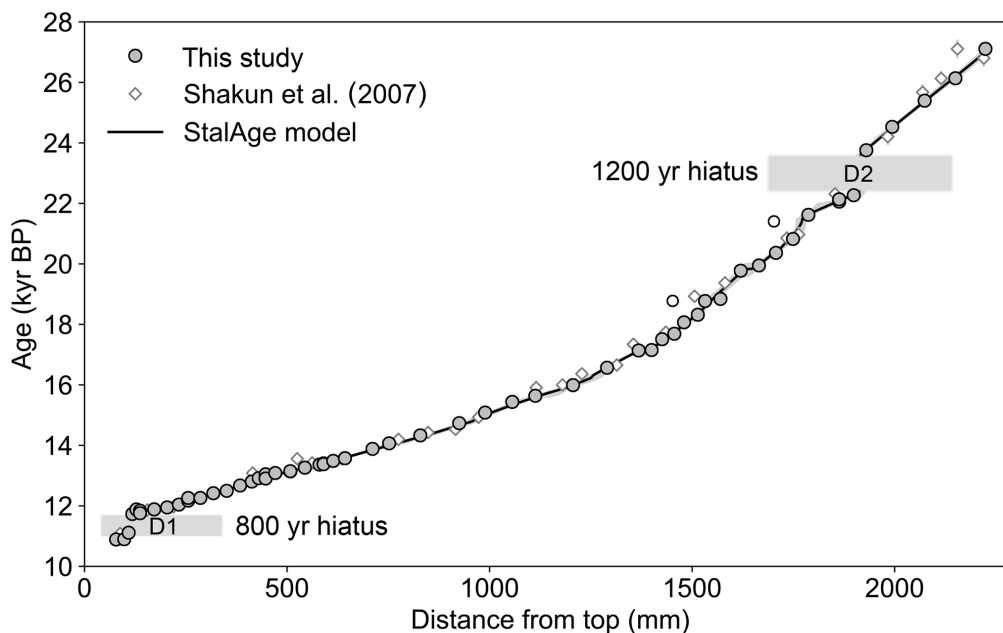


Figure 5.2: U-series ages vs. depth. Error bars reflect 2σ statistical uncertainty but are mostly covered by the data points. The solid line represents the established age model obtained by sectional implementation of the StalAge algorithm (Scholz and Hoffmann 2011). Two data points implying age inversions (empty circles) in an otherwise steady record were omitted. Diamonds represent data from a previous study (Shakun et al. 2007). Growth discontinuities D1 and D2 are highlighted by gray bars.

between 27.2 and 11 kyr BP implies a high temporal resolution. $\delta^{234}\text{U}_{\text{init}}$ of stalagmite M1-5 is consistently below zero with minimal values of around -130‰ , which implies a strongly leached and subsequently host rock. The isotopic signature increases from the ^{234}U -depleted LGM roughly 21 kyr BP towards the Bølling–Allerød warm period (-25‰ , ca. 21 kyr BP) where the growth rate is significantly higher.

5.3.2 Radiocarbon dating

The measured ^{14}C activities ($a^{14}\text{C}_{\text{meas}}$) range between the maximum (19.52 ± 0.20) pmC and the lowest value of (2.846 ± 0.035) pmC. The total uncertainty of ^{14}C activities is calculated as the square root of the squared sum of the statistical error from the measurement and the overall reproducibility, deduced from the long-term measurement of the IAEA C2 standard. By using the age-depth-model the initial ^{14}C activity at the time of calcite deposition can be determined, revealing a large offset between atmospheric ^{14}C concentration (Reimer et al. 2013) and initial ^{14}C levels in the stalagmite. The conversion of radiocarbon ages/activities into reservoir ages and DCF is detailed in Section 3.2.4.

For stalagmite M1-5, DCF values range from (27.33 ± 0.24) % at ca. 13 kyr BP to (64.6 ± 1.1) % at 20.7 kyr BP (Figure 5.3). The M1-5 DCF record shows very high values

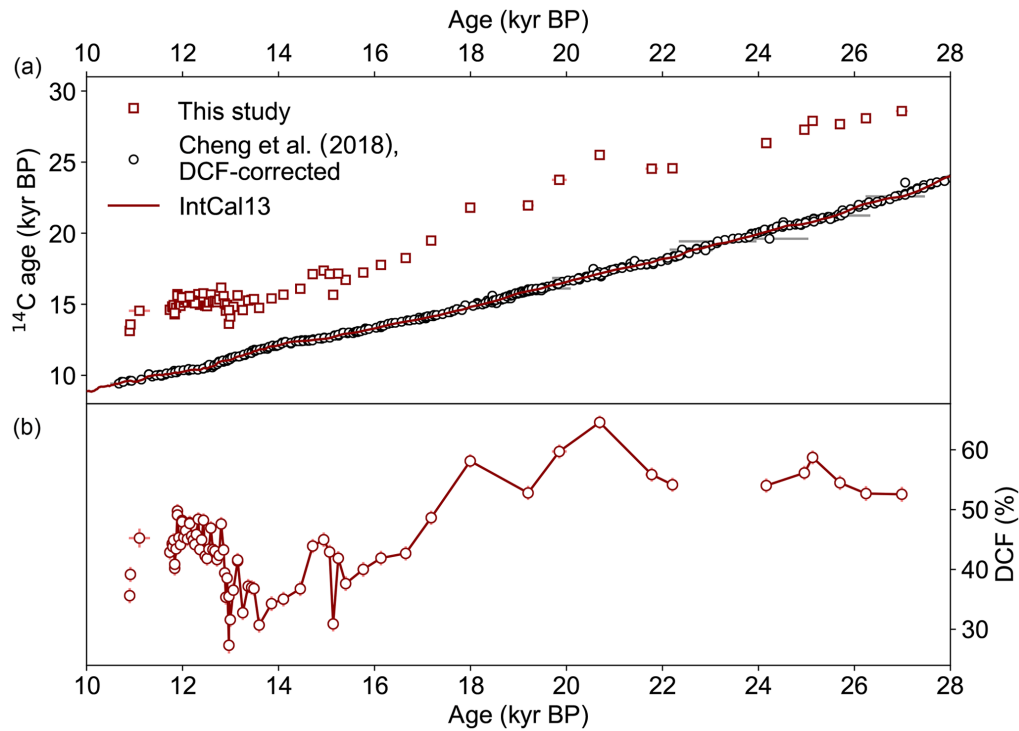


Figure 5.3: Upper graph (a) shows the ^{14}C ages of stalagmite M1-5 (red squares) plotted vs. modeled age. Error bars are mostly smaller than symbol size. Also shown is the atmospheric ^{14}C age (solid red line) from Reimer et al. (2013), with the DCF-corrected stalagmite record from Cheng et al. (2018). The DCF of stalagmite M1-5 is shown in (b).

before 18 kyr BP and a decreasing trend towards lower DCF values until 13 kyr BP. The following period between 13 and 11 kyr BP is characterized by higher, and highly variable, DCF values of between 40 and 50 %, and these values exhibit rapid fluctuations on decadal timescales as seen in a 9 % drop in a time interval of only 60 years modeled age at approximately 11.9 kyr BP.

5.3.3 Mg/Ca ratio

Mg/Ca ratios range from roughly 0.011 to 0.032 and display a continuous decrease from 22 to 12 kyr BP. After this decrease, a sharp rise by a factor 3 is observed around D1. The ratio then drops back to the level measured before the major excursion.

5.4 Discussion

5.4.1 U-series dating and age–depth model

In comparison to the previous study by Shakun et al. (2007), the revised chronology is far more precise and has a much higher data-resolution. The average relative data-uncertainty was more than halved to (0.408 ± 0.161) %. Two unresolved growth discontinuities were disclosed by the new data.

The age model reveals that the growth rates in the younger part of the stalagmite are roughly a factor 2 higher than during the last glacial period. The change in vertical accumulation rate can be seen by mere optical examination of the stalagmite lamination. The calcite layering in the upper segment is less distinct and the color is lighter. Synchronously, the width of the stalagmite decreases gradually from more than 15 cm at the base to less than 10 cm near the top (see Figure 5.1 d), where the growth rate is highest. Studies on stalagmite growth modeling (Dreybrodt 1999, Kaufmann 2003, Kaufmann and Dreybrodt 2004) found that higher drip rates and higher temperatures cause an increase in stalagmite diameter and growth rates. Rising temperatures on Socotra Island at the end of the last glacial period was postulated by Shakun et al. (2007), and a parallel precipitation increase will be discussed in Section 5.4.3. However, the width of the stalagmite is smaller in a time of most likely increased drip rates, which contrasts with the aforementioned studies. Nonetheless, the times of highest growth rates correlate with both increasing precipitation and temperatures.

5.4.2 DCF and implications for radiocarbon calibration

The dendrochronological atmospheric ^{14}C records till 12.4 kyr BP and the wiggle-matched floating late glacial pine tree-ring chronology go back to 14 kyr BP (Hua et al. 2009, Schaub et al. 2008). For this reference time, the atmospheric ^{14}C concentration is known with the highest accuracy in the IntCal13 record (Reimer et al. 2013). In this time frame, stalagmite M1-5 reveals high DCF variability regarding centennial and decadal timescales (from 27 % at ca. 13 kyr BP to 50 % at ca. 11.9 kyr BP). The sub-centennial DCF variability is in stark contrast to the IntCal13 stalagmite records. For instance, no comparable variability is visible in the Hulu Cave speleothem (Southon et al. 2012) and in the Bahamas record (Hoffmann et al. 2010).

Due to the high and variable DCF of stalagmite M1-5, it is not possible to reconstruct atmospheric ^{14}C concentration beyond the reference period. Although, for instance, the Hulu Cave speleothems originate from a comparable climatic setting (Southon et al. 2012, Cheng et al. 2018), the atmospheric ^{14}C signature is superimposed by site-specific carbon-cycling and limestone dissolution processes (Fohlmeister et al. 2011a, Griffiths et al. 2012). These climate-dependent factors can be investigated in this study.

5.4.3 Climatic controls of DCF at Moomi Cave

The very high DCF values during the last glacial period between 18 and 27 kyr BP with an average (56.2 ± 3.4) % (maximum of 65 %), strongly indicate closed-system limestone-dissolution conditions (Hendy 1971). However, considering only the two carbon end-members from near-atmospheric soil gas CO_2 and the ^{14}C -free carbonate from dissolved limestone, DCF values of 50 % are the theoretical maximum (Hendy 1971, Fohlmeister et al. 2011a, Griffiths et al. 2012). Non-organic (sulfuric) acids in the soil zone can be responsible for enhanced levels of DCF in stalagmites, as it was recently reported in a case study from Corchia Cave, Italy (Bajo et al. 2017). In this case, the additional dead carbon input shifts the $\delta^{13}\text{C}$ towards more positive values, as observed in the limestone host rock, and stable carbon isotopes and DCF correlate. Since neither of these aspects prevails in stalagmite M1-5 (average $\delta^{13}\text{C}$ at 6.2 ± 1.4 ‰, correlation with DCF $r^2 = 0.206$, $p < 0.01$), it is unlikely that non-organic acids are the determining factor for DCF variations in stalagmite M1-5.

An alternative approach to explain high DCF levels is to consider aged SOM (Genty et al. 2001). ^{14}C depleted CO_2 from older carbon stocks and labile soil organic matter above Moomi cave, together with nearly closed-system karst dissolution conditions could result in $\text{DCF} > 50$ % (Trumbore 2009, Fohlmeister et al. 2011b). Several studies on the flora and soil characteristics of Socotra Island (Mies and Beyhl 1998, Popov 1957) provide evidence for the presence of (aging) organic matter in the soil above the cave. In an assumed extreme case with closed-system conditions, i.e. a baseline DCF of 50 %, before 18 kyr BP, an age of the active carbon pool of 2500–3000 years can generate DCF values between 63 % and 65 %. If the carbon pool is composed of one young (root respiration) and one old carbon reservoir (microbial decomposition of aged SOM) in equal proportions, the aged carbon reservoir must be older than 5000 years to cause such extreme DCF values. None of these scenarios have been reported before in a study on speleothem ^{14}C , which makes M1-5 a unique record in terms of aged SOM contribution to stalagmite DCF. All available geochemical proxies (shown in Figure 5.4) indicate that the LGM is manifested in this stalagmite by low net-infiltration levels and low precipitation (Shakun et al. 2007). This is in agreement with the study by DiNezio et al. (2018) who found a positive ocean–atmosphere feedback loop in the Last Glacial Maximum causing hydroclimate changes, i.e., reduced moisture levels in the Arabian Sea. Towards the end of the glacial period (20 to 15 kyr BP) the long-term decrease of the Mg/Ca ratio suggests the climatic conditions on Socotra Island likely shifted to a higher net infiltration. This interpretation is based on numerous studies (Fairchild and Treble 2009, Fairchild et al. 2000, Noronha et al. 2014, Flohr et al. 2017, Warken et al. 2018) that showed a negative correlation between Mg/Ca ratio in stalagmite calcite and precipitation amount.

The increasing but still negative values in $\delta^{234}\text{U}_{\text{init}}$ after 22 kyr BP point to a shift towards less leached host rocks or a stronger contribution of excess ^{234}U from the leached rocks Dreybrodt (1999). At the same time, the growth rate rises from below 0.10 to more than 0.20 mm/yr, suggesting that $\delta^{234}\text{U}_{\text{init}}$ correlates with infiltration changes. Infiltration and subsequently drip rate are positively correlated to stalagmite width (Dreybrodt 1999, Kaufmann and Dreybrodt 2004). This study contrasts those studies, since stalagmite

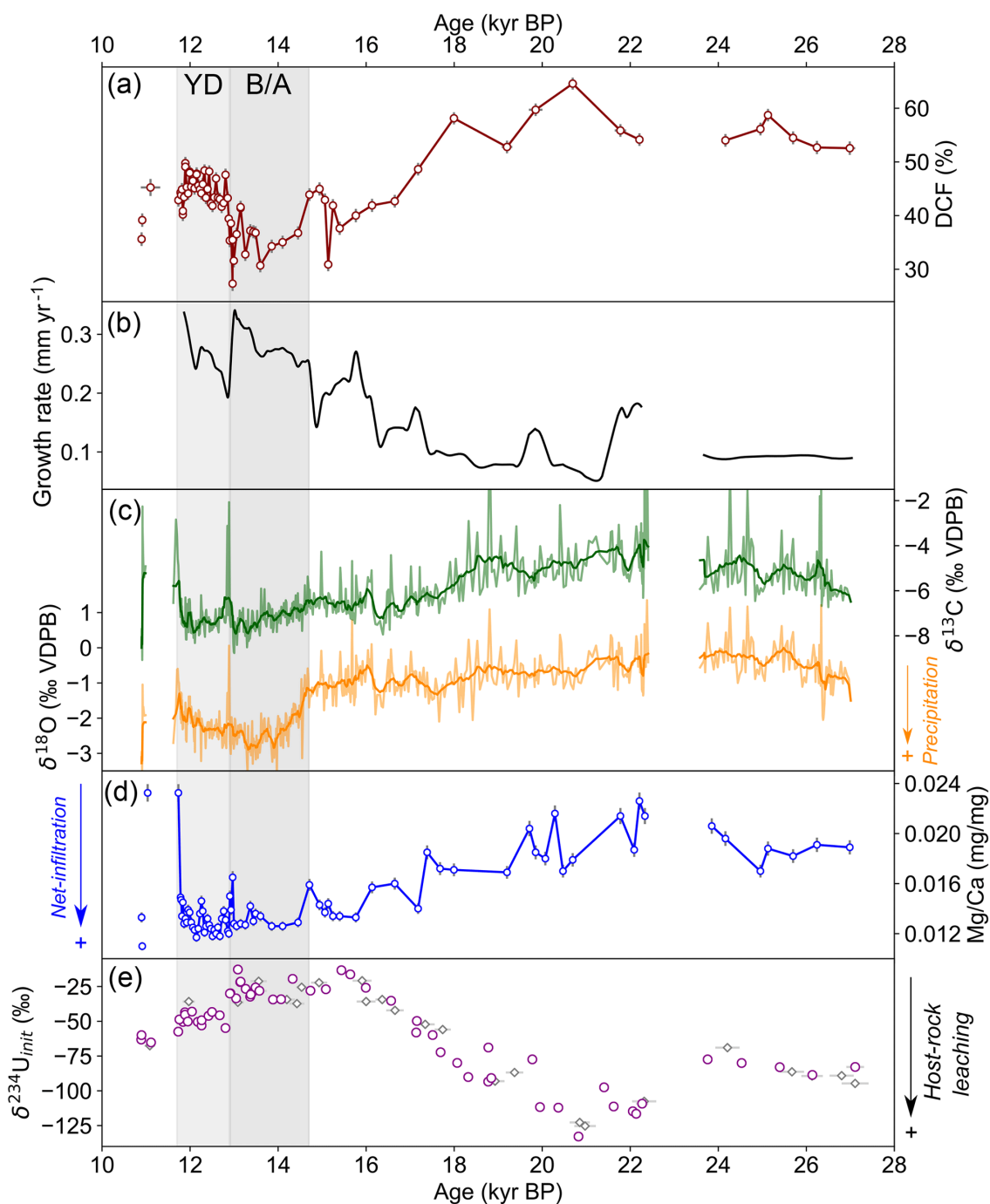


Figure 5.4: Combined results from stalagmite M1-5. DCF (a), growth rate from StalAge modeling (b), adapted stable isotope data from Shakun et al. (2007) (c), Mg/Ca mass ratio (d), and $\delta^{234}\text{U}$ from this study (violet circles) and Shakun et al. (2007) (gray diamonds) (e). The gray bars indicate Bølling–Allerød interstadial (B/A) and Younger Dryas (YD) cold reversal. Oxygen data and the Mg/Ca proxy show an increase in monsoonal rainfall over Termination I, where growth rate is highest. DCF decreases after the LGM but spikes at the onset of YD. $\delta^{18}\text{O}$ indicates an intensified monsoonal precipitation during the B/A (Shakun et al. 2007).

M1-5, decreases in width (see Figure 5.1 d) towards higher infiltration and 2 to 3.5 °C higher temperatures (Shakun et al. 2007).

The precipitation increase over Socotra Island after the LGM coincides with the steady southern hemispheric warming until 15 kyr BP, while $\delta^{13}\text{C}$ in M1-5 decreases by 2 ‰ revealing sub-centennial variability of the speleothem calcite composition. During the time of highly variable Northern Hemisphere climate from the warm and humid B/A to the cold and dry YD (Schulz et al. 1998, Ivanochko et al. 2005), $\delta^{13}\text{C}$ and Mg/Ca in M1-5 remain at low levels. $\delta^{18}\text{O}$ values show a 1.5 ‰ decrease across Termination I (20–11 kyr BP), occurring rather suddenly around 14.9 kyr BP. This was attributed to the amount effect (Dykoski et al. 2005, Griffiths et al. 2010), indicating a stronger rainfall towards the end of the glacial, in particular after 15 kyr BP (Shakun et al. 2007). While both stable isotopes share a common deglacial climate trend, they differ through the period from 19 to 14 kyr BP, indicating a dominant influence of vegetation above the cave, which affected $\delta^{13}\text{C}$ but not $\delta^{18}\text{O}$. Seasonal shifts towards more distributed rainfall may have increased the soil net infiltration without significant amount changes visible in $\delta^{18}\text{O}$ above Moomi Cave.

The inferred net infiltration increase after the LGM is not reflected in M1-5 ^{14}C data do, if the positive correlation of rainfall amount on stalagmite DCF is considered. This was postulated for more humid zones by Genty et al. (2001), Griffiths et al. (2012), Noronha et al. (2014), Lechleitner et al. (2016a). Instead, a less closed carbonate dissolution system together with enhanced ^{14}C levels in the soil gas CO_2 from root respiration seems to set in. Also, the contribution by CO_2 from the decomposition of aged SOM seems less significant. This decoupling of precipitation and DCF is evidence for a climate-induced forcing on stalagmite ^{14}C , which is to some extent decoupled from calcite dissolution systematics. It is conceivable that the vegetation in (semi)arid regions like Socotra Island (in contrast to temperate, more humid settings) is much more sensitive to small changes in net infiltration. Previous studies showed that an increased monsoonal activity during Termination I (Overpeck et al. 1996, Gupta et al. 2003, Shakun et al. 2007) can have dramatic effects on vegetation prevalence in arid and semiarid areas (Lotsch et al. 2003). An increase in soil CO_2 input by active vegetation above Moomi Cave triggered by higher net infiltration at the end of the last glacial is most responsible for the observed soil carbon dynamics with strongly lower DCF.

Consequently, we have traced a clear multimillennial increase in precipitation on the archipelago from the LGM to the 15 kyr BP Northern Hemisphere sudden warming, which is accompanied by major changes in soil activity and thus vegetation.

5.4.4 Glacial termination climate dynamics on Socotra Island

Subcentennial variability of DCF, $\delta^{234}\text{U}_{\text{init}}$, and Mg/Ca is resolved beyond the strong B/A warming. This indicates a strong local climate–monsoon coupling that is only resolved in the area with the highest temporal data density in the record. At approximately 13 kyr BP, the DCF abruptly jumps to values higher than 40 ‰, indicating sudden changes in soil carbon cycling. Singular events caused by climatic variations or wildfires can have a major influence on soil carbon dynamics (Trumbore 2009, Treble et al. 2016). In case of a

wildfire or landslide, the soil configuration may have changed and high CO₂ input to the soil zone was halted (Coleborn et al. 2016, Markowska et al. 2019), possible explaining the high DCF. All other proxies of M1-5 remain at virtually the same levels over this event. The high-resolution data from speleothem M1-5 (exemplified by DCF and Mg/Ca records in Figure 5.5) show vast sub-centennial DCF variability. The correlation of DCF and Mg/Ca in this period is insignificant ($r^2= 0.231$, $p < 0.01$). The high DCF volatility suggests a pronounced influence of local effects on the soil carbon dynamics on the Moomi Plateau. Other proxies do not reflect a significant shift for the YD. $\delta^{13}\text{C}$ values remain at low levels which indicates a high influence of organic or biogenic CO₂ on stalagmite formation and contradict enhanced limestone carbonate dissolution. None of the proxies suggests a persistent change in climatic conditions on Socotra Island for the YD. Although it is not possible to conclusively derive the direct cause for the observed fluctuations in DCF from the data, labile conditions of the soil carbon pool above the cave or short-term changes in carbonate dissolution systematics might have played a vital role.

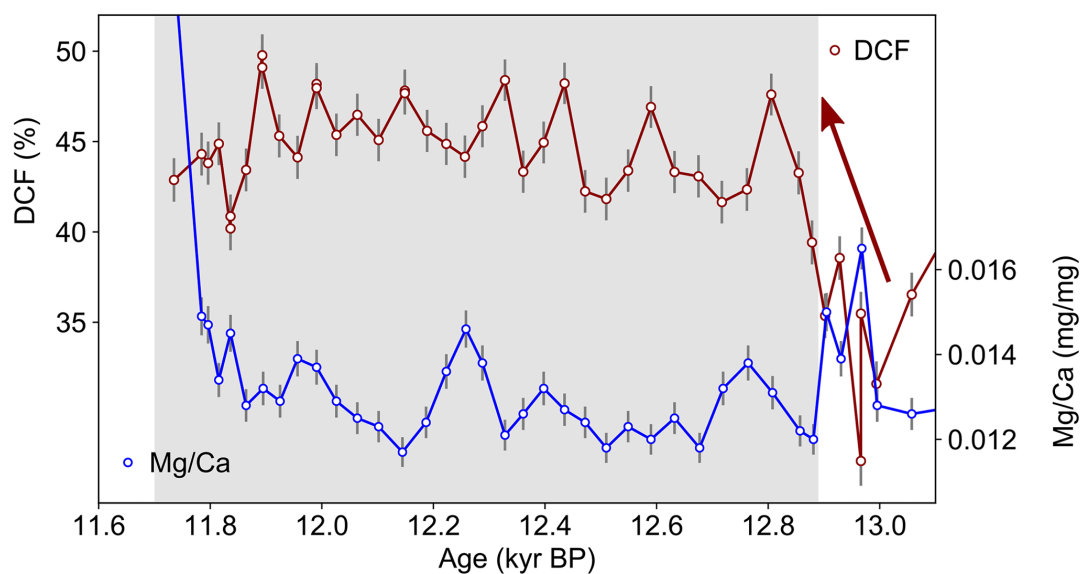


Figure 5.5: DCF and Mg/Ca of stalagmite M1-5 for the YD (gray area). DCF increases sharply at the onset of the YD (red arrow). The high data resolution reveals pronounced changes in DCF on extremely short time periods, highlighting the vast soil dynamics during the YD where growth rate was very high (> 0.20 mm/yr). The Mg/Ca ratio remains relatively low, indicating a high infiltration rate. The correlation between both proxies is insignificant in this time ($r^2= 0.231$, $p < 0.01$).

5.5 Conclusions

Although stalagmite M1-5 seems at first similar to those records used for radiocarbon calibration (high growth rate, comparable climate setting), the high DCF values do not allow atmospheric reconstruction of ¹⁴C concentration. The observed trends in the

generally very high DCF values prove a direct climatic impact on speleothem ^{14}C . Local fast carbon cycling variability is especially prominent in the Termination I ^{14}C data. Whereas the Hulu Cave record (Cheng et al. 2018, Southon et al. 2012), with its low DCF that remains constant even during pronounced climate changes, has been referred to as the “Holy Grail of ^{14}C dating”, records like M1-5 are crucial for the understanding of soil carbon cycling and karst hydrogeochemistry.

Stalagmite M1-5 shows high influence of aged SOM and grew at near-closed limestone dissolution conditions during the LGM, causing extremely high DCF levels. Wetter conditions toward later caused a higher input of ^{14}C enriched CO_2 through denser vegetation coverage above the cave. Since the proxy records indicate higher precipitation levels when DCF goes down, M1-5 data opposes the postulated correlation of soil humidity and DCF due to hydrological influence on karst dissolution.

These findings are the basis for the implementation of ^{14}C in stalagmite as a tracer for vegetation. It also becomes clear that the correlation between precipitation and speleothem DCF is subject to the climatic distinction between (semi)arid regions and temperate, more humid settings. The influence of soil carbon dynamics and (aged) SOM are proven by both long-term trends and sub-centennial variability of the DCF.

This study is an important contribution to future soil dynamics research and the connection to stalagmite DCF, in particular as this bears on the search for suitable ^{14}C calibration records.

6 Soil Carbon Dynamics and Atmospheric Signals in Stalagmite ^{14}C at Sofular Cave

6.1 Introduction

Recently, radiocarbon dating of stalagmites has contributed to significant advances in various fields of paleoclimatology. The versatile utilization of radiocarbon as climate proxy or environmental tracer has prompted numerous studies on the mechanisms of ^{14}C incorporation into stalagmites during their formation, on global carbon cycling and on climate change at time scales going back as far as 50 kyr BP. In combination with other climate proxies, the influence of different carbon reservoirs in a cave environment on the dead carbon fraction (DCF) of stalagmites was intensely investigated. Several case studies and modeling approaches showed that climate induced precipitation changes, as well as vegetation productivity and carbon cycling dynamics, can significantly influence stalagmite DCF (see studies of Genty et al. 1999, 2001, Fohlmeister et al. 2011a, Rudzka et al. 2011, Griffiths et al. 2012, Noronha et al. 2014, Therre et al. 2020).

In the last decade, speleothem data was increasingly used to determine past changes of atmospheric ^{14}C concentration (Beck et al. 2001, Hoffmann et al. 2010, Southon et al. 2012) and was subsequently included into inter-calibration datasets like IntCal13 (Reimer et al. 2013), adding to tree-ring, lacustrine and fossil coral records. However, the issue of a potentially climate dependent, non-constant DCF exacerbated these efforts, since the extent and cause of DCF variability over time are not entirely clear. With the combined Hulu Cave record from Cheng et al. (2018), a milestone was achieved by a high-resolution, multi-stalagmite record with a consistently low and constant DCF in the time of tree-ring derived atmospheric ^{14}C data. This DCF apparently persisted throughout Termination I reaching back as far as 53 kyr BP. While most features of the existing calibration data in IntCal13 were confirmed, significant discrepancies appeared in the data of Cheng et al. (2018) for times older than 35 kyr BP. The search for additional speleothem records that allow the determination of atmospheric ^{14}C is crucial to validate the findings of previous studies and to understand why only a very limited number of cave settings and stalagmites seem to provide favorable conditions to record atmospheric ^{14}C fluctuations.

Sofular Cave was previously studied with a focus on the response of the Black Sea environment to climate oscillations during the last glacial (Fleitmann et al. 2009) and with respect to the soil carbon cycling response to Termination I (Rudzka et al. 2011). The latter publication concluded that the stalagmite had grown in a near open system, in which

the observed changes in DCF could be attributed to changing soil carbon input rather than general shifts in the limestone dissolution systems. In this study, high-precision and high-resolution radiocarbon results in addition to a reliable U-series chronology and trace elemental analysis are used to gain insight into the soil carbon cycling processes during the last glacial and subsequently assess atmospheric ^{14}C variability, recorded by stalagmite So-1.

6.2 Sample location and methods

This study focuses on stalagmite So-1 from Sofular Cave in Northern Turkey. Stable isotope records of So-1 were already investigated by previous studies focusing on the Greenland interstadials (Fleitmann et al. 2009) and the Holocene (Göktürk et al. 2011). In addition, a multi-record radiocarbon study on soil and cave processes during the last glacial termination was conducted at Sofular Cave (Rudzka et al. 2011). The following chapters give a summary of the location and sample characteristics and describe the climatological background of the region in the considered time span.

6.2.1 Sofular Cave and stalagmite So-1

Sofular Cave is located in Northern Turkey less than 10 km from the coast of the Black Sea at $41^{\circ}26.8'N$, $31^{\circ}57.9'E$, approximately 440 m above sea level, on the northern foothills of the Akçakoca Mountain range in the western Pontic Mountains (see Figure 6.1). From the geological perspective, the cave is set in Early Cretaceous limestone and was formed during the Pliocene (Tüysüz 1999). According to Badertscher et al. (2014), the strongly fissured bedrock above Sofular Cave is approximately 40 m thick. Subsequently, cave drip rates are expected to respond quickly to changing infiltration levels on the surface. The cave lies at a depth of approximately 100 m below ground and has an extension of 490 m in length (Fleitmann et al. 2009). The modern mean cave temperature was measured at constant values (11.7 ± 0.1) $^{\circ}\text{C}$ (Krüger et al. 2011) and relative humidity is higher than 95 % (Badertscher et al. 2014). Modern vegetation above the cave is mainly consistent of shrubs and trees and C3 grasses with a soil thickness of less than 50 cm (Rudzka et al. 2011). The region near the southern Black Sea coast is among the wettest regions in Turkey with average annual precipitation rates of 1200 mm/yr. Most of the rainfall occurs during late autumn and winter with almost 50 % of the annual amount between October and January. However, the summer months also show a significant rainfall with an average monthly amount of more than 50 mm. The external mean annual temperature is ca. 13 to 14 $^{\circ}\text{C}$ (Rudzka et al. 2011, Göktürk et al. 2011, Badertscher et al. 2014) with monthly average temperatures between 6.0 $^{\circ}\text{C}$ (January) and 21.5 $^{\circ}\text{C}$ (July). Modern climate data refers to the nearest meteorological station at Zonguldak, 10 km from Sofular Cave. In terms of the updated Köppen-Geiger classification, Sofular Cave is situated in a warm temperate, fully humid maritime climate (Cfb).

Stalagmite So-1 is candle-shaped, 1.17 m in total length and was still actively growing when it was collected from the cave during an expedition in 2006 (Fleitmann et al. 2009)

(other sources: 2005, Göktürk et al. 2011). It started to grow approximately 50.3 kyr BP and shows only marginally increasing width with depth, making its diameter rather regular (see Figure 6.1). This suggests fairly constant drip rates at the growth site (Kaufmann 2003), which is corroborated by the aforementioned geological features of the overlying bedrock and the rather high infiltration levels above the cave.

6.2.2 Past climate on the southern Black Sea

The location around Sofular Cave is under the influence of subtropical Mediterranean, temperate European, and continental Asian air masses (Özsoy and Ünlüata 1997). It was shown that the Black Sea can be considered as the main source of precipitation for the proximity of Sofular Cave and northern Anatolia (Fleitmann et al. 2009).

Numerous studies have focused on the investigation of climate change in the East Mediterranean and Black Sea region since the Pleistocene. A special focus of the investigations was the response of the Black Sea region to the abrupt and pronounced climate fluctuations during the late last glacial which are prominent in Greenland ice core records. In the Black Sea region, the effects of these climatic changes were revealed by studies, which demonstrated the prompt response of local ecosystems to Heinrich stadials (HS) 1 and 2 (Bahr et al. 2008, Kwiecien et al. 2009), and to warmer/wetter conditions during the late-glacial Bølling-Allerød (B/A) interstadial, and cooling during the Younger Dryas



Figure 6.1: Location of the Sofular Cave in Northern Turkey at the southern coast of the Black Sea. The location of the cave is marked by the white star at $41^{\circ}26.8'N$, $31^{\circ}57.9'E$, approximately 440 m above sea level. The image of stalagmite So-1 from Sofular Cave is taken from Göktürk et al. (2011).

(YD) cold reversal (Bahr et al. 2005, Filipova-Marinova 2006, Bahr et al. 2008). Although several studies suggest more humid conditions during the Last Glacial Maximum (LGM) than today (Sarikaya et al. 2008), pollen records from the eastern Mediterranean indicate a dryer climate during the glacial, with a shift to wetter conditions only starting at the beginning of the B/A (Bottema et al. 1993, Kotthoff et al. 2008). Studies on pollen records from Black Sea sediment cores suggest dry and cold conditions at the end of the last glacial (18 to 14.5 kyr BP), while warmer, more humid conditions were observed during the B/A, followed by a cool and dry YD, and high temperatures and humidity at the beginning of the Holocene (Shumilovskikh et al. 2012).

Further back in the glacial period, other sediment based pollen studies revealed long-term climatic periods of arid conditions between 40 and 32 kyr BP and an extended phase of more humidity from 28 to 20 kyr BP, closely connected to changes of insolation (Shumilovskikh et al. 2014). Apart from long-term developments of the regional climate, it could also be shown that Dansgaard/Oeschger (D/O) events are clearly visible in sediment records, as well as stalagmite $\delta^{13}\text{C}$ (Shumilovskikh et al. 2014, Fleitmann et al. 2009). Both the increase in tree pollen in the sediment and the changes in stable isotopes at Sofular Cave indicate that the Northern hemispheric D/O fluctuations manifested in the Black Sea region by warmer and wetter conditions in northern Anatolia, while the Heinrich stadials are generally connected to cold, arid climate in the area (Shumilovskikh et al. 2014). Stalagmite and sediment records also revealed a quick adaptation to these climatic changes during the glacial with a lag of less than a hundred years between climate signal and full response of the ecosystem (Fleitmann et al. 2009).

6.2.3 Methods of dating and elemental measurements

The U-Series dating method was used for this study to establish an age-depth model. These measurements were performed at the Institute of Environmental Physics in Heidelberg on a MC-ICP-MS (Thermo Fisher Neptune) following the methods described by Arps (2017) and Wefing et al. (2017). Samples were taken in depths ranging from 950 to 1618 mm distance from top. These ages were measured in addition to the 60 data points from the same depth range previously reported in the study by Fleitmann et al. (2009) for reasons of more reliable age-depth allocation. In addition, a goal of the repeated measurement was to significantly increase the data precision and add data points where growth stops were not resolved by the previous data set.

Radiocarbon dating was performed following the procedure explained in Chapter 3 and Chapter 4 of this thesis and by Synal et al. (2007), Kromer et al. (2013) and (Therre et al. 2020). The samples for ^{14}C dating were taken from the stalagmite near its growth axis along growth layers. Since cutting samples was not possible due to the fragile structure of this stalagmite, samples had to be drilled from the stalagmite along the growth layers. The drill bits were previously cleaned by ethanol to avoid sample contamination. Once the calcite powder was sampled, it was chemically prepared in a two-step approach: Each sample was hydrolyzed not more than a few hours after sampling to extract CO_2 on an evacuated extraction setup. The isolated CO_2 was graphitized on a separate setup with iron powder as a catalyst. The resulting graphite-iron compound was mechanically

pressed into targets that were subsequently inserted into the iron source of the AMS facility. In this study, the measurements were performed on an AMS of type MICADAS at the Curt-Engelhorn-Centre Archaeometry, Mannheim (Synal et al. 2007, Kromer et al. 2013).

Elemental measurements of Mg/Ca and Sr/Ca ratios were conducted on calcite subsamples which were sampled in the same way as those for dating purposes. The analyses were performed on an ICP-QMS (Mg/Ca) and an ICP-OES (Mg/Ca, Sr/Ca) setup, with several samples or standards measured on both setups to ensure measurement comparability. The procedure that was followed for this study is described by Warken et al. (2018). A detailed account of the measurement procedures is given in the respective sections in Chapter 3.

6.3 Results

6.3.1 Age modeling of stalagmite So-1

The results of the 36 U-series dating measurements are listed in Table A.2 and show that in the investigated segment stalagmite So-1 grew from 41.34 kyr BP to 10.27 kyr BP with an average growth rate of 21.2 $\mu\text{m}/\text{yr}$. The ^{238}U concentrations range from 0.210 to 1.230 ppm, ^{232}Th concentrations are between 0.156 and 3.176 ppb. The mean activity ratio of $^{230}\text{Th}/^{232}\text{Th}$ is 975, which allows for precise age determination without major age corrections. In all cases, the corrected ages were within the 2σ uncertainty of the uncorrected data. However, the obtained ages are not exclusively in stratigraphic order. These age reversals were mostly excluded during the age-depth-modeling process, which is discussed in detail in section 6.4.1. A first dating record of So-1 was available from Fleitmann et al. (2009). Comparing their data to the new results from this study revealed that they are in excellent agreement (see Figure 6.2).

The age-depth-modeling was achieved by making use of the StalAge algorithm (Scholz and Hoffmann 2011) that uses an ensemble linear interpolation approach. To account for data outliers and likely hiatuses, the algorithm was manually implemented on several subsets of the data, and afterwards conflated to give the most accurate representation of growth patterns. The four data points implying age reversals (lab nos. 9225, 9226, 9227 and 9233) were manually excluded from age-depth modeling. The cause for these major outliers was identified as a malfunctioning drill bit that most likely contaminated the calcite powder during the sampling procedure. Through the resulting age-depth-model, different growth phases could be identified, and growth stops could be determined or confined, respectively (see Figure 6.2).

For the time-periods of steady growth, the accumulation rate of stalagmite So-1 ranges from 5 to 30 $\mu\text{m}/\text{yr}$, apart from a time of increased growth rate with values from 50 to 100 $\mu\text{m}/\text{yr}$ between approximately 15 and 12 kyr BP. A hiatus, that was already resolved by previous data, could be refined to range from 22.9 to 20.9 kyr BP. The growth rate analysis also suggests another period of slowed growth centered around 16.2 kyr BP (1200 mm) and one around 36 kyr BP (1520 mm). In Fig 6.2 the growth rate is shown over depth as a smoothed graph after applying a Gaussian filter covering a range of 11 mm.

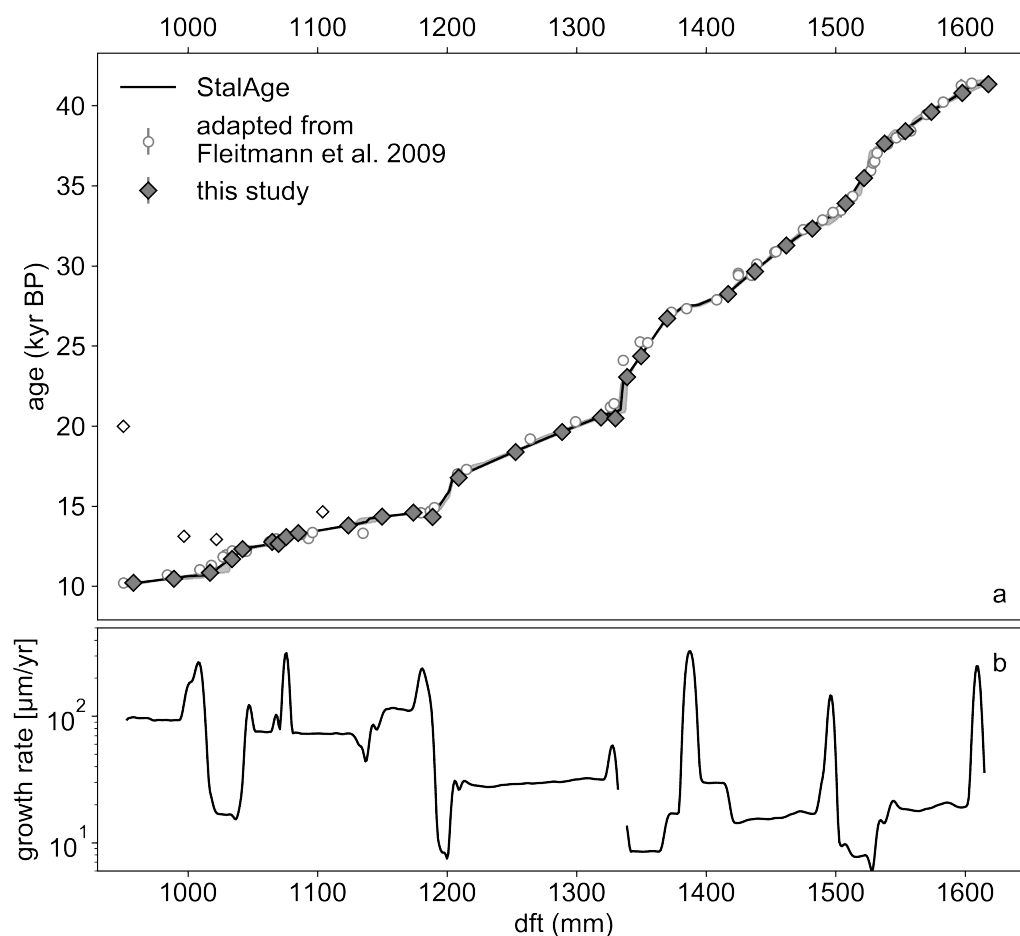


Figure 6.2: U-series dating results for stalagmite So-1 between 900 and 1650 mm distance from top (dft), with age-depth model (a). All ages are given as years before present (yr BP), referring to the year 1950 CE. The error bars are areas of 2σ uncertainty, but are covered by the data points. White circles represent data from Fleitmann et al. (2009), empty diamonds are points indicating significant age reversals that were omitted during age modeling. The black line represents the modified StalAge age-depth model. Time range uncertainties from modeling (shaded gray areas) are mostly covered by the age model. The growth rate is derived from the age-depth model, as a Gaussian-filtered with a range of 11 mm (b).

6.3.2 ^{14}C data reporting and Dead Carbon Fraction

Results in ^{14}C dating can be reported in the most common unit *conventional radiocarbon years*, but also as an equivalent activity ($a^{14}\text{C}$) in *percent modern carbon*, referring to the atmospheric ^{14}C concentration of the year 1950 CE. With the assigned modeled ages

(t_{mod}) the initial radiocarbon activity in the sampled stalagmite layer at the time of calcite precipitation ($a^{14}\text{C}_{\text{init}}$) can be reconstructed from the measured activity ($a^{14}\text{C}_{\text{meas}}$) by invoking the physical decay constant ($\lambda_{\text{decay}}^{-1} = 8267 \text{ yr}$) of the radioactive decay of the ^{14}C isotope and the conventional decay constant ($\lambda_{\text{Lib}}^{-1} = 8033 \text{ yr}$). This yields the following term for the initial activity ($a^{14}\text{C}_{\text{init}}$) in the speleothem:

$$a^{14}\text{C}_{\text{init}} = a^{14}\text{C}_{\text{meas}} \cdot \exp(\lambda_{\text{decay}} \cdot t_{\text{mod}}) \quad (6.1)$$

$$= \exp(-\lambda_{\text{Lib}} \cdot t_{14\text{C}}) \cdot \exp(\lambda_{\text{decay}} \cdot t_{\text{mod}}) \quad (6.2)$$

$$= \exp(\lambda_{\text{decay}} \cdot t_{\text{mod}} - \lambda_{\text{Lib}} \cdot t_{14\text{C}}) \quad (6.3)$$

A focus in this study lies on the comparison of the initial activity in the speleothem layer and the atmospheric radiocarbon concentration at the time of deposition. The atmospheric activity ($a^{14}\text{C}_{\text{atmo}}$) for this assessment is retrieved from atmospheric reconstruction data sets, the most important ones being the inter-calibration set IntCal13 (Reimer et al. 2013) and the recently published stalagmite radiocarbon record from Hulu Cave (Cheng et al. 2018). To obtain atmospheric activities and their uncertainties at a distinct time, the uncertainties of calendar ages as obtained from U-series dating and successive age modelling, as well as the uncertainties from radiocarbon dating are taken into account. Explicitly, a Monte Carlo approach was performed by generating a Gaussian data set of $N = 10^6$ ages around the modeled calendar age t_{mod} . Subsequently, the corresponding $a^{14}\text{C}_{\text{atmo}}$ for every age in the ensemble was determined from the respective interpolated atmospheric radiocarbon data set. Further explanations can be found in Griffiths et al. (2012), where this method was adapted from.

Two different atmospheric ^{14}C records from IntCal13 (Reimer et al. 2013) and Hulu Cave (Cheng et al. 2018) are taken into account. For this study, the published stalagmite ^{14}C data from Cheng et al. (2018) was combined into one set and smoothed by a Gaussian-based convolution spanning ± 5 data points. The resulting smooth and continuous record provides an alternative atmospheric ^{14}C reference in addition to IntCal13. Hereafter, the respective utilized reference is always declared as either ‘‘HuluCal’’ or ‘‘IntCal13’’ (Reimer et al. 2013).

Following section 2.3.2, the offset between the initial ^{14}C activity in the speleothem and the atmosphere is reported in terms of dead carbon fraction (DCF). With the equations introduced above, the DCF is given as

$$\text{DCF} = \left(1 - \frac{a^{14}\text{C}_{\text{init}}}{a^{14}\text{C}_{\text{atmo}}} \right). \quad (6.4)$$

Consequently, a DCF lower than 0 either suggests the sample was contaminated (e.g. by modern ^{14}C during preparation) or it indicates that the modeled age of a sample is systematically too old. If all these aspects can be excluded, a negative DCF can also indicate a systematic error of the used atmospheric reference, i.e. the actual atmospheric ^{14}C concentration was higher than the reference suggests.

6.3.3 DCF of stalagmite So-1

An extensive data set of radiocarbon ages was measured for stalagmite So-1. A total of 111 samples were taken, prepared and measured following the procedure described in Chapter 4. The samples were taken in the range covered by the age-depth modeling based on the U-series dating. The determined ^{14}C ages range from 10 131 to 37 525 yr (conventional ^{14}C years). Blanks used for background correction were mostly taken from a marble sample and have an apparent ^{14}C age of more than 48 kyr, equivalent to an apparent activity of less than 0.25 pmC. The international standard IAEA C2 was analyzed in the course of the ^{14}C measurements for stalagmite So-1 with a mean value of (41.058 ± 0.225) pmC ($N = 33$). This is in very good agreement with the expected value of (41.14 ± 0.03) pmC and is indicative of the high quality of the measurement and data correction procedure.

In general, the measured ^{14}C ages of the stalagmite show some significant and systematic deviations from a monotonous increase with distance from top. Roughly at 17 kyr BP, radiocarbon ages increase by approximately 2000 yr over 400 calendar years (vertical line in Figure 6.3) and then return fast to the previously observed trend. Each data point was assigned a modeled age and uncertainty by the implemented U-Series model. Figure 6.3 shows the determined ^{14}C ages vs. modeled calendar ages in context to atmospheric radiocarbon data from Reimer et al. (2013) and corrected ^{14}C data from the Hulu Cave stalagmites (Cheng et al. 2018).

The DCF values for stalagmite So-1 were determined by invoking eq. (6.4) and are shown in Figure 6.3 b for both reference records. For IntCal13, they range from (-0.40 ± 1.98) % to (39.09 ± 0.53) %, whereas HuluCal yields respective values between (4.97 ± 1.18) % and (38.73 ± 0.66) %. In both cases, the vast majority of values range between 10 % and 25 %. The overall mean DCF are (15.69 ± 6.17) % (IntCal13) and (17.02 ± 5.46) % (HuluCal). Discrepancies in the DCF data sets arise especially for modeled ages older than 30 kyr BP, where the Hulu Cave records suggest higher atmospheric ^{14}C concentration. In this time interval, the IntCal13 DCF values are often significantly lower, with a difference of up to $\Delta\text{DCF} = (-8.40 \pm 1.51)$ % (Figure 6.3 b).

In the temporal evolution of DCF distinct patterns can be observed over the growth period of the stalagmite for both references. From 16 to 10 kyr BP, the DCF values are between 10 and 20 %. Approximately at 17 kyr BP, values up to (39.09 ± 0.53) % are observed, where ^{14}C ages indicated a strong age inversion. For times older than 17 kyr BP, the DCF values range from 0 to 25 % with the lowest DCF values in the oldest parts around 41 kyr BP. High variation by more than 5 % DCF on sub-centennial scale can be seen several times (around 20 kyr BP) and also by more than 18 % (around 38 kyr BP).

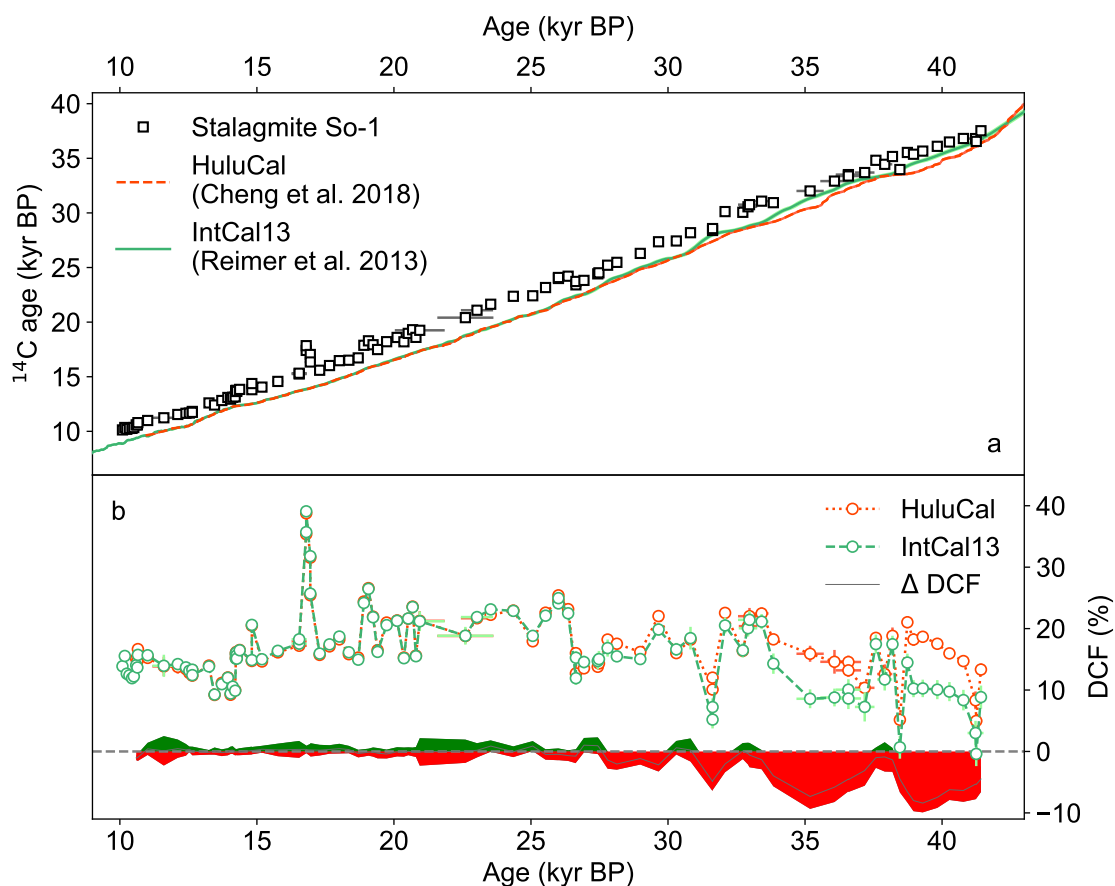


Figure 6.3: Radiocarbon dating results of stalagmite So-1. The conventional ^{14}C ages (squares) are shown vs. the modeled stalagmite age (a). Also shown is the atmospheric ^{14}C record from IntCal13 (Reimer et al. 2013) and the interpolated HuluCal data set from the Hulu Cave radiocarbon record (Cheng et al. 2018). The DCF is shown (b), in reference to both atmospheric data (IntCal13 and HuluCal). The difference in DCF depending on the reference data sets used is given by the shaded area in the lower segment. The discrepancy is significant in older parts beyond 30 kyr BP, where IntCal13 DCF is lower than those obtained by HuluCal. Error bars and areas reflect the 1σ uncertainty area. The vertical dashed line indicated the distinct, short excursion to high DCF at 16.9 kyr BP.

6.3.4 Elemental ratios

The elemental analysis of Mg/Ca and Sr/Ca ratios of the stalagmite was performed by drilling 98 samples of 1 to 3 mg calcite powder. In most instances the subsamples were taken from the same calcite material or sampling location that was used for ^{14}C analysis. The determined Mg/Ca ratios range from 2.25 to 11.34 $\mu\text{g}/\text{mg}$, with an overall mean of $(4.78 \pm 1.88) \mu\text{g}/\text{mg}$. The Mg/Ca ratio is rather constant and low between 14 and 10 kyr BP. A significant peak is seen around 17 kyr BP with Mg/Ca ratios of approximately 8 $\mu\text{g}/\text{mg}$. Between 29 and 19 kyr BP, the values are rather variable from 4 to 7 $\mu\text{g}/\text{mg}$. In the oldest part, the ratios are once again lower. For Sr/Ca, the values are significantly lower, ranging from 0.273 to 1.01 $\mu\text{g}/\text{mg}$, with a mean of $(0.434 \pm 0.117) \mu\text{g}/\text{mg}$. Sr/Ca also has a relative maximum around 17 kyr BP. Partly due to the lower data density, the variation from 42 to 20 kyr BP is smaller and the values are rather constant around 0.4 $\mu\text{g}/\text{mg}$. Comparing the mean values of the two sets yields a Sr concentration approximately 11 times lower than Mg.

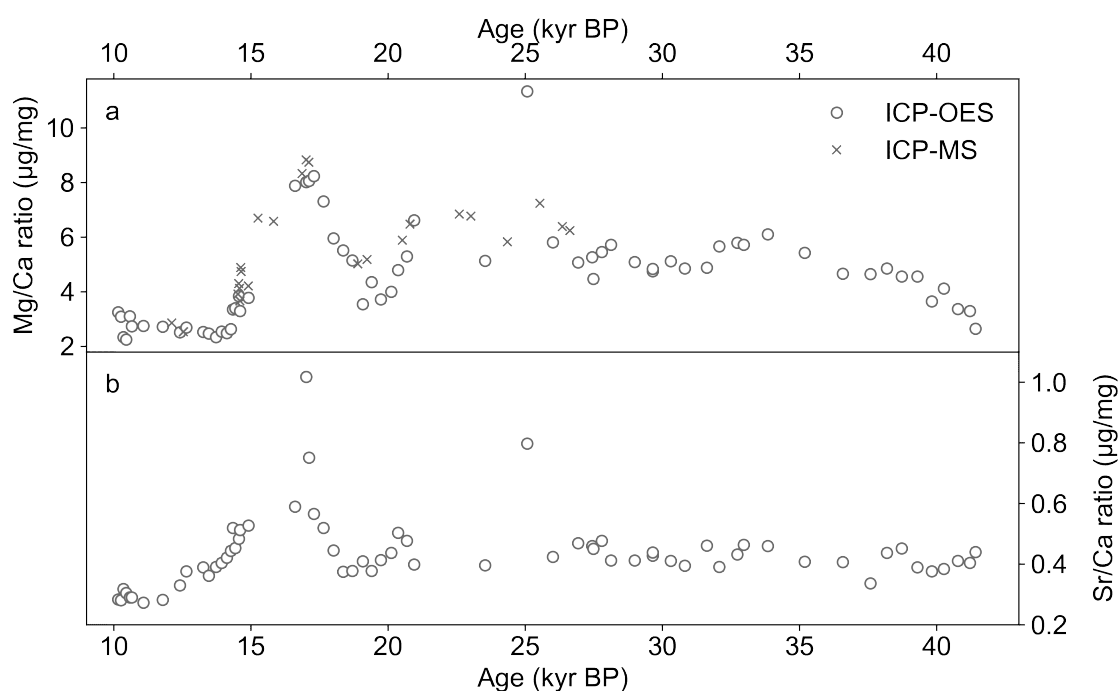


Figure 6.4: Measured elemental ratios of stalagmite So-1. The upper graph (a) shows Mg/Ca ratios from two different setups. The ICP-OES data is shown as a cross symbol, ICP-MS as circle. In the lower graph, the Sr/Ca ratios from the ICP-OES measurements are shown. The Sr/Ca ratios from ICP-OES measurements were determined together with Mg/Ca. The highest values of both records are found around 17 kyr BP and 25 kyr BP.

6.4 Discussion

In recent studies on stalagmite radiocarbon, the focus was mainly on two aspects.

On the one hand, the reconstruction of **past atmospheric ^{14}C concentration** to expand the range of ^{14}C calibration and increase its precision has been the focus of studies on stalagmites from subtropical (Beck et al. 2001, Hoffmann et al. 2010) and temperate monsoonal regions (Southon et al. 2012). The recently published study by Cheng et al. (2018) determined a constant and low DCF of $(5.6 \pm 0.8)\%$ between 14 and 10 kyr BP, where the atmospheric ^{14}C concentration is best constrained by dendrochronological records. Their multi-stalagmite record is assumed to show practically no climate-induced DCF variation, partly due to the sandstone ceiling above the cave that does not add dead carbon to the percolating water (Cheng et al. 2018). Their data can be used to refine the atmospheric record in the period reaching back beyond 50 kyr BP, which IntCal13 (Reimer et al. 2013) does not cover yet, or where there are still large uncertainties due to sparse data availability. The existing record of IntCal13 was mostly confirmed in the age range back to 35 kyr BP and the precision of atmospheric $\Delta^{14}\text{C}$ was increased. However, significant discrepancies were revealed, for instance between 42 and 38 kyr BP, around the Laschamp geomagnetic reversal (Muscheler et al. 2014, Lascu et al. 2016, Cheng et al. 2018).

On the other hand, stalagmites with varying DCF over time provide the opportunity to investigate the **impact of changing climate parameters and soil or cave processes**. For instance, hydrological changes caused by precipitation variation in a tropical setting were found to directly influence the incorporation of dead carbon into the stalagmite (Fohlmeister et al. 2011a, Griffiths et al. 2012). Similar effects were observed in a stalagmite record from Heshang Cave (Noronha et al. 2014). Other than the direct influence of net infiltration, aging soil organic matter (SOM) was found to exert a major impact on the spectrum of stalagmite radiocarbon age (Genty et al. 2001, Fohlmeister et al. 2010, 2011a, Rudzka-Phillips et al. 2013, Therre et al. 2020). Recent studies also pointed out that excess dissolution of limestone through sulfuric acid enables an increased input of very old carbonate into the cave, leading to extremely high DCF values (Spötl et al. 2016, Bajo et al. 2017).

For this study, stalagmite So-1 from Sofular Cave in Northern Turkey, a warm temperate climate regime, is investigated in detail, with a focus on its DCF during its growth from 10 to 42 kyr BP. The discussion will cover the age-modeling process, the assessment of dead carbon signature on different timescales, as well as the climatic implications and possible applications for paleoclimate reconstruction.

6.4.1 ^{14}C and U-series: A combined So-1 age model

The temporal DCF variability in stalagmite So-1 causes significant age reversals in the calibrated ^{14}C age vs. depth relation. Therefore, radiocarbon cannot be used as an overall dating tool for this speleothem. With the U-series dating method, a high-precision data profile was established which, due to the high ^{238}U concentration and low ^{232}Th in the stalagmite matrix, provides a reliable age modeling basis.

Apart from the already excluded points, which implied significant and unrealistic age reversals, the remaining data is in stratigraphic order. For this study, the StalAge algorithm (Scholz and Hoffmann 2011) was used to implement comprehensive age-depth relations, albeit with situational adaptation when the modeling failed to create realistic results in certain areas. StalAge handles outliers in data sets by either exclusion of the respective data point before modeling or by artificially increasing its uncertainty. However, if the age reversal is not manually removed, the resulting age-model could still converge, but produce unrealistically high growth rates.

A preliminary StalAge model of So-1 which was based on only U-series dating results suggested a growth rate of more than 10 mm/yr at approximately 1175 mm distance from top (see dashed line in Figure 6.5). This is directly connected to the data points 9235, 9236 and 10 103 at depths of 1150 mm, 1174 mm and 1189 mm, which imply no significant change of U-series age over 39 mm of growth. Due to the high data precision, the age modeling process is extremely sensitive to age reversals.

In these cases, ^{14}C can be used for age modeling under certain premises and assumptions to help solve this inconsistency. The ^{14}C results in the area, where the atmospheric ^{14}C concentration is precisely known, suggest a relatively constant $\text{DCF}_{\text{date}} = (13.24 \pm 1.55) \%$ between 14 kyr BP and 10 kyr BP. Assuming a constant DCF, it is possible to create an age model based on radiocarbon dates expanding beyond 14 kyr BP. To that end, the DCF was translated into an equivalent radiocarbon reservoir age of (1142 ± 143) yr, which was then subtracted from all measured ^{14}C ages that were considered for age modeling. The resulting reservoir-corrected ages were calibrated using the OxCal tool (Bronk Ramsey 2013) to account for atmospheric concentration changes and were subsequently treated like raw data for age modeling. It is important to note that the probability distributions of calibrated ^{14}C ages are no longer symmetrical, while StalAge is designed for Gaussian shaped uncertainties. However, for this partial verification of the already established age model, a conservative estimation of the data uncertainties as Gaussian shaped distributions seems justified.

A second StalAge approach with the calibrated ages then yielded the ^{14}C -based age model (red lines in Figure 6.5). Both models show a very good agreement and even overlap within their areas of uncertainties in the vast majority of time. Discrepancies between the age models mostly arise in depths from 1080 to 1160 mm, where calibrated radiocarbon ages are systematically younger compared to the U-series data. In this area where the original StalAge struggled to obtain realistic growth rates, the radiocarbon model now indicates that the U-series data point at 1189 mm is measured systematically too young. Even the decreasing growth rate and potential hiatus around 16 kyr BP (1200 mm) is confirmed by the radiocarbon approach. Considering the age model solely based on the

calibrated ^{14}C data (red line in Figure 6.5) shows that the mere ^{14}C age modeling is also not accurate, because it creates unrealistic growth rates as well. Therefore, the final age-depth relation (black solid line) that was consistently used for further analysis in this chapter is in general based on the U-series data, with the exception of the area around 1180 mm, where it was adjusted based on the radiocarbon dating approach. The different segments of the age modeling were individually connected and smoothed to produce realistic transitions (e.g. at 1200 mm). The growth rates of the final, combined age-model are far more realistic (below 10^3 mm/yr, see Figure 6.5 b).

Even though it remains difficult to create reliable age-depth-relations from radiocarbon data alone, this case shows that it is still possible to optimize the age modeling quality by utilizing ^{14}C data. Radiocarbon dating was successfully used in stalagmites with

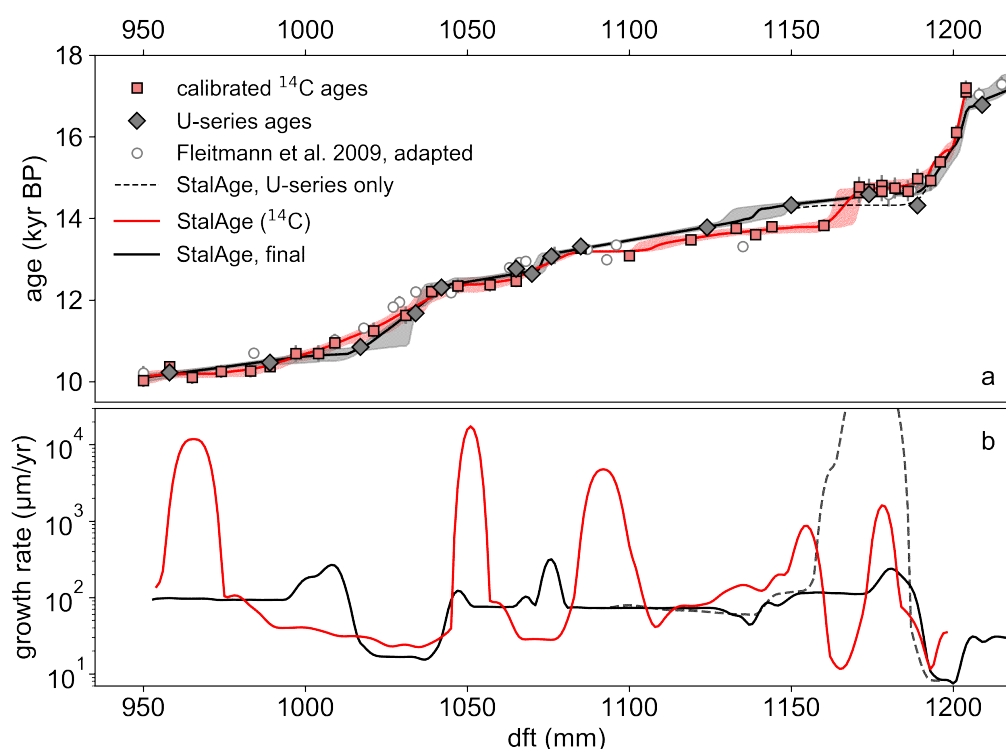


Figure 6.5: Revisited age model of stalagmite So-1. Assuming a constant offset between atmospheric and stalagmite ^{14}C in a time of virtually constant DCF enables the use of ^{14}C dates for age modeling. The resulting calibrated radiocarbon dating results (red boxes) and the modeled age depth relation (red line) are shown in the upper graph (a), compared to the results from U-series dating. The ^{14}C based age model translates to growth rates which differ from the original StalAge model (dashed line), although the age models mostly do not show significant discrepancies. With the additional information from ^{14}C -based age modeling, the initial StalAge model (dashed lines) was mostly confirmed, but adjusted in between 1150 and 1190 mm, for the final modified model (solid line).

similar assumptions in recent studies, where U-series dating was not possible or suitable (Lechleitner et al. 2016b, Fohlmeister et al. 2017, Hua et al. 2017, Warken et al. 2018). For stalagmite So-1, the age determination using ^{14}C data only makes sense for the period of low and relatively constant DCF. In the older areas, highly varying DCF and significant ^{14}C age reversals rule out successful ^{14}C age modeling.

6.4.2 DCF of a temperate climate stalagmite during Termination I

In the study by Rudzka et al. (2011), the radiocarbon signature of So-1 was previously discussed for the part between 16 and 10 kyr BP. Here, the results from Rudzka et al. (2011) were recalculated from their reported radiocarbon and U-series dating results, because the erroneous use of the conventional radiocarbon half-life resulted in systematically lower DCF values in that publication. After the correct calculation, the data structure remains the same, the DCF are merely shifted to higher values. The ^{14}C signature of stalagmite So-1 over Termination I was interpreted closely linked to the stable carbon isotopic signature. Here, the radiocarbon results of Rudzka et al. (2011) are put in context to the measurements of this study (see Figure 6.6).

Both ^{14}C data sets are in good agreement and – taking into account the uncertainties of the age model and of the radiocarbon dating – do not differ significantly for the majority of data points. The main share of DCF values measured in this study in the segment previously investigated by Rudzka et al. (2011) ranges from 9 to 16 % (after the recalculation). It can therefore be concluded that in this time-period, the carbon inputs above Sofular Cave were relatively young, i.e. only low amounts of dead carbon contributed to stalagmite formation during the last glacial termination. The thin soil coverage of mostly less than 50 cm above the cave site suggests that the formation of aged soil matter, which significantly shifts the soil gas CO_2 signature towards lower ^{14}C concentrations, is inhibited (Mathieu et al. 2015, Balesdent et al. 2018). However, distinct short-term variations were revealed by the high-resolution data set, which is presented here. For example, a decrease of more than 4 % in DCF is observed around 10.5 kyr BP over a time of about 200 yr. Relatively constant Mg/Ca ratios, except for the B/A (around 14.5 kyr BP), indicate that the hydrological conditions in the karst above the Sofular Cave remained virtually unchanged. In case of lower infiltration levels, which could have triggered more open limestone dissolution systematics and subsequently lower DCF, higher Mg/Ca ratios would be expected (Fairchild et al. 2000, Griffiths et al. 2012, Warken et al. 2018). Therefore, it is likely that soil carbon inputs have mainly caused these changes.

Shifts to lower DCF could indicate an increased input of carbon with high atmospheric ^{14}C concentration through substantially higher vegetation activity and root respiration. From the very low $\delta^{13}\text{C}$ signature around 11.5 kyr BP, Göktürk et al. (2011) deduced a fast re-vegetation at the southern Black Sea coast after the end of the YD cold interval. This period shows the lowest $\delta^{13}\text{C}$ of the entire record. Vegetation increase in the Holocene near Sofular Cave occurred much faster than in East-Mediterranean settings (Kotthoff et al. 2008). It was argued by Göktürk et al. (2011) that this supports the hypothesis of glacial refugia for temperate climate trees in the Black Sea mountains (Leroy and Arpe 2007). The warm, comparably more humid and summer-wet climate of the southern Black

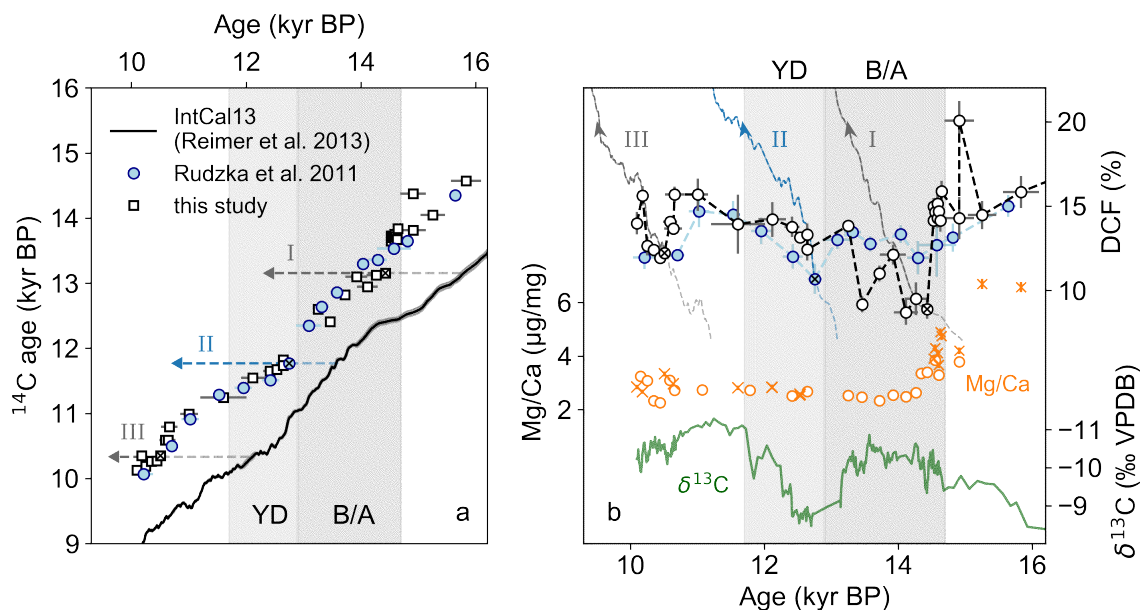


Figure 6.6: Radiocarbon data of stalagmite So-1 in Termination I compared to the data from Rudzka et al. (2011) (blue circles). The ^{14}C ages agree within the uncertainties of the age model and of ^{14}C dating (a). The DCF values for the Rudzka et al. (2011) data was re-calculated from the raw data given in the paper with the same approach used for this study (b). The dashed lines (a, b) represent the expected values if a decay of ^{14}C is assumed as the basis for ^{14}C age and DCF development of the stalagmite, starting from the values marked by an \times . This assumes a steady state of carbon cycling contributing to soil CO_2 without input of young SOM, and constant limestone dissolution conditions. Also shown are $\delta^{13}\text{C}$ data in green (Fleitmann et al. 2009) and Mg/Ca ratios (orange).

Sea coast established very shortly after the YD, and effective moisture reached levels for optimum vegetation development and soil microbial activity. Although Mg/Ca ratios from this study do not resolve a significant increase in infiltration, the combined stable isotope record from Fleitmann et al. (2009) and DCF time series confirm the thesis of Göktürk et al. (2011) that fast re-vegetation occurred after the YD cold period, when warmer climate at the beginning Holocene caused a fast revitalization of vegetation above Sofular cave and in the region.

Rudzka et al. (2011) suggested that stalagmite So-1 has grown under near-open conditions with substantial influence of soil activity and vegetation induced forcing on the ^{14}C signature. In Figure 6.6, the ^{14}C measurements and DCF from this study and Rudzka et al. (2011) are shown together with the adapted stable carbon signature from (Fleitmann et al. 2009) and the Mg/Ca ratio.

Several distinct DCF decreases and slower subsequent increases are observed in the data. For comparison, three potential pathways (path I–III) are added to the data as dashed lines. These pathways represent the ^{14}C or DCF development that would be observed in

the stalagmite, if – at a particular moment – fresh carbon input above the cave had been halted and the contribution of carbon from limestone dissolution remained constant. A similar feature in the ^{14}C signature of So-1 was already postulated by Rudzka et al. (2011) for the YD, starting at 12.75 kyr BP (path II, blue line), where DCF increase seemed to loosely follow the decay pattern after the initial DCF decrease. Two patterns that were discovered by the new ^{14}C measurements show a comparable behavior, beginning at 14.3 kyr BP (path I), and at 10.5 kyr BP (path III).

At 14.4 kyr BP (path I), the DCF sharply decreases by more than 5 % in less than a century at the beginning of the Bølling-Allerød (B/A). A coincident $\delta^{13}\text{C}$ decrease of roughly 1 ‰ indicates that the warming period has manifested by increasing temperature and humidity promoting the development of denser vegetation. Higher infiltration levels in the karst are also indicated by decreasing $\delta^{234}\text{U}_{\text{init}}$ (see Figure 6.7 e) after the HS1, since fast percolation rates (i.e. higher infiltration) is connected with a decrease in the $\delta^{234}\text{U}_{\text{init}}$ (Zhou et al. 2005, Griffiths et al. 2010). The lowest $\delta^{234}\text{U}_{\text{init}}$ values also coincide with the highest growth rate of So-1 in the B/A and YD, which is a consequence of reduced alpha recoil ^{234}U enrichment of the drip water during periods of a short residence time of the water in the epikarst (Plagnes et al. 2002, Griffiths et al. 2010). Higher vegetation density is corroborated by a sediment study from the southern Black Sea, where the onset of the B/A is clearly reflected by increasing pollen concentrations at around 14.5 kyr BP (Shumilovskikh et al. 2012), an increase that has been directly linked to the Northern Hemispheric warming by studies on pollen records in the Black Sea region (Filipova-Marinova 2006, Bottema et al. 1993) and the Aegean Sea (Kotthoff et al. 2008). Following this initial decrease of DCF due to strengthening of vegetation, DCF increases by a few percent following the decay of ^{14}C for approximately 400 yr (dashed lines in Figure 6.6 b, path I). This might be a consequence of the activation of an older SOM reservoir after 14.4 kyr BP or increased limestone dissolution after 14.3 kyr BP due to hydrological changes as indicated by the Mg/Ca decrease in this time. While the data seem to follow the pathway at first, it is not likely that ^{14}C -enriched input was completely halted during the B/A where the pollen records from sediment core studies (Shumilovskikh et al. 2012) suggest persistent productivity (vegetation activity).

The increase of DCF after 12.75 kyr BP (path II) reflects an enhanced input of old SOM throughout the emerging termination (Rudzka et al. 2011). The new data from this study confirms their hypothesis to some extent, although the DCF increase is not as pronounced as seen in the adapted data from Rudzka et al. (2011). The time interval of path II spans the YD cold reversal and coincides with lighter $\delta^{13}\text{C}$. A shift to more closed conditions in limestone dissolution can be ruled out, because it would cause both higher DCF and $\delta^{13}\text{C}$. Also, Mg/Ca ratios do not indicate that the precipitation and thus net-infiltration levels have significantly changed during this time.

The radiocarbon data in the youngest part (Figure 6.6) show another sharp decrease of roughly 4 % DCF around 10.5 kyr BP. The proxies indicate a still near-open carbonate dissolution system with high contribution of organic material decomposition. Since the beginning warming period in the Northern Hemisphere is manifested by increased vegetation in the Black Sea region (Shumilovskikh et al. 2012), it can be deduced that a

higher input of CO₂ at near-atmospheric ¹⁴C signature causes a lower DCF. Interestingly, this decrease is only very short-lived: After 10.5 kyr BP, the DCF rises by 4% and closely follows the decay path III. Radiocarbon data for younger ages is not available, but if the DCF were to develop further along the decay signature, this would point to an extremely stable carbon pool above the cave which remained isolated from a recovering vegetation after the YD cold reversal during the warmer and more humid early Holocene (Shumilovskikh et al. 2012). However, judging from the fast DCF decline only a few hundred years before, this appears rather unlikely.

The combined stable isotope, DCF and Mg/Ca data confirm the near-open system limestone dissolution systematics of stalagmite So-1 throughout Termination I and indicate periods of fast soil carbon cycling, as determined by (Rudzka et al. 2011). Additional patterns of fast DCF decrease and subsequent increase reflect climate-induced input of CO₂ at high ¹⁴C concentration in times of re-vegetation, while limestone dissolution might have contributed to increasing DCF in the B/A interstadial. These effects can be closely linked to the climatic changes in Northern Anatolia and the southern Black Sea region between the B/A warming and the beginning of the Holocene interglacial (Shumilovskikh et al. 2012).

6.4.3 Multi-proxy analysis of DCF controls in the glacial period

During the last glacial, the DCF values of So-1 showed the largest variability. Due to the high number of ¹⁴C data points before the glacial termination, the analysis will focus on the data distribution and possible correlations of the various available proxies. In the oldest part of the investigated data, the discrepancies of DCF derived from Reimer et al. (2013) and HuluCal, based on Cheng et al. (2018) are significant (see Figure 6.7).

Dry conditions in HS1 and their influence on DCF

Starting at the period of minimum growth rate after 16 kyr BP, the radiocarbon ages indicate relatively constant DCF throughout the glacial termination. Shortly before that period, the DCF is at the highest values of the record, with up to 38.5% at roughly 16.9 kyr BP. The high values were confirmed by four ¹⁴C measurements in this area, where all results indicate significantly higher DCF compared to the baseline DCF of 16 to 17%. This peak is coincident with the beginning of Heinrich Stadial 1 (HS1), an abrupt cooling event around 16 kyr BP which is well documented in Northern hemispheric climate archives (Broecker et al. 1992, Bond and Lotti 1995). Zhang and Delworth (2005) and Fleitmann et al. (2009) have investigated the influence of Heinrich coolings and the Dansgaard-Oeschger warming events on high and mid-latitudes in the Northern Hemisphere and found that HS1 in latitudes of the Sofular Cave was probably connected to lower precipitation with a subsequent two-step transition into the B/A warming. In addition to the $\delta^{13}\text{C}$ values of roughly -6‰ in stalagmite So-1, the elemental ratios are at their highest values at this time. The elemental ratios of stalagmite So-1 therefore indicate a shift towards dry conditions, with their maximum extent at 17 to 16 kyr BP. The growth rate sinks to very low values after 17 kyr BP, which might be manifestation

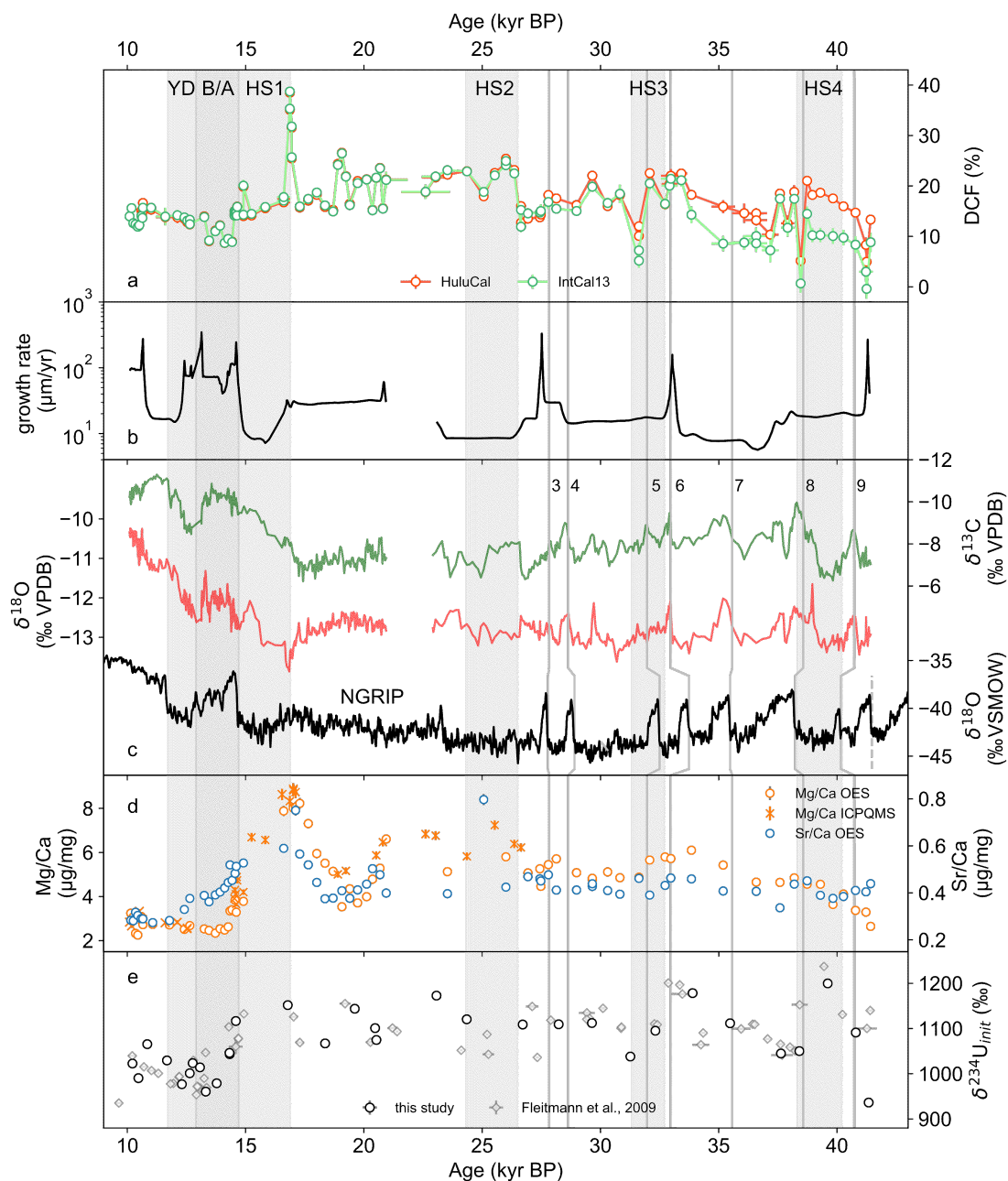


Figure 6.7: All measured proxies of stalagmite So-1 vs. modeled age from this study. Shown is the DCF (a) in reference to IntCal13 (Reimer et al. 2013) and HuluCal, based on Cheng et al. (2018), the smoothed growth rate derived from the implemented aged-model (b), stable isotopes of So-1 from Fleitmann et al. (2009) and NGRIP ice core data from Andersen et al. (2004) (c), element ratios Sr/Ca, Mg/Ca (d) and $\delta^{234}\text{U}_{\text{init}}$ (e) of So-1. The gray lines indicate the Dansgaard/Oeschger (D/O) events 3–9 as defined by Svensson et al. (2008) in the NGRIP data, and their respective peaks in So-1 $\delta^{13}\text{C}$. The timing of the D/O events were adapted from Fleitmann et al. (2009) to the new age model. The gray bars indicate: Younger Dryas (YD) cold reversal, Bølling-Allerød (B/A) interstadial and Heinrich Stadials (HS) 1–4, according to Sanchez Goñi and Harrison (2010).

of dryer periods at the end of the glacial period. In studies on tropical settings and caves under the influence of monsoonal climate, a negative correlation of trace element concentration and DCF was attributed to changes between closed and open limestone dissolution conditions (Griffiths et al. 2012, Noronha et al. 2014, Lechleitner et al. 2016a). For stalagmite So-1, the Mg/Ca ratio indicates dryer conditions at that time. In the considered age range, the peaks in both Mg/Ca and Sr/Ca indicate that changes in prior calcite precipitation (PCP) occurred (Fairchild et al. 2000, Sinclair et al. 2012), which is generally linked to changes in epikarst recharge higher residence times of the water (Stoll et al. 2012). In this scenario, Mg/Ca ratios rise due to enhanced residence times in the karst and dissolution of Mg in the limestone. This would also cause more ^{14}C -depleted calcite in the drip water, leading to higher DCF.

All proxies point to an event of reduced precipitation at the beginning of HS1 with low recharge and subsequently low drip rate, which is linked to longer residence times of the seepage water, resulting in higher element/Ca ratios, lower growth rates and rising DCF.

Carbon cycling modes in the LGM and their effect on DCF

The variability of DCF during the glacial period is evidently higher than during the transition towards the Holocene interglacial after 16 kyr BP. Apart from the aforementioned peak to the highest measured DCF values at 16.9 kyr BP, the data reveals centennial DCF variability with amplitudes larger than 5 % around 20 kyr BP after a growth discontinuity between 22.9 and 20.9 kyr BP. For this growth period, statistical approaches are used for further analysis. Due to the discrepancies of IntCal13 (Reimer et al. 2013) and HuluCal based on Cheng et al. (2018), the two DCF records diverge significantly between 42 and 34 kyr BP.

Figure 6.8 shows the DCF data for both atmospheric reference data sets in the period older than 17 kyr BP. To perform a general trend analysis of the ^{14}C data, a 2σ filter was applied to both DCF data sets to exclude extreme singularities from the following analysis. The effect of this filtering is limited to the lowest DCF values around 40 kyr BP which indicate very low levels of dead carbon, in case of the IntCal13 data even values around 0. In the IntCal13 DCF data, a significant trend over time can be seen, indicating a rise of roughly 10 % DCF between 42 and 17 kyr BP. The HuluCal record only shows a slight trend, although the confidence area of this fit suggests it is not significant. This discrepancy between the two references is a direct consequence of the diverging IntCal13 and HuluCal data around the Laschamp geomagnetic reversal event. Since it can be expected that this discrepancy will disappear once IntCal13 is updated by the Hulu Cave data and republished, the HuluCal data are preferred for the analysis of the absolute DCF values, especially for the older section.

The center panel of Figure 6.8 shows the detrended DCF (ΔDCF) which range from -10 to 10 %. In the lower graphs, histograms show the distributions of ΔDCF , revealing that most values diverge from the trend by not more than ± 6 %. While the IntCal13 histogram shows no distinct patterns and seems rather uniformly distributed around 0, a distinct bimodal distribution is observed for HuluCal, with medians at -3.0 and 3.1 % ΔDCF . A bimodal distribution is indicative of two configuration modes between which

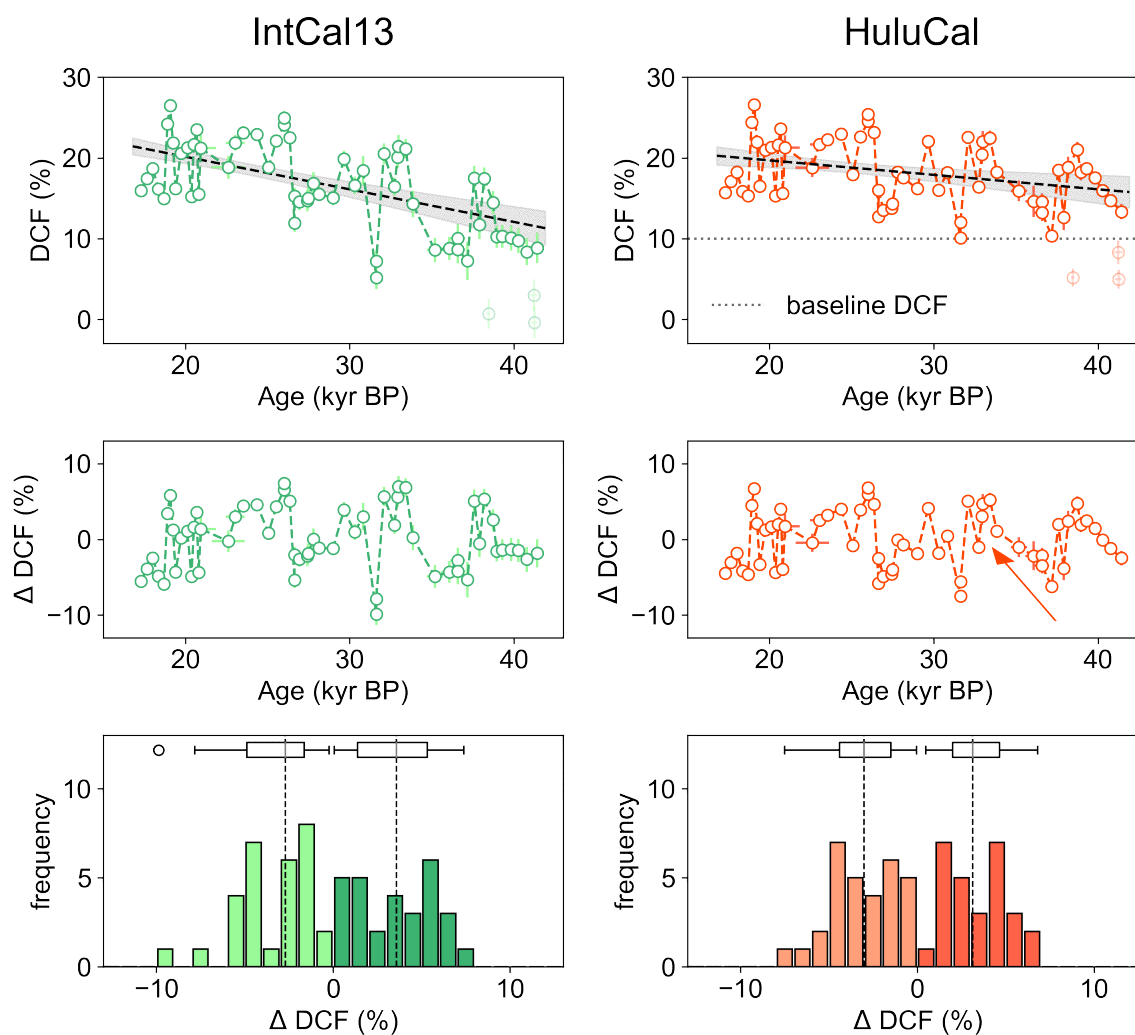


Figure 6.8: So-1 DCF modes in last glacial. The 2σ -filtered ^{14}C data (see text) are shown for both atmospheric references in the top plots for the time-period older than 17 kyr BP, where DCF values show larger variability. A linear approximation was done to correct for a secular DCF trend throughout the LGM (dashed line, gray area shows 90% confidence of the fit). Subsequently, the trend-corrected data are shown in terms of ΔDCF in the middle. In the lower plots the histograms of the distribution of ΔDCF is shown, with bar plots for the ΔDCF histograms, split in $\Delta\text{DCF} < 0$ and $\Delta\text{DCF} > 0$. A bimodal distribution (-3.0% vs. 3.1% ΔDCF) is observed only in the HuluCal data, which reflects the oscillation of So-1 radiocarbon between two glacial soil modes of high ^{14}C input, and a low turnover state of high ΔDCF . The smooth transition after 38 kyr BP (arrow in center right plot) is associated with dryer conditions and contribution of continuously aging SOM.

the Sofular soil environment oscillated. Limestone contribution can be excluded as a reason for DCF variation, due to the insignificant correlation of DCF with the Mg/Ca ratio before 17 kyr BP (see Figure 6.9). The lower mode of the distribution, or lower threshold is identified by high input of CO₂ at near atmospheric levels into the soil zone, bypassing aged SOM and causing low DCF in a near-open karst system. For So-1, the lower Δ DCF mode is equivalent to a lower threshold or baseline DCF at 10% which persistently contributes an offset to atmospheric ¹⁴C, due to dead carbon input from limestone and stable soil material reservoirs. Higher DCF values of So-1 are probably caused by contributions from aging soil material and changes in SOM cycling. The observed insignificant trend in the glacial DCF values (see upper left plot in Figure 6.8) might reflect a general aging process of the soil carbon after 42 kyr BP, which causes an increasing input of old CO₂ and subsequently higher DCF.

Approaches to determine the ¹⁴C age spectrum of soil gas CO₂ from aging SOM have been made by Genty and Massault (1999), Fohlmeister et al. (2011a) and Griffiths et al. (2012). In those studies, the age distribution of SOM was determined by a modeling approach, because fast and substantial changes in atmospheric ¹⁴C concentration, such as the bomb-peak, were quickly transported into the upper soil layers and stalagmite DCF. This enabled the precise modeling of the age and distribution of SOM. For Sofular Cave, this model was applied by Rudzka et al. (2011) to determine the changing soil age spectrum between the YD and the beginning of the Holocene. Their results showed a high input of young SOM at the beginning of the YD, and a balancing of the age spectrum towards the Holocene, which translates into a change of mean soil carbon age from 160 yr to 1100 yr, resulting in a DCF increase of roughly 6% (Rudzka et al. 2011).

This matches the observed shift between the glacial Δ DCF modes in this study (approximately 6% Δ DCF). Thus, the bimodal distribution in the older area could represent a repeating climate-induced oscillation between two distinct states of soil configuration: Firstly, a state of high-input of young SOM, when DCF is near the 10% baseline, which can be caused by strong vegetation development above the cave. Secondly, a steady state of more equilibrated soil reservoirs that is reached after the initially young soil compartment is shrinking and is subsequently replaced by CO₂ produced by microbial decomposition of aged soil organic matter.

The individual transitions from lower to higher Δ DCF in the time series are quite abrupt for the time between 30 and 17 kyr BP, while the shift after the relative minimum in Δ DCF at 38 kyr BP is relatively smooth (arrow in Figure 6.8). This suggests that before 30 kyr BP, soil carbon cycling was slower than after the LGM, where in turn the changes from high to low DCF happen on centennial timescales. The phase of contribution from aging SOM and slower soil carbon cycling coincides with rising Mg/Ca and reduced growth of the stalagmite after 38 kyr BP, which also indicates low infiltration and precipitation. Since decreasing precipitation levels can directly affect vegetation density and productivity (Shumilovskikh et al. 2014, Wegwerth et al. 2016), a reduced direct input of atmospheric ¹⁴C into the soil zone is the consequence, leading to rising DCF. Direct influences of precipitation variation on soil activity were also observed by Peng et al. (2013) in semi-arid

grasslands, who showed faster soil carbon turnover for phases of increased rainfall. The susceptibility of carbon cycling to precipitation variability was also highlighted by Knapp (2002). Shumilovskikh et al. (2014) have identified a major arid phase in Northern Anatolia between 40 and 32 kyr BP, which points to reduced infiltration and slower carbon cycling as a reason for the slower DCF variability. In contrast, the humid phase between 28 and 20 kyr BP which was also discovered by (Shumilovskikh et al. 2014) might have caused faster carbon cycling and higher SOM variability in that time, manifested by fast changes of So-1 DCF.

The D/O events are characterized in So-1 by shifts of -1 to -3 ‰ in $\delta^{13}\text{C}$ within decades to centuries, likely caused by more C3 vegetation and higher soil productivity due to rising temperature and effective moisture (Fleitmann et al. 2009). In the DCF, these events cannot be seen as consistently and their analysis is less conclusive. This might be due to the lower data density compared to stable isotopes or false depth adaptation of the stable isotope data from Fleitmann et al. (2009). The $\delta^{13}\text{C}$ transitions into the D/O interstadials suggest that the ecosystem above So-1 needed roughly 250 yr to adapt to climate change and reach an equilibrium (Fleitmann et al. 2009). After some of the D/O, such as D/O 5, 6 and 8, the DCF decreased (see Figure 6.7), which might indicate short-term input of elevated ^{14}C levels into the soil zone due to increased vegetation in a warmer climate. From 38 to 33 kyr BP, however, the ^{14}C data do not provide conclusive information on how D/O 7 affected the area. The Mg/Ca data do not suggest rapid hydrological change connected to the D/O cycles, which indicates that the observed DCF variability may be linked to temperature variability rather than changing amounts of rainfall.

Correlation analysis of So-1 climate proxies

In the following, the measured climate proxies are analyzed for correlation in the overall record, as well as on distinct timescales. The results of the analysis are summarized by a color coded graph, again for both atmospheric reference data sets (see Figure 6.9).

For the overall record, 84 data pairs were analyzed for IntCal13 (Reimer et al. 2013) and 78 for HuluCal due to the lack of data from Cheng et al. (2018) in the youngest part of So-1. Of the respective data sets, 51 are allocated to the time-span of 17–42 kyr BP, while the rest belongs to the category 10–17 kyr BP. The correlation was quantified by the Pearson's product moment correlation coefficient r and significance was evaluated by p -value determination as a probability of the null hypothesis being correct. While not all correlations will be considered in the text, the most important ones will be singled out. All values can be found in table A.4 and table A.5 in the appendix.

In the overall record, almost all proxies show strong correlation. DCF is significantly correlates to $\delta^{13}\text{C}$, Mg/Ca and Sr/Ca. The positive correlation of DCF and Mg/Ca (IntCal13: $N = 84$, $r = 0.54$, $p < 0.01$; HuluCal: $N = 78$, $r = 0.53$, $p < 0.01$) indicates that DCF is not primarily influenced by changes of limestone dissolution as it is found in studies by Griffiths et al. (2012) and Noronha et al. (2014). Positive correlations of DCF and Mg/Ca are also observed by Therre et al. (2020), where higher precipitation caused a persistently denser vegetation and an increased atmospheric ^{14}C flux into the soil and

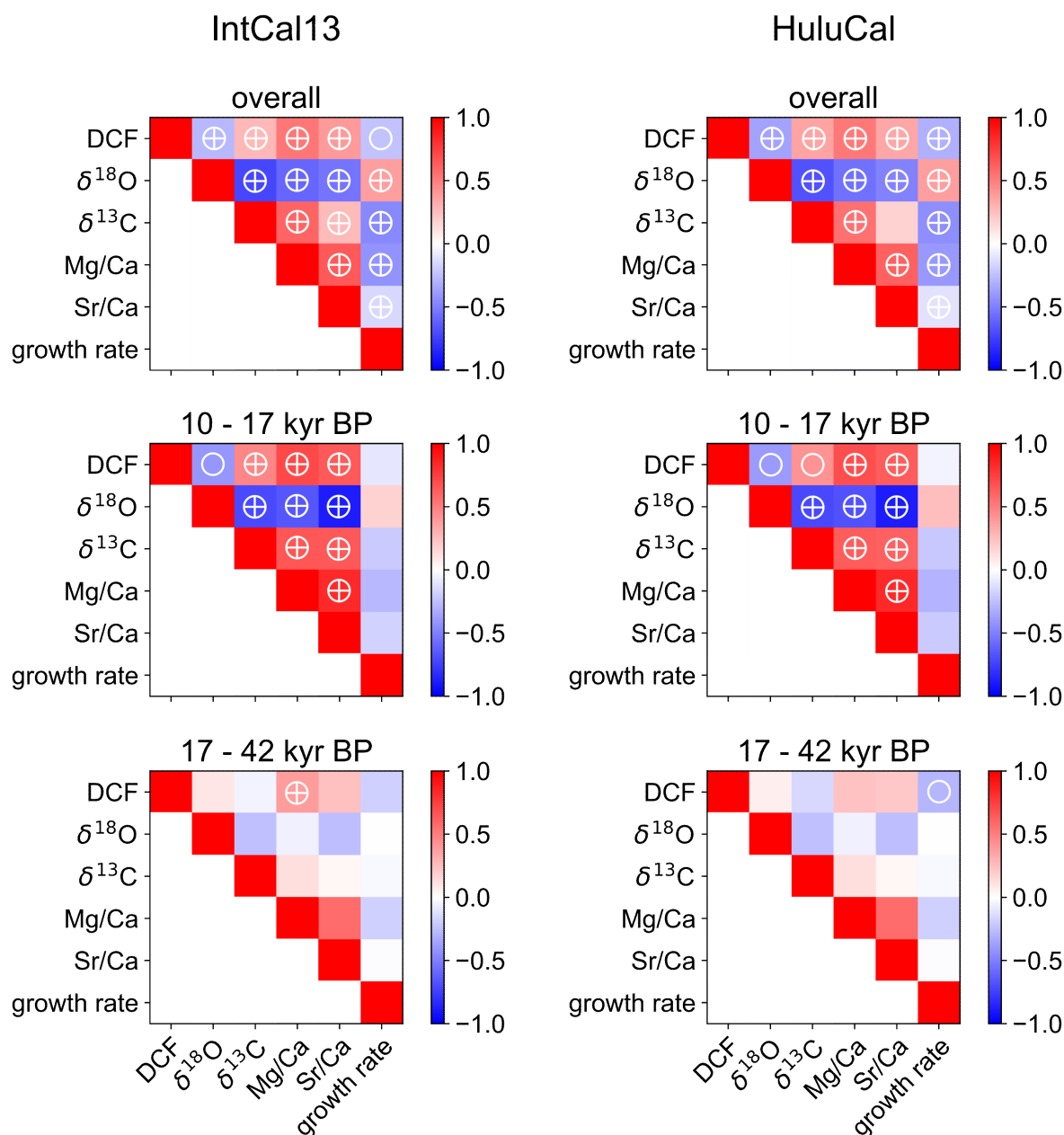


Figure 6.9: Overall correlation analysis of measured proxies of stalagmite So-1. The six plots show the correlation with DCF according to IntCal13 (Reimer et al. 2013) (left) and HuluCal (right) for three time periods, ordered from top to bottom: entire record (10 to 42 kyr BP, HuluCal: $N = 78$, IntCal13: $N = 84$), youngest part (10 to 17 kyr BP, HuluCal: $N = 27$, IntCal13: $N = 33$) and oldest part (17 to 42 kyr BP, $N = 51$). The plot shows the color-coded Pearson r -coefficient from positive (red) to negative correlation (blue). Symbols indicate the level of significance: \oplus for $p < 0.01$, \circ for $p < 0.05$ with respect to the null hypothesis. Significant correlation is observed between DCF, $\delta^{13}\text{C}$, $\delta^{18}\text{O}$ Mg/Ca and Sr/Ca in the youngest part, while the oldest segment does not show comparable levels of correlation. The overall record shows significant correlation for almost all proxies.

subsequently into the stalagmite calcite. However, if the record is split at 17 kyr BP, it becomes clear that the correlations do not hold for the glacial period. Only a few of the covariances are significant before 17 kyr BP (see bottom panels in Figure 6.9), some of the aforementioned trends even reverse. In contrast to the glacial period, the strongest levels of covariance are seen through Termination I, from the beginning HS1 into the emerging Holocene interglacial. The correlation of DCF with $\delta^{13}\text{C}$ could point to a direct climate influence on DCF where warmer periods (lower $\delta^{13}\text{C}$) are accompanied by lower DCF, i.e. more contribution from reservoirs at high ^{14}C concentration. The $\delta^{13}\text{C}$ signature is also sensitive to bio-productivity and C3/C4 plant variation. The increased occurrence of vegetation during warm climate episodes is corroborated by pollen studies from Black Sea sediment cores (Shumilovskikh et al. 2012). A positive correlation of $\delta^{13}\text{C}$ and DCF also suggests that higher C3-vegetation density at Sofular Cave causes ^{14}C input into the soil zone and, eventually, lower DCF. The effects of vegetation on $\delta^{13}\text{C}$ of stalagmite So-1 were described by Fleitmann et al. (2009).

For the time period older than 17 kyr BP, no significant correlations are observed. This indicates that the particular time series is controlled by a process, which is not captured by any of the other measured proxies. For example, yet unresolved atmospheric ^{14}C variations might be the cause for DCF variability, that are not manifested in any of the other proxies.

6.4.4 Atmospheric ^{14}C during the Laschamp geomagnetic event

The reconstruction of atmospheric ^{14}C concentration is the basis for radiocarbon age calibration. In all studies providing stalagmite data to IntCal13 (Reimer et al. 2013), the particular stalagmites hypothesized an overall low and constant reservoir age. Adding speleothem data to the calibration curve always relies on the assumption that the constant DCF, measured during a reference period, can be extrapolated to persist over the entire growth period of the speleothem, notwithstanding global or local climate variations that occurred while the stalagmite grew. This approach was successful in many studies and has provided valuable contributions to atmospheric $^{14}\text{C}/^{12}\text{C}$ determination (Beck et al. 2001, Hoffmann et al. 2010, Southon et al. 2012, Cheng et al. 2018).

In this study, one of these major prerequisites is fulfilled: Considering the youngest investigated part of stalagmite So-1 between 10 and 14 kyr BP, the DCF averages at 13.24 % with a low standard deviation of 1.55 %. Whereas in the Bahamas speleothem data (Beck et al. 2001, Hoffmann et al. 2010), a systematic shift in DCF is visible, no similar deviations over climatic changes can be found in the So-1 ^{14}C data. However, considering the large DCF variability between 17 and 25 kyr BP, it becomes clear that the mere extrapolation of the initially determined DCF will not reproduce the signal of atmospheric ^{14}C input. Rather, the high fluctuations of the DCF values are indicative of signals from hydrological or karst processes that are directly or indirectly connected to climatic influences. This is underlined by the hydrological proxies that exhibit large variability during the last glacial (especially Mg/Ca) throughout a period from 27 to 17 kyr BP.

Studies in tropical, warmer and humid conditions have documented the influence of

hydrological conditions on the DCF in stalagmites (Griffiths et al. 2012). The fairly constant Mg/Ca and Sr/Ca ratios in the oldest investigated part of So-1 indicate that limestone dissolution influence on the ^{14}C incorporation is unlikely in this time. If climatic influences did not significantly affect the ^{14}C concentration, the oldest part of So-1 could provide insights into atmospheric ^{14}C variation in that time. The approach of the performed analysis is to correct the radiocarbon data of So-1 by one reference DCF value for all data to fit best to the atmospheric data provided by HuluCal. In this case, the absolute ^{14}C concentration cannot be derived, but relative changes are manifested in the record. One example for a distinct feature in atmospheric ^{14}C which was recently revealed by Cheng et al. (2018) is the increase of $\Delta^{14}\text{C}$ at geomagnetic events, such as the Laschamp event which occurred between 42.25 and 39.7 kyr BP with a minimal strength of the geomagnetic field around (41.10 ± 0.35) kyr BP (Laj et al. 2000, Lascu et al. 2016). The consequence of the event was a higher input of cosmic and solar radiation into the atmosphere causing an increased flux of thermal neutrons and subsequently higher ^{14}C production rates (Elsasser et al. 1956, Lal and Peters 1967). The higher atmospheric ^{14}C concentration between 42 and 39 kyr BP was observed in stalagmite records for the first time by Cheng et al. (2018) in the Hulu Cave speleothems.

It can be assumed that a similar signal of higher radiocarbon concentrations in the atmosphere can also be seen in the So-1 stalagmite, if soil carbon cycling and dead carbon variations did not overprint the atmospheric signal. For the following analyses, only the *HuluCal* reference and the DCF values based on this curve are considered (see Figure 6.10), because IntCal13 does not reflect the Laschamp event. In the uncorrected $\Delta^{14}\text{C}$ data of So-1, a pattern can be distinguished between 37.5 to 41.5 kyr BP that seems to closely follow the atmospheric trends as seen in the data from Cheng et al. (2018). The mean DCF in the this period is $(15.87 \pm 4.17)\%$. So-1 data was subsequently corrected for this offset and the $\Delta^{14}\text{C}$ recalculated, resulting in a mean shift of $(273 \pm 18)\%$ with respect to the original ^{14}C data. In Figure 6.10, uncorrected and DCF-corrected $\Delta^{14}\text{C}$ values of So-1 are shown in comparison to the HuluCal curve and stalagmite data from Hulu Cave (Cheng et al. 2018). Now, the DCF-corrected time series ($\Delta^{14}\text{C}_{\text{corr}}$) between 37.5 to 41.5 kyr BP represent atmospheric ^{14}C variation, similar to those found by Cheng et al. (2018), which corroborates the higher atmospheric ^{14}C concentration between 37.5 to 41.5 kyr BP compared to IntCal13.

An interesting feature is the peak in So-1 data at approximately 41.2 kyr BP, centered at the time which is associated with the minimal geomagnetic field intensity during the Laschamp reversal (Lascu et al. 2016). In the So-1 record, the two data points are roughly 220 and 160 ‰ above the HuluCal reference data, which might indicate a short period of maximum atmospheric ^{14}C concentration in the time of lowest magnetic field intensity (dark-gray area in Figure 6.10). A Gaussian fit was applied around the residual ^{14}C signal ($\Delta\Delta^{14}\text{C}$, see lower axis in Figure 6.10), yielding an amplitude of roughly 190 ‰ $\Delta^{14}\text{C}$ and a timescale of 350 yr (FWHM).

The production rate modulation of ^{14}C and other cosmogenic nuclides during geomagnetic events was estimated by several studies (Masarik and Beer 1999, 2009, Hoffmann et al. 2010, Cauquoin et al. 2014), with differing results as for the Laschamp event's effect on

atmospheric radiocarbon. According to a review of Cauquoin et al. (2014), the production rate changes by a factor of 2 to 3 depending on the used model, which translates into an atmospheric $\Delta^{14}\text{C}$ increase to up to 500 ‰ and 600 ‰ at the minimal activity during the reversal. Similar implications were made by a study on modeled ^{14}C production rates based on ^{10}Be fluxes derived from the Vostok ice-cores (Adolphi et al. 2018). These predictions were confirmed by the Kauri tree-ring data (Muscheler et al. 2014) and the recent stalagmite-based atmospheric record (Cheng et al. 2018).

The question arises how fast a distinct and short-lived change in atmospheric radiocarbon can be transmitted into stalagmite calcite. Turnover times of the soil respired carbon were investigated in Adolphi et al. (2018) for stalagmites with various DCF and the soil turnover times. It was found that turnover times of soil carbon act as an integrator (i.e. low-pass filter) on the input signal depending on the assumed soil CO_2 age. Mean soil

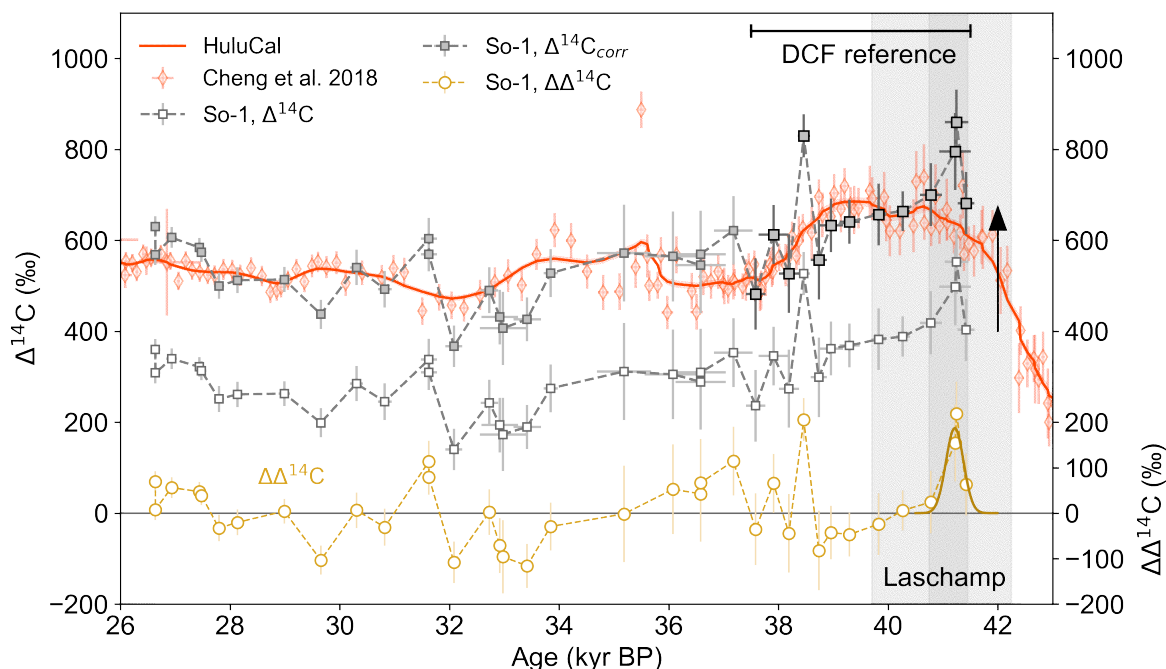


Figure 6.10: $\Delta^{14}\text{C}$ of stalagmite So-1 from 25 to 43 kyr BP. The measured $\Delta^{14}\text{C}$ is shown as white squares. In the DCF reference area, the mean DCF of $(15.87 \pm 4.17)\%$ was corrected for (equivalent $\Delta^{14}\text{C}$ shift represented by black arrow), and the corrected data ($\Delta^{14}\text{C}_{\text{corr}}$, gray squares) are shown in relation to HuluCal. $\Delta^{14}\text{C}_{\text{corr}}$ of So-1 show a good agreement with the relative changes in atmospheric $\Delta^{14}\text{C}$ (HuluCal), implying the stalagmite can potentially determine relative atmospheric variability. The rise of atmospheric ^{14}C concentration during the Laschamp maximum around 41.2 kyr BP is visible as a peak in the residual data ($\Delta\Delta^{14}\text{C}$) of the DCF-correction plotted on the lower axis.

ages of less than 250 yr in their model reflected short-term signal changes of atmospheric $\Delta^{14}\text{C}$ on sub-centennial timescales for both assumed DCF (5.8 % and 25.7 %, respectively) with lags in the stalagmite signal of less than 100 yr. This means that short soil turnover times are the determining factor for an atmospheric ^{14}C peak signal to be represented in stalagmite ^{14}C data. Rudzka et al. (2011) have determined soil carbon ages of less than 500 yr as a maximum value for the soil configuration above Sofular Cave from radiocarbon ages of So-1. The influence of SOM and carbon cycling variability was corroborated by the elaborate analysis in section 6.4.2, where short term inputs of ^{14}C signals manifested in fast declines of So-1 DCF and subsequent recovery to higher values. This implies relatively short mean turnover times in the soil zone and supports the assumption that the intensified increase in $\Delta^{14}\text{C}_{\text{corr}}$ of So-1 with an approximated timescale of 350 yr could reflect an atmospheric signal, connected to the coinciding Laschamp minimum and subsequently higher ^{14}C production rates (Lascu et al. 2016).

Consequently, the presented data confirm that IntCal13 systematically underestimated $\Delta^{14}\text{C}$ during the Laschamp reversal between 38 and 42 kyr BP, as it was discussed by Cauquoin et al. (2014), Muscheler et al. (2014), Adolphi et al. (2018), shown by Cheng et al. (2018), Staff et al. (2019). The timing of the assumed maximum production rate of ^{14}C during the Laschamp reversal coincides with a previously unresolved peak in ^{14}C activity in stalagmite So-1 by an additional 190 ‰ $\Delta^{14}\text{C}$ on a timescale of roughly 350 years. The sufficiently low soil carbon turnover times above Sofular Cave indicate that a so far not resolved strong, short-lived increase of atmospheric $\Delta^{14}\text{C}$ is present in So-1 ^{14}C data. Future efforts to investigate the intensity and amplitude of this singularity and its influence on stalagmite records require further modeling and radiocarbon-based studies on stalagmites.

Although So-1 cannot be utilized to determine the absolute values of past atmospheric $\Delta^{14}\text{C}$, it provides, nonetheless, a confirmation of the relative changes in the atmospheric ^{14}C concentration. Robust age modeling by the U-series method ensures that the timing of relative ^{14}C change is precisely and accurately determined. If limestone dissolution dynamics can be excluded as the cause for DCF variability and if soil turnover times are sufficiently low to reflect short-term atmospheric changes, stalagmites can be considered for relative atmospheric ^{14}C reconstruction and thus contribute to radiocarbon calibration. These prerequisites are fulfilled for the stalagmite So-1 in the considered time frame.

6.5 Conclusion

Stalagmite So-1 has been previously investigated as an environmental archive that reflects the vast climatic changes during the last glacial and in the Holocene (Fleitmann et al. 2009, Göktürk et al. 2011, Rudzka et al. 2011). Based on the comprehensive record that was created by a new, high-precision and high-accuracy age model, an extensive radiocarbon data set and elemental ratio measurements, it was possible to gain insight into the carbon cycling processes and climate dependence of stalagmite ^{14}C signature. Stalagmite So-1 grew under near-open system conditions and shows high influence of soil organic matter dynamics over most parts of the investigated period. The DCF is

relatively constant after 16 kyr BP which was used to refine the age-depth model in areas of ambivalent results from U-series dating. In contrast, high fluctuations of DCF before 16 kyr BP reflect to climate-induced changes of soil carbon cycling. The glacial DCF data show that an oscillation existed between a lower threshold DCF mode on the one hand, and a mode of additional contribution from aged SOM to the soil gas CO_2 on the other hand. By a multi-proxy correlation analysis, it could be shown that glacial DCF is mostly uncorrelated to other measured proxies. Similar to the Moomi Cave stalagmite ^{14}C study (Therre et al. 2020), So-1 DCF does not exhibit negative correlation with Mg/Ca, showing that the DCF is not controlled by hydrological variability and associated karst dissolution systematics. The determined relative structure of So-1 ^{14}C in the time of the Laschamp geomagnetic reversal (Laj et al. 2000, Lascu et al. 2016) confirms a rise in atmospheric $\Delta^{14}\text{C}$ between 42 and 38 kyr BP, which was first shown by Cheng et al. (2018). An additionally discovered pattern in So-1 ^{14}C also strongly indicates even higher atmospheric ^{14}C concentrations than assumed at the time of minimal geomagnetic activity.

Thus, it is suggested that stalagmite So-1 can contribute to the reconstruction of atmospheric ^{14}C . If the climatological proxies can exclude influence of limestone dissolution or soil variability on DCF, limited and relative reconstruction of atmospheric ^{14}C concentration changes can be achieved from stalagmite ^{14}C records. Considering the Hulu Cave record (Cheng et al. 2018), it is important to note that a constant DCF during Termination I, as observed for both So-1 and Hulu Cave, is still potentially subject to significant changes in the glacial period. Therefore, the carbon cycling system of considered records need to be carefully assessed before atmospheric reconstruction is feasible.

While several records from stalagmites have been used in the past for absolute determination of DCF (Beck et al. 2001, Hoffmann et al. 2010, Southon et al. 2012), it is clear that the robust chronology and continuous deposition of this climate archive is a major advantage in the effort to improve the calibration data sets. This study proves that even without a constant offset to the atmosphere, stalagmites can be an important contribution to atmospheric ^{14}C reconstruction.

7 Reviewing Stalagmite DCF Drivers in Various Climate Settings

Several stalagmites have been investigated with respect to their radiocarbon signature during the last years at the Institute of Environmental Physics (IUP) in Heidelberg, some during Bachelors' theses that were supervised in the course of this dissertation. The two most comprehensive records were presented in the previous chapters, together with an extensive investigation on the control mechanisms of radiocarbon incorporation. In this final chapter of the dissertation, all records that were analyzed will be brought together in a summary of the observed processes in stalagmite radiocarbon. The data are compared to selected published records, which are exemplary for distinct forcing aspects like carbon cycling, climate parameters, and limestone dissolution.

7.1 Introduction

The mechanisms of isotope geochemistry in stalagmites and their influence on radiocarbon signature and stable carbon isotopes have been investigated intensively in the past (Hendy 1971, Genty et al. 1999, 2001). Limestone carbonate dissolution in the karst zone above the cave has been identified as a crucial parameter for the stable carbon and radiocarbon signature in stalagmite calcite. It was argued that in an extreme case of a closed system, where the water phase in the karst is isolated from soil air CO_2 , the precipitated stalagmite calcite will theoretically have a 50 % ratio of each dead carbon and atmospheric (modern) carbon, i.e. a dead carbon fraction (DCF) of 50 %. Under conditions approaching an open system, in which the solution partially equilibrates with residual soil gas in the epikarst, this balance will shift towards higher ^{14}C concentrations in the drip water (Hendy 1971). Using hydro-geological proxies, it could be shown for caves in tropical settings and under monsoonal influence, that a varying precipitation amount had a direct impact on limestone dissolution (Griffiths et al. 2012, Noronha et al. 2014, Lechleitner et al. 2016a). In these cases, higher rainfall amount results in a waterlogged soil and epikarst, which inhibits the exchange across the water-gas phase, and is therefore associated with more closed conditions, and vice versa. Apart from the root respiration CO_2 at atmospheric levels and the limestone carbonate, the third major component to determine the ^{14}C signature of stalagmites is the age spectrum of the soil organic matter (SOM) above the cave. The climatic influence on soil carbon cycling and the consequence for dead carbon in stalagmites was reported by numerous case studies in multiple climate zones (Genty et al. 2001, Oster et al. 2010, Fohlmeister et al. 2011b, Rudzka et al. 2011, Therre et al. 2020).

However, studies from the recent years have reported DCF values that cannot be

explained by any of the aforementioned mechanism alone. Two speleothems with highly increased DCF from Italy (Bajo et al. 2017) and an alpine cave in Austria (Spötl et al. 2016) showed how sulfuric acid input from the soil zone can cause excessive carbonate dissolution, even without large contribution from respired or SOM-derived CO₂ in the soil. The consequences are DCF values even higher than the theoretical limit of 50 % and $\delta^{13}\text{C}$ significantly shifted to the limestone signature. The other extreme of a very low and constant DCF in Hulu Cave has been associated with a partial sandstone ceiling above the cave, instead of limestone, which minimizes dead carbon input from carbonate dissolution (Southon et al. 2012, Cheng et al. 2018).

Over the last years, numerous stalagmites were investigated at the IUP in Heidelberg, which will be compiled and discussed with respect to the possible environmental drivers in this chapter. In addition, DCF records from some of the aforementioned studies are included in this general discussion for comparison, focusing on the processes that determine the DCF variability. The summary and review of the gathered data will provide overview and give implications for the future use of DCF as a climate proxy in combination with other proxies.

7.2 Compiled stalagmite DCF studies and sites

The compiled records are graphically summarized in the map (see fig. 7.2). They cover several climate zones and vary substantially in their level of DCF and stable carbon signature. Moomi Cave (Socotra Island) and Sofular Cave (Northern Turkey) were discussed in the two previous chapters of this dissertation. In addition, data from Hoti Cave (Oman), Schratten Cave (Switzerland), and Cueva Larga (Puerto Rico), is presented, which was gathered over the last years at the IUP, during Bachelors' projects (Therre 2014, Proß 2018, Schandl 2019). In these cases, the sample preparation and measurements were conducted according to the procedures, which was utilized for the other case studies in this dissertation. With U-series derived age models, the ^{14}C reveal significant deviations from the chronological stratigraphy, which reflects in temporal variability of the DCF. A graphical summary of the records in context with the atmospheric radiocarbon calibration record IntCal13 (Reimer et al. 2013) is given in Figure 7.1.

The selected published stalagmite ^{14}C records from external sources are from Corchia Cave (Italy, Bajo et al. 2017), Heshang Cave (China, Noronha et al. 2014), Hulu Cave (China, Cheng et al. 2018), Liang Luar (Indonesia, Griffiths et al. 2012), Obstanser Ice Cave (Austria, Spötl et al. 2016) and Yok Balum Cave (Belize, Lechleitner et al. 2016a). Besides ^{14}C data, mean $\delta^{13}\text{C}$ values and cave temperatures were retrieved for the respective samples. The multi-site study of European caves from Genty et al. (2001)

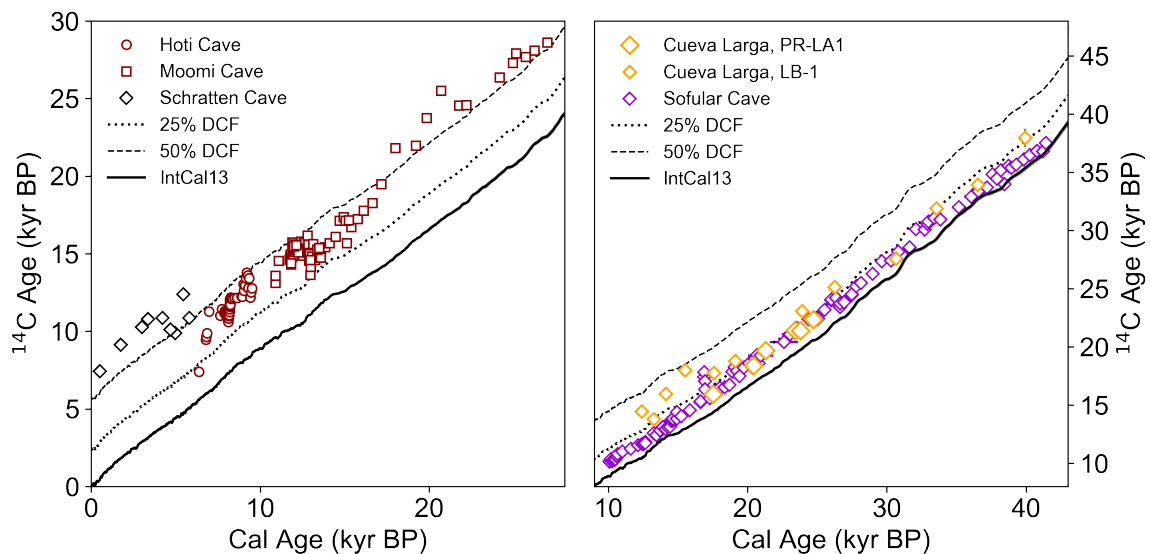


Figure 7.1: Stalagmite ^{14}C data from Hoti Cave (Therre 2014), Moomi Cave (Therre et al. 2020), Schratten Cave (Proß 2018), Cueva Larga (Schandl 2019, and unpublished data) and Sofular Cave in context to atmospheric radiocarbon reference IntCal13 (Reimer et al. 2013). The dashed lines indicate the expected ^{14}C ages for two different DCF values (25 % and 50 %). Differences can be seen in the offset between atmospheric and stalagmite DCF between the two subplots.

was also included. The data are summarized in Table A.8. Here, IntCal13 (Reimer et al. 2013) is consistently utilized as reference for the determination of DCF to preserve the independence of the Hulu cave as an individual record. It must be noted that a significant part of the Hulu cave data (Southon et al. 2012) is already included in the IntCal13 compilation. Thus, the atmospheric reference from IntCal13 is partially biased by stalagmite records between 27 and 14 kyr BP (Reimer et al. 2013).

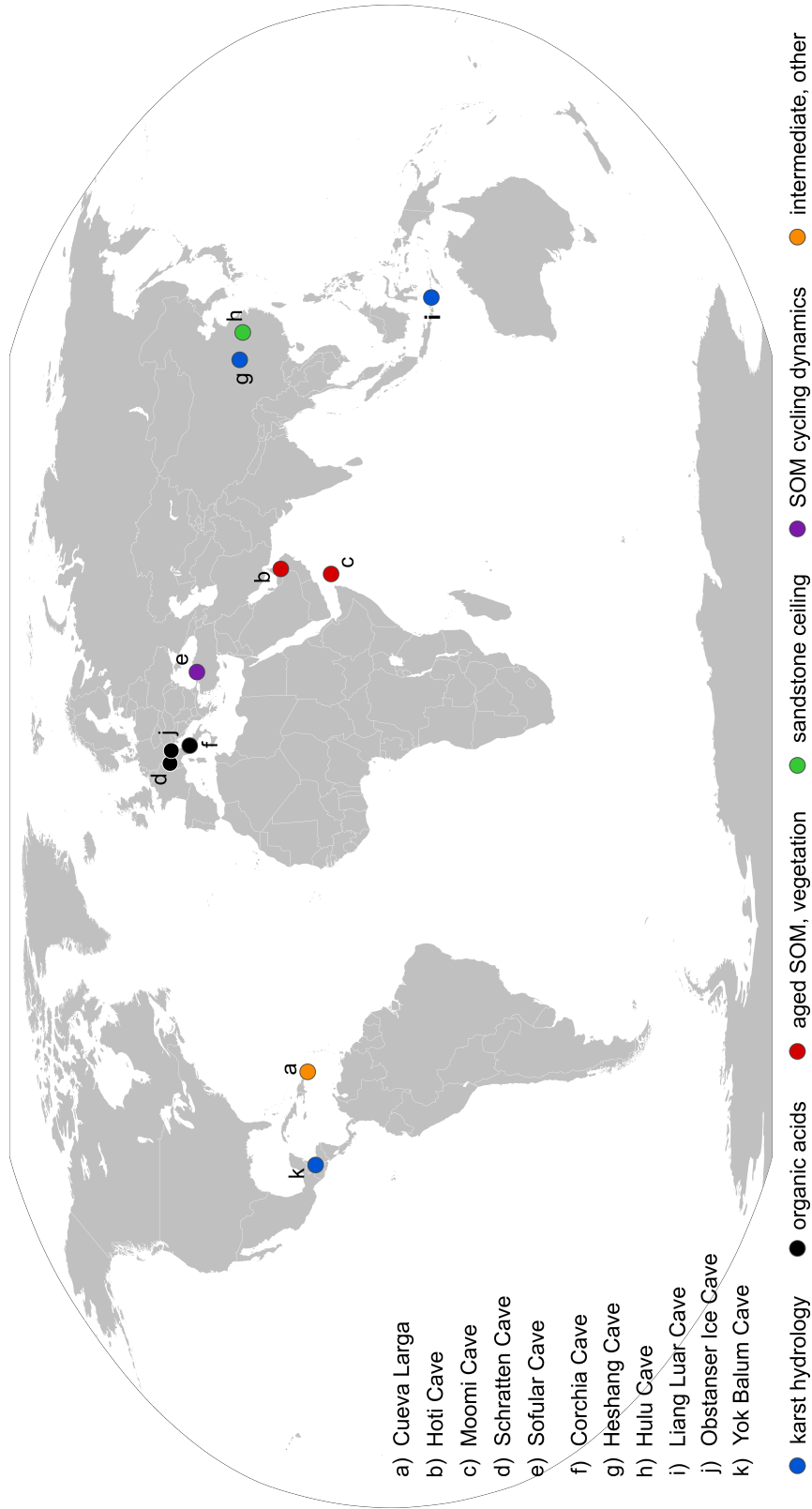


Figure 7.2: Location of selected caves with ^{14}C studies on stalagmites. Data from caves a) through e) is presented in this dissertation. Other caves and the references for ^{14}C data are Corchia Cave (Bajo et al. 2017, f), Heshang Cave (Noronha et al. 2014, g), Hulu Cave (Cheng et al. 2018, h), Liang Luar Cave (Griffiths et al. 2012, i), Obstanzer Ice Cave (Spötl et al. 2016, j) and Yok Balum Cave (Lechleitner et al. 2016a, k). The color of the symbols refers to the dominant processes in ^{14}C incorporation. Blue: hydrological variations, red: aged SOM with vegetation influence, black: increased limestone dissolution by organic acids. Sofular Cave and Cueva Larga show intermediate behavior, which is explained in the discussion. The European sites from Genty et al. (2001) are omitted in the map.

7.3 Discussion

7.3.1 Carbon cycling influence on DCF

The radiocarbon signature of the soil gas CO₂ above a cave is a crucial factor to determine the level of radiocarbon in the formed stalagmite calcite. The input of CO₂ at modern (i.e. atmospheric) ¹⁴C signature into the soil matrix through root respiration acts as the carbon reservoir with the highest ¹⁴C concentration in speleothem formation. However, deviations of the effective soil gas ¹⁴C signature from the atmospheric level are observed, if aged organic material contributes a ¹⁴C-depleted signal to the gas mixture. This leads to a decreased level of stalagmite radiocarbon (Genty et al. 2001, Fohlmeister et al. 2011a). Studies focusing on the age spectra of organic soil material have proved that the ¹⁴C signature of SOM strongly depends on the soil dynamics and turnover characteristics (Trumbore 2000, 2009). It was also determined, that the dynamics of soil carbon are dependent on the depth of the respective soil profiles (Mathieu et al. 2015, Balesdent et al. 2018). For instance in tropical soil profiles, the emergence of very old carbon stocks is directly linked to soil depth (see Figure 7.3), where roughly 60 % of the upper 10 cm of soil are younger than 100 yr, whereas at 50 cm, the share drops to 20 % (Balesdent et al. 2018). Carbon stocks older than 1000 yr predominantly form in deep, stable soil layers, where turnover times increase significantly and the reservoirs are stabilized from fast decay (Balesdent et al. 2018). Stabilization processes are linked to climate factors like low temperature, but can also be associated with physical SOM inclusion or inhibition of microbial decay (Trumbore 2009). Modeling efforts were made to infer the ¹⁴C signature

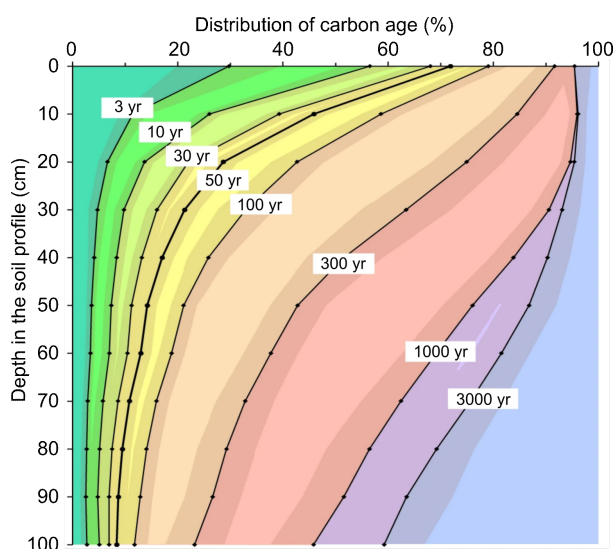


Figure 7.3: In a tropical soil study covering 55 sites, it was shown that the age distribution of old SOM depends on soil layer depth. Carbon stocks younger than 100 yr make up roughly 60 % at 10 cm. In layers deeper than 60 cm, more than 80 % of the carbon matter is older than 100 yr. Carbon stocks older than 1000 yr are predominantly formed in deep soil layers. Figure taken from Balesdent et al. (2018).

of soil CO₂ from the proportion and age distribution of soil compartments (Genty and Massault 1999) and have been successfully used to deduce the soil configuration above caves from stalagmite ¹⁴C and δ¹³C (Fohlmeister et al. 2011a, Rudzka et al. 2011, Griffiths et al. 2012).

The temperature dependence of DCF has been directly linked to SOM cycling variations above the investigated caves in a multi-site comparison study on speleothems in temperate climate conditions (Genty et al. 2001). They found that rising temperatures cause a significant increase in soil carbon turnover rates and therefore shift the soil gas CO₂ signature to higher ¹⁴C concentrations, causing lower stalagmite DCF. In turn, colder climate conditions favor organic matter accumulation with lower turnover rates than in warmer settings.

When the ¹⁴C data from temperate sites (Genty et al. 2001) are put into context with the other records of this chapter from different climate settings, it becomes clear that the

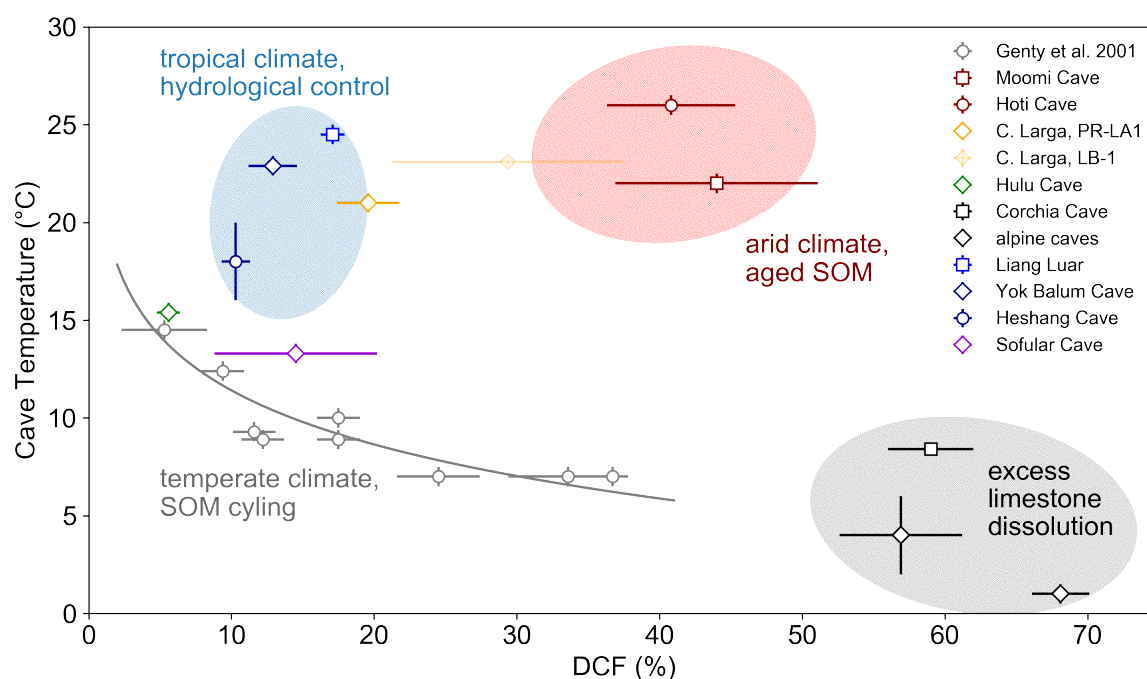


Figure 7.4: DCF in relation to modern cave temperature for the selected sites. The originally proposed logarithmic functional relationship for European caves is shown together with the respective data in gray (Genty et al. 2001). Hulu Cave and Sofular data seem to be in agreement with the proposed model. However, the postulated relation does not hold for caves governed by excess limestone dissolution with higher DCF (gray area). For tropical caves where hydrological changes are directly connected to DCF (blue) and arid regions in lower latitudes (red), the relation also does not hold. The data for Cueva Larga show large uncertainties for stalagmite LB-1, but PR-LA1 data seems to display no significant influence of aged SOM.

proposed logarithmic relationship of cave temperature and DCF does not hold. Figure 7.4 shows that the records from Hoti Cave and Moomi Cave in warmer and more arid settings show higher DCF than projected by the temperature-dependent model. The proxies of both records indicate a high influence of very old SOM on the DCF signature. This contradicts the predictions for carbon cycling in warmer climates and proves that carbon stocks at very high age can form in very warm climates as well (Therre et al. 2020). In Chapter 5, the strong influence of climate change on the DCF signature was shown, effectively proving that in arid conditions, the SOM cycling is far more sensitive to small changes in infiltration variability, which affects SOM turnover times in warm climates and subsequently stabilizes or mobilizes old carbon stocks (Therre et al. 2020).

In the studies on tropical stalagmites (Griffiths et al. 2012, Noronha et al. 2014, Lechleitner et al. 2016a), DCF variability over time is controlled by hydrological conditions and their impact on limestone dissolution. The mean DCF value of the individual records is higher than expected from the proposed model by Genty et al. (2001). The higher overall level could reflect generally enhanced contribution from host rock dissolution than in the European sites from Genty et al. (2001), but might also be indicative of a deeper soil layer with a larger share of older SOM at higher depths, as demonstrated for tropical soil profiles by Balesdent et al. (2018).

Three stalagmites show an exceptionally high DCF, even higher than the theoretical limit of 50% DCF (Spötl et al. 2016, Bajo et al. 2017, Proß 2018). This is most likely a consequence of low contribution from soil CO₂ and of limestone dissolution driven by the input of sulphuric acids, which caused extremely high DCF. The implications of this scenario on $\delta^{13}\text{C}$ are discussed in section 7.3.2.

For the Sofular and Hulu records, the radiocarbon levels indicate near-open system conditions throughout the growth period of the stalagmites (Rudzka et al. 2011, Cheng et al. 2018, and chapter 6). Considering that Hulu Cave and Sofular Cave are at least partially glacial records, the modern cave temperatures, which are used in Figure 7.4 are systematically too high. Therefore, both records are likely compatible with the proposed temperature dependence on the stability of soil carbon cycling. This corroborates the model for temperate, humid climates and shows that Hulu Cave and Sofular Cave mean DCF mainly reflect climate controlled SOM turnover rate due to temperature, humidity, and vegetation density variability Genty et al. (2001). This was discussed in detail for Sofular Cave (Rudzka et al. 2011, and this study). It was hypothesized that at Hulu Cave, the exceptionally low and constant DCF is linked to sandstone host rock, in which dead carbon contribution is virtually switched off. The observed DCF is believed to be derived from dissolution of particulate carbonate in the soil and CO₂ from aged SOM.

The combined records indicate that a direct influence of temperature on DCF can only hold for temperate climates, where soil turnover rates are determined by temperature. In tropical climates, higher DCF might be caused by deep soil layers and contribution from aged SOM, while hydrological changes mainly cause temporal DCF variability. In arid settings, the SOM is far more sensitive to climate change, and the enhanced formation of very old soil matter in dry conditions is favored.

7.3.2 Limestone dissolution processes and climate dependence

Limestone dissolution by percolation water is described by its two extreme cases of open and closed systems (Hendy 1971, Genty et al. 1999). Depending on the carbon exchange rate across the interface between the soil gas and the water in the epikarst, the ^{14}C content of drip water and stalagmite carbonate is sensitive to the nature of limestone dissolution. A correlation of hydrological proxies with stalagmite DCF was determined by several studies. Hence, hydrological conditions in the karst are believed to affect limestone dissolution (Griffiths et al. 2012, Noronha et al. 2014, Lechleitner et al. 2016a). It is therefore possible to trace climate change and precipitation changes in speleothem records which are governed by the shifts between open and closed karst dissolution (Noronha et al. 2014). The influence of limestone dissolution on stable carbon isotopes was already described by Hendy (1971) and shown in many case studies (Fohlmeister et al. 2010, Minami et al. 2015) and modeling approaches (Fohlmeister et al. 2011b, 2020, Griffiths et al. 2012). However, it was demonstrated for some instances that the influence of closed vs. open conditions on $\delta^{13}\text{C}$ of stalagmite calcite may be weak (McDermott 2004, Fohlmeister et al. 2011b). For instance, speleothems from Baradla Cave, Hungary exhibit large differences in open to closed dissolution system conditions, but almost negligible $\delta^{13}\text{C}$ effects (Demény et al. 2017).

The theoretical approach by Hendy (1971) modeled the expected DCF and stalagmite $\delta^{13}\text{C}$ for open and closed system conditions at typical parameters (soil CO_2 at $\delta^{13}\text{C} \approx -24\text{‰}$, $T = 10^\circ\text{C}$) assuming isotopic equilibrium between solution and calcite. Diffusion processes in the soil cause the $\delta^{13}\text{C}$ to be approximately 4‰ higher than initially assumed by the model (Cerling 1984), therefore, the modeled relation by Hendy (1971) underestimates the calcite $\delta^{13}\text{C}$. Nonetheless, the general trend is still valid (see dashed line in fig. 7.5). It was shown by Fohlmeister et al. (2011b), that very high partial CO_2 pressures in the soil zone can cause lower $\delta^{13}\text{C}$ signatures and lower DCF than initially modeled by Hendy (1971). This can be seen for the SU2 record from (Genty et al. 2001), where higher CO_2 concentrations in a peat bog above the respective cave resulted in significantly lower $\delta^{13}\text{C}$ than seen in the other records.

Enhanced limestone dissolution by organic acid can cause highly increased DCF in stalagmites, which was shown in studies at Obstanser Ice Cave (Spötl et al. 2016) and Corchia Cave, Italy (Bajo et al. 2017), where the DCF exceeds 50%. Sulphuric acids may originate from oxidized pyrite in the host rock, which is a sulphate containing mineral (Borsato et al. 2015). In these cases, the contribution of soil gas CO_2 from root respiration and microbial decomposition of SOM to limestone dissolution is significantly reduced. Therefore, the $\delta^{13}\text{C}$ values of the speleothems approach the signature of the limestone endmember (see fig. 7.5). This effect is visible in the Corchia Cave data (Bajo et al. 2017), as well as in both alpine records (Spötl et al. 2016, Proß 2018). At Corchia Cave (Bajo et al. 2017), a positive correlation of the DCF and $\delta^{13}\text{C}$ time series is observed.

Once the drip water reaches the cave, a significant increase in $\delta^{13}\text{C}$ can occur due to enhanced kinetic fractionation. This is especially important for prior calcite precipitation (PCP). In this scenario, enhanced CO_2 degassing and carbonate precipitation will shift the isotopic signature of the remaining carbon to higher values. This causes an increase

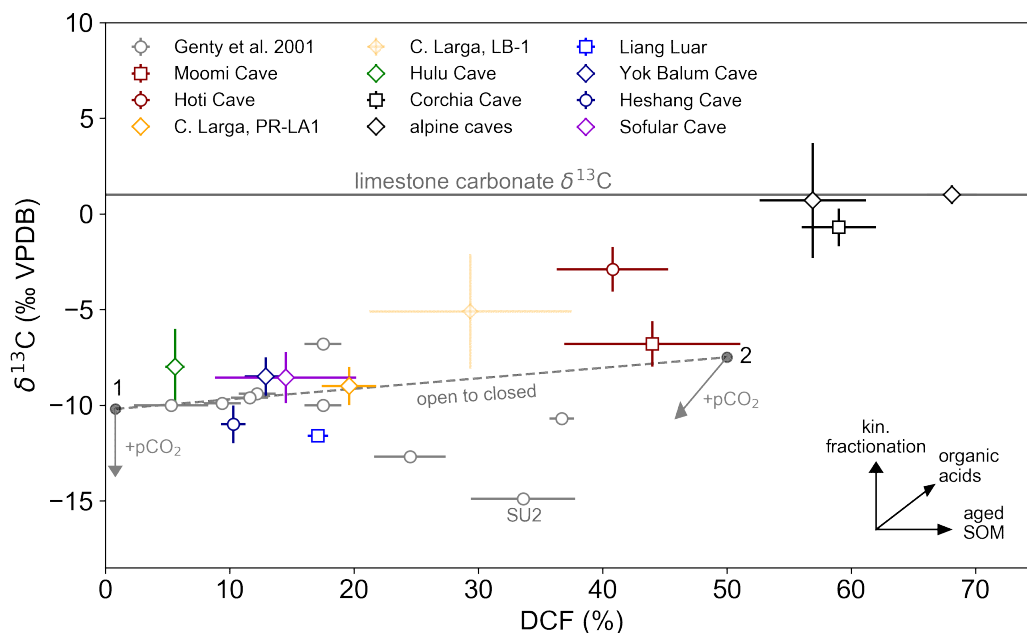


Figure 7.5: DCF in relation to stalagmite $\delta^{13}\text{C}$ for the selected sites. The dashed line connects two points of extreme cases of limestone dissolution, where "1" corresponds to open and "2" to closed conditions (adapted from Hendy 1971). The relevant processes causing deviations from the model are indicated by arrows, included are aging SOM, sulphuric acid dissolution, kinetic fractionation, and increasing partial CO_2 pressure in the soil zone (Hendy 1971, Scholz et al. 2009, Fohlmeister et al. 2011a,b, Bajo et al. 2017). The gray horizontal illustrates a typical limestone $\delta^{13}\text{C}$ signature (Hendy 1971). For the alpine records (Spötl et al. 2016, Proß 2018) and Corchia Cave (Bajo et al. 2017), the high DCF $\delta^{13}\text{C}$ is closely related to enhanced limestone dissolution by sulphuric acids. Moomi and Hoti Cave (Therre 2014, Therre et al. 2020) data suggests near-closed system conditions with a high influence of aged SOM on DCF, while low $\delta^{13}\text{C}$ values are measured, probably caused by kinetic fractionation (Shakun et al. 2007). A high contribution of aged SOM was also determined for stalagmites SU-96-7 and SU2 (Genty et al. 2001), while high partial CO_2 pressures in the peat bog environments cause lower $\delta^{13}\text{C}$ (Fohlmeister et al. 2011b). The other records are mostly compatible with regular calcite dissolution systematics, and short-term soil carbon cycling.

of stable isotope signature in stalagmite calcite (Scholz et al. 2009, Frisia et al. 2011, Dreybrodt and Scholz 2011, Deininger et al. 2012).

Figure 7.5 gives an overview of the described processes and relationships between mean DCF and mean $\delta^{13}\text{C}$ for the considered sites. The records from the arid Hoti Cave (Therre 2014) and Moomi Cave (Therre et al. 2020) exhibit high DCF, near the theoretical maximum of 50%. At Moomi Cave, a combination of near-closed system dissolution, kinetic fractionation and aged SOM caused the observed $\delta^{13}\text{C}$ and DCF (Shakun et al. 2007, Therre et al. 2020). At Hoti Cave, $\delta^{13}\text{C}$ is relatively high and might be influenced by C4-vegetation. A clear influence of the vegetation type on soil gas $\delta^{13}\text{C}$ was shown by numerous studies (Dorale et al. 1992, Denniston et al. 2000, Fleitmann et al. 2009). This is in accordance with a study by Clark and Fontes (1990), which showed a trend towards C4-vegetation in Northern Oman when the stalagmite was growing. Kinetic fractionation might also play a major role for Hoti Cave stable isotopes and could be assessed by a covariance and trace element time series. The high DCF additionally suggests near-closed system limestone dissolution conditions at Hoti Cave.

In general, most sites plot along the proposed model between closed and open system limestone dissolution, while significant deviations can be explained by a limited number of factors which affect ^{13}C and ^{14}C . Therefore, the comparison of DCF and $\delta^{13}\text{C}$ of numerous stalagmite sites can be used to gain insight into the soil and karst processes governing the calcite dissolution, even without explicit time series analysis.

7.3.3 Climate controls on stalagmite carbon mechanisms

Apart from the dependence of overall DCF on the climatic setting of a cave, the temporal variability of DCF was proven to be subject to direct or indirect climatic influences. For instance, the Moomi Cave records of stalagmite M1-5 shows extreme DCF variability over time with values above 60% during the Last Glacial Maximum (LGM). A decreasing DCF trend is observed towards Transition I as net-infiltration at the cave site rises (as indicated by decreasing Mg/Ca ratios), causing increasing vegetation density (Therre et al. 2020). A correlation of net infiltration and DCF is observed during certain time periods of the Moomi Cave record (throughout the LGM) and the Sofular Cave record (after 17 kyr BP). Figure 7.6 a shows a linear positive relationship of Mg/Ca and DCF for these two particular time periods, even though the covariance of both proxies over the entire growth may be insignificant. Still, in the considered periods, the correlations reveal a connection between net-infiltration and dead carbon incorporation. Interestingly, this correlation is reversed with respect to the observation of Griffiths et al. (2012), Noronha et al. (2014) and Lechleitner et al. (2016a), which suggested that higher infiltration (i.e. low trace element ratios) is linked to closed system conditions (i.e. higher DCF). In contrast, the here observed positive correlation indicates that dryer conditions inhibit the input of CO_2 at high ^{14}C concentration, causing the high DCF values at Moomi Cave (Therre et al. 2020). At Sofular Cave, the activation of older soil reservoirs is a likely scenario for higher DCF at less humid conditions during Transition I (Rudzka et al. 2011).

In these two high-resolution data sets, the other measured proxies (Mg/Ca, $\delta^{13}\text{C}$, $\delta^{18}\text{O}$) are closely covariant with stalagmite ^{14}C in the previously considered time frames (see

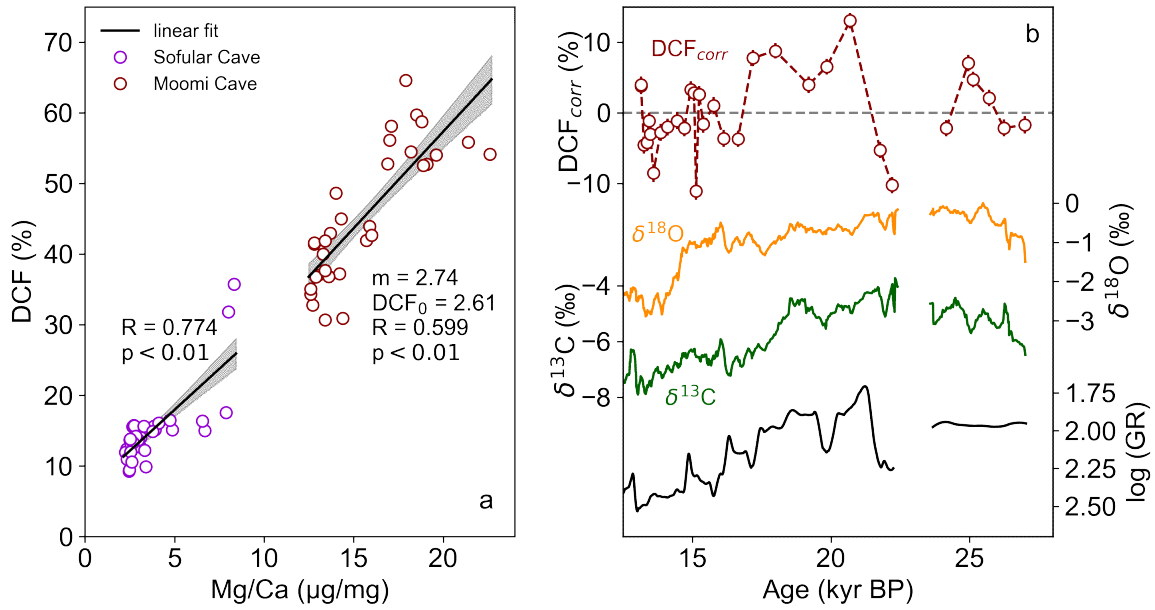


Figure 7.6: Mg/Ca ratios vs. DCF of stalagmite M1-5 from Moomi Cave and stalagmite So-1 from Sofular Cave (a). The data was plotted for the periods, in which ^{14}C is closely coupled to infiltration proxies and exhibits direct covariance with climate parameters (So-1: 17 to 10 kyr BP, M1-5: 27 to 13 kyr BP). For both records, dryer conditions are linked to high Mg/Ca and high DCF. The line and shaded areas represent a linear fit with areas of 90% confidence. The right plot (b) shows the Mg/Ca-corrected DCF (DCF_{corr}) compared to stable isotopes ($\delta^{13}C$ and $\delta^{18}O$) and $\log(GR)$ (logarithmic growth rate, inverted y-axis to show similar data patterns).

table A.5 and table A.7). From these correlations, it is possible to determine cross-connections to the carbon cycling processes, limestone systematics or general climatic changes, like they were described in the previous chapters.

A first exemplary attempt to apply a transfer function between DCF and Mg/Ca variation based on a linear fit was made for stalagmite M1-5 from Moomi Cave, which shows the highest covariance of DCF and Mg/Ca ($N = 32$, $R = 0.816$, $p < 0.01$, see Figure 7.6 a). The idea is to correct the DCF time series for precipitation induced Mg/Ca variability and reevaluate the residual DCF_{corr} :

$$DCF_{corr}(t) = DCF(t) - (m \cdot [Mg/Ca](t) + DCF_0) \quad (7.1)$$

In this equation, m and DCF_0 are the determined linear fit parameters from the regression in Figure 7.6 a. With the determined function, the DCF of stalagmite M1-5 was de-trended from the soil infiltration proxy Mg/Ca and the resulting DCF_{corr} was put into context with the other measured data. In Figure 7.6 b, it can be seen that DCF_{corr} shows values higher than zero around 20 kyr BP. This means that an additional input of old or dead carbon, which is not captured by Mg/Ca variability, occurred on top of the subtracted

climate induced DCF variation. While, at this point, it can only be speculated on the exact reasons for the temporal evolution of DCF_{corr} , it can be observed that higher dead carbon input seems to coincide with the highest values in $\delta^{13}\text{C}$, and also with a time of low growth rate (see Figure 7.6 b, note the inverted log-scale). Since $\delta^{13}\text{C}$ and $\delta^{18}\text{O}$ are not highly correlated in this time, kinetic fractionation can be excluded as a reason for the observed proxy variability. These observations point towards a karst process as a cause for high DCF_{corr} , driven by excess limestone dissolution which is not captured by Mg/Ca ratios. One reason might be that organic or non-carbonic acids played a more significant role in stalagmite formation in this time, perhaps due to reduced input of carbonic acid. This, in turn, might be a consequence of relatively decreased soil CO_2 concentration above Moomi Cave at the end of the LGM.

Further research is undoubtedly necessary on the exact nature of these processes, but the transfer function approach is worthwhile to be pursued for stalagmite ^{14}C records with a distinct influence of infiltration on long-term DCF trends.

7.4 Conclusion

In recent years, the mechanisms which determine the radiocarbon signature in stalagmites have been intensely investigated. A major focus was put on the influence of limestone dissolution on the dissolved inorganic carbon (DIC) in the seepage water, and the climate factors that determine whether open or closed systematics are present (Fohlmeister et al. 2011b, Griffiths et al. 2012, Noronha et al. 2014, Lechleitner et al. 2016a). In recent years, an increasing number of studies reporting on dead carbon levels in stalagmites exceeding 50 % has highlighted mechanisms in stalagmite formation that were not considered before. While near-closed system limestone dissolution in combination with very old carbon stocks in the SOM contributing to the soil gas can trigger a significant increase of DCF with relatively low $\delta^{13}\text{C}$ (Therre et al. 2020), high values in DCF and stable isotopes were linked to enhanced sulphuric acid dissolution of limestone (Spötl et al. 2016, Bajo et al. 2017, Proß 2018). In comparison to the multi-site record from Genty et al. (2001), it was shown that the mechanisms of dead carbon incorporation for central and western European, temperate sites are largely dependent on climate zones and cannot be readily applied for arid or tropical speleothem records. In arid settings, where soil carbon cycling is much more sensitive to small precipitation changes, DCF records can show significant short-term and long-term variability, which proves the climate influence on DCF in these areas (Therre 2014, Therre et al. 2020). The observed correlation of DCF and Mg/Ca in the investigated records from Moomi Cave and Sofular Cave is in contrast to limestone dissolution influence as observed in tropical records and might enable the investigation of additional karst processes at Moomi Cave during the last glacial. Additionally, a decoupling of climatic impacts on ^{14}C with the help of similar transfer functions as introduced above could enable atmospheric calibration on stalagmites, even if their DCF is not constant over time.

The nature of the climatic processes in stalagmite formation cannot be assessed by stable isotopes and element ratios alone. Rather, a proxy with the ability to trace carbon

contributions depending on their ^{14}C signature on both short time scales and long-term trends is required. Stalagmite DCF can serve that purpose and should be considered in future speleothem studies.

8 Conclusions and Outlook

In this thesis, radiocarbon in stalagmites was investigated as an environmental proxy of climate change and tracer of vegetation and soil carbon dynamics. The dead carbon fraction (DCF) of stalagmites was used in the past as a proxy for limestone dissolution and has been in the focus of studies on carbon cycling and on the dynamics of aging organic material in the soil zone. However, most available studies focused on records with relatively low DCF values or near-open limestone dissolution conditions. Especially in the effort to contribute stalagmite records to atmospheric inter-calibration records like IntCal13 (Reimer et al. 2013), a low and constant DCF is particularly desirable. While this goal was recently achieved by the exceptional Hulu Cave record (Cheng et al. 2018), the interpretation of high DCF records still seemed difficult. The main goal of this thesis was to investigate the climate-dependent mechanisms of ^{14}C incorporation into stalagmites and to establish DCF as a tracer of vegetation dynamics and indicator of past climate change. Moreover, the possibility of atmospheric ^{14}C reconstruction was investigated on stalagmite samples with non-constant DCF over time.

Summary

The methodical part of this dissertation describes the construction and implementation of a new carbon dioxide extraction line for ^{14}C analysis, which was achieved in the scope of a supervised Bachelor's thesis. In a subsequent performance analysis of the first years of sampling, the blanks are at a constant and sufficiently low activity (<0.25 pmC) and the reproducibility of international standard measurements has increased significantly. This provides excellent prerequisites for future ^{14}C studies on carbonate paleoclimate archives at the Institute of Environmental Physics.

For two stalagmites from Moomi Cave (Socotra Island) and Sofular Cave (Northern Turkey), high-precision U-Series dating was utilized to create accurate and highly resolved age-depth models and extensive radiocarbon datasets were measured. The inferred DCF, together with paleoclimate proxies like trace elements and stable isotopes, revealed a wide range of climate dependent processes which determine the incorporation of ^{14}C into the stalagmite.

At Moomi Cave, stalagmite M1-5 grew under conditions approaching a closed system of limestone dissolution throughout the Last Glacial Maximum (LGM) with a high influence of aged soil material degradation on soil gas ^{14}C signature. With observed DCF values higher than 60% in peak-glacial conditions, this record is amongst the stalagmite studies with the highest reported DCF. The long-term trends in DCF revealed a strong coupling to increasing net infiltration as derived from declining Mg/Ca ratios throughout the last glacial. Together with decreasing $\delta^{13}\text{C}$ values, the proxies show a vegetation increase on

the Socotra archipelago at the end of the glacial period, which caused increased input of CO₂ at high ¹⁴C concentration into the soil zone, and subsequently lower DCF values. Vast sub-centennial DCF variability of more than 10% was revealed during the Younger Dryas (YD) which indicates strong carbon cycling dynamics in that period. This study was recently published as a first-author paper in a peer-reviewed journal (Therre et al. 2020).

In a second case study, the comprehensive ¹⁴C data set of stalagmite So-1 from Sofular Cave in Northern Turkey supported the findings of Rudzka et al. (2011), that a near-open system behavior with strong imprint of soil carbon cycling on DCF persisted through Termination I between 17 and 10 kyr BP. The new data from this project reveal quick responses of the soil carbon cycling to climatic changes, such as the warming during the B/A stadial and showed a bimodal configuration of soil carbon dynamics throughout the glacial. Due to the large DCF variability at the end of the last glacial, the Sofular stalagmite cannot be used for absolute reconstruction of atmospheric ¹⁴C concentration. However, the stable hydro-geological conditions in the oldest part of the stalagmite enable the reconstruction of relative atmospheric ¹⁴C variability during the Laschamp geomagnetic reversal event. So-1 ¹⁴C data suggests systematically increased atmospheric Δ¹⁴C compared to IntCal13 (Reimer et al. 2013) and thus corroborates the comprehensive records from Hulu Cave (Cheng et al. 2018). A potential additional peak of atmospheric ¹⁴C production rate during the minimum of the geomagnetic field was discovered around 41.2 kyr BP, which suggests that stalagmite So-1 can contribute to ¹⁴C calibration efforts.

In the last chapter of this dissertation, selected stalagmite ¹⁴C studies of recent years from various climate zones were summarized, focusing on a review of the determining factors of stalagmite DCF in different climate zones. Recent studies and non-published records from the Institute of Environmental Physics give an overview of the characteristic imprints of limestone dissolution, aged soil organic matter and climate-induced influence of vegetation on both DCF and δ¹³C signature.

While stalagmites from tropical climate show a strong coupling of DCF to limestone dissolution systematics in the karst (Griffiths et al. 2012, Noronha et al. 2014, Lechleitner et al. 2016a), caves from arid regions like Socotra Island show a reversed relationship, where DCF is highly sensitive to aboveground vegetation changes and carbon cycling dynamics. The sensitivity of DCF on climate-dependent factors demonstrates, that stalagmite ¹⁴C can be used successfully as an environmental proxy and tracer of climate change. In a first attempt to decouple DCF from climate-induced precipitation variability, the resulting residual signal suggests previously unresolved signals of karst processes in the Moomi Cave record.

The findings in the course of this dissertation clearly show that stalagmite ¹⁴C is an indispensable tool for the assessment of climate impact on soil carbon dynamics and may be the key to past atmospheric ¹⁴C concentration.

Open questions and outlook

The forthcoming publication of the new IntCal20 calibration data set will unequivocally move stalagmite ¹⁴C further into the focus of paleoclimate research, due to the expected

inclusion of the most comprehensive and highly precise speleothem record from Hulu Cave (Cheng et al. 2018). Since continuous tree-ring records will most likely not be able to substantiate the new data, future efforts to contribute other suitable stalagmite records must be made. Already published records and the data from the presented studies in this thesis indicate that stalagmites from temperate climate conditions might be preferable for atmospheric ^{14}C reconstruction in contrast to arid climates. Furthermore, novel modeling approaches need to be made, which implement the influences of climate change and soil dynamics on stalagmite ^{14}C signature. While substantial progress has already been achieved in this field for records with near-open system conditions, low DCF and hydrological control on limestone dissolution, the lack of high DCF records in the published literature might point to a weakness of the current models. For additional speleothem data to contribute to radiocarbon calibration, providing multi-proxy data sets of stalagmites covering the entire range of DCF will unquestionably be beneficial for future approaches. For instance, at the tropical site of Cueva Larga, Puerto Rico, preliminary results from the Institute of Environmental Physics indicate vast differences in DCF of two different stalagmites from the same cave. This provides the opportunity to analyze the carbon cycling dynamics at one site, combined with the possibility to monitor modern cave parameters and soil cycling.

Concerning stalagmite So-1, additional analysis and modeling will most likely provide even further insight into the nature of DCF variability and soil organic carbon. For example, highly resolved laser-ablation profiles of element ratios and quantitative modeling of the soil carbon age spectrum in combination with the already collected ^{14}C and trace element data might promise deeper insight into the carbon cycling dynamics especially in times of higher DCF variability. The achieved relative atmospheric reconstruction based on data from So-1 shows that additional valuable information on past ^{14}C variability might be available in numerous records that have previously been discarded due to their temporal DCF variability. With the results presented in this dissertation, it seems worthwhile to reconsider and reevaluate some of these records for future calibration efforts

For the highly resolved multi-proxy records at Sofular Cave and Moomi Cave, the correlation analysis revealed large covariance between the measured climate proxies, considering the overall records. It was determined in this dissertation that the significant correlation was in both cases confined to certain time periods of the respective records. The results from the analysis suggest that a further investigation on the underlying mechanisms causing the correlation is promising. The covariance of Mg/Ca and DCF, which was found in substantial parts of both records, and its interpretation provided insight into the hydrological impact on DCF that were not captured by previous studies. A first attempt shows that a great potential lies in the prospect of transfer functions that decouple stalagmite ^{14}C from overprinted climate signals and provide insight into previously unresolved processes.

9 List of Publications of the Author

Therre, S., Fohlmeister, J., Fleitmann, D., Matter, A., Burns, S.J., Arps, J., Schröder-Ritzrau, A., Friedrich, R., and Frank, N.: Climate-induced speleothem radiocarbon variability on Socotra Island from the Last Glacial Maximum to the Younger Dryas, *Climate of the Past*, 16(1):409–421, 2020, doi: 10.5194/cp-16-409-2020.

Appendix

A Supplementary Data

A.1 Stalagmite So-1, Sofular Cave

The data measured for the project of this dissertation concerning stalagmite So-1 are presented in the following tables.

- Radiocarbon dating results and calculated reservoir ages and DCF for two reference sets of the atmospheric radiocarbon concentration (Table A.1)
- U-series dating results with ^{230}Th -corrected ages (Table A.2)
- Elemental mass ratios of Mg/Ca and Sr/Ca, measured on two different setups: ICP-OES and ICPQMS (Table A.3)

Table A.1: Radiocarbon dating results for stalagmite So-1. All samples were prepared in the Heidelberg radiocarbon lab (Lab No. HD) and measured on by AMS at Curt-Engelhorn-Centre Archaeometry, Mannheim (Lab No. MA) Radiocarbon ages (t_{14C}) and reservoir ages ($t_{14C, res}$) are reported in units of conventional 14C years. Modeled ages (t_{mod}) were derived from the age-depth model and are reported in kyr before 1950 CE. All uncertainties are 1σ . * denotes samples that were excluded due to contamination. † marks samples that have a DCF < 0 with respect to IntCal13 (Reimer et al. 2013), but not for HuluCal, (according to Cheng et al. 2018).

HD	Lab No. MA	label	depth mm	t_{mod} kyr BP	t_{14C} yr	$t_{14C, res}$ yr	DCF %	$t_{14C, res}$ yr	DCF %
HD18-205	38956	So-1-950	950	10.10 ± 0.09	10 131 ± 28	1210 ± 86	13.99 ± 0.69	-	-
HD18-206	38957	So-1-958	958	10.18 ± 0.07	10 351 ± 27	1363 ± 114	15.61 ± 0.58	-	-
HD18-207	38958	So-1-24	965	10.25 ± 0.06	10 188 ± 29	1085 ± 103	12.63 ± 0.57	-	-
10312	29212	So-1-974	974	10.35 ± 0.04	10 267 ± 33	1063 ± 40	12.40 ± 0.38	-	-
10310	29213	So-1-983	983	10.44 ± 0.05	10 271 ± 33	1020 ± 47	11.92 ± 0.32	-	-
HD18-208	38959	So-1-989	989	10.51 ± 0.07	10 348 ± 28	1047 ± 66	12.23 ± 0.30	-	-
HD18-175	38939	So-1-25	997	10.59 ± 0.11	10 591 ± 31	1217 ± 96	14.07 ± 0.31	949 ± 34	15.10 ± 0.19
HD18-176	38941	So-1-1004	1004	10.64 ± 0.13	10 591 ± 32	1181 ± 114	13.67 ± 0.39	939 ± 38	14.67 ± 0.20
-	28012	So-1-1009	1009	10.66 ± 0.15	10 797 ± 37	1370 ± 123	15.69 ± 0.47	1139 ± 45	16.62 ± 0.20
HD18-177	38940	So-1-160	1021	11.01 ± 0.16	10 994 ± 31	1370 ± 113	15.69 ± 0.96	1297 ± 62	15.31 ± 0.28
HD18-178	38943	So-1-1031	1031	11.61 ± 0.40	11 242 ± 31	1206 ± 249	13.93 ± 1.76	1191 ± 236	13.81 ± 1.54
HD18-179	38942	So-1-1039	1039	12.12 ± 0.21	11 545 ± 32	1230 ± 119	14.20 ± 1.04	1220 ± 95	13.76 ± 1.14
HD18-181	38945	So-1-1047	1047	12.41 ± 0.12	11 653 ± 32	1190 ± 89	13.77 ± 0.60	1190 ± 105	13.48 ± 0.50
HD18-209	38960	So-1-35	1057	12.54 ± 0.06	11 676 ± 32	1131 ± 69	13.13 ± 0.37	1134 ± 74	12.78 ± 0.25
-	28013	So-1-1065	1065	12.64 ± 0.06	11 822 ± 38	1147 ± 111	13.31 ± 0.66	1160 ± 79	12.35 ± 0.27
HD18-182	38944	So-1-1065o	1065	12.64 ± 0.06	11 740 ± 33	1065 ± 109	12.43 ± 0.66	1078 ± 77	12.35 ± 0.27
-	28016	So-1-26	1085	13.25 ± 0.04	12 602 ± 41	1196 ± 60	13.84 ± 0.30	1237 ± 64	13.97 ± 0.22
HD17-038	31080	So-1-1100	1100	13.46 ± 0.04	12 409 ± 34	773 ± 66	9.18 ± 0.48	799 ± 115	9.04 ± 0.31
HD17-039	31081	So-1-1119	1119	13.72 ± 0.05	12 822 ± 33	937 ± 75	11.01 ± 0.47	971 ± 66	11.17 ± 0.27
10311	29214	So-1-1133	1133	13.92 ± 0.19	13 101 ± 38	1038 ± 167	12.13 ± 0.60	1051 ± 73	12.21 ± 0.37
HD17-040	31082	So-1-1139	1139	14.11 ± 0.18	12 946 ± 32	731 ± 143	8.70 ± 0.75	794 ± 91	8.67 ± 0.63
HD17-041	31083	So-1-1144	1144	14.27 ± 0.17	13 122 ± 35	802 ± 109	9.50 ± 0.97	886 ± 73	9.50 ± 0.93
HD17-042	31084	So-1-1160	1160	14.43 ± 0.04	13 153 ± 37	747 ± 55	8.88 ± 0.56	852 ± 40	9.00 ± 0.43
HD18-077	36569	So-1-1171a	1171	14.53 ± 0.03	13 650 ± 41	1223 ± 56	14.13 ± 0.49	1344 ± 43	14.16 ± 0.36
HD18-078	36570	So-1-1171b	1171	14.53 ± 0.03	13 730 ± 37	1303 ± 53	14.98 ± 0.49	1424 ± 39	15.01 ± 0.35

HD	Lab No.	MA	label	depth mm	t_{mod} kyr BP	$t_{14\text{C}}$ yr	$t_{14\text{C}, \text{res}}$ yr	DCF %	$t_{14\text{C}, \text{res}}$ yr	DCF %	$t_{14\text{C}, \text{res}}$ yr	DCF %
								<i>IntCal13</i>				<i>HuluCal</i>
-	28014		So-1-1174	1174	14.55 ± 0.04	13701 ± 43	1270 ± 57	14.63 ± 0.52	1394 ± 45	14.65 ± 0.39	1394 ± 45	14.65 ± 0.39
HD18-079	36571		So-1-1178a	1178	14.59 ± 0.05	13755 ± 37	1318 ± 52	15.14 ± 0.56	1446 ± 39	15.16 ± 0.46	1446 ± 39	15.16 ± 0.46
HD18-080	36572		So-1-1178b	1178	14.59 ± 0.05	13673 ± 39	1237 ± 54	14.28 ± 0.57	1364 ± 41	14.29 ± 0.47	1364 ± 41	14.29 ± 0.47
HD17-043*	31085		So-1-39	1182	14.60 ± 0.06	12610 ± 35	169 ± 51	2.09 ± 0.71	299 ± 37	2.13 ± 0.61	299 ± 37	2.13 ± 0.61
HD18-081	36573		So-1-39II	1182	14.60 ± 0.06	13716 ± 38	1275 ± 53	14.69 ± 0.62	1405 ± 40	14.72 ± 0.53	1405 ± 40	14.72 ± 0.53
HD18-082	36574		So-1-1186	1186	14.63 ± 0.07	13672 ± 37	1224 ± 53	14.14 ± 0.65	1359 ± 39	14.18 ± 0.58	1359 ± 39	14.18 ± 0.58
HD18-083	36575		So-1-1189	1189	14.65 ± 0.07	13841 ± 38	1387 ± 54	15.87 ± 0.63	1501 ± 40	15.92 ± 0.55	1501 ± 40	15.92 ± 0.55
HD17-044	31086		So-1-40	1193	14.91 ± 0.22	13816 ± 39	1239 ± 127	14.29 ± 1.26	1307 ± 43	14.01 ± 0.99	1307 ± 43	14.01 ± 0.99
HD18-084	36576		So-1-40II	1193	14.91 ± 0.22	14376 ± 40	1799 ± 127	20.06 ± 1.18	1867 ± 44	19.80 ± 0.92	1867 ± 44	19.80 ± 0.92
HD18-085	36577		So-1-1192	1196	15.25 ± 0.22	14051 ± 38	1255 ± 160	14.46 ± 0.84	1334 ± 50	14.13 ± 0.75	1334 ± 50	14.13 ± 0.75
HD18-087	36578		So-1-1201	1201	15.83 ± 0.27	14571 ± 39	1384 ± 193	15.83 ± 0.94	1435 ± 146	15.57 ± 0.76	1435 ± 146	15.57 ± 0.76
-	28015		So-1-1204	1204	16.61 ± 0.28	15252 ± 50	1504 ± 190	17.08 ± 1.10	1557 ± 193	16.73 ± 0.92	1557 ± 193	16.73 ± 0.92
HD18-088	36579		So-1-1204II	1204	16.61 ± 0.28	15321 ± 42	1573 ± 188	17.79 ± 1.09	1627 ± 191	17.45 ± 0.92	1627 ± 191	17.45 ± 0.92
-	28017		So-1-27*	1209	16.87 ± 0.19	17411 ± 56	3500 ± 132	35.32 ± 0.69	3554 ± 71	35.06 ± 0.61	3554 ± 71	35.06 ± 0.61
HD18-089	36580		So-1-1209	1209	16.87 ± 0.19	17845 ± 53	3934 ± 130	38.73 ± 0.66	3988 ± 68	38.47 ± 0.58	3988 ± 68	38.47 ± 0.58
HD17-045	31087		So-1-1213	1213	16.95 ± 0.21	17036 ± 44	3072 ± 145	31.79 ± 0.74	3080 ± 148	31.55 ± 0.67	3080 ± 148	31.55 ± 0.67
HD18-090	36581		So-1-1213II	1213	16.95 ± 0.21	16350 ± 47	2386 ± 146	25.70 ± 0.80	2393 ± 149	25.44 ± 0.73	2393 ± 149	25.44 ± 0.73
HD17-046	31088		So-1-1223	1223	17.29 ± 0.17	15593 ± 43	1393 ± 126	15.93 ± 0.75	1395 ± 125	15.72 ± 0.44	1395 ± 125	15.72 ± 0.44
HD17-047	31089		So-1-1233	1233	17.65 ± 0.12	16024 ± 43	1538 ± 114	17.43 ± 0.64	1538 ± 139	17.11 ± 0.25	1538 ± 139	17.11 ± 0.25
10313	29215		So-1-1243	1243	18.01 ± 0.11	16473 ± 45	1663 ± 116	18.71 ± 0.70	1668 ± 90	18.25 ± 0.35	1668 ± 90	18.25 ± 0.35
HD17-048	31090		So-1-1253	1253	18.36 ± 0.09	16511 ± 46	1414 ± 92	16.14 ± 0.52	1418 ± 105	15.83 ± 0.30	1418 ± 105	15.83 ± 0.30
HD17-049	31091		So-1-1263	1263	18.70 ± 0.09	16725 ± 44	1299 ± 105	14.94 ± 0.55	1351 ± 105	15.29 ± 0.28	1351 ± 105	15.29 ± 0.28
HD18-189	38946		So-1-28	1269	18.90 ± 0.15	17879 ± 52	2223 ± 168	24.18 ± 0.50	2260 ± 178	24.40 ± 0.33	2260 ± 178	24.40 ± 0.33
10314	29216		So-1-1274	1274	19.07 ± 0.14	18290 ± 51	2469 ± 135	26.47 ± 0.49	2495 ± 143	26.59 ± 0.29	2495 ± 143	26.59 ± 0.29
HD18-190	38947		So-1-1279	1279	19.24 ± 0.13	17931 ± 51	1980 ± 111	21.85 ± 0.58	2003 ± 105	21.94 ± 0.46	2003 ± 105	21.94 ± 0.46
HD17-050	31092		So-1-1284	1284	19.40 ± 0.11	17490 ± 45	1420 ± 99	16.21 ± 0.64	1464 ± 83	16.49 ± 0.55	1464 ± 83	16.49 ± 0.55
HD17-051	31093		So-1-1294	1294	19.73 ± 0.10	18209 ± 51	1848 ± 89	20.57 ± 0.69	1925 ± 106	20.98 ± 0.22	1925 ± 106	20.98 ± 0.22
HD17-052	31094		So-1-42	1306	20.12 ± 0.12	18598 ± 50	1921 ± 117	21.27 ± 0.69	1976 ± 106	21.33 ± 0.30	1976 ± 106	21.33 ± 0.30
HD17-053	31095		So-1-1314	1314	20.36 ± 0.11	18200 ± 51	1322 ± 100	15.18 ± 0.68	1366 ± 113	15.29 ± 0.31	1366 ± 113	15.29 ± 0.31
HD18-099	36582		So-1-1319	1319	20.52 ± 0.11	18970 ± 57	1958 ± 118	21.64 ± 0.58	1989 ± 122	21.61 ± 0.27	1989 ± 122	21.61 ± 0.27
HD17-054	31096		So-1-1324	1324	20.68 ± 0.13	19304 ± 51	2152 ± 126	23.51 ± 0.58	2188 ± 121	23.58 ± 0.40	2188 ± 121	23.58 ± 0.40
HD18-100	36583		So-1-1330	1330	20.80 ± 0.16	18604 ± 57	1352 ± 142	15.51 ± 0.70	1387 ± 150	15.60 ± 0.41	1387 ± 150	15.60 ± 0.41
HD17-055	31097		So-1-18	1334	20.94 ± 0.91	19251 ± 51	1913 ± 742	21.20 ± 1.60	1956 ± 738	21.27 ± 1.56	1956 ± 738	21.27 ± 1.56

Lab No.	MA	label	depth mm	t_{mod} kyr BP	$t_{14\text{C}}$ yr	$t_{14\text{C}, \text{res}}$ yr	DCF %	$t_{14\text{C}, \text{res}}$ yr	DCF %
HD18-101	36584	So-1-1336	1336	22.61 ± 1.02	20 410 ± 62	1677 ± 886	18.84 ± 1.44	1717 ± 905	18.80 ± 1.22
HD18-102	36585	So-1-1339	1339	23.03 ± 0.59	21 089 ± 67	1983 ± 522	21.87 ± 1.00	2010 ± 554	21.68 ± 0.57
HD17-056	31098	So-1-M21	1343	23.53 ± 0.12	21 637 ± 61	2112 ± 129	23.13 ± 0.83	2092 ± 96	22.25 ± 0.40
HD18-111	36586	So-1-1350	1350	24.36 ± 0.07	22 366 ± 74	2087 ± 109	22.89 ± 0.77	2113 ± 122	22.93 ± 0.40
HD17-057	31099	So-1-43	1356	25.06 ± 0.07	22 414 ± 66	1673 ± 100	18.82 ± 0.77	1606 ± 93	17.94 ± 0.24
HD18-203	38952	So-1-1360	1360	25.53 ± 0.07	23 168 ± 81	2005 ± 111	22.10 ± 0.74	2083 ± 93	22.59 ± 0.41
HD17-058	31100	So-1-1364	1364	26.00 ± 0.08	23 997 ± 68	2214 ± 133	24.10 ± 0.92	2318 ± 106	24.57 ± 0.29
HD18-200	38953	So-1-1364	1364	26.00 ± 0.08	24 087 ± 91	2305 ± 146	24.95 ± 0.91	2408 ± 122	25.41 ± 0.29
HD18-201	38954	So-1-1367	1367	26.36 ± 0.09	24 205 ± 92	2045 ± 124	22.49 ± 0.82	2161 ± 116	23.17 ± 0.27
HD18-112	36587	So-1-1370	1370	26.64 ± 0.09	23 415 ± 78	1019 ± 124	11.93 ± 1.09	1134 ± 105	12.70 ± 0.31
HD18-202	38955	So-1-1370	1370	26.64 ± 0.09	23 724 ± 88	1329 ± 131	15.26 ± 1.05	1443 ± 113	16.00 ± 0.29
HD17-059	31101	So-1-1375	1375	26.93 ± 0.10	23 822 ± 70	1262 ± 114	14.56 ± 1.05	1217 ± 148	13.53 ± 0.53
HD17-060	31102	So-1-1384	1384	27.44 ± 0.09	24 420 ± 75	1278 ± 153	14.72 ± 1.33	1252 ± 116	13.79 ± 0.25
HD17-061	31103	So-1-M20	1393	27.48 ± 0.09	24 516 ± 72	1308 ± 157	15.03 ± 1.33	1303 ± 116	14.33 ± 0.25
HD17-150	32986	So-1-1403	1403	27.80 ± 0.10	25 211 ± 132	1480 ± 208	16.83 ± 1.39	1676 ± 161	18.22 ± 0.24
HD17-151	32987	So-1-1413	1413	28.13 ± 0.08	25 473 ± 136	1350 ± 159	15.48 ± 0.88	1615 ± 162	17.53 ± 0.26
HD17-152*	32988	So-1-1428	1428	28.99 ± 0.11	24 938 ± 127	-47 ± 160	-0.57 ± 1.10	114 ± 164	0.80 ± 0.37
HD18-193	38948	So-1-1428	1428	28.99 ± 0.11	26 293 ± 113	1308 ± 149	15.04 ± 0.93	1469 ± 154	16.19 ± 0.31
HD17-153	32989	So-1-1438	1438	29.65 ± 0.08	27 359 ± 173	1776 ± 202	19.85 ± 1.04	2047 ± 188	22.04 ± 0.26
HD17-154	32990	So-1-1448	1448	30.30 ± 0.12	27 431 ± 178	1458 ± 202	16.62 ± 1.06	1469 ± 205	16.01 ± 0.32
HD17-155	32991	So-1-46	1456	30.82 ± 0.13	28 188 ± 194	1637 ± 291	18.44 ± 1.84	1775 ± 247	18.20 ± 0.36
HD17-156	32992	So-1-1469	1469	31.63 ± 0.15	28 392 ± 193	427 ± 255	5.19 ± 1.44	996 ± 254	10.08 ± 0.55
HD18-194	38949	So-1-1469	1469	31.63 ± 0.15	28 566 ± 147	601 ± 222	7.22 ± 1.41	1171 ± 221	12.02 ± 0.54
HD17-157	32993	So-1-1477	1477	32.08 ± 0.16	30 121 ± 237	1843 ± 255	20.51 ± 1.29	2182 ± 301	22.55 ± 0.37
HD17-158	32994	So-1-1488	1488	32.73 ± 0.16	30 056 ± 238	1442 ± 267	16.45 ± 1.16	1569 ± 262	16.38 ± 0.60
HD20-028	45135	So-1-1494	1494	32.92 ± 0.34	30 563 ± 136	1798 ± 287	20.06 ± 1.34	1957 ± 263	20.40 ± 1.16
HD17-159	32995	So-1-1498	1498	32.97 ± 0.42	30 757 ± 258	1937 ± 421	21.43 ± 1.45	2120 ± 384	22.02 ± 1.35
HD20-027	45136	So-1-1504	1504	33.42 ± 0.25	31 076 ± 147	1906 ± 299	21.14 ± 1.23	2154 ± 213	22.47 ± 0.96
HD17-160	32996	So-1-1508	1508	33.84 ± 0.13	30 939 ± 265	1238 ± 330	14.29 ± 1.66	1748 ± 281	18.25 ± 0.45
HD17-161	32997	So-1-1519	1519	35.18 ± 0.50	32 010 ± 302	718 ± 601	8.58 ± 1.53	1517 ± 615	15.91 ± 1.31
HD20-026	45137	So-1-1526	1526	36.07 ± 0.52	32 913 ± 175	737 ± 537	8.78 ± 1.45	1337 ± 685	14.60 ± 1.93
HD17-162	32998	So-1-1529	1529	36.58 ± 0.46	33 508 ± 359	851 ± 542	10.06 ± 1.70	1331 ± 612	14.56 ± 1.03
HD18-195	38950	So-1-1529	1529	36.58 ± 0.46	33 381 ± 252	724 ± 478	8.63 ± 1.72	1203 ± 556	13.20 ± 1.05

Lab No.	MA	label	depth mm	t_{mod} kyr BP	$t_{14\text{C}}$ yr	$t_{14\text{C}, \text{res}}$ yr	DCF %	$t_{14\text{C}, \text{res}}$ yr	DCF %
HD20-025	45138	So-1-1532	1532	37.18 ± 0.36	33 696 ± 183	604 ± 264	7.25 ± 2.37	925 ± 378	10.36 ± 0.67
HD17-163	32999	So-1-1538	1538	37.58 ± 0.18	34 818 ± 412	1542 ± 429	17.48 ± 1.55	1676 ± 443	18.49 ± 0.58
HD20-018	45139	So-1-1543	1543	37.91 ± 0.28	34 450 ± 204	1001 ± 267	11.72 ± 1.79	1113 ± 252	12.60 ± 1.57
HD17-164	33000	So-1-1549	1549	38.19 ± 0.19	35 165 ± 440	1539 ± 471	17.45 ± 1.39	1708 ± 443	18.82 ± 1.36
HD20-017	45140	So-1-1554	1554	38.46 ± 0.11	33 972 ± 188	53 ± 247	0.68 ± 1.85	451 ± 192	5.16 ± 1.14
HD17-165	33001	So-1-1559	1559	38.73 ± 0.15	35 536 ± 451	1254 ± 485	14.47 ± 1.44	1952 ± 455	21.03 ± 0.97
HD20-016	45141	So-1-1563	1563	38.96 ± 0.22	35 373 ± 220	865 ± 304	10.22 ± 1.39	1669 ± 258	18.22 ± 1.03
HD17-222	35250	So-1-1569	1569	39.30 ± 0.19	35 661 ± 171	868 ± 224	10.26 ± 1.42	1701 ± 244	18.67 ± 0.50
HD17-223*	35251	So-1-1579	1579	39.83 ± 0.13	33 685 ± 138	-1563 ± 196	-21.45 ± 2.10	-803 ± 226	-11.36 ± 0.95
HD18-196	38951	So-1-1579	1579	39.83 ± 0.13	36 098 ± 320	850 ± 348	10.06 ± 1.56	1610 ± 366	17.53 ± 0.71
HD17-224	35252	So-1-1588	1588	40.27 ± 0.12	36 493 ± 185	822 ± 231	9.75 ± 1.56	1460 ± 202	15.97 ± 0.62
HD20-015*	45142	So-1-1593	1593	40.52 ± 0.16	34 323 ± 200	-1572 ± 246	-21.58 ± 2.19	-875 ± 243	-12.63 ± 1.02
HD17-225*	35550	So-1-1598	1598	40.78 ± 0.20	35 574 ± 166	-541 ± 240	-6.95 ± 1.95	88 ± 297	0.47 ± 0.91
HD18-113	36588	So-1-1598II	1598	40.78 ± 0.20	36 815 ± 279	699 ± 328	8.36 ± 1.67	1329 ± 372	14.71 ± 0.78
HD20-014†	45143	So-1-1603	1603	41.04 ± 0.25	35 783 ± 228	-581 ± 340	-7.48 ± 2.00	-42 ± 399	-1.05 ± 1.21
HD17-226*	35551	So-1-1608	1608	41.22 ± 0.29	36 238 ± 170	-326 ± 373	-4.12 ± 2.13	167 ± 438	1.59 ± 1.56
HD18-114	36589	So-1-1608II	1608	41.22 ± 0.29	36 808 ± 280	243 ± 434	3.00 ± 1.98	736 ± 491	8.32 ± 1.45
HD20-013	45144	So-1-1613	1613	41.25 ± 0.22	36 548 ± 241	-34 ± 348	-0.40 ± 1.98	446 ± 387	4.97 ± 1.18
HD17-227*	35552	So-1-1618	1618	41.42 ± 0.15	36 523 ± 171	-260 ± 261	-3.27 ± 2.13	178 ± 289	1.82 ± 1.11
HD18-115	36590	So-1-1618II	1618	41.42 ± 0.15	37 525 ± 307	742 ± 365	8.85 ± 1.88	1181 ± 386	13.34 ± 0.98

Table A.2: U-series dating results of stalagmite So-1. The measurements were performed on a MC-ICP-MS. All ages are reported as yr before 1950 CE. $\delta^{234}\text{U}_{\text{init}}$ was corrected for $\delta^{234}\text{U}_{\text{meas}}$ with the corrected age age_{corr} . All uncertainties are 2σ . Samples marked by † were omitted from age modeling due to significant age inversions. Sample 10103 was excluded after revised age modeling in combination with ^{14}C chronology (marked *).

Lab No.	dft mm	label	^{238}U ng/g	^{232}Th ng/g	$^{230}\text{Th}/^{238}\text{U}$ Act. ratio	$^{230}\text{Th}/^{232}\text{Th}$ Act. ratio	$\delta^{234}\text{U}_{\text{corr}}$ ‰	age kyr BP	age_{corr} kyr BP	$\delta^{234}\text{U}_{\text{init}}$ ‰
9225†	950	So-1-950	210.376 ± 0.024	0.621 ± 0.002	0.345 ± 0.002	358 ± 2	1024.9 ± 3.6	20.02 ± 0.13	19.99 ± 0.12	1085 ± 4
10099	958	So-1-958	227.985 ± 0.048	0.693 ± 0.002	0.181 ± 0.001	183 ± 1	993.3 ± 3.9	10.26 ± 0.07	10.22 ± 0.06	1023 ± 4
10100	989	So-1-989	209.324 ± 0.058	0.436 ± 0.001	0.182 ± 0.001	269 ± 1	961.2 ± 3.8	10.50 ± 0.06	10.47 ± 0.06	990 ± 4
9226†	997	So-1-997	245.680 ± 0.030	0.713 ± 0.002	0.231 ± 0.001	244 ± 2	1011.0 ± 3.2	13.14 ± 0.08	13.11 ± 0.09	1049 ± 3
10101	1017	So-1-1017	271.345 ± 0.057	0.349 ± 0.001	0.195 ± 0.001	466 ± 3	1033.1 ± 3.5	10.86 ± 0.08	10.84 ± 0.08	1065 ± 4
9227†	1022	So-1-1022	287.736 ± 0.035	0.509 ± 0.001	0.225 ± 0.001	389 ± 2	982.7 ± 2.7	12.95 ± 0.07	12.92 ± 0.07	1019 ± 3
9228	1034	So-1-1034	311.622 ± 0.032	0.766 ± 0.002	0.206 ± 0.001	256 ± 2	995.8 ± 2.9	11.71 ± 0.09	11.68 ± 0.08	1029 ± 3
9229	1042	So-1-1042	352.616 ± 0.037	0.718 ± 0.002	0.210 ± 0.001	315 ± 2	943.2 ± 2.2	12.34 ± 0.08	12.31 ± 0.08	977 ± 2
9230	1065	So-1-1065	493.733 ± 0.024	0.221 ± 0.001	0.222 ± 0.001	1519 ± 8	987.0 ± 1.4	12.77 ± 0.06	12.76 ± 0.06	1023 ± 1
10102	1070	So-1-1070	373.575 ± 0.042	0.156 ± 0.000	0.218 ± 0.001	1602 ± 7	965.8 ± 1.5	12.65 ± 0.05	12.64 ± 0.04	1001 ± 2
9231	1076	So-1-1076	356.247 ± 0.022	0.347 ± 0.001	0.226 ± 0.001	713 ± 4	977.1 ± 1.9	13.09 ± 0.07	13.07 ± 0.07	1014 ± 2
9232	1085	So-1-1085	463.619 ± 0.083	0.295 ± 0.001	0.224 ± 0.001	1077 ± 6	924.8 ± 2.0	13.33 ± 0.07	13.32 ± 0.07	960 ± 2
9233†	1104	So-1-1104	483.664 ± 0.033	1.267 ± 0.002	0.246 ± 0.001	287 ± 1	926.6 ± 1.2	14.67 ± 0.06	14.63 ± 0.06	966 ± 1
9234	1124	So-1-1124	563.824 ± 0.106	0.303 ± 0.001	0.233 ± 0.001	1334 ± 6	941.3 ± 1.2	13.79 ± 0.06	13.78 ± 0.06	979 ± 1
9235	1150	So-1-1150	767.195 ± 0.067	0.463 ± 0.001	0.250 ± 0.001	1267 ± 6	1001.7 ± 2.3	14.34 ± 0.06	14.33 ± 0.06	1043 ± 2
9236	1174	So-1-1174	584.291 ± 0.148	0.477 ± 0.002	0.263 ± 0.001	982 ± 5	1071.3 ± 1.8	14.60 ± 0.07	14.59 ± 0.07	1117 ± 2
10103*	1189	So-1-1189	571.869 ± 0.043	0.299 ± 0.001	0.250 ± 0.001	1470 ± 7	1004.4 ± 2.0	14.33 ± 0.06	14.32 ± 0.06	1046 ± 2
9237	1209	So-1-1209	1230.417 ± 0.088	0.544 ± 0.001	0.304 ± 0.001	2099 ± 8	1098.2 ± 0.9	16.79 ± 0.05	16.78 ± 0.06	1152 ± 1
9238	1253	So-1-1253	514.017 ± 0.040	1.034 ± 0.002	0.317 ± 0.001	484 ± 3	1012.9 ± 1.8	18.39 ± 0.10	18.36 ± 0.09	1067 ± 2
9239	1289	So-1-1289	482.036 ± 0.049	0.986 ± 0.003	0.349 ± 0.002	523 ± 3	1081.9 ± 1.9	19.64 ± 0.10	19.61 ± 0.10	1144 ± 2
9240	1319	So-1-1319	458.757 ± 0.032	0.916 ± 0.002	0.352 ± 0.001	539 ± 2	1013.9 ± 1.5	20.55 ± 0.07	20.53 ± 0.07	1075 ± 2
9241	1330	So-1-1330	486.969 ± 0.036	1.618 ± 0.004	0.355 ± 0.001	328 ± 1	1038.8 ± 2.0	20.52 ± 0.08	20.47 ± 0.07	1101 ± 2
9242	1339	So-1-1339	339.052 ± 0.035	3.139 ± 0.012	0.409 ± 0.002	136 ± 1	1098.5 ± 3.9	23.18 ± 0.11	23.07 ± 0.12	1173 ± 4
9243	1350	So-1-1350	480.572 ± 0.039	1.871 ± 0.007	0.418 ± 0.002	330 ± 2	1045.7 ± 2.1	24.40 ± 0.11	24.35 ± 0.13	1120 ± 2

Lab No.	dft mm	label	^{238}U ng/g	^{232}Th ng/g	$^{230}\text{Th}/^{238}\text{U}$ Act. ratio	$^{230}\text{Th}/^{232}\text{Th}$ Act. ratio	$\delta^{234}\text{U}_{\text{corr}}$ ‰	age kyr BP	age_{corr} kyr BP	$\delta^{234}\text{U}_{\text{init}}$ ‰
9244	1370	So-1-1370	455.451 ± 0.069	0.505 ± 0.001	0.450 ± 0.001	1245 ± 5	1028.0 ± 1.7	26.73 ± 0.10	26.71 ± 0.10	1109 ± 2
9245	1417	So-1-1417	512.769 ± 0.028	0.786 ± 0.001	0.472 ± 0.001	942 ± 3	1024.1 ± 1.6	28.25 ± 0.08	28.23 ± 0.08	1109 ± 2
9246	1438	So-1-1438	537.321 ± 0.035	0.529 ± 0.001	0.492 ± 0.001	1531 ± 5	1022.6 ± 1.6	29.65 ± 0.08	29.64 ± 0.08	1112 ± 2
9247	1462	So-1-1462	396.594 ± 0.039	0.319 ± 0.001	0.497 ± 0.001	1891 ± 7	950.1 ± 2.2	31.27 ± 0.10	31.26 ± 0.12	1038 ± 2
9248	1482	So-1-1482	486.200 ± 0.062	0.407 ± 0.001	0.525 ± 0.001	1915 ± 7	999.3 ± 2.0	32.33 ± 0.11	32.32 ± 0.11	1095 ± 2
9249	1508	So-1-1508	476.299 ± 0.068	0.480 ± 0.001	0.567 ± 0.002	1724 ± 8	1070.4 ± 2.5	33.91 ± 0.17	33.89 ± 0.16	1178 ± 3
10104	1522	So-1-1522	545.440 ± 0.053	0.780 ± 0.002	0.571 ± 0.001	1228 ± 4	1005.3 ± 1.7	35.50 ± 0.11	35.48 ± 0.11	1112 ± 2
9250	1538	So-1-1538	334.066 ± 0.070	3.176 ± 0.013	0.582 ± 0.003	188 ± 1	939.3 ± 2.9	37.75 ± 0.21	37.63 ± 0.21	1045 ± 3
9251	1554	So-1-1554	710.936 ± 0.064	0.416 ± 0.001	0.592 ± 0.002	3117 ± 13	941.9 ± 1.6	38.41 ± 0.15	38.41 ± 0.15	1050 ± 2
9252	1574	So-1-1574	346.797 ± 0.035	1.169 ± 0.002	0.650 ± 0.002	595 ± 2	1072.5 ± 2.2	39.65 ± 0.13	39.60 ± 0.14	1200 ± 2
9253	1598	So-1-1598	485.495 ± 0.051	0.471 ± 0.001	0.633 ± 0.002	2019 ± 9	972.2 ± 1.9	40.80 ± 0.17	40.79 ± 0.17	1091 ± 2
9254	1618	So-1-1618	501.239 ± 0.034	0.605 ± 0.001	0.594 ± 0.002	1520 ± 6	832.9 ± 2.3	41.35 ± 0.17	41.34 ± 0.16	936 ± 3

Table A.3: Mg/Ca and Sr/Ca mass ratios of stalagmite So-1 as determined by ICP-OES measurements. A relative uncertainty of 3% is assumed, reflecting the internal standard reproducibility.

depth mm	t_{mod} kyr BP	Mg/Ca $\mu\text{g}/\text{mg}$	Sr/Ca $\mu\text{g}/\text{mg}$	depth mm	t_{mod} kyr BP	Mg/Ca $\mu\text{g}/\text{mg}$	Sr/Ca $\mu\text{g}/\text{mg}$
955	10.15 ± 0.08	3.24	0.284	1314	20.36 ± 0.12	4.79	0.503
965	10.25 ± 0.06	3.08	0.281	1324	20.68 ± 0.14	5.28	0.477
974	10.35 ± 0.04	2.33	0.318	1334	20.94 ± 0.92	6.61	0.399
983	10.44 ± 0.05	2.25	0.304	1343	23.53 ± 0.11	5.13	0.397
996	10.58 ± 0.10	3.10	0.291	1356	25.06 ± 0.06	11.34	0.797
1009	10.66 ± 0.15	2.73	0.290	1364	26.00 ± 0.07	5.80	0.424
1022	11.07 ± 0.17	2.74	0.273	1375	26.93 ± 0.06	5.07	0.469
1034	11.78 ± 0.06	2.71	0.283	1384	27.44 ± 0.04	5.26	0.460
1047	12.41 ± 0.10	2.51	0.330	1393	27.48 ± 0.08	4.46	0.451
1065	12.64 ± 0.06	2.68	0.376	1403	27.80 ± 0.09	5.45	0.477
1085	13.25 ± 0.04	2.53	0.389	1413	28.13 ± 0.07	5.71	0.412
1100	13.46 ± 0.07	2.46	0.362	1428	28.99 ± 0.10	5.08	0.412
1119	13.72 ± 0.06	2.34	0.391	1438	29.65 ± 0.07	4.74	0.427
1133	13.92 ± 0.19	2.54	0.404	1438	29.65 ± 0.07	4.83	0.439
1139	14.11 ± 0.18	2.48	0.421	1448	30.30 ± 0.11	5.12	0.410
1144	14.27 ± 0.17	2.62	0.444	1456	30.82 ± 0.12	4.85	0.394
1150	14.34 ± 0.05	3.35	0.519	1469	31.63 ± 0.16	4.88	0.462
1160	14.43 ± 0.04	3.40	0.453	1477	32.08 ± 0.17	5.66	0.391
1174	14.55 ± 0.04	3.84	0.483	1488	32.73 ± 0.22	5.80	0.432
1182	14.60 ± 0.06	3.29	0.513	1498	32.97 ± 0.36	5.72	0.463
1193	14.91 ± 0.22	3.78	0.527	1508	33.84 ± 0.13	6.10	0.459
1204	16.61 ± 0.28	7.88	0.589	1519	35.18 ± 0.49	5.43	0.408
1213	17.02 ± 0.21	8.01	1.017	1529	36.58 ± 0.44	4.65	0.407
1218	17.11 ± 0.09	8.06	0.751	1538	37.58 ± 0.17	4.64	0.337
1223	17.29 ± 0.12	8.23	0.565	1549	38.19 ± 0.18	4.85	0.437
1233	17.65 ± 0.12	7.31	0.519	1559	38.73 ± 0.15	4.56	0.451
1243	18.01 ± 0.10	5.95	0.444	1569	39.30 ± 0.18	4.56	0.390
1253	18.36 ± 0.09	5.51	0.375	1579	39.83 ± 0.12	3.64	0.377
1263	18.70 ± 0.08	5.14	0.378	1588	40.27 ± 0.12	4.11	0.385
1274	19.07 ± 0.15	3.54	0.409	1598	40.78 ± 0.20	3.37	0.410
1284	19.40 ± 0.12	4.35	0.377	1608	41.22 ± 0.29	3.29	0.404
1294	19.73 ± 0.10	3.71	0.413	1618	41.42 ± 0.16	2.65	0.439
1306	20.12 ± 0.12	3.99	0.437	-	-	-	-

Mg/Ca mass ratios of stalagmite So-1 as determined by ICPQMS measurements. A relative uncertainty of 3% is assumed, reflecting the internal standard reproducibility.

depth mm	t_{mod} kyr BP	Mg/Ca $\mu\text{g}/\text{mg}$	depth mm	t_{mod} kyr BP	Mg/Ca $\mu\text{g}/\text{mg}$
950	10.09 ± 0.10	2.84	1201	15.83 ± 0.27	6.56
958	10.18 ± 0.08	2.67	1204	16.54 ± 0.03	8.63
989	10.51 ± 0.07	3.33	1209	16.87 ± 0.19	8.32
1004	10.64 ± 0.14	2.96	1213	17.02 ± 0.21	8.82
1031	11.60 ± 0.40	2.81	1213	17.02 ± 0.21	8.87
1039	12.11 ± 0.18	2.84	1218	17.11 ± 0.09	8.74
1039	12.11 ± 0.18	2.83	1269	18.90 ± 0.17	5.01
1057	12.54 ± 0.05	2.52	1279	19.24 ± 0.13	5.17
1057	12.54 ± 0.05	2.57	1319	20.52 ± 0.11	5.87
1171	14.53 ± 0.03	3.91	1330	20.80 ± 0.14	6.47
1174	14.55 ± 0.04	4.29	1336	22.61 ± 1.03	6.83
1178	14.59 ± 0.05	4.11	1339	23.03 ± 0.59	6.77
1182	14.60 ± 0.06	3.66	1350	24.36 ± 0.07	5.82
1186	14.63 ± 0.07	4.89	1360	25.53 ± 0.07	7.24
1189	14.65 ± 0.07	4.73	1367	26.36 ± 0.08	6.38
1193	14.91 ± 0.22	4.20	1370	26.64 ± 0.05	6.23
1196	15.25 ± 0.22	6.69	-	-	-

Table A.4: Correlation coefficients of the So-1 data considering the IntCal13 DCF. Given are Pearson product-moment correlation coefficients for the entire record ($N = 84$, subtable **a**), the time after 17 kyr BP ($N = 33$, subtable **b**), and before 17 kyr BP ($N = 51$, subtable **c**). The considered data are DCF, stable isotopes, elemental ratios and growth rate (GR).

a	DCF	$\delta^{18}\text{O}$	$\delta^{13}\text{C}$	Mg/Ca	Sr/Ca	GR
DCF	1.00	-0.28	0.28	0.54	0.39	-0.24
$\delta^{18}\text{O}$	-0.28	1.00	-0.72	-0.60	-0.55	0.38
$\delta^{13}\text{C}$	0.28	-0.72	1.00	0.60	0.27	-0.46
Mg/Ca	0.54	-0.60	0.60	-1.00	0.64	-0.42
Sr/Ca	0.39	-0.55	0.27	0.64	1.00	-0.15
GR	-0.24	0.38	-0.46	-0.42	-0.15	1.00

b	DCF	$\delta^{18}\text{O}$	$\delta^{13}\text{C}$	Mg/Ca	Sr/Ca	GR
DCF	1.00	-0.41	0.47	0.71	0.64	-0.10
$\delta^{18}\text{O}$	-0.41	1.00	-0.71	-0.66	-0.89	0.18
$\delta^{13}\text{C}$	0.47	-0.71	-1.00	0.66	0.65	-0.20
Mg/Ca	0.71	-0.66	0.66	1.00	0.83	-0.28
Sr/Ca	0.64	-0.89	0.65	0.83	1.00	-0.18
GR	-0.10	0.18	-0.20	-0.28	-0.18	1.00

c	DCF	$\delta^{18}\text{O}$	$\delta^{13}\text{C}$	Mg/Ca	Sr/Ca	GR
DCF	1.00	0.10	-0.04	0.39	0.24	-0.19
$\delta^{18}\text{O}$	0.10	1.00	-0.25	-0.05	-0.26	0.00
$\delta^{13}\text{C}$	-0.04	-0.25	-1.00	0.13	0.04	-0.03
Mg/Ca	0.39	-0.05	0.13	1.00	0.57	-0.18
Sr/Ca	0.24	-0.26	0.04	0.57	1.00	-0.02
GR	-0.19	0.00	-0.03	-0.18	-0.02	1.00

Table A.5: Correlation coefficients of the So-1 data considering the HuluCal DCF. Given are Pearson product-moment correlation coefficients for the entire record ($N = 78$, subtable **a**), the time after 17 kyr BP ($N = 27$, subtable **b**), and before 17 kyr BP ($N = 51$, subtable **c**). The considered data are DCF, stable isotopes, elemental ratios and growth rate (GR).

a	DCF	$\delta^{18}\text{O}$	$\delta^{13}\text{C}$	Mg/Ca	Sr/Ca	GR
DCF	1.00	-0.35	0.35	0.53	0.35	-0.31
d18O	-0.35	1.00	-0.67	-0.55	-0.49	0.38
d13C	0.35	-0.67	-1.00	0.55	0.18	-0.44
Mg/Ca	0.53	-0.55	0.55	1.00	0.61	-0.40
Sr/Ca	0.35	-0.49	0.18	0.61	1.00	-0.11
GR	-0.31	0.38	-0.44	-0.40	-0.11	1.00

b	DCF	$\delta^{18}\text{O}$	$\delta^{13}\text{C}$	Mg/Ca	Sr/Ca	GR
DCF	1.00	-0.39	0.42	0.69	0.63	-0.04
d18O	-0.39	1.00	-0.71	-0.67	-0.89	0.25
d13C	0.42	-0.71	-1.00	0.64	0.61	-0.21
Mg/Ca	0.69	-0.67	0.64	1.00	0.84	-0.29
Sr/Ca	0.63	-0.89	0.61	0.84	1.00	-0.21
GR	-0.04	0.25	-0.21	-0.29	-0.21	1.00

c	DCF	$\delta^{18}\text{O}$	$\delta^{13}\text{C}$	Mg/Ca	Sr/Ca	GR
DCF	1.00	0.06	-0.15	0.24	0.21	-0.29
d18O	0.06	1.00	-0.25	-0.05	-0.26	0.00
d13C	-0.15	-0.25	-1.00	0.13	0.04	-0.03
Mg/Ca	0.24	-0.05	0.13	1.00	0.57	-0.18
Sr/Ca	0.21	-0.26	0.04	0.57	1.00	-0.02
GR	-0.29	0.00	-0.03	-0.18	-0.02	1.00

A.2 Stalagmite M1-5, Moomi Cave

The radiocarbon and U-series data of stalagmite M1-5 from Moomi Cave, Socotra Island are published in the paper by Therre et al. (2020) and are available at the database PANGAEA:

<https://doi.org/10.1594/PANGAEA.906003>.

The Mg/Ca ratios were measured by ICP-OES and ICPQMS and are given in Table A.6.

Table A.6: Mg/Ca mass ratios of stalagmite M1-5 as determined by ICP-OES measurements. The uncertainties of Mg/Ca ratios and modeled ages is 1σ .

depth mm	t_{mod} kyr BP	Mg/Ca $\mu\text{g}/\text{mg}$	depth mm	t_{mod} kyr BP	Mg/Ca $\mu\text{g}/\text{mg}$
88	10.90 ± 0.07	13.30 ± 0.40	481	13.06 ± 0.04	12.60
98	10.91 ± 0.07	11.00 ± 0.33	510.5	13.15 ± 0.03	12.80
103	10.92 ± 0.07	32.40 ± 0.97	544	13.25 ± 0.03	12.70
108	11.04 ± 0.14	23.25 ± 0.70	579	13.37 ± 0.03	14.20
118	11.74 ± 0.06	23.25 ± 0.70	600	13.44 ± 0.03	13.00
128	11.78 ± 0.05	14.90 ± 0.45	614	13.49 ± 0.03	13.60
138	11.80 ± 0.06	14.70 ± 0.44	644	13.60 ± 0.04	13.40
148	11.82 ± 0.05	13.40 ± 0.40	712	13.85 ± 0.04	12.60
158	11.84 ± 0.05	14.50 ± 0.44	780	14.10 ± 0.03	12.60
168	11.86 ± 0.05	12.80 ± 0.38	873	14.45 ± 0.05	12.90
178	11.89 ± 0.04	13.20 ± 0.40	938	14.71 ± 0.06	15.90
188	11.93 ± 0.05	12.90 ± 0.39	977	14.94 ± 0.10	14.30
198	11.96 ± 0.05	13.90 ± 0.42	1000	15.06 ± 0.05	13.70
208	11.99 ± 0.05	13.70 ± 0.41	1015	15.14 ± 0.05	14.40
218	12.03 ± 0.06	12.90 ± 0.39	1036	15.25 ± 0.05	13.40
228	12.06 ± 0.06	12.50 ± 0.38	1069	15.40 ± 0.05	13.40
238	12.10 ± 0.06	12.30 ± 0.37	1154	15.77 ± 0.09	13.30
248	12.14 ± 0.06	11.70 ± 0.35	1234	16.13 ± 0.08	15.70
258	12.19 ± 0.05	12.40 ± 0.37	1300	16.65 ± 0.03	16.00
268	12.22 ± 0.05	13.60 ± 0.41	1390	17.18 ± 0.07	14.00
277.5	12.26 ± 0.05	14.60 ± 0.44	1420	17.39 ± 0.05	18.50
286	12.29 ± 0.04	13.80 ± 0.41	1450	17.68 ± 0.06	17.20
296.75	12.33 ± 0.04	12.10 ± 0.36	1480	17.99 ± 0.04	17.10
306	12.36 ± 0.04	12.60 ± 0.38	1579	19.20 ± 0.12	16.90
316	12.40 ± 0.03	13.20 ± 0.40	1620	19.71 ± 0.17	20.40
326	12.44 ± 0.03	12.70 ± 0.38	1651	19.85 ± 0.15	18.50
336	12.47 ± 0.04	12.40 ± 0.37	1675	20.07 ± 0.07	18.00
346	12.51 ± 0.04	11.80 ± 0.35	1695	20.29 ± 0.06	21.60
356	12.55 ± 0.04	12.30 ± 0.37	1715	20.47 ± 0.08	17.00
366	12.59 ± 0.04	12.00 ± 0.36	1731	20.69 ± 0.10	17.90
376	12.63 ± 0.03	12.50 ± 0.38	1811	21.78 ± 0.13	21.40
386.5	12.68 ± 0.03	11.80 ± 0.35	1863	22.09 ± 0.04	18.70
396.5	12.72 ± 0.04	13.20 ± 0.40	1885	22.21 ± 0.07	22.60
406.5	12.76 ± 0.04	13.80 ± 0.41	1910	22.33 ± 0.71	21.40
416.5	12.81 ± 0.04	13.10 ± 0.39	1936	23.85 ± 0.05	20.60
425.5	12.86 ± 0.05	12.20 ± 0.37	1963	24.16 ± 0.07	19.60
430.5	12.88 ± 0.05	12.00 ± 0.36	2035	24.96 ± 0.05	17.00
435.5	12.90 ± 0.04	15.00 ± 0.45	2051	25.13 ± 0.05	18.80
440.5	12.93 ± 0.04	13.90 ± 0.42	2104	25.70 ± 0.07	18.20
450.5	12.97 ± 0.03	16.50 ± 0.50	2155	26.24 ± 0.08	19.10
460.5	13.00 ± 0.04	12.80 ± 0.38	2222	26.99 ± 0.12	18.90

Table A.7: Correlation coefficients of the M1-5 data. Given are Pearson product-moment correlation coefficients for the entire record ($N = 78$, subtable **a**), the YD ($N = 43$, subtable **b**), and before the YD ($N = 32$, subtable **c**). The considered data are DCF, stable isotopes, Mg/Ca ratios and growth rate (GR).

a	DCF	$\delta^{18}\text{O}$	$\delta^{13}\text{C}$	Mg/Ca	GR
DCF	1.00	0.61	0.45	0.46	-0.52
$\delta^{18}\text{O}$	0.61	1.00	0.80	0.52	-0.63
$\delta^{13}\text{C}$	0.45	0.80	1.00	0.56	-0.61
Mg/Ca	0.46	0.52	0.56	1.00	-0.60
GR	-0.52	-0.63	-0.61	-0.60	1.00

b	DCF	$\delta^{18}\text{O}$	$\delta^{13}\text{C}$	Mg/Ca	GR
DCF	1.00	0.32	0.05	-0.30	-0.07
$\delta^{18}\text{O}$	0.32	1.00	0.78	0.12	-0.25
$\delta^{13}\text{C}$	0.05	0.78	1.00	0.18	-0.42
Mg/Ca	-0.30	0.12	0.18	1.00	-0.26
GR	-0.07	-0.25	-0.42	-0.26	1.00

c	DCF	$\delta^{18}\text{O}$	$\delta^{13}\text{C}$	Mg/Ca	GR
DCF	1.00	0.71	0.71	0.82	-0.82
$\delta^{18}\text{O}$	0.71	1.00	0.84	0.72	-0.78
$\delta^{13}\text{C}$	0.71	0.84	1.00	0.82	-0.68
Mg/Ca	0.82	0.72	0.82	1.00	-0.71
GR	-0.82	-0.78	-0.68	-0.71	1.00

A.3 Compiled stalagmite ^{14}C records from various studies

For a review of stalagmite ^{14}C studies, data was summarized from theses and projects at the IUP from the last years, as well as from several publications with studies on the mechanisms of stalagmite DCF.

External records are taken from publications on stalagmite ^{14}C of the last decade and the inter-site comparison study on European cave sites by Genty et al. (2001). The gathered data are summarized in Table A.8 with a description of the site and sample, mean DCF, stable carbon isotopes, age range and cave temperature.

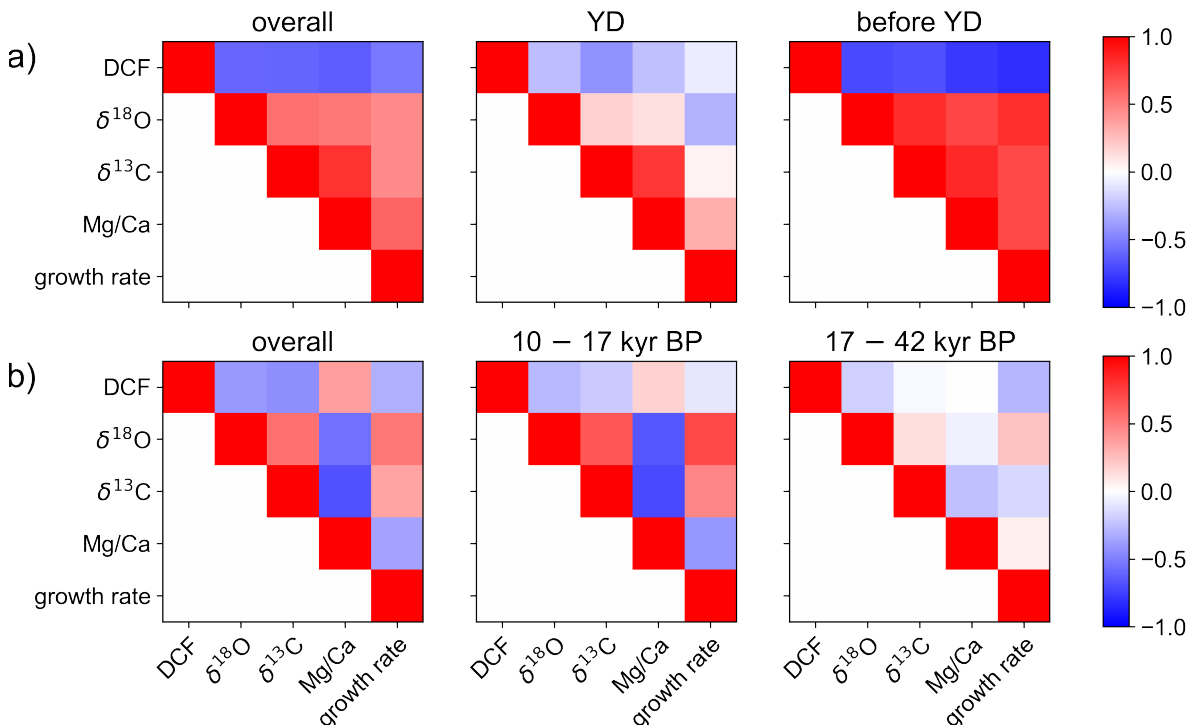


Figure A.1: Correlation plot of stalagmites M1-5 (a) and So-1 (b) for selected time spans. The measured proxies show strong overall correlation for both records. If certain times are cropped out, it becomes clear, that the overall covariance can be traced back to certain periods, where climate mechanism acts on all measured proxies. For stalagmite M1-5, this is the area throughout the LGM until the beginning of the Younger Dryas. The Sofular record of So-1 shows strong cross connection of the proxies between 17 to 10 kyr BP.

Table A.8: Summary of stalagmite data relevant for the review of processes determining stalagmite DCF. Given are sample description and location, as well as the mean DCF and mean $\delta^{13}\text{C}$ with 1σ standard deviations, the age of the respective stalagmites, cave temperatures with annual variability and the relevant references. Above the first bar, the ^{14}C measurements were conducted at the Institute of Environmental Physics over the last years as part of several Bachelor theses and of this dissertation. In the mid-section, data is collected from various studies focusing on stalagmite DCF, while the last part contains data reported by Genty et al. (2001) from several European sites. For stalagmites marked by †, the stable isotope data is retrieved from AMS measurements during the ^{14}C determination.

Stalagmite	Cave	Location	DCF %	$\delta^{13}\text{C}$ ‰ VPDB	Age kyrBP	Cave T °C	References
M1-5	Moomi Cave	Socotra Island	44.0 ± 7.1	-6.8 ± 1.2	27 to 11	22.0 ± 0.5	Shakun et al. (2007), Therre et al. (2020)
H5	Hoti Cave	Oman	40.8 ± 4.5	-2.9 ± 1.2	9.5 to 6.5	26.0 ± 0.5	Therre (2014)
So-1	Sofular Cave	Sofular (Turkey)	14.5 ± 5.7	-8.6 ± 1.3	43 to 10	13.3 ± 0.5	Fleitmann et al. (2009), Badertscher et al. (2014)
LB-1†	Cueva Larga	Puerto Rico	29.4 ± 8.1	-5.1 ± 3.0	40 to 0	23.1 ± 0.2	Vieten et al. (2016), Schandl (2019)
PR-LA1	Cueva Larga	Puerto Rico	19.6 ± 2.2	-9.0 ± 1.0	45 to 15	21.0 ± 0.5	Vieten et al. (2016), Warken (2017)
M6_1/20†	Schratten Cave	Switzerland	56.9 ± 4.3	0.7 ± 3.0	6 to 0	4.0 ± 2.0	Proß (2018)
CC27	Corchia Cave	Tuscany (Italy)	59.0 ± 3.0	-0.7 ± 1.0	12 to 0	8.4 ± 0.3	Bajo et al. (2017)
LR06-B1	Liang Luar	Flores (Indonesia)	17.1 ± 0.9	-11.6 ± 0.3	2.8 to 2.4	24.5 ± 0.5	Griffiths et al. (2012)
HS4	Heshang Cave	Wuhan (China)	10.3 ± 1.0	-11.0 ± 1.0	9.6 to 0.5	18.0 ± 2.0	Hu et al. (2008), Noronha et al. (2014)
H82	Hulu Cave	Nanjing (China)	5.6 ± 0.8	-8.0 ± 1.0	14 to 10	15.4 ± 0.5	Wang et al. (2001), Cheng et al. (2018)
OB12	Obstanser Eishöhle	Austria	68.1 ± 2.0	1.0 ± 0.5	12.5 to 9	1.0 ± 0.5	Spötl et al. (2016)
YOK-I	Yok Balum Cave	Belize	12.9 ± 1.7	-8.5 ± 1.0	1.4 to 0	22.9 ± 0.5	Lechleitner et al. (2016a)
Fau-stm14	La Faurie	Dordogne (SW-France)	9.0 ± 1.5	-10.3 ± 0.1	modern	12.9 ± 0.5	
Han-stm5	Grottes de Han	Han-sur-Lesse (Belgium)	12.2 ± 1.5	-9.4 ± 0.1	modern	8.9 ± 0.5	
Pos-stm4	Postojna Cave	Postojna (Slovenia)	11.6 ± 1.5	-9.6 ± 0.1	modern	9.3 ± 0.5	
BFM-Boss	Browns Folly mine	England	17.5 ± 1.5	-10.0 ± 0.1	modern	10.0 ± 0.5	
Vil-stm1	Villars	Dordogne (SW-France)	9.4 ± 1.5	-9.9 ± 0.1	3.1 to 0	12.4 ± 0.5	all from
Han-stm1	Grottes de Han	Han-sur-Lesse (Belgium)	17.5 ± 1.5	-6.8 ± 0.1	11 to 4.8	8.9 ± 0.5	Genty et al. (2001)
SU-96-7	Uamb-an-Tartair cave	Sutherland (Scotland)	36.7 ± 1.0	-10.7 ± 0.1	1.0 to 0	7.0 ± 0.5	
SU2	Uamb-an-Tartair cave	Sutherland (Scotland)	33.6 ± 4.2	-14.9 ± 0.1	2.6 to 1.0	7.0 ± 0.5	
SU-96-1	Uamb-an-Tartair cave	Sutherland (Scotland)	24.5 ± 2.9	-12.7 ± 0.1	3.8 to 2.0	7.0 ± 0.5	
Sal-stm1	Salamandre	Gard (SE-France)	5.3 ± 3.0	-10.0 ± 0.1	6.6 to 0.1	14.5 ± 0.5	

B List of Figures

2.1	Formation process of stalagmites	17
2.2	Graphical solution to U-series dating equations	19
2.3	Natural production and distribution of ^{14}C	21
2.4	IntCal13 (Reimer et al. 2013) and Hulu Cave record (Cheng et al. 2018)	26
2.5	Carbon sources and carbon isotope signature of stalagmite formation .	30
2.6	Climate variability since 50 kyr in ice core and stalagmite data	35
3.1	Schematic illustration of the Thermo Fisher Neptune Plus MC-ICP-MS	38
3.2	Schematic illustration of the MICADAS AMS	42
4.1	Extraction line schematic view	49
4.2	Calibration volume data and fit, ideal gas law	51
4.3	Histograms of blank results for powdered and piece samples	54
4.4	Histogram and isotopic analysis of measured IAEA C2 samples	55
4.5	Carbonate extraction efficiency	57
4.6	Combined speleothem radiocarbon results	58
5.1	Socotra Island geography, topography and stalagmite M1-5	65
5.2	Stalagmite M1-5 U-series ages vs. depth and age model	67
5.3	Stalagmite M1-5 ^{14}C ages and DCF vs. modeled age	68
5.4	Stalagmite M1-5 combined records	71
5.5	Stalagmite M1-5 DCF and Mg/Ca for the YD	73
6.1	Map of the Black Sea region with Sofular Cave location	77
6.2	Stalagmite So-1 U-series age model	80
6.3	Stalagmite So-1 ^{14}C and DCF results	83
6.4	Stalagmite So-1 Mg/Ca and Sr/Ca ratios	84
6.5	Stalagmite So-1 ^{14}C aided age model	87
6.6	Stalagmite So-1 ^{14}C during Termination I in comparison with Rudzka et al. (2011)	89
6.7	Stalagmite So-1 combined proxy plot	92
6.8	Stalagmite So-1 DCF modes in last glacial	94
6.9	Stalagmite So-1 correlation measured proxies	97
6.10	Stalagmite So-1 $\Delta^{14}\text{C}$ and relative calibration	100
7.1	Stalagmite ^{14}C data from IUP in context to IntCal13 (Reimer et al. 2013)	105
7.2	Location of selected caves with stalagmite ^{14}C studies	107

LIST OF FIGURES

7.3	Carbon age distribution vs. soil depth (Balesdent et al. 2018)	108
7.4	Dependence of DCF on cave temperature for selected records	109
7.5	$\delta^{13}\text{C}$ vs. DCF for selected records	112
7.6	Mg/Ca vs. DCF correlation in selected time spans of Moomi Cave and Sofular Cave and normalized DCF of stalagmite M1-5	114
A.1	Correlation plot of stalagmites M1-5 and So-1 for selected time spans .	XV

C List of Tables

2.1	Carbon sources in stalagmite formation	32
4.1	Measured radiocarbon activities for different blank materials	53
4.2	Terrestrial archives prepared in the Heidelberg ¹⁴ C lab	59
A.1	Radiocarbon dating results and DCF of stalagmite So-1	IV
A.2	U-series dating results of stalagmite So-1	VIII
A.3	Elemental ratio results of stalagmite So-1	X
A.4	Correlation coefficients of stalagmite So-1 (IntCal13 dataset)	XI
A.5	Correlation coefficients of stalagmite So-1 (HuluCal dataset)	XII
A.6	Elemental ratio results of stalagmite M1-5	XIII
A.7	Correlation coefficients of stalagmite M1-5 proxies	XIV
A.8	Summary of selected stalagmite ¹⁴ C records from recent studies	XVI

D List of Abbreviations

AMS	Accelerator Mass Spectrometry
BP	Before Present (before 1950 CE)
B/A	Bølling–Allerød interstadial
CE	Common Era
CEZA	Curt-Engelhorn-Center Archaeometry
DCF	Dead carbon fraction
DIC	Dissolved inorganic carbon
DOC	Dissolved organic carbon
D/O	Dansgaard/Oeschger (events/cycles)
ESA	Electrostatic Analyzer
GR	Growth rate
HS	Heinrich Stadial
IAEA	International Atomic Energy Agency
ICP	Inductively Coupled Plasma
ICPQMS	Inductively Coupled Plasma Quadrupole Mass Spectrometry
ICP-OES	Inductively Coupled Plasma Optical Emission Spectrometry
ITCZ	Intertropical Convergence Zone
IUP	Institute of Environmental Physics (<i>Institut für Umweltphysik</i>)
LGM	Last Glacial Maximum
MC-ICP-MS	Multi Collector Inductively Coupled Plasma Mass Spectrometry
MICADAS	Mini Carbon Dating System
MS	Mass Spectrometry
NGRIP	North Greenland Ice Core Project
PCP	Prior calcite precipitation
pmC	Percent modern Carbon
POM	Particulate organic matter
SOM	Soil organic matter
VPDB	Vienna Pee Dee Belemnite
VSMOW	Vienna Standard Mean Ocean Water
YD	Younger Dryas stadial

Bibliography

- Adolphi, F., Bronk Ramsey, C., Erhardt, T., Lawrence Edwards, R., Cheng, H., Turney, C. S., Cooper, A., Svensson, A., Rasmussen, S. O., Fischer, H., and Muscheler, R. (2018). Connecting the Greenland ice-core and U/Th timescales via cosmogenic radionuclides: Testing the synchronicity of Dansgaard-Oeschger events. *Climate of the Past*.
- Andersen, K. K., Azuma, N., Barnola, J. M., Bigler, M., Biscaye, P., Caillon, N., Chappellaz, J., Clausen, H. B., Dahl-Jensen, D., Fischer, H., Flückiger, J., Fritzsche, D., Fujii, Y., Goto-Azuma, K., Grønvold, K., Gundestrup, N. S., Hansson, M., Huber, C., Hvidberg, C. S., Johnsen, S. J., Jonsell, U., Jouzel, J., Kipfstuhl, S., Landais, A., Leuenberger, M., Lorrain, R., Masson-Delmotte, V., Miller, H., Motoyama, H., Narita, H., Popp, T., Rasmussen, S. O., Raynaud, D., Rothlisberger, R., Ruth, U., Samyn, D., Schwander, J., Shoji, H., Siggard-Andersen, M. L., Steffensen, J. P., Stocker, T., Sveinbjörnsdóttir, A. E., Svensson, A., Takata, M., Tison, J. L., Thorsteinsson, T., Watanabe, O., Wilhelms, F., and White, J. W. (2004). High-resolution record of Northern Hemisphere climate extending into the last interglacial period. *Nature*, 431(7005):147–151.
- Anderson, E. (1947). Radiocarbon from Cosmic Radiation. *Science*, 105(1934):576.
- Arnold, J. R. and Libby, W. F. (1951). Radiocarbon Dates. *Science*, 113(2927):111–120.
- Arps, J. (2017). *Towards ϵ -Precision of U-series Age Determinations of Secondary Carbonates*. Dissertation, Heidelberg University.
- Badertscher, S., Borsato, A., Frisia, S., Cheng, H., Edwards, R. L., Tüysüz, O., and Fleitmann, D. (2014). Speleothems as sensitive recorders of volcanic eruptions - the Bronze Age Minoan eruption recorded in a stalagmite from Turkey. *Earth and Planetary Science Letters*.
- Bahr, A., Lamy, F., Arz, H., Kuhlmann, H., and Wefer, G. (2005). Late glacial to Holocene climate and sedimentation history in the NW Black Sea. *Marine Geology*, 214(4):309–322.
- Bahr, A., Lamy, F., Arz, H. W., Major, C., Kwiecien, O., and Wefer, G. (2008). Abrupt changes of temperature and water chemistry in the late Pleistocene and early Holocene Black Sea. *Geochemistry, Geophysics, Geosystems*, 9(1).
- Bajo, P., Borsato, A., Drysdale, R., Hua, Q., Frisia, S., Zanchetta, G., Hellstrom, J., and Woodhead, J. (2017). Stalagmite carbon isotopes and dead carbon proportion (DCP)

- in a near-closed-system situation: An interplay between sulphuric and carbonic acid dissolution. *Geochimica et Cosmochimica Acta*, 210:208–227.
- Baker, A., Ito, E., Smart, P. L., and McEwan, R. F. (1997). Elevated and variable values of ^{13}C in speleothems in a British cave system. *Chemical Geology*, 136(3-4):263–270.
- Balesdent, J., Basile-Doelsch, I., Chadoeuf, J., Cornu, S., Derrien, D., Fekiacova, Z., and Hatté, C. (2018). Atmosphere–soil carbon transfer as a function of soil depth. *Nature*, 559(7715):599–602.
- Bard, E., Hamelin, B., Fairbanks, R. G., and Zindler, A. (1990). Calibration of the ^{14}C timescale over the past 30000 years using mass spectrometric U-Th ages from Barbados corals. *Nature*, 345:405–410.
- Bard, E., Ménot, G., Rostek, F., Licari, L., Böning, P., Edwards, R. L., Cheng, H., Wang, Y., and Heaton, T. J. (2013). Radiocarbon Calibration/Comparison Records Based on Marine Sediments from the Pakistan and Iberian Margins. *Radiocarbon*, 55(4):1999–2019.
- Beck, J. W., Richards, D. A., Edwards, R. L., Silverman, B. W., Smart, P. L., Donahue, D. J., Herrera-Osterheld, S., Burr, G. S., Calsoyas, L., Jull, A. T., and Biddulph, D. (2001). Extremely large variations of atmospheric ^{14}C concentration during the last glacial period. *Science*, 292(5526):2453–2458.
- Bond, G. C. and Lotti, R. (1995). Iceberg Discharges into the North Atlantic on Millennial Time Scales During the Last Glaciation. *Science*, 267(5200):1005–1010.
- Borsato, A., Frisia, S., Wynn, P. M., Fairchild, I. J., and Miorandi, R. (2015). Sulphate concentration in cave dripwater and speleothems: long-term trends and overview of its significance as proxy for environmental processes and climate changes. *Quaternary Science Reviews*, 127:48–60.
- Bottema, S., Woldring, H., and Aytuğ, B. (1993). Late Quaternary vegetation of Northern Turkey. *Palaeohistoria*, 35/36:13–72.
- Broecker, W., Bond, G., Klas, M., Clark, E., and McManus, J. (1992). Origin of the northern Atlantic’s Heinrich events. *Climate Dynamics*, 6(3-4):265–273.
- Broecker, W. S. (1994). Massive iceberg discharges as triggers for global climate change. *Nature*, 372(6505):421–424.
- Bronk Ramsey, C. (2008). Radiocarbon dating: revolutions in understanding. *Archaeometry*, 50(2):249–275.
- Bronk Ramsey, C. (2013). Recent and Planned Developments of the Program OxCal. *Radiocarbon*, 55(3–4).

- Bronk Ramsey, C., Staff, R. A., Bryant, C. L., Brock, F., Kitagawa, H., van der Plicht, J., Schlolaut, G., Marshall, M. H., Brauer, A., Lamb, H. F., Payne, R. L., Tarasov, P. E., Haraguchi, T., Gotanda, K., Yonenobu, H., Yokoyama, Y., Tada, R., and Nakagawa, T. (2012). A Complete Terrestrial Radiocarbon Record for 11.2 to 52.8 kyr B.P. *Science*, 338(6105):370–374.
- Burchuladze, A. A., Pagava, S. V., Povinec, P., Togonidze, G. I., and Usačev, S. (1980). Radiocarbon variations with the 11-year solar cycle during the last century. *Nature*, 287(5780):320–322.
- Burke, A. and Robinson, L. F. (2012). The Southern Ocean’s Role in Carbon Exchange During the Last Deglaciation. *Science*, 335(6068):557–561.
- Burns, S. J., Fleitmann, D., Matter, A., Kramers, J., and Al-Subbary, A. A. (2003). Indian Ocean Climate and an Absolute Chronology over Dansgaard/Oeschger Events 9 to 13. *Science*, 301(5638):1365–1367.
- Cauquoin, A., Raisbeck, G., Jouzel, J., and Paillard, D. (2014). Use of ^{10}Be to Predict Atmospheric ^{14}C Variations during the Laschamp Excursion: High Sensitivity to Cosmogenic Isotope Production Calculations. *Radiocarbon*, 56(1):67–82.
- Cerling, T. E. (1984). The stable isotopic composition of modern soil carbonate and its relationship to climate. *Earth and Planetary Science Letters*, 71(2):229–240.
- Cheng, H., Edwards, R., Hoff, J., Gallup, C., Richards, D., and Asmerom, Y. (2000). The half-lives of uranium-234 and thorium-230. *Chemical Geology*, 169(1-2):17–33.
- Cheng, H., Edwards, R. L., Sinha, A., Spötl, C., Yi, L., Chen, S., Kelly, M., Kathayat, G., Wang, X., Li, X., Kong, X., Wang, Y., Ning, Y., and Zhang, H. (2016). The Asian monsoon over the past 640,000 years and ice age terminations. *Nature*, 534(7609):640–646.
- Cheng, H., Edwards, R. L., Southon, J., Matsumoto, K., Feinberg, J. M., Sinha, A., Zhou, W., Li, H., Li, X., Xu, Y., Chen, S., Tan, M., Wang, Q., Wang, Y., and Ning, Y. (2018). Atmospheric $^{14}\text{C}/^{12}\text{C}$ changes during the last glacial period from Hulu Cave. *Science*, 362(6420):1293–1297.
- Clark, I. D. and Fontes, J.-C. (1990). Paleoclimatic Reconstruction in Northern Oman Based on Carbonates from Hyperalkaline Groundwaters. *Quaternary Research*, 33(3):320–336.
- Clark, I. D. and Fritz, P. (2013). *Environmental Isotopes in Hydrogeology*. CRC Press.
- Clark, P., Dyke, A., Shakun, J., Carlson, A., Clark, J., Wohlfarth, B., Mitrovica, J., Hostetler, S., and McCabe, M. (2009). The Last Glacial Maximum. *Science*, 325(5941):710–714.

- Cole, J. E., Rind, D., Webb, R. S., Jouzel, J., and Healy, R. (1999). Climatic controls on interannual variability of precipitation δ 18 O: Simulated influence of temperature, precipitation amount, and vapor source region. *Journal of Geophysical Research: Atmospheres*, 104(D12):14223–14235.
- Coleborn, K., Spate, A., Tozer, M., Andersen, M. S., Fairchild, I. J., MacKenzie, B., Treble, P. C., Meehan, S., Baker, A., and Baker, A. (2016). Effects of wildfire on long-term soil CO₂ concentration: implications for karst processes. *Environmental Earth Sciences*, 75(4):330.
- Cook, G. T., Dunbar, E., Tripney, B. G., and Fabel, D. (2020). Using Carbon Isotopes to Fight the Rise in Fraudulent Whisky. *Radiocarbon*, 62(1):51–62.
- Craig, H. (1961). Isotopic Variations in Meteoric Waters. *Science*, 133(3465):1702–1703.
- Cruz, F. W., Burns, S. J., Jercinovic, M., Karmann, I., Sharp, W. D., and Vuille, M. (2007). Evidence of rainfall variations in Southern Brazil from trace element ratios (Mg/Ca and Sr/Ca) in a Late Pleistocene stalagmite. *Geochimica et Cosmochimica Acta*, 71(9):2250–2263.
- Damon, P. E. and Linick, T. W. (1986). Geomagnetic-Heliomagnetic Modulation of Atmospheric Radiocarbon Production. *Radiocarbon*, 28(2A):266–278.
- Dansgaard, W. (1964). Stable isotopes in precipitation. *Tellus*, 16(4):436–468.
- Dansgaard, W., Johnsen, S. J., Clausen, H. B., Dahl-Jensen, D., Gundestrup, N. S., Hammer, C. U., Hvidberg, C. S., Steffensen, J. P., Sveinbjörnsdottir, A. E., Jouzel, J., and Bond, G. (1993). Evidence for general instability of past climate from a 250-kyr ice-core record. *Nature*, 364(6434):218–220.
- Deininger, M., Fohlmeister, J., Scholz, D., and Mangini, A. (2012). Isotope disequilibrium effects: The influence of evaporation and ventilation effects on the carbon and oxygen isotope composition of speleothems – A model approach. *Geochimica et Cosmochimica Acta*, 96:57–79.
- Demény, A., Németh, A., Kern, Z., Czuppon, G., Molnár, M., Leél-Őssy, S., Óvári, M., and Stieber, J. (2017). Recently forming stalagmites from the Baradla Cave and their suitability assessment for climate-proxy relationships. *Central European Geology*, 60(1):1–34.
- Denniston, R. F., González, L. A., Asmerom, Y., Reagan, M. K., and Recelli-Snyder, H. (2000). Speleothem carbon isotopic records of Holocene environments in the Ozark Highlands, USA. *Quaternary International*.
- DiNezio, P. N., Tierney, J. E., Otto-Bliesner, B. L., Timmermann, A., Bhattacharya, T., Rosenbloom, N., and Brady, E. (2018). Glacial changes in tropical climate amplified by the Indian Ocean. *Science Advances*, 4(12):eaat9658.

- Dorale, J. A. (1998). Climate and Vegetation History of the Midcontinent from 75 to 25 ka: A Speleothem Record from Crevice Cave, Missouri, USA. *Science*, 282(5395):1871–1874.
- Dorale, J. A., Gonzalez, L. A., Reagan, M. K., Pickett, D. A., Murrell, M. T., and Baker, R. G. (1992). A High-Resolution Record of Holocene Climate Change in Speleothem Calcite from Cold Water Cave, Northeast Iowa. *Science*, 258(5088):1626–1630.
- Douville, E., Sallé, E., Frank, N., Eisele, M., Pons-Branchu, E., and Ayrault, S. (2010). Rapid and accurate U-Th dating of ancient carbonates using inductively coupled plasma-quadrupole mass spectrometry. *Chemical Geology*, 272(1-4):1–11.
- Dreybrodt, W. (1999). Chemical kinetics, speleothem growth and climate. *Boreas*, 28(3):347–356.
- Dreybrodt, W. and Scholz, D. (2011). Climatic dependence of stable carbon and oxygen isotope signals recorded in speleothems: From soil water to speleothem calcite. *Geochimica et Cosmochimica Acta*, 75(3):734–752.
- Durand, N., Deschamps, P., Bard, E., Hamelin, B., Camoin, G., Thomas, A. L., Henderson, G. M., Yokoyama, Y., and Matsuzaki, H. (2013). Comparison of 14 C and U-Th Ages in Corals from IODP #310 Cores Offshore Tahiti. *Radiocarbon*, 55(4):1947–1974.
- Dykoski, C. A., Edwards, R. L., Cheng, H., Yuan, D., Cai, Y., Zhang, M., Lin, Y., Qing, J., An, Z., and Revenaugh, J. (2005). A high-resolution, absolute-dated Holocene and deglacial Asian monsoon record from Dongge Cave, China. *Earth and Planetary Science Letters*, 233(1-2):71–86.
- Elsasser, W., Ney, E. P., and Winckler, J. R. (1956). Cosmic-Ray Intensity and Geomagnetism. *Nature*, 178(4544):1226–1227.
- Fairchild, I. J. and Baker, A. (2012). *Speleothem Science*. John Wiley & Sons, Ltd, Chichester, UK.
- Fairchild, I. J., Baker, A., Borsato, A., Frisia, S., Hinton, R. W., McDermott, F., and Tooth, A. F. (2001). Annual to sub-annual resolution of multiple trace-element trends in speleothems. *Journal of the Geological Society*, 158(5):831–841.
- Fairchild, I. J., Borsato, A., Tooth, A. F., Frisia, S., Hawkesworth, C. J., Huang, Y., McDermott, F., and Spiro, B. (2000). Controls on trace element (Sr–Mg) compositions of carbonate cave waters: implications for speleothem climatic records. *Chemical Geology*, 166(3-4):255–269.
- Fairchild, I. J., Smith, C. L., Baker, A., Fuller, L., Spötl, C., Matthey, D., McDermott, F., and E.I.M.F. (2006). Modification and preservation of environmental signals in speleothems. *Earth-Science Reviews*, 75(1-4):105–153.
- Fairchild, I. J. and Treble, P. C. (2009). Trace elements in speleothems as recorders of environmental change. *Quaternary Science Reviews*, 28(5-6):449–468.

- Filipova-Marinova, M. (2006). *Late Pleistocene/Holocene dinoflagellate cyst assemblages from the Southwestern Black Sea shelf*. Pensoft Publishers & University Publishing House, Sofia-Moscow.
- Fleitmann, D., Burns, S. J., Mangini, A., Mudelsee, M., Kramers, J., Villa, I., Neff, U., Al-Subbary, A. A., Buettner, A., Hippler, D., and Matter, A. (2007). Holocene ITCZ and Indian monsoon dynamics recorded in stalagmites from Oman and Yemen (Socotra). *Quaternary Science Reviews*, 26(1):170–188.
- Fleitmann, D., Burns, S. J., Mudelsee, M., Neff, U., Kramers, J., Mangini, A., and Matter, A. (2003). Holocene forcing of the Indian monsoon recorded in a stalagmite from southern Oman. *Science (New York, N.Y.)*, 300(5626):1737–9.
- Fleitmann, D., Cheng, H., Badertscher, S., Edwards, R. L., Mudelsee, M., Göktürk, O. M., Fankhauser, A., Pickering, R., Raible, C. C., Matter, A., Kramers, J., and Tüysüz, O. (2009). Timing and climatic impact of Greenland interstadials recorded in stalagmites from northern Turkey. *Geophysical Research Letters*, 36(19):L19707.
- Flohr, P., Fleitmann, D., Zorita, E., Sadekov, A., Cheng, H., Bosomworth, M., Edwards, L., Matthews, W., and Matthews, R. (2017). Late Holocene droughts in the Fertile Crescent recorded in a speleothem from northern Iraq. *Geophysical Research Letters*.
- Fohlmeister, J., Kromer, B., and Mangini, A. (2011a). The influence of soil organic matter age spectrum on the reconstruction of atmospheric ^{14}C levels via stalagmites. *Radiocarbon*, 53(1):99–115.
- Fohlmeister, J., Plessen, B., Dudashvili, A. S., Tjallingii, R., Wolff, C., Gafurov, A., and Cheng, H. (2017). Winter precipitation changes during the Medieval Climate Anomaly and the Little Ice Age in arid Central Asia. *Quaternary Science Reviews*, 178:24–36.
- Fohlmeister, J., Scholz, D., Kromer, B., and Mangini, A. (2011b). Modelling carbon isotopes of carbonates in cave drip water. *Geochimica et Cosmochimica Acta*, 75(18):5219–5228.
- Fohlmeister, J., Schröder-Ritzrau, A., Spötl, C., Frisia, S., Miorandi, R., Kromer, B., and Mangini, A. (2010). The Influences of Hydrology on the Radiogenic and Stable Carbon Isotope Composition of Cave Drip Water, Grotta di Ernesto (Italy). *Radiocarbon*, 52(4):1529–1544.
- Fohlmeister, J., Voarintsoa, N. R. G., Lechleitner, F. A., Boyd, M., Brandtstätter, S., Jacobson, M. J., and Oster, J. L. (2020). Main controls on the stable carbon isotope composition of speleothems. *Geochimica et Cosmochimica Acta*.
- Förstel, J. P. (2017). *Uranium Series Dating with a New Laser Ablation Multi Collector Inductively Coupled Plasma Mass Spectrometry Setup - Development of a Measurement Routine and First Findings*. Master's thesis, Heidelberg University.

- Frisia, S., Fairchild, I. J., Fohlmeister, J., Miorandi, R., Spötl, C., and Borsato, A. (2011). Carbon mass-balance modelling and carbon isotope exchange processes in dynamic caves. *Geochimica et Cosmochimica Acta*, 75(2):380–400.
- Genty, D., Baker, A., Massault, M., Proctor, C., Gilmour, M., Pons-Branchu, E., and Hamelin, B. (2001). Dead carbon in stalagmites: Carbonate bedrock paleodissolution vs. ageing of soil organic matter. Implications for ^{13}C variations in speleotherms. *Geochimica et Cosmochimica Acta*, 65(20):3443–3457.
- Genty, D., Blamart, D., Ouahdi, R., Gilmour, M., Baker, A., Jouzel, J., and Van-Exter, S. (2003). Precise dating of Dansgaard–Oeschger climate oscillations in western Europe from stalagmite data. *Nature*, 421(6925):833–837.
- Genty, D. and Massault, M. (1999). Carbon transfer dynamics from bomb- ^{14}C and $\delta^{13}\text{C}$ time series of a laminated stalagmite from SW France—modelling and comparison with other stalagmite records. *Geochimica et Cosmochimica Acta*, 63(10):1537–1548.
- Genty, D., Massault, M., Gilmour, M., Baker, A., Verheyden, S., and Kepens, E. (1999). Calculation of past dead carbon proportion and variability by the comparison of AMS(^{14}C) and TIMS U/Th ages on two holocene stalagmites. *Radiocarbon*, 41(3):251–270.
- Godwin, H. (1962). Half-life of Radiocarbon. *Nature*, 195(4845):984–984.
- Göktürk, O., Fleitmann, D., Badertscher, S., Cheng, H., Edwards, R., Leuenberger, M., Fankhauser, A., Tüysüz, O., and Kramers, J. (2011). Climate on the southern Black Sea coast during the Holocene: implications from the Sofular Cave record. *Quaternary Science Reviews*, 30(19-20):2433–2445.
- Griffiths, M. L., Drysdale, R. N., Gagan, M. K., Frisia, S., xin Zhao, J., Ayliffe, L. K., Hantoro, W. S., Hellstrom, J. C., Fischer, M. J., Feng, Y. X., and Suwargadi, B. W. (2010). Evidence for Holocene changes in Australian-Indonesian monsoon rainfall from stalagmite trace element and stable isotope ratios. *Earth and Planetary Science Letters*.
- Griffiths, M. L., Fohlmeister, J., Drysdale, R. N., Hua, Q., Johnson, K. R., Hellstrom, J. C., Gagan, M. K., and Zhao, J. x. (2012). Hydrological control of the dead carbon fraction in a Holocene tropical speleothem. *Quaternary Geochronology*, 14:81–93.
- Gupta, A. K., Anderson, D. M., and Overpeck, J. T. (2003). Abrupt changes in the Asian southwest monsoon during the Holocene and their links to the North Atlantic Ocean. *Nature*, 421(6921):354–357.
- Hansen, M., Scholz, D., Schöne, B. R., and Spötl, C. (2019). Simulating speleothem growth in the laboratory: Determination of the stable isotope fractionation ($\delta^{13}\text{C}$ and $\delta^{18}\text{O}$) between H_2O , DIC and CaCO_3 . *Chemical Geology*, 509:20–44.
- Heaton, T. J., Bard, E., and Hughen, K. A. (2013). Elastic Tie-Pointing—Transferring Chronologies between Records via a Gaussian Process. *Radiocarbon*, 55(4):1975–1997.

- Heinrich, H. (1988). Origin and Consequences of Cyclic Ice Rafting in the Northeast Atlantic Ocean During the Past 130,000 Years. *Quaternary Research*, 29(2):142–152.
- Hellstrom, J. (2006). U-Th dating of speleothems with high initial ^{230}Th using stratigraphical constraint. *Quaternary Geochronology*, 1(4):289–295.
- Hemming, S. R. (2004). Heinrich events: Massive late Pleistocene detritus layers of the North Atlantic and their global climate imprint. *Reviews of Geophysics*, 42(1):RG1005.
- Hendy, C. (1971). The isotopic geochemistry of speleothems - I. The calculation of the effects of different modes of formation on the isotopic composition of speleothems and their applicability as paleoclimatic indicators. *Geochimica et Cosmochimica Acta*, 35(386):801–824.
- Hendy, C. H. and Wilson, A. T. (1968). Palaeoclimatic Data from Speleothems. *Nature*, 219(5149):48–51.
- Hoffmann, D. L., Beck, J. W., Richards, D. A., Smart, P. L., Singarayer, J. S., Ketchum, T., and Hawkesworth, C. J. (2010). Towards radiocarbon calibration beyond 28 ka using speleothems from the Bahamas. *Earth and Planetary Science Letters*, 289(1-2):1–10.
- Hu, C., Henderson, G. M., Huang, J., Xie, S., Sun, Y., and Johnson, K. R. (2008). Quantification of Holocene Asian monsoon rainfall from spatially separated cave records. *Earth and Planetary Science Letters*, 266(3-4):221–232.
- Hua, Q., Barbetti, M., Fink, D., Kaiser, K. F., Friedrich, M., Kromer, B., Levchenko, V. A., Zoppi, U., Smith, A. M., and Bertuch, F. (2009). Atmospheric ^{14}C variations derived from tree rings during the early Younger Dryas. *Quaternary Science Reviews*, 28(25-26):2982–2990.
- Hua, Q., Cook, D., Fohlmeister, J., Penny, D., Bishop, P., and Buckman, S. (2017). Radiocarbon Dating of a Speleothem Record of Paleoclimate for Angkor, Cambodia. *Radiocarbon*, 59(6):1873–1890.
- Hughen, K., Southon, J., Lehman, S., Bertrand, C., and Turnbull, J. (2006). Marine-derived ^{14}C calibration and activity record for the past 50,000 years updated from the Cariaco Basin. *Quaternary Science Reviews*, 25(23-24):3216–3227.
- IPCC (2013). *Climate Change 2013 - The Physical Science Basis. Contribution of Working Group I to the Fifth Assessment Report of the Intergovernmental Panel on Climate Change*. Stocker, T.F., D. Qin, G.-K. Plattner, M. Tignor, S.K. Allen, J. Boschung, A. Nauels, Y. Xia, V. Bex and P.M. Midgley (eds.). Cambridge University Press, Cambridge.
- Ivanochko, T., Ganeshram, R., Brummer, G., Ganssen, G., Jung, S., Moreton, S., and Kroon, D. (2005). Variations in tropical convection as an amplifier of global climate change at the millennial scale. *Earth and Planetary Science Letters*, 235(1-2):302–314.

- Ivanovich, M. (1994). Uranium Series Disequilibrium: Concepts and Applications. *Radiochimica Acta*, 64(2).
- Ivanovich, M. and Harmon, R. S. (1992). Uranium-series disequilibrium: applications to earth, marine, and environmental sciences, 2nd edition. *Uranium-series disequilibrium: applications to earth, marine, and environmental sciences, 2nd edition*.
- Johnsen, S. J., Clausen, H. B., Dansgaard, W., Fuhrer, K., Gundestrup, N., Hammer, C. U., Iversen, P., Jouzel, J., Stauffer, B., and Steffensen, J. P. (1992). Irregular glacial interstadials recorded in a new Greenland ice core. *Nature*, 359(6393):311–313.
- Johnson, K., Hu, C., Belshaw, N., and Henderson, G. (2006). Seasonal trace-element and stable-isotope variations in a Chinese speleothem: The potential for high-resolution paleomonsoon reconstruction. *Earth and Planetary Science Letters*, 244(1-2):394–407.
- Kaufmann, G. (2003). Stalagmite growth and palaeo-climate: the numerical perspective. *Earth and Planetary Science Letters*, 214(1-2):251–266.
- Kaufmann, G. and Dreybrodt, W. (2004). Stalagmite growth and palaeo-climate: an inverse approach. *Earth and Planetary Science Letters*, 224(3-4):529–545.
- Knapp, A. K. (2002). Rainfall Variability, Carbon Cycling, and Plant Species Diversity in a Mesic Grassland. *Science*, 298(5601):2202–2205.
- Köhler, P., Muscheler, R., and Fischer, H. (2006). A model-based interpretation of low-frequency changes in the carbon cycle during the last 120,000 years and its implications for the reconstruction of atmospheric $\Delta 14\text{C}$. *Geochemistry, Geophysics, Geosystems*, 7(11):n/a–n/a.
- Kotthoff, U., Pross, J., Müller, U. C., Peyron, O., Schmiidl, G., Schulz, H., and Bordon, A. (2008). Climate dynamics in the borderlands of the Aegean Sea during formation of sapropel S1 deduced from a marine pollen record. *Quaternary Science Reviews*, 27(7-8):832–845.
- Kromer, B., Lindauer, S., Synal, H. A., and Wacker, L. (2013). MAMS - A new AMS facility at the Curt-Engelhorn-Centre for Archaeometry, Mannheim, Germany. *Nuclear Instruments and Methods in Physics Research, Section B: Beam Interactions with Materials and Atoms*, 294:11–13.
- Kromer, B., Manning, S. W., Friedrich, M., Talamo, S., and Trano, N. (2010). 14C Calibration in the 2nd and 1st Millennia BC—Eastern Mediterranean Radiocarbon Comparison Project (EMRCP). *Radiocarbon*, 52(3):875–886.
- Kromer, B. and Münnich, K. O. (1992). CO_2 Gas Proportional Counting in Radiocarbon Dating — Review and Perspective. In *Radiocarbon After Four Decades*, pp. 184–197, Springer New York, New York, NY.

- Krüger, Y., Marti, D., Staub, R. H., Fleitmann, D., and Frenz, M. (2011). Liquid-vapour homogenisation of fluid inclusions in stalagmites: Evaluation of a new thermometer for palaeoclimate research. *Chemical Geology*.
- Kwiecien, O., Arz, H. W., Lamy, F., Plessen, B., Bahr, A., and Haug, G. H. (2009). North Atlantic control on precipitation pattern in the eastern Mediterranean/Black Sea region during the last glacial. *Quaternary Research*, 71(3):375–384.
- Laj, C., Kissel, C., and Beer, J. (2013). High Resolution Global Paleointensity Stack Since 75 kyr (GLOPIS-75) Calibrated to Absolute Values. In J. Channell, D. Kent, W. Lowrie, and J. Meert, editors, *Geophysical Monograph Series*, pp. 255–265, Washington DC American Geophysical Union Geophysical Monograph Series.
- Laj, C., Kissel, C., Mazaud, A., Channell, J. E. T., and Beer, J. (2000). North Atlantic palaeointensity stack since 75ka (NAPIS-75) and the duration of the Laschamp event. *Philosophical Transactions of the Royal Society of London. Series A: Mathematical, Physical and Engineering Sciences*, 358(1768):1009–1025.
- Lal, D. and Charles, C. (2007). Deconvolution of the atmospheric radiocarbon record in the last 50,000 years. *Earth and Planetary Science Letters*, 258(3-4):550–560.
- Lal, D. and Peters, B. (1967). Cosmic Ray Produced Radioactivity on the Earth. In S. Flügge, editor, *Kosmische Strahlung II / Cosmic Rays II. Handbuch der Physik / Encyclopedia of Physics*, pp. 551–612, Springer, Berlin, Germany.
- Lascu, I., Feinberg, J. M., Dorale, J. A., Cheng, H., and Edwards, R. L. (2016). Age of the Laschamp excursion determined by U-Th dating of a speleothem geomagnetic record from North America. *Geology*, 44(2):139–142.
- Lea, D. W., Martin, P. A., Pak, D. K., and Spero, H. J. (2002). Reconstructing a 350ky history of sea level using planktonic Mg/Ca and oxygen isotope records from a Cocos Ridge core. *Quaternary Science Reviews*, 21(1-3):283–293.
- Lechleitner, F. A., Baldini, J. U., Breitenbach, S. F., Fohlmeister, J., McIntyre, C., Goswami, B., Jamieson, R. A., van der Voort, T. S., Prufer, K., Marwan, N., Culleton, B. J., Kennett, D. J., Asmerom, Y., Polyak, V., and Eglinton, T. I. (2016a). Hydrological and climatological influences on a very high resolution tropical stalagmite radiocarbon record. *Geochimica et Cosmochimica Acta*, 194:233–252.
- Lechleitner, F. A., Fohlmeister, J., McIntyre, C., Baldini, L. M., Jamieson, R. A., Hercman, H., Ga siorowski, M., Pawlak, J., Stefaniak, K., Socha, P., Eglinton, T. I., and Baldini, J. U. (2016b). A novel approach for construction of radiocarbon-based chronologies for speleothems. *Quaternary Geochronology*, 35:54–66.
- Leroy, S. A. G. and Arpe, K. (2007). Glacial refugia for summer-green trees in Europe and south-west Asia as proposed by ECHAM3 time-slice atmospheric model simulations. *Journal of Biogeography*, 34(12):2115–2128.

- Levin, I., Hammer, S., Kromer, B., and Meinhardt, F. (2008). Radiocarbon observations in atmospheric CO₂: Determining fossil fuel CO₂ over Europe using Jungfrauoch observations as background. *Science of The Total Environment*, 391(2-3):211–216.
- Levin, I., Naegler, T., Kromer, B., Diehl, M., Francey, R. J., Gomez-Pelaez, A. J., Steele, L. P., Wagenbach, D., Weller, R., and Worthy, D. E. (2010). Observations and modelling of the global distribution and long-term trend of atmospheric ¹⁴CO₂. *Tellus, Series B: Chemical and Physical Meteorology*, 62(1):26–46.
- Libby, W. F. (1946). Atmospheric helium three and radiocarbon from cosmic radiation [8]. *Physical Review*, 69(11-12):671–672.
- Libby, W. F., Anderson, E. C., and Arnold, J. R. (1949). Age determination by radiocarbon content: World-wide assay of natural radiocarbon. *Science*.
- Lotsch, A., Friedl, M. A., Anderson, B. T., and Tucker, C. J. (2003). Coupled vegetation-precipitation variability observed from satellite and climate records. *Geophysical Research Letters*.
- Lund, S., Benson, L., Negrini, R., Liddicoat, J., and Mensing, S. (2017). A full-vector paleomagnetic secular variation record (PSV) from Pyramid Lake (Nevada) from 47–17 ka: Evidence for the successive Mono Lake and Laschamp Excursions. *Earth and Planetary Science Letters*, 458:120–129.
- Markowska, M., Fohlmeister, J., Treble, P. C., Baker, A., Andersen, M. S., and Hua, Q. (2019). Modelling the ¹⁴C bomb-pulse in young speleothems using a soil carbon continuum model. *Geochimica et Cosmochimica Acta*, 261:342–367.
- Masarik, J. and Beer, J. (1999). Simulation of particle fluxes and cosmogenic nuclide production in the Earth’s atmosphere. *Journal of Geophysical Research Atmospheres*.
- Masarik, J. and Beer, J. (2009). An updated simulation of particle fluxes and cosmogenic nuclide production in the Earth’s atmosphere. *Journal of Geophysical Research Atmospheres*.
- Mathieu, J. A., Hatté, C., Balesdent, J., and Parent, É. (2015). Deep soil carbon dynamics are driven more by soil type than by climate: a worldwide meta-analysis of radiocarbon profiles. *Global Change Biology*, 21(11):4278–4292.
- McDermott, F. (2004). Palaeo-climate reconstruction from stable isotope variations in speleothems: a review. *Quaternary Science Reviews*, 23(7-8):901–918.
- Mies, B. and Beyhl, F. E. (1998). *Vegetation ecology of Socotra. - Socotra Proc. First Int. Symp., Aden, March 1996*. United Nations Publications, Global Environment Facility, Conservation and Sustainable Use of Biodiversity of Soqotra Archipelago, New York, NY, USA, vol. 1 edition.

- Minami, M., Kato, T., Horikawa, K., and Nakamura, T. (2015). Seasonal variations of ^{14}C and $\delta^{13}\text{C}$ for cave drip waters in Ryugashi Cave, Shizuoka Prefecture, central Japan. *Nuclear Instruments and Methods in Physics Research Section B: Beam Interactions with Materials and Atoms*, 362:202–209.
- Mook, W. G. (2000). Environmental isotopes in the hydrological cycle: Principles and applications. Technical report, IAEA-UNESCO.
- Munnich, K. O. (1957). Heidelberg Natural Radiocarbon Measurements I. *Science*, 126(3266):194–199.
- Muscheler, R., Adolphi, F., and Svensson, A. (2014). Challenges in ^{14}C dating towards the limit of the method inferred from anchoring a floating tree ring radiocarbon chronology to ice core records around the Laschamp geomagnetic field minimum. *Earth and Planetary Science Letters*.
- Muscheler, R., Beer, J., Kubik, P. W., and Synal, H.-A. (2005). Geomagnetic field intensity during the last 60,000 years based on ^{10}Be and ^{36}Cl from the Summit ice cores and ^{14}C . *Quaternary Science Reviews*, 24(16-17):1849–1860.
- Muscheler, R., Beer, J., Wagner, G., Laj, C., Kissel, C., Raisbeck, G. M., Yiou, F., and Kubik, P. W. (2004). Changes in the carbon cycle during the last deglaciation as indicated by the comparison of ^{10}Be and ^{14}C records. *Earth and Planetary Science Letters*, 219(3-4):325–340.
- Noronha, A. L., Johnson, K. R., Hu, C., Ruan, J., Southon, J. R., and Ferguson, J. E. (2014). Assessing influences on speleothem dead carbon variability over the Holocene: Implications for speleothem-based radiocarbon calibration. *Earth and Planetary Science Letters*, 394:20–29.
- Noronha, A. L., Johnson, K. R., Southon, J. R., Hu, C., Ruan, J., and McCabe-Glynn, S. (2015). Radiocarbon evidence for decomposition of aged organic matter in the vadose zone as the main source of speleothem carbon. *Quaternary Science Reviews*, 127:37–47.
- Nydal, R. (1968). Further investigation on the transfer of radiocarbon in nature. *Journal of Geophysical Research*, 73(12):3617–3635.
- Oster, J. L., Montañez, I. P., Guilderson, T. P., Sharp, W. D., and Banner, J. L. (2010). Modeling speleothem $\delta^{13}\text{C}$ variability in a central Sierra Nevada cave using ^{14}C and $^{87}\text{Sr}/^{86}\text{Sr}$. *Geochimica et Cosmochimica Acta*, 74(18):5228–5242.
- Overpeck, J., Anderson, D., Trumbore, S., and Prell, W. (1996). The southwest Indian Monsoon over the last 18000 years. *Climate Dynamics*.
- Özsoy, E. and Ünlüata, Ü. (1997). Oceanography of the Black Sea: A review of some recent results. *Earth-Science Reviews*, 42(4):231–272.

- Peng, S., Piao, S., Shen, Z., Ciais, P., Sun, Z., Chen, S., Bacour, C., Peylin, P., and Chen, A. (2013). Precipitation amount, seasonality and frequency regulate carbon cycling of a semi-arid grassland ecosystem in Inner Mongolia, China: A modeling analysis. *Agricultural and Forest Meteorology*, 178-179:46–55.
- Plagnes, V., Causse, C., Genty, D., Paterne, M., and Blamart, D. (2002). A discontinuous climatic record from 187 to 74 ka from a speleothem of the Clamouse Cave (south of France). *Earth and Planetary Science Letters*, 201(1):87–103.
- Popov, G. B. (1957). The vegetation of Socotra. *Journal of the Linnean Society of London, Botany*, 55(362):706–720.
- Proß, L. (2018). *Radiokohlenstoffmessung von natürlichen Karbonaten am Beispiel des holozänen Stalagmiten M6*. Bachelor's thesis, Heidelberg University.
- Rahmstorf, S. (2003). Timing of abrupt climate change: A precise clock. *Geophysical Research Letters*, 30(10):n/a–n/a.
- Rasmussen, S. O., Andersen, K. K., Svensson, A. M., Steffensen, J. P., Vinther, B. M., Clausen, H. B., Siggaard-Andersen, M. L., Johnsen, S. J., Larsen, L. B., Dahl-Jensen, D., Bigler, M., Röthlisberger, R., Fischer, H., Goto-Azuma, K., Hansson, M. E., and Ruth, U. (2006). A new Greenland ice core chronology for the last glacial termination. *Journal of Geophysical Research Atmospheres*, 111(6).
- Reimer, P. J., Bard, E., Bayliss, A., Beck, J. W., Blackwell, P. G., Bronk Ramsey, C., Buck, C. E., Cheng, H., Edwards, R. L., Friedrich, M., Grootes, P. M., Guilderson, T. P., Hafliðason, H., Hajdas, I., Hatté, C., Heaton, T. J., Hoffmann, D. L., Hogg, A. G., Hughen, K. A., Kaiser, K. F., Kromer, B., Manning, S. W., Niu, M., Reimer, R. W., Richards, D. A., Scott, E. M., Southon, J. R., Staff, R. A., Turney, C. S. M., and van der Plicht, J. (2013). IntCal13 and Marine13 Radiocarbon Age Calibration Curves 0–50,000 Years cal BP. *Radiocarbon*, 55(4):1869–1887.
- Richards, D. A. (2003). Uranium-series Chronology and Environmental Applications of Speleothems. *Reviews in Mineralogy and Geochemistry*, 52(1):407–460.
- Rozanski, K., Araguás-Araguás, L., and Gonfiantini, R. (2013). Isotopic Patterns in Modern Global Precipitation. In *Climate Change in Continental Isotopic Records*, volume 78, pp. 1–36, American Geophysical Union (AGU).
- Rudzka, D., McDermott, F., Baldini, L., Fleitmann, D., Moreno, A., and Stoll, H. (2011). The coupled $\delta^{13}\text{C}$ -radiocarbon systematics of three Late Glacial/early Holocene speleothems; insights into soil and cave processes at climatic transitions. *Geochimica et Cosmochimica Acta*, 75(15):4321–4339.
- Rudzka-Phillips, D., McDermott, F., Jackson, A., and Fleitmann, D. (2013). Inverse modelling of the ^{14}C bomb pulse in stalagmites to constrain the dynamics of soil carbon cycling at selected European cave sites. *Geochimica et Cosmochimica Acta*, 112:32–51.

- Sanchez Goñi, M. F. and Harrison, S. P. (2010). Millennial-scale climate variability and vegetation changes during the Last Glacial: Concepts and terminology. *Quaternary Science Reviews*, 29(21-22):2823–2827.
- Sarıkaya, M. A., Zreda, M., Çiner, A., and Zweck, C. (2008). Cold and wet Last Glacial Maximum on Mount Sandiras, SW Turkey, inferred from cosmogenic dating and glacier modeling. *Quaternary Science Reviews*, 27(7-8):769–780.
- Schandl, J. (2019). *Untersuchung der Klimasensitivität des Einbaus von Radiokohlenstoff in einem Stalagmiten aus Cueva Larga , Puerto Rico*. Bachelor's thesis, Heidelberg University.
- Schaub, M., Büntgen, U., Kaiser, K. F., Kromer, B., Talamo, S., Andersen, K. K., and Rasmussen, S. O. (2008). Lateglacial environmental variability from Swiss tree rings. *Quaternary Science Reviews*, 27(1-2):29–41.
- Schlüter, T. (2008). *Geological Atlas of Africa with Notes on Stratigraphy, Tectonics, Economic Geology, Geohazards, Geosites and Geoscientific Education of Each Country*. Springer Berlin Heidelberg, Berlin, Heidelberg, 2nd edition.
- Scholte, P. and De Geest, P. (2010). The climate of Socotra Island (Yemen): A first-time assessment of the timing of the monsoon wind reversal and its influence on precipitation and vegetation patterns. *Journal of Arid Environments*, 74(11):1507–1515.
- Scholz, D., Frisia, S., Borsato, A., Spötl, C., Fohlmeister, J., Mudelsee, M., Miorandi, R., and Mangini, A. (2012a). Holocene climate variability in north-eastern Italy: potential influence of the NAO and solar activity recorded by speleothem data. *Climate of the Past*, 8(4):1367–1383.
- Scholz, D. and Hoffmann, D. (2008). $^{230}\text{Th}/\text{U}$ -dating of fossil corals and speleothems. *Quaternary Science Journal*, 57(1):52–76.
- Scholz, D. and Hoffmann, D. L. (2011). StalAge - An algorithm designed for construction of speleothem age models. *Quaternary Geochronology*, 6(3-4):369–382.
- Scholz, D., Hoffmann, D. L., Hellstrom, J., and Bronk Ramsey, C. (2012b). A comparison of different methods for speleothem age modelling. *Quaternary Geochronology*, 14:94–104.
- Scholz, D., Mühlinghaus, C., and Mangini, A. (2009). Modelling $\delta^{13}\text{C}$ and $\delta^{18}\text{O}$ in the solution layer on stalagmite surfaces. *Geochimica et Cosmochimica Acta*, 73(9):2592–2602.
- Schulz, H., van Rad, U., and Erlenkeuser, H. (1998). Correlation between Arabian Sea and Greenland climate oscillations of the past 110,000 years. *Nature*, 393(May):54–57.
- Scifo, A., Kuitens, M., Neocleous, A., Pope, B. J. S., Miles, D., Jansma, E., Doeve, P., Smith, A. M., Miyake, F., and Dee, M. W. (2019). Radiocarbon Production Events and their Potential Relationship with the Schwabe Cycle. *Scientific Reports*, 9(1):17056.

- Shakun, J. D., Burns, S. J., Fleitmann, D., Kramers, J., Matter, A., and Al-Subbary, A. A. (2007). A high-resolution, absolute-dated deglacial speleothem record of Indian Ocean climate from Socotra Island, Yemen. *Earth and Planetary Science Letters*, 259(3):442–456.
- Shen, C.-C., Wu, C.-C., Cheng, H., Lawrence Edwards, R., Hsieh, Y.-T., Gallet, S., Chang, C.-C., Li, T.-Y., Lam, D. D., Kano, A., Hori, M., and Spötl, C. (2012). High-precision and high-resolution carbonate ^{230}Th dating by MC-ICP-MS with SEM protocols. *Geochimica et Cosmochimica Acta*, 99:71–86.
- Shumilovskikh, L. S., Fleitmann, D., Nowaczyk, N. R., Behling, H., Marret, F., Wegwerth, A., and Arz, H. W. (2014). Orbital- and millennial-scale environmental changes between 64 and 20 ka BP recorded in Black Sea sediments. *Climate of the Past*, 10(3):939–954.
- Shumilovskikh, L. S., Tarasov, P., Arz, H. W., Fleitmann, D., Marret, F., Nowaczyk, N., Plessen, B., Schlütz, F., and Behling, H. (2012). Vegetation and environmental dynamics in the southern Black Sea region since 18kyr BP derived from the marine core 22-GC3. *Palaeogeography, Palaeoclimatology, Palaeoecology*, 337-338:177–193.
- Sinclair, D. J., Banner, J. L., Taylor, F. W., Partin, J., Jenson, J., Mylroie, J., Goddard, E., Quinn, T., Jocson, J., and Miklavič, B. (2012). Magnesium and strontium systematics in tropical speleothems from the Western Pacific. *Chemical Geology*, 294-295:1–17.
- Southon, J., Noronha, A. L., Cheng, H., Edwards, R. L., and Wang, Y. (2012). A high-resolution record of atmospheric ^{14}C based on Hulu Cave speleothem H82. *Quaternary Science Reviews*, 33:32–41.
- Spötl, C., Fairchild, I. J., and Tooth, A. F. (2005). Cave air control on dripwater geochemistry, Obir Caves (Austria): Implications for speleothem deposition in dynamically ventilated caves. *Geochimica et Cosmochimica Acta*, 69(10):2451–2468.
- Spötl, C., Fohlmeister, J., Cheng, H., and Boch, R. (2016). Modern aragonite formation at near-freezing conditions in an alpine cave, Carnic Alps, Austria. *Chemical Geology*, 435:60–70.
- Spötl, C. and Mangini, A. (2002). Stalagmite from the Austrian Alps reveals Dansgaard-Oeschger events during isotope stage 3: Implications for the absolute chronology of Greenland ice cores. *Earth and Planetary Science Letters*, 203(1):507–518.
- Spötl, C., Mangini, A., and Richards, D. A. (2006). Chronology and paleoenvironment of Marine Isotope Stage 3 from two high-elevation speleothems, Austrian Alps. *Quaternary Science Reviews*, 25(9-10):1127–1136.
- Staff, R. A., Hardiman, M., Bronk Ramsey, C., Adolphi, F., Hare, V. J., Koutsodendris, A., and Pross, J. (2019). Reconciling the Greenland ice-core and radiocarbon timescales through the Laschamp geomagnetic excursion. *Earth and Planetary Science Letters*, 520:1–9.

- Steffensen, J. P., Andersen, K. K., Bigler, M., Clausen, H. B., Dahl-Jensen, D., Fischer, H., Goto-Azuma, K., Hansson, M., Johnsen, S. J., Jouzel, J., Masson-Delmotte, V., Popp, T., Rasmussen, S. O., Rothlisberger, R., Ruth, U., Stauffer, B., Siggaard-Andersen, M.-L., Sveinbjornsdottir, A. E., Svensson, A., and White, J. W. C. (2008). High-Resolution Greenland Ice Core Data Show Abrupt Climate Change Happens in Few Years. *Science*, 321(5889):680–684.
- Stenström, K. E., Skog, G., Georgiadou, E., Genberg, J., and Johansson, A. (2011). A guide to radiocarbon units and calculations. *LUNFD*, 6(October):0–17.
- Stoll, H. M., Müller, W., and Prieto, M. (2012). I-STAL, a model for interpretation of Mg/Ca, Sr/Ca and Ba/Ca variations in speleothems and its forward and inverse application on seasonal to millennial scales. *Geochemistry, Geophysics, Geosystems*, 13(9).
- Stuiver, M. (1983). International Agreements and the Use of the New Oxalic Acid Standard. *Radiocarbon*, 25(2):793–795.
- Stuiver, M. and Polach, H. A. (1977). Discussion Reporting of ^{14}C Data. *Radiocarbon*, 19(3):355–363.
- Stuiver, M. and Robinson, S. W. (1974). University of Washington Geosecs North Atlantic carbon-14 results. *Earth and Planetary Science Letters*, 23(1):87–90.
- Suter, M., Müller, A. M., Alfimov, V., Christl, M., Schulze-König, T., Kubik, P. W., Snyal, H.-A., Vockenhuber, C., and Wacker, L. (2010). Are Compact AMS Facilities a Competitive Alternative to Larger Tandem Accelerators? *Radiocarbon*, 52(2):319–330.
- Svensson, A., Andersen, K. K., Bigler, M., Clausen, H. B., Dahl-Jensen, D., Davies, S. M., Johnsen, S. J., Muscheler, R., Parrenin, F., Rasmussen, S. O., Röthlisberger, R., Seierstad, I., Steffensen, J. P., and Vinther, B. M. (2008). A 60 000 year Greenland stratigraphic ice core chronology. *Climate of the Past*, 4(1):47–57.
- Snyal, H. A., Stocker, M., and Suter, M. (2007). MICADAS: A new compact radiocarbon AMS system. *Nuclear Instruments and Methods in Physics Research, Section B: Beam Interactions with Materials and Atoms*, 259(1):7–13.
- Tans, P. P., de Jong, A. F. M., and Mook, W. G. (1979). Natural atmospheric ^{14}C variation and the Suess effect. *Nature*, 280(5725):826–828.
- Therre, S. (2014). *Radiokohlenstoff als Vegetationstracer - Messung des toten Kohlenstoffanteils am holozänen Stalagmit H5 aus dem Oman*. Bachelor's thesis, Heidelberg University.
- Therre, S. (2016). *Climate variations in the Arabian Sea from LGM to Holocene: A stalagmite radiocarbon record from Socotra Island*. Master's thesis, Heidelberg University.

- Therre, S., Fohlmeister, J., Fleitmann, D., Matter, A., Burns, S. J., Arps, J., Schröder-Ritzrau, A., Friedrich, R., and Frank, N. (2020). Climate-induced speleothem radiocarbon variability on Socotra Island from the Last Glacial Maximum to the Younger Dryas. *Climate of the Past*, 16(1):409–421.
- Tisnérat-Laborde, N., Poupeau, J. J., Tannau, J. F., and Paterne, M. (2001). Development of a Semi-Automated System for Routine Preparation of Carbonate Samples. *Radiocarbon*.
- Treble, P., Fairchild, I., Baker, A., Meredith, K., Andersen, M., Salmon, S., Bradley, C., Wynn, P., Hankin, S., Wood, A., and McGuire, E. (2016). Roles of forest bioproductivity, transpiration and fire in a nine-year record of cave dripwater chemistry from southwest Australia. *Geochimica et Cosmochimica Acta*, 184:132–150.
- Treble, P. C., Fairchild, I. J., Griffiths, A., Baker, A., Meredith, K. T., Wood, A., and McGuire, E. (2015). Impacts of cave air ventilation and in-cave prior calcite precipitation on Golgotha Cave dripwater chemistry, southwest Australia. *Quaternary Science Reviews*, 127:61–72.
- Trumbore, S. (2000). Age of soil organic matter and soil respiration: Radiocarbon constraints on belowground C dynamics. *Ecological Applications*, 10(2):399–411.
- Trumbore, S. (2009). Radiocarbon and Soil Carbon Dynamics. *Annual Review of Earth and Planetary Sciences*.
- Turney, C. S., Fifield, L. K., Hogg, A. G., Palmer, J. G., Hughen, K., Baillie, M. G., Galbraith, R., Ogden, J., Lorrey, A., Tims, S. G., and Jones, R. T. (2010). The potential of New Zealand kauri (*Agathis australis*) for testing the synchronicity of abrupt climate change during the Last Glacial Interval (60,000–11,700 years ago). *Quaternary Science Reviews*, 29(27-28):3677–3682.
- Tüysüz, O. (1999). Geology of the Cretaceous sedimentary basins of the Western Pontides. *Geological Journal*, 34(1-2):75–93.
- Unkel, I. (2006). *AMS-14C-Analysen zur Rekonstruktion der Landschafts- und Kulturgeschichte in der Region Palpa (S-Peru)*. Phd thesis, Heidelberg University.
- Verheyden, S., Keppens, E., Fairchild, I. J., McDermott, F., and Weis, D. (2000). Mg, Sr and Sr isotope geochemistry of a Belgian Holocene speleothem: implications for paleoclimate reconstructions. *Chemical Geology*, 169(1-2):131–144.
- Vieten, R., Winter, A., Warken, S. F., Schröder-Ritzrau, A., Miller, T. E., and Scholz, D. (2016). Seasonal temperature variations controlling cave ventilation processes in cueva larga, Puerto Rico. *International Journal of Speleology*.
- Wacker, L., Bonani, G., Friedrich, M., Hajdas, I., Kromer, B., Němec, M., Ruff, M., Suter, M., Synal, H.-A., and Vockenhuber, C. (2010a). MICADAS: Routine and High-Precision Radiocarbon Dating. *Radiocarbon*, 52(2):252–262.

- Wacker, L., Christl, M., and Synal, H.-A. (2010b). Bats: A new tool for AMS data reduction. *Nuclear Instruments and Methods in Physics Research Section B: Beam Interactions with Materials and Atoms*, 268(7-8):976–979.
- Wagner, G., Beer, J., Laj, C., Kissel, C., Masarik, J., Muscheler, R., and Synal, H.-A. (2000). Chlorine-36 evidence for the Mono Lake event in the Summit GRIP ice core. *Earth and Planetary Science Letters*, 181(1-2):1–6.
- Walker, M., Johnsen, S., Rasmussen, S. O., Popp, T., Steffensen, J.-P., Gibbard, P., Hoek, W., Lowe, J., Andrews, J., Björck, S., Cwynar, L. C., Hughen, K., Kershaw, P., Kromer, B., Litt, T., Lowe, D. J., Nakagawa, T., Newnham, R., and Schwander, J. (2009). Formal definition and dating of the GSSP (Global Stratotype Section and Point) for the base of the Holocene using the Greenland NGRIP ice core, and selected auxiliary records. *Journal of Quaternary Science*, 24(1):3–17.
- Wang, Y. J., Cheng, H., Edwards, R. L., An, Z. S., Wu, J. Y., Shen, C. C., and Dorale, J. A. (2001). A high-resolution absolute-dated Late Pleistocene monsoon record from Hulu Cave, China. *Science*, 294(5550):2345–2348.
- Warren, S. F. (2017). *Potentials and limitations of multi-proxy records in speleothem research - Case studies in complex climate systems*. Dissertation, Heidelberg University.
- Warren, S. F., Fohlmeister, J., Schröder-Ritzrau, A., Constantin, S., Spötl, C., Gerdes, A., Esper, J., Frank, N., Arps, J., Terente, M., Riechelmann, D. F., Mangini, A., and Scholz, D. (2018). Reconstruction of late Holocene autumn/winter precipitation variability in SW Romania from a high-resolution speleothem trace element record. *Earth and Planetary Science Letters*, 499:122–133.
- Warren, S. F., Scholz, D., Spötl, C., Jochum, K. P., Pajón, J. M., Bahr, A., and Mangini, A. (2019). Caribbean hydroclimate and vegetation history across the last glacial period. *Quaternary Science Reviews*, 218:75–90.
- Wassenburg, J. A., Immenhauser, A., Richter, D. K., Jochum, K. P., Fietzke, J., Deininger, M., Goos, M., Scholz, D., and Sabaoui, A. (2012). Climate and cave control on Pleistocene/Holocene calcite-to-aragonite transitions in speleothems from Morocco: Elemental and isotopic evidence. *Geochimica et Cosmochimica Acta*, 92:23–47.
- Wedepohl, K. H. (1995). The composition of the continental crust. *Geochimica et Cosmochimica Acta*, 59(7):1217–1232.
- Wefing, A. M., Arps, J., Blaser, P., Wienberg, C., Hebbeln, D., and Frank, N. (2017). High precision U-series dating of scleractinian cold-water corals using an automated chromatographic U and Th extraction. *Chemical Geology*, 475:140–148.
- Wegwerth, A., Kaiser, J., Dellwig, O., Shumilovskikh, L. S., Nowaczyk, N. R., and Arz, H. W. (2016). Northern hemisphere climate control on the environmental dynamics in the glacial Black Sea “Lake”. *Quaternary Science Reviews*, 135:41–53.

- Wild, E., Arlamovsky, K., Golser, R., Kutschera, W., Priller, A., Puchegger, S., Rom, W., Steier, P., and Vycudilik, W. (2000). ^{14}C dating with the bomb peak: An application to forensic medicine. *Nuclear Instruments and Methods in Physics Research Section B: Beam Interactions with Materials and Atoms*, 172(1-4):944–950.
- Zhang, R. and Delworth, T. L. (2005). Simulated tropical response to a substantial weakening of the Atlantic thermohaline circulation. *Journal of Climate*, 18(12):1853–1860.
- Zhou, J., Lundstrom, C. C., Fouke, B., Panno, S., Hackley, K., and Curry, B. (2005). Geochemistry of speleothem records from southern Illinois: Development of $(^{234}\text{U})/(^{238}\text{U})$ as a proxy for paleoprecipitation. *Chemical Geology*, 221(1-2):1–20.

Danksagung

In den dreieinhalb Jahren dieser Doktorarbeit haben mich viele Menschen begleitet, denen ich nun noch danken möchte.

Zuallererst möchte ich mich bei Prof. Norbert Frank herzlich bedanken für die Betreuung während meiner Doktorarbeit und dafür, dass er mir die Möglichkeit gegeben hat, an diesem spannenden Projekt zu arbeiten. Seitdem ich vor mittlerweile sechs Jahren zu seiner Arbeitsgruppe gestoßen bin, weiß ich seine begeisternde und motivierende Art sehr zu schätzen.

Prof. André Butz möchte ich dafür danken, dass er sich bereiterklärt hat Zweitgutachter meiner Dissertation zu sein. Prof. Aeschbach und Prof. Raimund Muscheler bin ich sehr dankbar dafür, dass sie sich als Mitbetreuer meiner Doktorarbeit zur Verfügung gestellt haben. I would also like to thank Prof. Monica Dunford and Prof. Maurits W. Haverkort for agreeing to be additional examiners.

Ein großer Dank gilt Jens Fohlmeister, von dem ich unglaublich viel über Stalagmiten und Radiokohlenstoff gelernt habe, und der mir in den vergangenen Jahren und in den letzten Wochen immer mit sehr guten Ratschlägen zur Seite gestanden hat. Außerdem möchte ich Sophie Warken danken, die mich nicht nur mit auf einen unvergesslichen Field Trip nach Puerto Rico genommen hat, sondern mir während meiner Doktorarbeit immer mit Rat und Tat zur Seite stand.

In meiner Zeit im ^{14}C -Labor haben mich viele Menschen tatkräftig unterstützt: Helene Hoffmann hat mir den Start meiner Arbeit sehr erleichtert und ohne die die Leistung von Lukas Proß wäre dieses Projekt nicht möglich gewesen. Auch der IUP-Werkstatt möchte ich für ihre Arbeit danken, sowie ganz herzlich Rainer Stadler aus der Glasbläserei. Auch den Mitarbeiterinnen des IUP-Sekretariats möchte ich Danke sagen.

Die Arbeit, die in den hunderten Proben im Laufe einer Promotion steckt, kann man nicht alleine bewältigen. Daher ein ganz großer Dank an alle, die mir in den letzten dreieinhalb Jahren geholfen haben: René Eichstädter, Ronny Friedrich, Andrea Schröder-Ritzrau und Marleen Lausecker danke ich für das Messen meiner Proben, außerdem allen Hiwis, die bei der Aufbereitung geholfen haben. Fürs Korrekturlesen und für Feedback zu meiner Arbeit geht ein großes Dankeschön an Jens, Sophie, Julius und Ronny.

Bei meiner gesamten Arbeitsgruppe möchte ich mich für die unglaublich gute Zeit bedanken, die ich mit euch hatte und habe: Für die gemeinsamen Stunden in der Mensa und im Botanik, in denen bei einem Geesten und einem Stück Rüblikuchen die großen Fragen der Weltpolitik diskutiert wurden, für unsere Gruppenevents, die gemeinsam erlebten Konferenzen und Retreats und die vielen Stunden bei Dart, Kicker und Grillen. Der Übergang vom Studium zur Promotion war ein großer Schritt. Für die Unterstützung und Motivation in dieser Zeit möchte ich unserer Doktoranden-Vorgängergeneration danken: Jennifer Arps, Patrick Blaser, und besonders Freya Hemsing, die ich bei allen Problemen und Sorgen um Rat fragen konnte.

Besonders bei der Gang aus dem fünften Stock möchte ich mich, stellvertretend für alle Ehemaligen, bei Evan, Inga, Markus und Elvira für die lustige Zeit im Büro bedanken. Mit euch hat es sehr viel Spaß gemacht. Vor allem meinem buchstäblichen Gegenüber Evan Border danke ich für die dreieinhalb Jahre Fun with Flags, Trivia, Tea Time und einfach für die gute, lockere und unglaublich lustige Zeit im Café on Fifth.

Einige Erlebnisse aus meiner Doktorandenzeit bleiben nachhaltig in Erinnerung. Neben den Reisen zu Konferenzen in Austin und Trondheim und der Klassenfahrt mit fast der gesamten Gruppe nach Paris werde ich den Field Trip nach Puerto Rico nie vergessen. Danke an Sophie, Nils, Julius und Rolf für diese tolle Woche mit Windsurfen, mit langen aber mindestens genauso lustigen Autofahrten und mit den fantastischen Trips zu Don Felipe und seiner Höhle.

In meiner Zeit am Institut und in Heidelberg sind mir viele Menschen sehr ans Herz gewachsen. Bei allen meinen Freund*innen möchte ich mich dafür bedanken, dass es euch gibt und dass ihr mein Leben bereichert. Ihr seid großartig.

Tobi, dir danke ich dafür, dass du es mit mir auch in der anstrengenden Zeit der letzten Wochen ausgehalten hast und für mich da bist. Du hast mich immer unterstützt und das bedeutet mir sehr viel.

Zuletzt bin ich meiner Familie dankbar dafür, dass sie mir ermöglicht hat, diesen Weg einzuschlagen. Ganz besonderes möchte ich meinen Eltern Danke sagen, die mir immer den größten Rückhalt geben, den man sich wünschen kann. Ich danke euch dafür von ganzem Herzen.

